CHARACTERIZATION FRAMEWORK FOR BOND MECHANICS AT THE MINERALIZED TISSUE – ADHESIVE INTERFACE

By

Author: Rizacan Sarikaya

Submitted to the graduate degree program in Mechanical Engineering and the Graduate Faculty of the University of Kansas in partial fulfillment of the requirements for the degree of Doctor of Philosophy

Dr. Anil Misra, Chairperson

Dr. Paulette Spencer

Committee members

Dr. Candan Tamerler

Dr. Huazhen Fang

Dr. Mikhail Medvedev

Date Defended: Nov 20th, 2020

The Dissertation Committee for Rizacan Sarikaya certifies that this is the approved version of the following dissertation:

Characterization Framework for Bond Mechanics at the Mineralized Tissue – Adhesive Interface

Dr. Anil Misra, Chairperson

Date approved: Nov 20th, 2020

Abstract

The mechanical performance of the dentin-adhesive interface controls the overall failure of the dental restorations. This performance is evaluated by the bond strength tests, such as the micro-tensile test. The conventional bond strength tests suffer from large variations in the test results. They are also not capable of monitoring the local failure mechanisms. These challenges limit their ability to effectively support the design of dental restorative materials. Therefore, this present study focuses on a mechanical characterization framework to overcome these challenges. In this characterization framework, mechanical testing is complemented by mathematical modeling for a comprehensive understanding of the material behaviors. A granular micromechanics nonlinear material model was developed and implemented into a commercial finite element (FE) analysis software. This model captured the rate dependent nonlinear material behavior with damage and plasticity. The diametral compression test application overcame the challenges in the tensile and the interfacial mechanical tests. The mechanical behavior of the mineralized tissue, the adhesive polymer and the mineralized tissue – adhesive interface was obtained by using the diametral compression test. The dentin-adhesive interface consists of the dentin (the mineralized tissue), the adhesive polymer and the hybrid layer. The hybrid layer is composed of the demineralized dentin and the adhesive resin. Physical experiments can obtain the overall mechanical strength at the mineralized tissue – adhesive interface. However, it is critical to characterize the hybrid layer's mechanical behavior locally. Therefore, the developed diametral compression test simulations enabled obtaining the mechanical behavior of the mineralized tissue, the adhesive polymer and the hybrid layer. Two different adhesive formulations were studied to investigate the self-strengthening property. Building on the learnings of the mechanical characterization and the design

criteria, the simulations successfully captured the nonlinear rate dependent mechanical behavior of materials in the physical experiments. The self-strengthening property was shown to provide superior mechanical performance to the adhesive polymer and the mineralized tissue – adhesive interface. The results also indicated that a local failure might be initiated in the hybrid layer while the interface is still intact. This local failure was shown to affect stress distributions in the mineralized tissue and eventually lead to its failure.

Acknowledgements

First of all, I would like to express my gratitude to my advisor, Dr. Anil Misra, for providing me invaluable supervision, precious guidance, and continuous support during my graduate studies.

I would also like to thank Dr. Paulette Spencer and Dr. Candan Tamerler for their constant support, invaluable guidance while providing me inspiring perspectives and serving on my doctoral committee.

I also wish to thank Dr. Huazhen Fang and Dr. Mikhail Medvedev for providing me their invaluable suggestions and serving on my doctoral committee.

I also gratefully acknowledge the support for this work from the National Institute of Dental and Craniofacial Research, the National Institutes of Health, Bethesda, Maryland, grant number R01DE025476 and the United States National Science Foundation grant number CMMI-1727433.

I would also like to thank my fellow lab members for their positive support and motivation for my research.

Finally, I would like to express my gratitude to my family for their infinite love, emotional support, and encouragement.

Table of Contents

List of figures

List of tables

CHAPTER 1

INTRODUCTION

1.1 Motivation

Dental caries constitutes a worldwide health problem. 3.5 billion cases were reported worldwide regarding this health problem in 2017 [1-7]. In practice, dental caries is treated with resin-based composites [8, 9]. This treatment is a temporary solution due to its limited service lifetime between 5 and 7 years [10]. The lifetime and the performance of dental restorative materials can be improved with an effective design of materials. Design procedures for dental restorative materials involve labor-intensive and long-term steps such as synthesis, characterization, and optimization. In particular, the characterization of their mechanical behavior is relatively challenging. Mechanical characterization is performed to evaluate the bond strength at the dentin–adhesive interface. Commonly preferred techniques are tensile, micro tensile, shear, micro shear, pull- and push-out tests [11-18]. From this variety of techniques, the micro tensile tests are reported to allow relatively reliable characterization of the mechanical behavior [17-19]. However, the bond strength data reported on the dentin – adhesive interface also contains large variations in micro tensile mode [20, 21]. Even after tedious and time-taking specimen preparation and test steps, conventional characterization methods might inform the design with very limited level of accuracy. Accuracy of the measured mechanical properties is critical for estimating clinical performance.

Complementary methods are required to improve the accuracy and capabilities of the conventional characterization methods. Mathematical modeling is an advanced and complementary technique

to further improve the insight provided by mechanical characterization. Mechanical tests can be modeled using Finite Element (FE) Analysis. This analysis provides (a) the estimation of the material properties and (b) the prediction of mechanical performance under different conditions. However, the commonly used classical elastic continuum mechanics limits the capabilities of mathematical modeling [22]. The dentin-adhesive interface consists of the dentin and a methacrylate-based polymer. These materials are known to have a rate dependent nonlinear mechanical behavior [23-25]. Therefore, mathematical modeling of the dentin-adhesive interface requires to cover the phenomena, such as the nonlinear mechanical behavior and the rate-dependence. The nonlinear viscoelastic nature of materials was modeled by a number of researchers as reported earlier [26-32]. Moreover, numerous studies addressed various phenomena in models, such as the enhanced description of elasticity and the rate-dependence, as well as the plasticity and damage with nonlocal effects [33-43]. Many recent studies focused on modeling granular material systems such as rock, concrete, soils and asphalt [37, 39, 44-54]. These models may provide the abovementioned mathematical modeling assistance for an improved understanding of the mechanical behavior of the dentin-adhesive interface. However, these studies mainly considered the mechanical phenomena at macro-scales. The dentin (mineralized tissue) and the adhesive polymers are materials with granular microstructures. Their macroscopic behavior significantly depends on their micro-scale features, such as the microstructure and the micromechanical properties. This dependence needs to be considered in mathematical modeling of the dentin-adhesive interface.

1.2 Objective and scope

This Ph.D. work proposed a characterization framework for evaluating the bond strength at the mineralized tissue - adhesive interface. The framework was established on correlations between physical experimentations and mathematical modeling. Therefore, the developed characterization framework addresses two major aspects stated in the Motivation. For the experimental aspect, the diametral compression test was preferred for evaluating the mechanical behavior of each material and the bond strength at the interface. The main advantage of the diametral compression test is the load application without any additional attachment or fixation, unlike the complicated conventional tensile tests. This advantage provides a relatively successful application of the desired boundary conditions. Therefore, the repeatability of the test results improves drastically. For the mathematical modeling aspect, the method of granular micromechanics was utilized. The advantage of this method is bridging the material's macro-scale mechanical behavior with its micro-scale features. A granular micromechanics nonlinear material model with damage and plasticity was developed by merging two preceding granular micromechanics models [55, 56]. This development enhanced the model's capability to capture the nonlinear rate dependent mechanical behavior of strongly granular systems, such as the mineralized tissue and the highly cross-linked polymers.

In this research, the granular micromechanics material model was developed and implemented into a commercial FE code. Moreover, the diametral compression test was used to characterize (i) the tensile mechanical behavior of the mineralized tissue, (ii) the tensile mechanical behavior of the adhesive polymer, and (iii) the bond strength at the mineralized tissue – adhesive interface at two different loading rates: (a) 0.2 mm/min and (b) 1 mm/min. Furthermore, the diametral compression test FE models were optimized for the numerical accuracy and the computational time. The

nonlinear material model parameters were subsequently calibrated and validated against the generated experimental data to capture the nonlinear rate dependent mechanical behavior of the materials. These material model parameters were uniquely assigned for each material: (1) the mineralized tissue, (2) the adhesive polymer, (3) the mineralized tissue – adhesive hybrid layer. Mechanical behaviors of the adhesive polymer and the mineralized tissue-adhesive polymer interface were studied for two adhesive formulations. These adhesive formulations differed by means of their self-strengthening properties. After determining the model parameters for each material, their failure and damage mechanisms were investigated. Finally, FE simulations were performed to predict the clinical mechanical performance of each material as well as their uniaxial tensile behavior under the studied loading rates.

1.3 Dissertation outline

Chapter 1 – Introduction: This chapter covers the addressed scientific challenge, the developed approach to target this challenge, and the outline of this research work.

Chapter 2 – Granular Micromechanics Based Nonlinear Material Model: This chapter presents the development of the granular micromechanics nonlinear material model. The developed material model was implemented into a commercial FE code. The material model's numerical accuracy was evaluated by using a single patch test model. Moreover, the material model's nonlinear rate dependent capability was demonstrated.

Chapter 3 – Experimental Investigation of Tensile Nature of the Mineralized Tissue and Polymer Adhesive, and the Bond Strength at the Mineralized Tissue – Adhesive Interface: This chapter presents the results from the diametral compression test of the mineralized tissue and the adhesive

polymer as well as the interfacial test of the mineralized tissue – adhesive interface. The generated experimental data were used for the material model parameters in Chapter 5 and Chapter 6.

Chapter 4 – Parametric Study for Computational Analysis of the Diametral Compression Test: This chapter presents the optimization of the developed material model's numerical accuracy and computational time when it is implemented into the diametral compression FE model. Moreover, the rate dependent capability of the model was demonstrated in the diametral compression test simulations with the estimated material model parameters for the mineralized tissue and the adhesive polymer.

Chapter 5 – Prediction of Rate-dependent Tensile Damage and Failure of the Mineralized Tissue and Adhesive Polymers: Calibration, Validation and Prediction: This chapter presents the calibration and the validation of the material model parameters using the experimental data obtained for the mineralized tissue and the adhesive polymers in Chapter 3. After the calibration and the validation were completed, each material's failure mechanism was investigated and their behavior was predicted at clinical loading conditions. Moreover, the uniaxial tensile behavior of each material was simulated under the studied loading rates.

Chapter 6 – Prediction of Bond Mechanics at the Mineralized Tissue and Adhesive Interface: Calibration, Validation and Prediction: This chapter presents the calibration and the validation of the hybrid layers' material model parameters against the experimental data presented in Chapter 3. The calibrated and validated model parameters were utilized to investigate the failure mechanism at the mineralized tissue – adhesive interface. Moreover, the clinical mechanical performance of the interface was simulated. The uniaxial tensile behavior of each hybrid layer material was predicted under the studied loading rates.

Chapter 7 – Summary, Conclusions and Future Directions: This chapter summarizes this research work's findings and conclusions. It also states the possible future directions.

CHAPTER 2

GRANULAR MICROMECHANICS BASED NONLINEAR MATERIAL MODEL

2.1 Introduction

Materials, such as the mineralized tissue, polymers, concrete and soft materials, possess nonlinear and rate dependent mechanical properties. Methacrylate-based polymers, a member this material family, are typically used for repairing damaged teeth. A composite tooth restoration consists of methacrylate-based polymer adhesive and the dentin. The rate-dependent nonlinear mechanical behavior of these materials [23-25] dictates the overall performance of dental restoration. Dental restorative material design benefits mechanical tests to understand the mechanical behavior of adhesives and the mineralized tissue. However, physical experiments have limited access to the true nature of materials. It is also noted that there may be difficulties in applying the desired boundary conditions in mechanical tests [57, 58]. These difficulties may eventually lead to errors in the interpretation of the results and evaluation of the mechanical properties. For this reason, dental restorative material design requires the assistance of an advanced and complementary technique, such as mathematical modeling. Mathematical modeling can represent nonlinear and rate-dependent mechanical behavior without intensive physical experimentation. Modeling can also unlock the information that is not directly available through mechanical testing. In other words, it can inform stress and strain distributions within the domain of interest. This information is critical to investigate damage and failure mechanisms of the mineralized tissue and polymer

adhesive as well as the mineralized tissue – adhesive interface. Moreover, mathematical modeling can serve as a predictive tool to estimate clinical performance of dental restorative materials.

Many constitutive models were proposed in the literature to represent nonlinear viscoelastic nature of materials [26-32]. Numerous models also target various aspects, such as enhanced elasticity description, rate-dependence, plasticity and damage with nonlocal effects [33-43]. Additionally, recent studies developed models focusing on granular material systems such as rocks, concrete, soils, and asphalt [37, 39, 44-54]. While addressing various phenomena in mechanics, these studies mainly consider the macroscopic mechanisms. However, granular materials' macro-scale mechanical behavior significantly depends on their features, such as microstructure and micromechanical properties. Hence, the granular micromechanics approach arises to bridge discrete and continuum modeling. This bridging informs material's macroscopic behavior with its micro-scale nature. This modeling approach originates from grain packing continuum model studies [59-63]. Later, it developed a method for introducing micro-scale mechanisms' influence into continuum description [64, 65]. Recently, the granular micromechanics approach resulted in material models addressing various phenomena, such as rate-dependent damage, rate-independent coupled damage and plasticity, and rate-dependent coupled damage and plasticity [66-68].

The method of granular micromechanics conceptualizes a material point as an assembly of grains where each grain interacts with adjacent grains. The macroscopic constitutive laws are established by relating the Cauchy stress to micro-scale force-displacement relationships. These relationships are derived for inter-granular interactions. Accordingly, the micro-scale constitutive equations are established based on a micro-scale Clausius-Duhem type inequality with free energy and dissipation functions applicable to grain interactions.

This study proceeded with the granular micromechanics method as it is a suitable method to represent the nature of materials, such as the mineralized tissue and adhesive polymers. The mineralized tissue possesses a granular nature where grains of apatite mineral interact with each other at local scales. At the same time, collagen molecules mediate these interactions. Similarly, mechanical behavior of cross-linked polymers can be defined from the viewpoint of granular micromechanics. In cross-linked polymers, covalent bonds can be treated as local interactions at cross-links. Consequently, this study combined two preceding granular micromechanics nonlinear material models [55, 56] to develop a rate-dependent coupled damage and plasticity model (see the Appendix A). Uniquely, this material model coupled normal and shear interactions at grain-scale. Due to this enhancement, the nonlinear material model's capability was improved to capture grain interactions in strongly granular systems, such as the mineralized tissue and highly cross-linked polymers. Furthermore, the developed granular micromechanics material model was implemented into finite element analysis. The model was written as a user-defined nonlinear material model in visual Fortran composer (Intel, Santa Clara, CA) (see the Appendix B) and implemented into a commercial finite element analysis software (Simulia/ABAQUS V 6.13-3, Dassault Systémes, RI, USA). Subsequently, a single element patch test was performed to investigate the material model's numerical accuracy and demonstrate its rate-dependent capability.

2.2 Materials and Methods

2.2.1 Thermomechanics at Macro-scale

Granular micromechanics conceptualizes the material point as an assembly of grains interacting with adjacent grains. Particularly, volume averages of the contributions of grain-pair interactions

to dissipation potential and free energy are used to establish the dissipation potential and Helmholtz free energy functions, respectively, at macro-scale. Proper constitutive laws are defined for grain-pair interactions based upon a Clausius-Duhem type inequality, which is derived for grain-scale interactions [68].

This study merged two preceding nonlinear granular micromechanics material models created by Misra and Poorsolhjouy [55, 56]. To start with, Clausius-Duhem inequality is considered for a rate-dependent material with damage and plasticity as:

$$p^i - \dot{W} - S\dot{\theta} - \frac{q_k \theta_{,k}}{\theta} = d \geq 0 \tag{2.1}$$

where the power density function, the Helmholtz free energy, the entropy per unit volume, the heat flux vector and the dissipation per unit volume are denoted as p^i, W, S, θ, q_k and d, respectively. In particular, the power density function is incorporated using $p^i = \sigma_{ij}\dot{\varepsilon}_{ij}$ where σ_{ij} and $\dot{\varepsilon}_{ij}$ are the Cauchy stress and the symmetric part of the first gradient of displacement, respectively. It is important to realize that the superimposed dot ($\dot{}$) indicates the time derivative.

The Helmholtz free energy density is written as $W = W(\varepsilon_{ij}, \varepsilon_{ij}^v, \varepsilon_{ij}^p, D_{ij}, \theta)$ where it is a function of the independent kinematic variable, the rate-dependent internal variable, the second internal variable related to plastic processes, the third internal variable related to damage and the temperature, respectively [68]. In like manner, the dissipation potential, ψ, is taken as the function $\psi = \psi(\varepsilon_{ij}, \theta, \varepsilon_{ij}^v, \dot{\varepsilon_{ij}^v}, D_{ij}, \dot{D_{ij}}, \varepsilon_{ij}^p, \dot{\varepsilon_{ij}^p})$ and the dissipation per unit volume is expressed as:

$$d = \frac{\partial \psi}{\partial \dot{\varepsilon}_{ij}^v}\dot{\varepsilon}_{ij}^v + \frac{\partial \psi}{\partial \dot{D}_{ij}}\dot{D}_{ij} + \frac{\partial \psi}{\partial \dot{\varepsilon}_{ij}^p}\dot{\varepsilon}_{ij}^p \geq 0 \tag{2.2}$$

The following equation is derived by incorporating (2.2) into (2.1) in consideration with the stated Helmholtz free energy density function and neglecting the heat flux:

$$\left(\sigma_{ij}-\frac{\partial W}{\partial \varepsilon_{ij}}\right)\dot{\varepsilon}_{ij}-\left(\frac{\partial W}{\partial \varepsilon_{ij}^{v}}+\frac{\partial \psi}{\partial \dot{\varepsilon}_{ij}^{v}}\right)\dot{\varepsilon}_{ij}^{v}-\left(\frac{\partial W}{\partial D_{ij}}+\frac{\partial \psi}{\partial \dot{D}_{ij}}\right)\dot{D}_{ij} - \left(\frac{\partial W}{\partial \varepsilon_{ij}^{p}}+\frac{\partial \psi}{\partial \dot{\varepsilon}_{ij}^{p}}\right)\dot{\varepsilon}_{ij}^{p}-\left(\frac{\partial W}{\partial \theta}+S\right)\dot{\theta}=0 \tag{2.3}$$

where the definition of the Cauchy stress is resulted in the first term. Moreover, Ziegler's orthogonality conditions related to rate-dependence, damage and plasticity are retrieved from the second, the third and the fourth terms, respectively. The relationship between entropy and free energy is given in the last term.

2.2.2 Kinematics at Micro-scale

At this point, the method of granular micromechanics diverges from conventional continuum approaches. The granular system is assessed at its micro-scale through micro-scale quantities in consideration of grain-pair interactions. To this end, kinematics of a granular meso-structure is taken into account to start with. A relative displacement, δ_i^{α}, is resulted between two grains, *n* and *p*, by applying an external load. The following relationship is derived where these grains are involved in α-th grain-pair interaction and they are considered to translate but their rotation is neglected:

$$\delta_i^{\alpha} = u_i^{p} - u_i^{n} \tag{2.4}$$

Displacements of grains are denoted as u_i each with corresponding superscript referring to each grain. This discrete model transitions into a continuum description by deriving the displacement of grain *p* where the Taylor series expansion of the displacement is considered:

$$u_i^{p} = u_i^{n} + u_{i,j}^{n}(x_j^{p} - x_j^{n}) \tag{2.5}$$

The centroid of grain *n* is taken as the expansion point and the displacement gradient, the position vectors to the centroid of grains *n* and *p* are denoted as $u_{i,j}^{n}$, x_j^n and x_j^p, respectively. The relative displacement of the α-th grain-pair interaction is derived in terms of the displacement gradient by incorporating (2.5) into (2.4) as the following:

$$\delta_i^{\alpha} = u_{i,j}^{n}\left(x_j^p - x_j^n\right) = u_{i,j}^{n} l_j^{\alpha} \tag{2.6}$$

where l_j^{α} denotes the branch vector joining centroids of grains *n* and *p*.

Furthermore, a local Cartesian coordinate system is introduced to derive force-displacement relationships for intergranular interactions conveniently. In detail, the local coordinate system is composed of three unit vectors. The first one is the unit normal vector, n_i, in direction of the branch vector joining centroids of grain-pair. The second and the third ones are the unit vectors, s_i and t_i, that lie on a plane perpendicular to the unit normal vector as the following:

$$\begin{aligned} n_i &= \langle cos\theta, sin\theta cos\emptyset, sin\theta sin\emptyset \rangle \\ s_i &= \langle -sin\theta, cos\theta cos\emptyset, cos\theta sin\emptyset \rangle \\ t_i &= \langle 0, -sin\emptyset, cos\emptyset \rangle \end{aligned} \tag{2.7}$$

The relative displacement of a grain-pair is decomposed into a normal component, δ_n, and a shear component, δ_w. These two vectors are derived by using the local coordinate system as:

$$\begin{aligned} \delta_n &= \delta_i\, n_i \\ \delta_s &= \delta_i\, s_i \\ \delta_t &= \delta_i\, t_i \\ \delta_w &= \sqrt{(\delta_i s_i)^2 + (\delta_i t_i)^2} \end{aligned} \tag{2.8}$$

Besides, further decomposition of the relative displacement is carried out to incorporate the rate-dependence into the grain-pair interaction in consideration with an analogy to a Zener element as:

$$\delta_j^\alpha = \delta_j^{e\alpha} + \delta_j^{v\alpha} \tag{2.9}$$

where the elastic component and the rate-dependent component are denoted using superscripts *e* and *v*, respectively. Accordingly, the inter-granular displacements in normal and shear directions are expressed as $\delta_n^\alpha = \delta_n^{e\alpha} + \delta_n^{v\alpha}$ and $\delta_w^\alpha = \delta_w^{e\alpha} + \delta_w^{v\alpha}$, respectively.

2.2.3 Thermomechanics at Micro-scale

Moreover, macroscopic Helmholtz free energy density and dissipation potential functions are derived accounting for the volume averages of their counterparts at grain-scale in order to establish the thermomechanics framework for a granular material as the following [68]:

$$W = \frac{1}{V}\sum_{\alpha}^{N} W^\alpha(\delta_j^\alpha, \delta_j^{v\alpha}, D_j^\alpha, \delta_j^{p\alpha}, \theta^\alpha) \tag{2.10a}$$

$$\psi = \frac{1}{V}\sum_{\alpha=1}^{N} \psi^\alpha(\delta_j^\alpha, \delta_j^{v\alpha}, \dot{\delta}_j^{v\alpha}, D_j^\alpha, \dot{D}_j^\alpha, \delta_j^{p\alpha}, \dot{\delta}_j^{p\alpha}, \theta^\alpha) \tag{2.10b}$$

where the total number of grain-pair interactions, the contributions of α-th grain-pair interaction to the free energy and to the dissipation potential, the grain-scale displacement vector, the grain-scale rate-dependent internal variable, the grain-scale internal variable related to damage, the grain-scale internal variable related to plasticity and micro-scale temperature related to α-th grain-pair interaction are denoted as N, W^α, ψ^α, δ_j^α, $\delta_j^{v\alpha}$, D_j^α, $\delta_j^{p\alpha}$ and θ^α, respectively.

In this case, the expression for the macroscopic Cauchy stress is established by incorporating (2.10a) into the first term of (2.3) as the following:

$$\sigma_{ij} = \frac{\partial W}{\partial \varepsilon_{ij}} = \frac{1}{V}\sum_{\alpha=1}^{N} \frac{\partial W^\alpha}{\partial \delta_k^\alpha}\frac{\partial \delta_k^\alpha}{\partial \varepsilon_{ij}} = \frac{1}{V}\sum_{\alpha=1}^{N} f_k^\alpha \frac{\partial \delta_k^\alpha}{\partial \varepsilon_{ij}} \tag{2.11}$$

where chain rule of differentiation is applied and the intergranular force, f_k^α, is taken to be the derivative of inter-granular energy with respect to the displacement: $f_k^\alpha = \frac{\partial W^\alpha}{\partial \delta_k^\alpha}$.

Furthermore, the Clausius-Duhem inequality for α-th grain-pair interaction is obtained by incorporating (2.10a), (2.10b) and (2.11) into (2.1) as the following:

$$f_j^\alpha \dot{\delta}_j^\alpha - \dot{W}^\alpha - S^\alpha \dot{\theta}^\alpha = d^\alpha \geq 0 \tag{2.12}$$

where the inter-granular force, the inter-granular displacement and contributions of α-th grain-pair interaction to the free energy and the entropy and micro-scale temperature related to α-th grain-pair interaction are denoted as f_j^α, δ_j^α, W^α, S^α, θ^α. Additionally, the dissipation potential contributed by α-th grain-pair interaction is represented as d^α and it is defined by using the micro-scale dissipative potential, ψ^α, as the following:

$$d^\alpha = \frac{\partial \psi^\alpha}{\partial \dot{\delta}_j^{v\alpha}} \dot{\delta}_j^{v\alpha} + \frac{\partial \psi^\alpha}{\partial \dot{\delta}_j^{p\alpha}} \dot{\delta}_j^{p\alpha} + \frac{\partial \psi^\alpha}{\partial \dot{D}_j^\alpha} \dot{D}_j^\alpha \tag{2.13}$$

The following relationship is established by incorporating contributions of α-th grain-pair interaction to the free energy and the dissipation potential, W^α and d^α, respectively, into (2.12):

$$\begin{aligned} &\left(f_j^\alpha - \frac{\partial W^\alpha}{\partial \delta_j^\alpha}\right)\dot{\delta}_j^\alpha - \left(\frac{\partial W}{\partial \delta_j^{v\alpha}} + \frac{\partial \psi^\alpha}{\partial \dot{\delta}_j^{v\alpha}}\right)\dot{\delta}_j^{v\alpha} - \left(\frac{\partial W}{\partial D_j^\alpha} + \frac{\partial \psi^\alpha}{\partial \dot{D}_j^\alpha}\right)\dot{D}_j^\alpha \\ &\qquad - \left(\frac{\partial W}{\partial \delta_j^{p\alpha}} + \frac{\partial \psi^\alpha}{\partial \dot{\delta}_j^{p\alpha}}\right)\dot{\varepsilon}_{ij}^p - \left(\frac{\partial W^\alpha}{\partial \theta_j^\alpha} + S^\alpha\right)\dot{\theta}_j^\alpha = 0 \end{aligned} \tag{2.14}$$

where the micro-scale quasi-conservative inter-granular force, f_j^α, is retrieved from the first term.

2.2.4 Rate-dependent Coupled Damage and Plasticity at Micro-scale

Moreover, the micro-scale orthogonality conditions and the entropy production of the α-th grain-pair interaction are resulted in the second, the third and the fourth terms, respectively. In this particular model, the temperature effects are neglected.

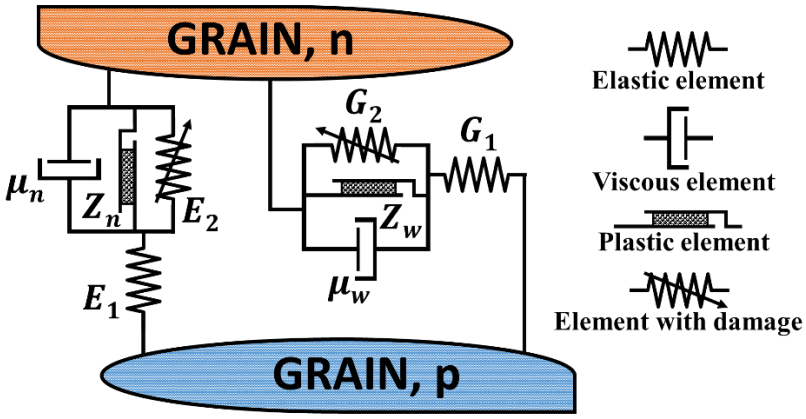

Figure 2.1: Rheological model representing inter-granular interactions.

A micro-scale rheological element is used to model inter-granular interactions in the normal and shear directions (Figure 2.1). In further discussion, normal and shear components are represented with subscripts *n* and *w*, respectively. The grain-scale mechanical dissipative potential is expressed as the sum of dissipations related to viscous, damage and plastic processes as the following classical form:

$$\psi_n^\alpha = \frac{1}{2}\mu_n^\alpha\left(\dot{\delta}_n^{v\alpha}\right)^2 + Y_n^\alpha\left|\dot{D}_n^\alpha\right| + Z_n^\alpha\left|\dot{\delta}_n^{p\alpha}\right| \tag{2.15}$$

$$\psi_w^\alpha = \frac{1}{2}\mu_w^\alpha\left(\dot{\delta}_w^{v\alpha}\right)^2 + Y_w^\alpha\left|\dot{D}_w^\alpha\right| + Z_w^\alpha\left|\dot{\delta}_w^{p\alpha}\right|$$

$$\psi^{\alpha} = \psi_n^{\alpha} + \psi_w^{\alpha}$$

where the micro-scale viscosity and the conjugate forces to the grain-scale damage and plastic dissipation are denoted as μ, Y and Z, respectively. Moreover, the micro-scale dissipative potential is written as the sum of the normal and shear components.

The grain-scale free energy is expressed in consideration with elastic deformation and the rate-dependent process that is subject to damage and plasticity as the following:

$$\begin{aligned} W_n^{\alpha} &= \frac{1}{2} E_1^{\alpha} (\delta_n^{e\alpha})^2 + \frac{1}{2} E_n^{\alpha} (1 - D_n^{\alpha}) (\delta_n^{v\alpha})^2 (1 - \beta_n^{\alpha}) \\ W_w^{\alpha} &= \frac{1}{2} G_1^{\alpha} (\delta_w^{e\alpha})^2 + \frac{1}{2} G_w^{\alpha} (1 - D_w^{\alpha}) (\delta_w^{v\alpha})^2 (1 - \beta_w^{\alpha}) \\ W^{\alpha} &= W_n^{\alpha} + W_w^{\alpha} \end{aligned} \tag{2.16}$$

where E_1^{α} and E_n^{α} denote the grain-scale elastic stiffnesses in the normal direction whereas G_1^{α} and G_w^{α} are elastic stiffnesses in the shear direction. D^{α} is the inter-granular damage parameter. Moreover, β^{α} is the constant plastic parameter whose value varies between 0 and 1. It is separately defined for each normal and shear directions as $\beta_n^{\alpha} = \frac{\delta_n^{p\alpha}}{\delta_n^{v\alpha}}$ and $\beta_w^{\alpha} = \frac{\delta_w^{p\alpha}}{\delta_w^{v\alpha}}$ where the viscous component and the plastic component are denoted by superscripts *v* and *p*, respectively. The following expression is obtained by substituting β_n^{α} and β_w^{α} into (2.16):

$$\begin{aligned} W_n^{\alpha} &= \frac{1}{2} E_1^{\alpha} (\delta_n^{e\alpha})^2 + \frac{1}{2} E_n^{\alpha} (1 - D_n^{\alpha}) \delta_n^{v\alpha} (\delta_n^{v\alpha} - \delta_n^{p\alpha}) \\ W_w^{\alpha} &= \frac{1}{2} G_1^{\alpha} (\delta_w^{e\alpha})^2 + \frac{1}{2} G_w^{\alpha} (1 - D_w^{\alpha}) \delta_w^{v\alpha} (\delta_w^{v\alpha} - \delta_w^{p\alpha}) \end{aligned} \tag{2.17}$$

Correspondingly, the grain-scale mechanical dissipative potential is further derived as the following by using (2.15) in consideration with the constant plastic parameter, β^{α}, defined above:

$$\psi_n^{\alpha} = \frac{1}{2} \mu_n^{\alpha} \left(\dot{\delta}_n^{v\alpha}\right)^2 + Y_n^{\alpha} \left|\dot{D}_n^{\alpha}\right| + Z_{1n}^{\alpha} \left|\dot{\delta}_n^{v\alpha}\right| + Z_{2n}^{\alpha} \left|\dot{\delta}_n^{p\alpha}\right| \tag{2.18}$$

$$\psi_w^\alpha = \frac{1}{2}\mu_w^\alpha\left(\dot{\delta}_w^{v\alpha}\right)^2 + Y_w^\alpha\left|\dot{D}_w^\alpha\right| + Z_{1w}^\alpha\left|\dot{\delta}_w^{v\alpha}\right| + Z_{2w}^\alpha\left|\dot{\delta}_w^{p\alpha}\right|$$

where the plastic dissipation is expressed by using viscous and plastic components.

Furthermore, the dissipative force duals in normal and shear directions, χ_n^α and χ_w^α, of grain-scale plastic displacements, $\delta_n^{p\alpha}$ and $\delta_w^{p\alpha}$, are derived by incorporating (2.17) and (2.18) into the inter-granular orthogonality condition provided in the fourth term of (2.14) associated with plasticity as:

$$\begin{aligned}\chi_n^\alpha &= -\frac{\partial W^\alpha}{\partial \delta_n^{p\alpha}} = Z_{2n}^\alpha sign(\dot{\delta}_n^{p\alpha}) \\ \chi_w^\alpha &= -\frac{\partial W^\alpha}{\partial \delta_w^{p\alpha}} = Z_{2w}^\alpha sign(\dot{\delta}_w^{p\alpha})\end{aligned} \tag{2.19}$$

where Z_{2n}^α and Z_{2w}^α are defined as:

$$\begin{aligned}Z_{2n}^\alpha &= \frac{1}{2}E_n^\alpha(1-D_n^\alpha)\delta_n^{v\alpha} \\ Z_{2w}^\alpha &= \frac{1}{2}G_w^\alpha(1-D_w^\alpha)\delta_w^{v\alpha}\end{aligned} \tag{2.20}$$

Since (2.15) provides the force, *Z*, conjugate to micro-scale plastic dissipation in classical form as $Z_n^\alpha = \beta_n^\alpha E_n(1-D_n)\,\delta_n^{v\alpha}$ and $Z_w^\alpha = \beta_w^\alpha G_w(1-D_w)\,\delta_w^{v\alpha}$ [68], the following expressions are derived by using (2.18) and (2.20):

$$\begin{aligned}Z_{1n}^\alpha &= \frac{1}{2}E_n^\alpha(1-D_n^\alpha)\delta_n^{p\alpha} \\ Z_{1w}^\alpha &= \frac{1}{2}G_w^\alpha(1-D_w^\alpha)\delta_w^{p\alpha}\end{aligned} \tag{2.21}$$

Furthermore, the following relationships are derived in order to obtain micro-scale constitutive equations in normal and shear directions during loading by incorporating (2.9) into the second term of (2.14) accounting for grain-scale free energy and dissipative potential given in (2.17) and (2.18):

$$-E_1^\alpha(\delta_n^\alpha-\delta_n^{v\alpha})+E_n^\alpha\delta_n^{v\alpha}(1-D_n^\alpha)-\frac{1}{2}E_n^\alpha\delta_n^{p\alpha}(1-D_n^\alpha)+\mu_n^\alpha\dot{\delta}_n^{v\alpha}+Z_{1n}^\alpha=0$$
$$-G_1^\alpha(\delta_w^\alpha-\delta_w^{v\alpha})+E_w^\alpha\delta_w^{v\alpha}(1-D_w^\alpha)-\frac{1}{2}E_w^\alpha\delta_w^{p\alpha}(1-D_w^\alpha)+\mu_w^\alpha\dot{\delta}_w^{v\alpha}+Z_{1w}^\alpha=0 \quad (2.22)$$

Finally, the micro-scale constitutive relationship is established as the following by grouping the terms in (2.22) to form $f_j^\alpha=f_j^\alpha(\delta_j^\alpha,\dot{\delta}_j^\alpha,\dot{f}_j^\alpha)$ in consideration with (2.22) and the first term of (2.14) combined with (2.9) resulting $f_n^\alpha=\frac{\partial W^\alpha}{\partial\delta_n^\alpha}=E_1^\alpha(\delta_n^\alpha-\delta_n^{v\alpha})$ and $f_w^\alpha=\frac{\partial W^\alpha}{\partial\delta_w^\alpha}=G_1^\alpha(\delta_w^\alpha-\delta_w^{v\alpha})$:

$$f_n^\alpha=\frac{E_1^\alpha E_n^\alpha(1-D_n^\alpha)}{E_1^\alpha+E_n^\alpha(1-D_n^\alpha)}\delta_n^\alpha+\frac{E_1^\alpha\mu_n^\alpha}{E_1^\alpha+E_n^\alpha(1-D_n^\alpha)}\dot{\delta}_n^\alpha-\frac{\mu_n^\alpha}{E_1^\alpha+E_n^\alpha(1-D_n^\alpha)}\dot{f}_n^\alpha$$
$$f_w^\alpha=\frac{G_1^\alpha G_n^\alpha(1-D_w^\alpha)}{G_1^\alpha+G_w^\alpha(1-D_w^\alpha)}\delta_w^\alpha+\frac{G_1^\alpha\mu_w^\alpha}{G_1^\alpha+G_w^\alpha(1-D_w^\alpha)}\dot{\delta}_w^\alpha-\frac{\mu_w^\alpha}{G_1^\alpha+G_w^\alpha(1-D_w^\alpha)}\dot{f}_w^\alpha \quad (2.23)$$

Moreover, the micro-scale constitutive relationships in normal and shear directions are simplified as the following:

$$f_n^\alpha=K_n^\alpha\delta_n^\alpha+\eta_n^\alpha\dot{\delta}_n^\alpha-\zeta_n^\alpha\dot{f}_n^\alpha \quad (2.24a)$$
$$f_w^\alpha=K_w^\alpha\delta_w^\alpha+\eta_w^\alpha\dot{\delta}_w^\alpha-\zeta_w^\alpha\dot{f}_w^\alpha$$

where K, η and ζ denote the grain-scale stiffness, the grain-scale viscosity parameter and the grain-scale relaxation parameter, respectively, and defined as the following:

$$K_n^\alpha=\frac{E_1^\alpha E_n^\alpha(1-D_n^\alpha)}{E_1^\alpha+E_n^\alpha(1-D_n^\alpha)};\ \eta_n^\alpha=\frac{E_1^\alpha\mu_n^\alpha}{E_1^\alpha+E_n^\alpha(1-D_n^\alpha)};\ \zeta_n^\alpha=\frac{\mu_n^\alpha}{E_1^\alpha+E_n^\alpha(1-D_n^\alpha)};$$
$$K_w^\alpha=\frac{G_1^\alpha G_n^\alpha(1-D_w^\alpha)}{G_1^\alpha+G_w^\alpha(1-D_w^\alpha)};\ \eta_w^\alpha=\frac{G_1^\alpha\mu_w^\alpha}{G_1^\alpha+G_w^\alpha(1-D_w^\alpha)};\ \zeta_w^\alpha=\frac{\mu_w^\alpha}{G_1^\alpha+G_w^\alpha(1-D_w^\alpha)} \quad (2.24b)$$

2.2.5 Loading, Unloading and Reloading at Micro-scale

The micro-scale stiffness, viscosity and relaxation parameters in normal direction are calculated differently by evaluating whether the inter-granular interaction is under tension or compression in normal direction [56, 66]. In detail, the inter-granular displacement in normal direction, δ_n^α, is assessed to determine whether the α-th grain-pair interaction experiences tension or compression. The grain-scale stiffness in normal, E_n^α and the grain-scale viscosity parameter in normal, μ_n^α are computed as the following:

$$E_n^\alpha = \begin{cases} E_{no}^{T\alpha}; & \delta_n^\alpha(t) \geq 0 \quad \text{(tension)} \\ E_{no}^{C\alpha}(1+\alpha_4 p); & \delta_n^\alpha(t) < 0 \quad \text{(compression)} \end{cases}$$
$$\mu_{no}^\alpha = \begin{cases} \mu_{no}^{T\alpha}; & \delta_n^\alpha(t) \geq 0 \quad \text{(tension)} \\ \mu_{no}^{C\alpha}; & \delta_n^\alpha(t) < 0 \quad \text{(compression)} \end{cases} \tag{2.25a}$$

where the grain-scale stiffness accounts for the stiffening under compression. To clarify, the mean stress, the inter-granular normal stiffness in tension, the constant associated with growth of stiffness during increasing confinement and the grain-scale tensile viscosity parameter in normal direction are denoted as p, $E_{no}^{T\alpha}$, α_4 and $\mu_{no}^{T\alpha}$, respectively. Additionally, the inter-granular normal stiffness in compression and the grain-scale normal viscosity parameter in compression are denoted as $E_{no}^{C\alpha}$ and $\mu_{no}^{C\alpha}$, respectively, and obtained as the following (Figure 2.2(a)):

$$E_{no}^{C\alpha} = \frac{2}{\pi e}\frac{B_n^\alpha}{\delta_n^\alpha}E_{no}^{T\alpha}R$$
$$\mu_{no}^{C\alpha} = \frac{2}{\pi e}\frac{\beta B_n^\alpha}{\delta_n^\alpha}\mu_{no}^{T\alpha}R \tag{2.25b}$$

where the parameter R represents the ratio of the maximum inter-granular normal force in compression to the maximum inter-granular normal force in tension. The displacement where the

viscous element starts losing integrity in consideration with the rheological model is denoted as β. Moreover, the intergranular damage parameter in normal direction, D_n^α, and the viscosity in normal direction, μ_n^α, are expressed as:

$$D_n^\alpha = \begin{cases} 1 - e^{-\left|\frac{\left(\delta_n^\alpha(t-\Delta t) - \frac{f_n^\alpha(t-\Delta t)}{E_1^\alpha}\right)}{B_n^\alpha}\right|}; & \delta_n^\alpha(t) \geq 0 \quad \text{(tension)} \\ 1 - \tan^{-1}\left(\frac{\pi e}{2}\frac{\delta_n^\alpha(t-\Delta t)}{B_n^\alpha R}\frac{\left(\delta_n^\alpha(t-\Delta t) - \frac{f_n^\alpha(t-\Delta t)}{E_1^\alpha}\right)}{B_{nc}^\alpha}\right); & \delta_n^\alpha(t) < 0 \quad \text{(compression)} \end{cases}$$

$$\mu_n^\alpha = \begin{cases} \mu_{n0}^\alpha e^{-\left|\frac{\left(\delta_n^\alpha(t-\Delta t) - \frac{f_n^\alpha(t-\Delta t)}{E_1^\alpha}\right)}{\beta B_n^\alpha}\right|}; & \delta_n^\alpha(t) \geq 0 \quad \text{(tension)} \\ \mu_{n0}^\alpha \tan^{-1}\left(\frac{\pi e}{2}\frac{\delta_n^\alpha(t-\Delta t)}{\beta B_n^\alpha R}\frac{\left(\delta_n^\alpha(t-\Delta t) - \frac{f_n^\alpha(t-\Delta t)}{E_1^\alpha}\right)}{\beta B_{nc}^\alpha}\right); & \delta_n^\alpha(t) < 0 \quad \text{(compression)} \end{cases} \tag{2.26}$$

where the constant damage model parameters B_n^α and B_{nc}^α represent the inter-granular displacements that correspond to the peak force in tension and the initial force diverging from linearity in compression, respectively. Additionally, t denotes the current time step whereas $t - \Delta t$ is the previous time step.

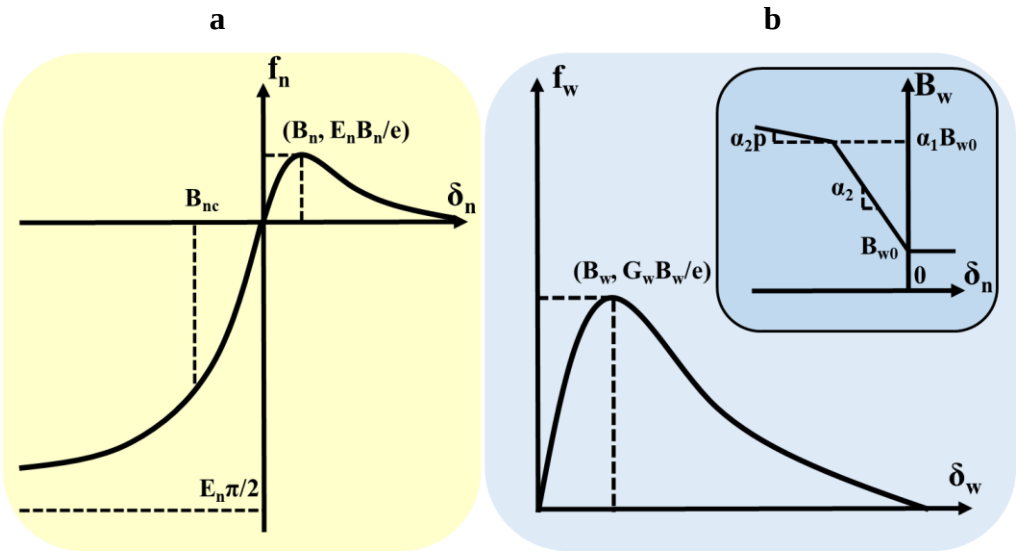

Figure 2.2: Inter-granular normal force-displacement relationship in (a) tension-compression and (b) shear. The inset figure shows the relationship of micro-scale shear damage parameter with inter-granular normal displacement.

Similarly, the micro-scale stiffness, viscosity and relaxation parameters in shear direction are calculated by first determining whether the inter-granular interaction undergoes tension or compression in normal direction [56, 68]. The α-th grain-pair interaction is under tension or compression depending on the inter-granular displacement in normal direction, δ_n^α. To this end, the micro-scale damage parameter in shear direction, D_w^α, and the viscosity in shear direction, μ_w^α, are defined as the following:

$$D_w^\alpha = 1 - e^{-\left|\frac{\left(\delta_w^\alpha(t-\Delta t) - \frac{f_w^\alpha(t-\Delta t)}{G_1^\alpha}\right)}{B_w^\alpha}\right|}$$

$$\mu_w^\alpha = \mu_{w0}^\alpha e^{-\left|\frac{\left(\delta_w^\alpha(t-\Delta t) - \frac{f_w^\alpha(t-\Delta t)}{G_1^\alpha}\right)}{\beta B_w^\alpha}\right|} \quad (2.27a)$$

where the shear damage parameter, B_w^α, is defined as a bilinear function of the inter-granular displacement in normal direction that is established by using parameters α_1, α_2 and α_3 as (Figure 2.2(b)):

$$B_w^\alpha = \begin{cases} B_{w0}^\alpha & ;\ \delta_n^\alpha(t) \geq 0 \quad \text{(tension)} \\ B_{w0}^\alpha - \alpha_2 \delta_n^\alpha(t - \Delta t\,) & ;\ \frac{1-\alpha_1}{\alpha_2} B_{w0}^\alpha \leq \delta_n^\alpha(t) < 0 \quad \text{(compression)} \\ \alpha_2 B_{w0}^\alpha - \alpha_3 p(\delta_n^\alpha(t - \Delta t\,) - \dfrac{1-\alpha_1}{\alpha_2} B_{w0}^\alpha) & ;\ \delta_n^\alpha(t) < \frac{(1-\alpha_1)}{\alpha_2} B_{w0}^\alpha \quad \text{(compression)} \end{cases} \tag{2.27b}$$

Additionally, it is considered that each grain-pair can experience different loading conditions. To this end, a micro-scale yield function, F, is implemented as the following in order to determine if a grain-pair undergoes loading, unloading or reloading [66]:

$$\begin{aligned} F_n^\alpha &= |\delta_n^\alpha| - {}^{max}|\delta_n^\alpha| \leq 0; \\ F_w^\alpha &= \delta_w^\alpha - {}^{max}\delta_w^\alpha \leq 0; \end{aligned} \tag{2.28}$$

where the instantaneous maximum normal and shear displacement components of α-th grain-pair interaction are denoted using the left superscript "max". Type of loading is evaluated by using the yield function as the following:

(1) Loading: $F_n^\alpha = 0\ and\ \dot{\delta}_n^\alpha > 0;$

$F_w^\alpha = 0\ and\ \dot{\delta}_w^\alpha > 0.$

(2) Unloading: $F_n^\alpha < 0\ and\ \dot{\delta}_n^\alpha < 0;$

$F_w^\alpha < 0\ and\ \dot{\delta}_w^\alpha < 0.$

(3) Reloading: $F_n^\alpha < 0\ and\ \dot{\delta}_n^\alpha > 0;$

$F_w^\alpha < 0\ and\ \dot{\delta}_w^\alpha > 0.$

If the grain-pair interaction is evaluated to be under loading, then the micro-scale constitutive relationships (2.24) are used by incorporating the inter-granular damage and viscosity parameters expressed in (2.26) and (2.27). Moreover, if the inter-granular interaction undergoes unloading,

then the micro-scale constitutive laws (2.24) are used by assigning the inter-granular damage and viscosity parameters as the following:

$$D_n^\alpha = \begin{cases} 1 - e^{-\left|\frac{\left(max\delta_n^\alpha(t-\Delta t) - \frac{max f_n^\alpha(t-\Delta t)}{E_1^\alpha}\right)}{B_n^\alpha}\right|}; & \delta_n^\alpha(t) \geq 0 \quad \text{(tension)} \\ 1 - \tan^{-1}\left(\frac{\pi e}{2}\frac{max\delta_n^\alpha(t-\Delta t)}{B_n^\alpha R}\frac{\left(max\delta_n^\alpha(t-\Delta t) - \frac{max f_n^\alpha(t-\Delta t)}{E_1^\alpha}\right)}{B_{nc}^\alpha}\right); & \delta_n^\alpha(t) < 0 \quad \text{(compression)} \end{cases}$$

$$D_w^\alpha = 1 - e^{-\left|\frac{\left(max\delta_w^\alpha(t-\Delta t) - \frac{max f_w^\alpha(t-\Delta t)}{G_1^\alpha}\right)}{B_w^\alpha}\right|}$$

$$\mu_n^\alpha = \begin{cases} \mu_{n0}^\alpha e^{-\left|\frac{\left(max\delta_n^\alpha(t-\Delta t) - \frac{max f_n^\alpha(t-\Delta t)}{E_1^\alpha}\right)}{\beta B_n^\alpha}\right|}; & \delta_n^\alpha(t) \geq 0 \quad \text{(tension)} \\ \mu_{n0}^\alpha \tan^{-1}\left(\frac{\pi e}{2}\frac{max\delta_n^\alpha(t-\Delta t)}{\beta B_n^\alpha R}\frac{\left(max\delta_n^\alpha(t-\Delta t) - \frac{max f_n^\alpha(t-\Delta t)}{E_1^\alpha}\right)}{\beta B_{nc}^\alpha}\right); & \delta_n^\alpha(t) < 0 \quad \text{(compression)} \end{cases} \tag{2.29}$$

$$\mu_w^\alpha = \mu_{w0}^\alpha e^{-\left|\frac{\left(max\delta_w^\alpha(t-\Delta t) - \frac{max f_w^\alpha(t-\Delta t)}{G_1^\alpha}\right)}{\beta B_w^\alpha}\right|}$$

where the instantaneous maximum displacement and force in normal and shear directions at grain-scale are denoted by using the left superscript "max".

Following the study of Misra [69], a backward Euler method is used to solve for inter-granular forces given in the micro-scale constitutive relationships (2.24)(2.24a) that are nonlinear first order differential equations in force and displacement. In general, the inter-granular normal and shear forces at current time step, *t*, are discretized in time as the following:

$$f_n^t = K_n^{t-\Delta t}\delta_n^t + \eta_n^{t-\Delta t}\frac{(\delta_n^t - \delta_n^{t-\Delta t})}{\Delta t} - \zeta_n^{t-\Delta t}\frac{(f_n^t - f_n^{t-\Delta t})}{\Delta t} \tag{2.30}$$

$$f_w^t = K_w^{t-\Delta t}\delta_w^t + \eta_w^{t-\Delta t}\,\frac{(\delta_w^t - \delta_w^{t-\Delta t})}{\Delta t} - \zeta_w^{t-\Delta t}\,\frac{(f_w^t - f_w^{t-\Delta t})}{\Delta t}$$

where the superscript $t-\Delta t$ denotes the previous time step.

Furthermore, the inter-granular forces at current time step, t, are treated in the given form below:

$$\begin{aligned} f_n^t &= C_n^{t-\Delta t}\delta_n^t + P_n^{t-\Delta t}\,\delta_n^{t-\Delta t} - \mathrm{Q}_n^{t-\Delta t}\,f_n^{t-\Delta t} \\ f_w^t &= C_w^{t-\Delta t}\delta_w^t + P_w^{t-\Delta t}\,\delta_w^{t-\Delta t} - \mathrm{Q}_w^{t-\Delta t}\,f_w^{t-\Delta t} \end{aligned} \tag{2.31a}$$

where *C*, *P* and *Q* are the coefficients that are functions of force and displacement at micro-scale and given as:

$$\begin{aligned} C_n^{t-\Delta t} &= \frac{K_n^{t-\Delta t}\Delta t + \eta_n^{t-\Delta t}}{\Delta t + \zeta_n^{t-\Delta t}} \quad ; \quad P_n^{t-\Delta t} = -\frac{\eta_n^{t-\Delta t}}{\Delta t + \zeta_n^{t-\Delta t}} \quad \text{and} \quad Q_n^{t-\Delta t} = \frac{\zeta_n^{t-\Delta t}}{\Delta t + \zeta_n^{t-\Delta t}} \\ C_w^{t-\Delta t} &= \frac{K_w^{t-\Delta t}\Delta t + \eta_w^{t-\Delta t}}{\Delta t + \zeta_w^{t-\Delta t}} \quad ; \quad P_w^{t-\Delta t} = -\frac{\eta_w^{t-\Delta t}}{\Delta t + \zeta_w^{t-\Delta t}} \quad \text{and} \quad Q_w^{t-\Delta t} = \frac{\zeta_w^{t-\Delta t}}{\Delta t + \zeta_w^{t-\Delta t}} \end{aligned} \tag{2.31a}$$

2.2.6 Constitutive Law at Macro-Scale

Moreover, the constitutive law at macro-scale is derived by considering (2.11) with (2.6):

$$\sigma_{ij} = \frac{1}{V}\sum_{\alpha=1}^{N} f_k^\alpha l_l^\alpha \frac{\partial \varepsilon_{kl}^n}{\partial \varepsilon_{ij}} \qquad \text{where } \varepsilon_{kl}^n = u_{(k,l)}^n \tag{2.32}$$

The symmetric part of the displacement gradient is denoted as ε_{kl}^n. Eventually, the average macroscopic stress tensor, σ_{ij}, is expressed as the following:

$$\sigma_{ij} = \frac{1}{V}\sum_{\alpha=1}^{N} f_i^\alpha l_j^\alpha \tag{2.33}$$

Subsequently, (2.33) is evaluated by using the integral given as:

$$\sigma_{ij} = Nl \int_0^{2\pi} \int_0^{\pi} f_j(\theta, \emptyset) n_i(\theta, \emptyset) \xi(\theta, \emptyset) sin\theta d\theta d\emptyset \tag{2.34}$$

where the number density of grain-pair interactions are denoted as *N*, a directional probability density function, $\xi(\theta, \emptyset)$, is defined such that the term $N\xi(\theta, \emptyset) sin\theta d\theta d\emptyset$ provides the number density of grain-pair interactions at the solid angle $sin\theta d\theta d\emptyset$. Finally, the explicit form of the macroscopic constitutive law is established by incorporating (2.31) into (2.34):

$$\sigma_{ij}^{t} = C_{ijkl}^{t-\Delta t} \varepsilon_{kl}^{t} + P_{ijkl}^{t-\Delta t} \varepsilon_{kl}^{t-\Delta t} + \tilde{\sigma}_{ij}^{t-\Delta t} \tag{2.35a}$$

where the terms $C_{ijkl}^{t-\Delta t}$, $P_{ijkl}^{t-\Delta t}$ and $\tilde{\sigma}_{ij}^{t-\Delta t}$ are defined as:

$$C_{ijkl}^{t-\Delta t} = Nl \int_0^{2\pi} \int_0^{\pi} \left(C_n^{t-\Delta t} n_j n_k + C_w^{t-\Delta t} \left(s_j s_k + t_j t_k \right) \right) n_i n_l \xi(\theta, \emptyset) \, sin\theta d\theta d\emptyset$$

$$P_{ijkl}^{t-\Delta t} = Nl \int_0^{2\pi} \int_0^{\pi} \left(P_n^{t-\Delta t} n_j n_k + P_w^{t-\Delta t} \left(s_j s_k + t_j t_k \right) \right) n_i n_l \xi(\theta, \emptyset) \, sin\theta d\theta d\emptyset \tag{2.35b}$$

$$\tilde{\sigma}_{ij}^{t-\Delta t} = Nl \int_0^{2\pi} \int_0^{\pi} \left(Q_n^{t-\Delta t} f_n^{t-\Delta t} n_j + Q_w^{t-\Delta t} f_w^{t-\Delta t} \left(s_j + t_j \right) \right) n_i \xi(\theta, \emptyset) \, sin\theta d\theta d\emptyset$$

2.3 Implementation of Granular Micromechanics Material Model into Finite Element Analysis

The developed material model was utilized to create a user-defined nonlinear material model (UMAT). The model was written in visual Fortran composer (Intel, Santa Clara, CA). Visual Fortran was linked with a commercial finite element (FE) analysis software (Simulia/ABAQUS V 6.13-3, Dassault Systémes, RI, USA) and the UMAT was called to FE analysis for material property. In FE analyses, single element patch test was simulated. The results from the simulations were post-processed to investigate the numerical accuracy of the material model with respect to

the time incrementation size and to show capability of the material model to simulate rate-dependent nonlinear mechanical behavior of a granular material.

Initially, FE model for the single element patch test (Figure 2.3) was created by using a cubic geometry where it has a side length of 1 mm. The material model parameters were assigned for the bovine cortical bone tissue based on a recent study [70] (see the Appendix C, Table 10.1). Since one single quadrilateral element is assigned for the whole geometry, the model consists of 8 nodes. The displacements in all directions were restricted to be zero at each node except for the nodes on the y-z surface. The displacement on those nodes was set to be zero only in y- and z-directions and additionally, the displacement in positive x-direction was set to be 1 mm. The displacement load was applied in a time period of 1 minute such that the applied load simulates the load rate of 1 mm/min. Furthermore, the time incrementation size was assigned as 0.00025 min, 0.0005 min, 0.001 min, 0.0025 min and 0.005 min to evaluate a large range of time incrementation sizes. Additionally, three more models were created with loading rates of 0.2 mm/min, 0.5 mm/min and 1 mm/min to demonstrate the model's rate-dependent capability. These three models had a time incrementation size of 0.0025 min.

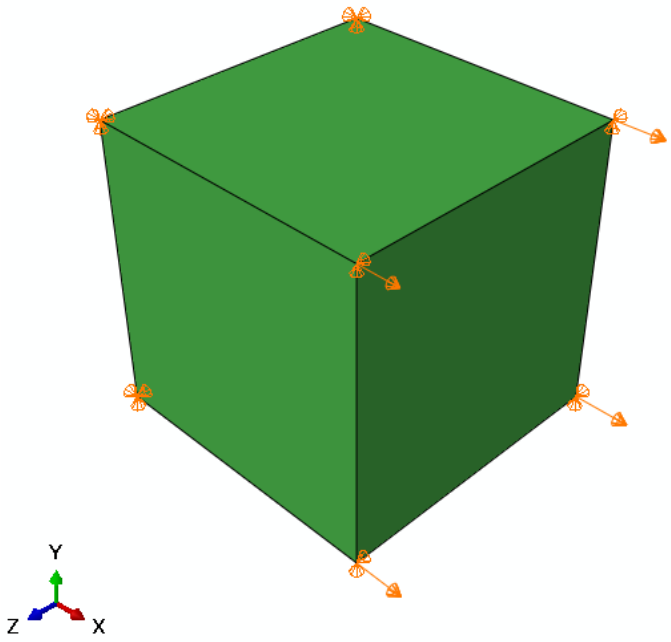

Figure 2.3: FE model representation of single element patch test.

2.4 Results and Discussion

The results obtained from the single element patch tests were assessed to investigate the numerical accuracy of the material model. Five single patch test models had the same loading rate but they were simulated with time incrementation sizes varying between 0.00025 min and 0.005 min. Their results were post-processed to obtain stress-strain relationship of each test. Mainly, the results show that the model nicely captured initial linear stress-strain trend, softening before failure and softening after failure. It is also seen that the stress-strain relationships overlapped quite close (Figure 2.4). The inset figure clarifies how the time incrementation size affected the stress-strain results. It shows that the results with the time incrementation size of 0.005 min were slightly higher compared to the other four time incrementation sizes in fairly good agreement.

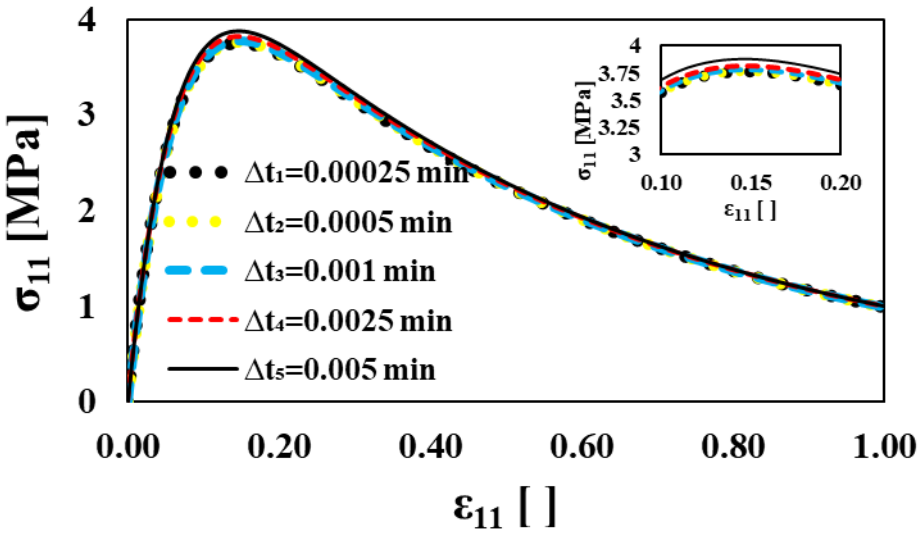

Figure 2.4: Stress-strain relationships obtained from the single patch test by using different time incrementation sizes, Δt. The inset figure provides the same stress-strain relationships with refined x- and y-axes.

To reinforce this evaluation, a quantitative comparison was preferred to provide better estimation in terms of the effect of the time incrementation size of the solution. To this end, L_2 norms of the peak strain were computed for each case as the following so that the error can be revealed [69]:

$$L_{2_{\varepsilon_{11}}} = \frac{(\varepsilon_{11}^0 - \varepsilon_{11})^2}{(\varepsilon_{11}^0)^2} \tag{2.36}$$

where ε_{11}^0 denotes the peak strain of the single patch test conducted using the minimum time incrementation size that is 0.00025 min. The peak strain value of each case were determined by using stress-strain relationships. In Figure 2.5, the L_2 norm of the peak strain is presented at varying time incrementation sizes from 0.0005 min to 0.005 min where the time increments were

normalized by using the initial retardation time, $\tau_{n\delta}(0)$. In detail, $\tau_{n\delta}(0)$ is calculated by using the alternative form of (2.24a) [69]:

$$f_n^t = K_n^{t-\Delta t}\delta_n^t + \tau_{n\delta}^{t-\Delta t}K_n^{t-\Delta t}\dot{\delta}_n^t - \tau_{nf}^{t-\Delta t}\dot{f}_n^t$$
$$f_w^\alpha = K_w^{t-\Delta t}\delta_w^t + \tau_{w\delta}^{t-\Delta t}K_w^{t-\Delta t}\dot{\delta}_w^t - \tau_{wf}^{t-\Delta t}\dot{f}_w^t \quad (2.37)$$

where $\tau_{n\delta}$ and $\tau_{w\delta}$ are the retardation times in normal and shear directions, respectively, and τ_{nf} and τ_{wf} are the relaxation times, respectively.

It is clear that L_2 norm of the peak strain in the single element patch test went up by increasing the time incrementation size, Δt (Figure 2.5). Even though the increasing L_2 norm of the peak strain shows that the solution diverged from the true solution, all the studied time incrementation sizes provided relatively accurate solutions since the calculated L_2 norms were quite small.

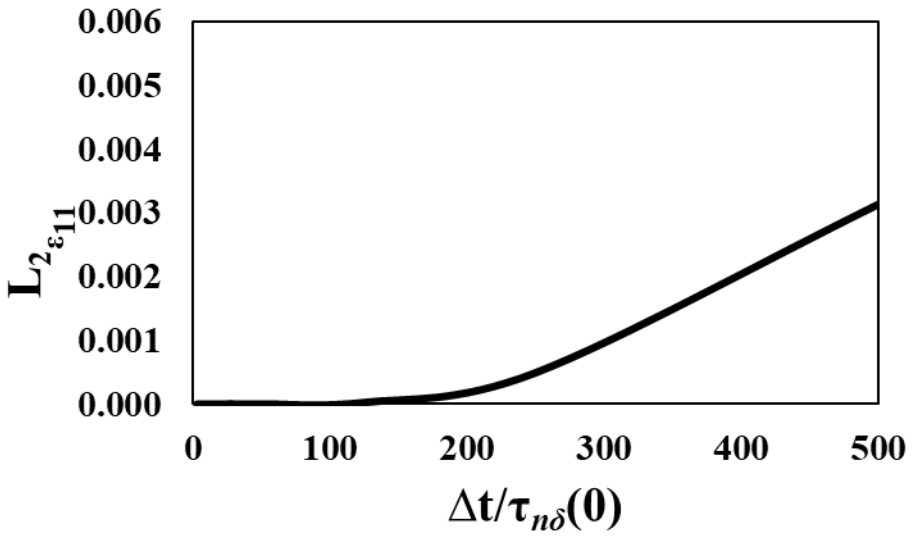

Figure 2.5: The error of peak strain in single patch tests with respect to the normalized time incrementation size.

Similarly, the error in peak stress can were assessed by calculating L_2 norms of the peak stress of each case as the following [69]:

$$L_{2_{\sigma_{11}}} = \frac{(\sigma_{11}^0 - \sigma_{11})^2}{(\sigma_{11}^0)^2} \tag{2.38}$$

where σ_{11}^0 is the peak stress obtained from the single patch test with the minimum time incrementation size, 0.00025 min. The peak stress value of each case was determined by using stress-strain relationships. In Figure 2.6, the L_2 norm of the peak stress is shown at various time incrementation sizes between 0.0005 min and 0.005 min where the time increments were normalized with respect to the initial retardation time, $\tau_{n\delta}(0)$.

Figure 2.6 clearly shows that L_2 norm of the peak stress increased in the single element patch test when the time incrementation size was larger. All of the time inrementation sizes in the studied range appeared reasonable for providing the true solution. Although the higher L_2 norm of the peak stress indicates a divergence from the true solution, the calculated L_2 norms were found in a relatively small range. Both peak strain peak and stress peak error calculations suggested that the time incrementation size is 0.0025 min to establish the optimum numerical accuracy and computational time.

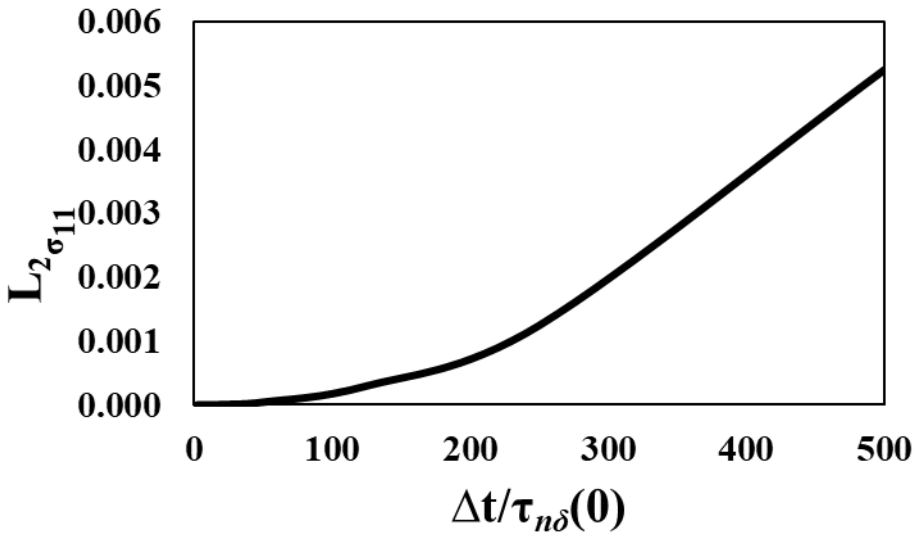

Figure 2.6: The error of peak stress in single patch tests with respect to the normalized time incrementation size.

Furthermore, material model's capability to predict rate-dependent behavior was demonstrated by using the single patch test. In Figure 2.7, the stress-strain relationship of three different loading rates is presented where the time incrementation size was assigned 0.0025 min and the loading rates varied as 0.2 mm/min, 0.5 mm/min and 1 mm/min. The inset figure clearly reveals that the stress response increases with the increase in the loading rate. In detail, high loading rate results in the highest peak stress, whereas the mid loading rate and low loading rate have the medium and the lowest peak stress values, respectively.

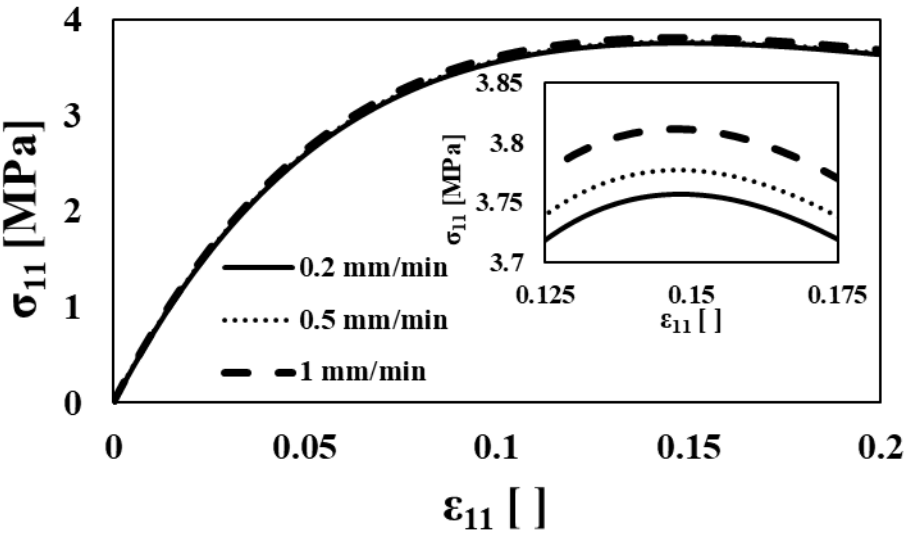

Figure 2.7: Stress-strain relationship from the single element patch test at loading rates of 0.2 mm/min, 0.5 mm/min and 1 mm/min.

2.5 Summary and Conclusions

This study presents a theoretical possibility for modeling the mechanical behavior of strongly granular systems. For this purpose, two preceding nonlinear material models based on granular micromechanics were combined. The developed nonlinear material model is rate-dependent and coupled with damage and plasticity. This model was also enhanced by coupling micro-scale normal and shear interactions. This enhancement provides the capability to capture the mechanical nature of strongly granular systems such as the mineralized tissue and highly cross-linked polymers. After the material model was developed, it was implemented into finite element analysis. Therefore, the model was written as a user-defined nonlinear material model (UMAT). The user-defined nonlinear material model was linked to a commercial finite element analysis code (Abaqus). A single element patch test was performed in finite element analysis with the nonlinear material model. The model parameters were assigned for bovine cortical bone tissue based on a

recent study [70]. The single patch test was performed to investigate the numerical accuracy of the material model and to demonstrate the model's capability to capture rate-dependent nonlinear nature of a granular material. In general, the stress-strain relationships obtained from the analyses represented the overall nonlinear trend of mechanical behavior. In particular, the initial linear regime, pre-peak and post-peak softening were consistently captured by the model. Furthermore, the results revealed the time interementation size to optimize numerical accuracy and computational time of the solution. In practice, an analysis achieves a true solution with the choice of a refined time incrementation size. However, this analysis requires longer computational time. Time incrementation size becomes critical while dealing with larger domains in finite element analysis.

After selecting the most efficient time incrementation size, the single patch test was conducted at three different loading rates. The simulations were able to capture the strengthening due to the increased loading rate. The stress-strain results showed that the peak stress went up with the increase in the loading rate. Hence, the material model was successful in capturing the nonlinear rate-dependent nature of materials. However, the assigned material model parameters were calibrated at only one loading rate and this study was conducted with speculated material parameters related to rate-dependence. With these model parameters, the model was successful in capturing a typical trend of stress and strain. Therefore, the material model parameters require calibration and validation against experimental data at different loading rates to capture the true rate-dependent nature of each material of interest.

CHAPTER 3

EXPERIMENTAL INVESTIGATION OF TENSILE NATURE OF THE MINERALIZED TISSUE AND POLYMER ADHESIVE, AND THE BOND STRENGTH AT THE MINERALIZED TISSUE – ADHESIVE INTERFACE

3.1 Introduction

The comprehensive understanding of the bond mechanics at dentin – adhesive interface is critical to address a major health problem: dental caries. It was estimated that 3.5 billion cases related to dental caries were reported worldwide in 2017 [1-7]. Unhealthy teeth are treated widely with resin-based composites [8, 9]. The treatment aims at regaining the natural appearance and load bearing ability in oral conditions. This particular treatment (i.e., dental restoration) provides relief to patients. However, the relief has a limited lifetime (i.e., 5 to 7 years) [10]. This lifetime can be potentially extended by materials design. The overall clinical performance of the dental restoration is determined by the contribution of each component at the dentin-adhesive interface [71-73]. Therefore, it is necessary to understand the load bearing nature of the materials involved at the dentin – adhesive interface. A comprehensive understanding is essential to develop an effective design. Mechanical properties of the dentin–adhesive interface have the potential to help us predict if a dental restoration will fail while performing the load bearing function under clinical conditions. Mechanical testing methods are utilized to characterize the properties of this interface. Bond

strength is the typical property that demonstrates the load bearing capacity of the dentin – adhesive interface. Bond strength tests are employed to measure this property. A variety of loading modes and applications are utilized for these tests, including tensile, micro tensile, shear, micro shear, pull- and push-out tests [11-18]. Interfacial imperfections, specimen geometry, specimen size and loading configuration are the factors that significantly affect the bond strength [57]. Micro tensile and shear tests achieve relatively reliable characterization of bond strength when performed over a small interfacial cross-sectional area (i.e., approximately 1 mm^2) [17-19]. Cohesive type of failure is prevented in micro tests as the cross-sectional area is small compared to macro-scale applications [74]. However, the materials design for dental adhesive relies on the accuracy of the testing method in characterizing the material properties. An adhesive design's performance might be unexpectedly poor in clinical conditions if the obtained bond strength data exhibit large variation. This deviation may eventually lead to inaccurate estimations on the true nature of the interface. In the literature, these large variations are reported for micro tensile and shear modes in bond strength of various adhesives with the dentin. Broad variations were observed in micro tensile (i.e., 6 to 75 MPa) and micro shear modes (i.e., 6 to 39 MPa) [20, 21]. This large variation, particularly in conventional tensile testing, can be devoted to its underlying mechanics. In detail, this type of mechanical testing inherently consists of challenges in the preparation of samples and consistent application of boundary conditions. These boundary conditions diverge from the application of relatively pure tensile loading and uniform distribution of stress. The diametral compression test constitutes an efficient alternative to inform the design of dental restorative material system as it overcomes the abovementioned challenges. This type of testing is also known as split tensile test and indirect tensile test [75] and is commonly used for tensile strength measurements on single material systems and composites [75-81]. The typical test configuration

is based on a specimen with a disk geometry. The disk is compressed on its curved edges between two load platens [75]. This load application induces tensile action that is perpendicular to the axis of loading [78]. Notably, the diametral compression test allows a convenient specimen preparation and load application compared to the conventional tensile test. The geometry is simplified to a disk and the load is applied without any attachment, fixation or grips. The disk specimen is simply placed between load platens. In this study, the diametral compression test was modified to improve the repeatability of the experiments by introducing a hole in the disk center [70]. This central hole constitutes a preset weakness location in heterogeneously defective materials, such as the mineralized tissue. The preset weakness location stimulates the initiation of diametral failure (Figure 3.5). The performance of the interfacial material system is determined by each component's behavior, such as the dentin, adhesive polymer, and, more importantly the hybrid layer. Therefore, the tensile nature of the involved components at the interface requires particular attention during the investigation of the bond strength at the dentin-adhesive interface. After the dentin is acid etched for the application of dental adhesive, the adhesive resin infiltrates into the demineralized collagen. This particular material system is called the hybrid layer [82-84]. Due to its inherent weakness in load bearing capacity [85-89], the hybrid layer dictates the bond strength at the dentin-adhesive interface. This study considered the bovine femur cortical bone tissue as a surrogate material for human dentin. Cortical bone tissue possesses microstructural and compositional similarities with dentin. These similarities include relatively comparable organic to volume ratio and complementary organic matrix mainly composed of calcium phosphate based apatite, type-I collagen and fluid [90]. Besides these similarities, the bovine femur has greater accessibility for specimen preparation compared to the human tooth. The complete nature of the mineralized tissue – adhesive interface was investigated in this study. These investigations focused

on two aspects by using the diametral compression test. The first aspect concentrated on exploring the tensile damage and failure of each single component of the mineralized tissue – adhesive interface. For this aspect, a modified diametral compression test was performed on the mineralized tissue and the adhesive polymer. The second aspect was the interfacial characterization via the diametral compression test to characterize the bond strength at the mineralized tissue – adhesive interface. Both single material and interfacial diametral compression tests were conducted at different loading rates. Different loading rates helped reveal the rate-dependent nature of these material systems. Moreover, recent studies led to the development of new polymer chemistries for dental adhesives. These new polymer chemistries significantly improve the mechanical performance of adhesive polymer by introducing photoacid-induced sol-gel reaction [91-94]. Accordingly, two adhesive formulations were evaluated using both single material and interfacial mechanical tests. These two adhesives differ in their composition in terms of the existence of γ-methacryloxypropyl trimethoxysilane (MPS). MPS is reported to provide self-strengthening property to dental adhesives [95].

3.2 Materials and Methods

3.2.1 Sample Preparation

The experimental characterization was done on two types of specimens. The first type is the ring specimen, where a disk geometry has a hole in the center. The second type is the interfacial specimen, where the ring specimen has an adhesive inclusion in the hole. The specimens were derived from the mineralized tissue and adhesive resins.

3.2.1.1 **Mineralized Tissue**

The mineralized tissue specimens were obtained from a bovine femur's cortical bone tissue (Figure 3.1) [70]. Initially, the bovine femur was coarsely cut into large sections. Afterwards, the sections along the diaphysis of the bone were cut into smaller sections via a diamond saw cutting machine (Isomet 1000, Buehler, Lake Bluff, IL) to extract the cortical bone tissue. The diametral compression test specimens were shaped by using a mini lathe (Mini lathe G8688, Grizzly, Bellingham, WA). The machining processes were conducted while keeping the specimens hydrated. The geometry of each specimen was achieved to be a 1.5 mm thick disk with a diameter of 3 mm and with a hole diameter of 1 mm. The hole was placed with a drill bit by using the mini lathe. The given dimensions were achieved with a tolerance of +/- 0.05 mm. In total, 30 specimens were prepared from the cortical bone tissue. 10 specimens were used as ring specimens and 20 specimens were used for preparing interfacial specimens. All these disks were stored in phosphate-buffered saline solution with a pH of 7.4 (Sigma-Aldrich, St. Louis, MO) and ~0.1 wt% sodium azide in order to prevent surface demineralization by mimicking in vivo conditions with a solution close to tissue fluid [96].

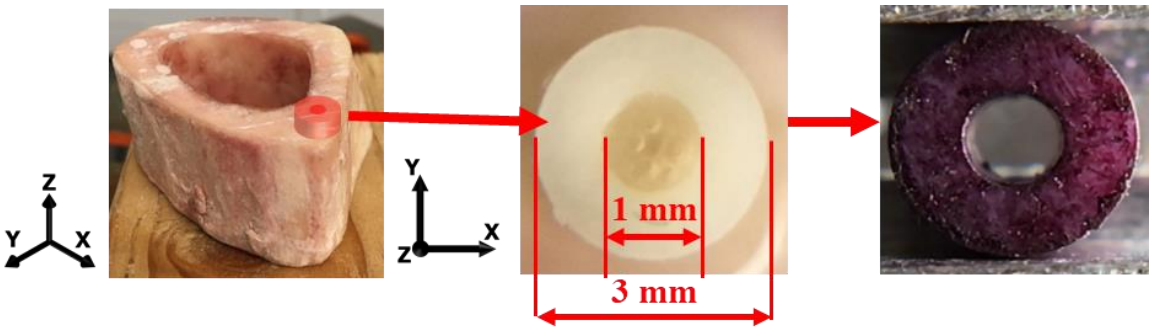

Figure 3.1: Bovine cortical bone tissue (mineralized tissue) ring specimen derived from the diaphysis of the bone. All specimens were dyed with a black permanent marker before the

mechanical test to reveal the fracture path. After machining, all specimens have a diameter of 3 mm, a thickness of 1.5 mm and a hole diameter of 1 mm.

3.2.1.2 **Adhesive Polymers**

The adhesive polymers were prepared following a particular protocol. Initially, 2,2-Bis[4-(2-hydroxy-3-methacryloxypropoxy) phenyl]propane (BisGMA), 2-hydroxyethyl methacrylate (HEMA), camphoroquinone (CQ), ethyl-4-(dimethylamino) benzoate (EDMAB), and diphenyliodonium hexafluorophosphate (DPIHP) were purchased from Sigma-Aldrich (St. Louis, MO). They were used with no further purification as they were received. γ-methacryloxypropyl trimethoxysilane (MPS) was obtained from MP Biomedicals (Solon, OH). It was also used as it was received. Moreover, Methacryloxyethoxytrimethylsilane (MES, 95%) was obtained from Gelest Inc. (Morrisville, PA). Figure 3.2 presents the chemical structures of components that were used in the formulations.

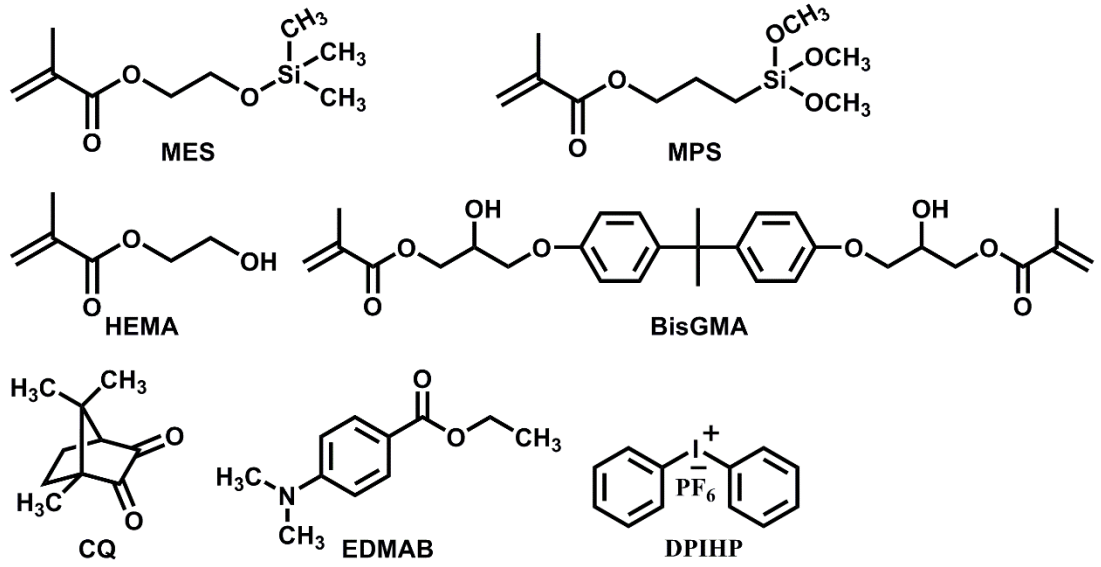

Figure 3.2: Chemical structures of components that were used in the formulations [95].

The control and experimental adhesive formulations, C1 and E1, respectively, were prepared by making the neat methacrylate resins (Table 3.1). In detail, 58 wt% HEMA, 30 wt% BisGMA, and 10 wt% MES (C1) or MPS (E1) were mixed in order to make neat methacrylate resins and CQ (0.5 wt%), EDMAB(0.5 wt%), and DPIHP (1.0 wt%) were used as the three component photoinitiator (PIs) system [97-99]. The resin mixtures of monomers/PIs were prepared in vials made of brown glass under amber light [94]. All chemicals were used as received with no further purification.

Table 3.1: Composition of C1 and E1 formulations. (C1: Control and E1: Experimental)

Run (wt%)	**C1**	**E1**
HEMA	58	58
BisGMA	30	30
MES	10	-
MPS	-	10
CQ	0.5	0.5
EDMAB	0.5	0.5
DPIHP	1.0	1.0
Total	100	100

In order to obtain the desired geometry for the diametral compression test, the adhesive polymer specimens were initially prepared as cylindrical samples. The prepared resin (~400 µL) was

injected into a Celprogen clear 96-well microplates (CAT#E36110-37-96well), covered with a mylar film, and cured with a commercial visible-light-curing unit (Spectrum®800, Dentsply, Milford, DE) at 550 mW/cm2 for 40 s. The polymerized cylindrical samples (~6.4 mm diameter and 11 mm height) were stored in the dark at 37 °C for 5 days before further processing. Following the same approach as the sample preparation of the mineralized tissue, adhesive polymer specimens were shaped using the mini lathe, where the specimens were kept hydrated during the machining process. The adhesive polymer specimens were prepared with the same geometry and dimensions as the cortical bone tissue disk specimens (Figure 3.3). In total, 6 specimens were prepared from each formulation. In order to ensure that the specimens provided the behavior of formulations in wet conditions as in the mouth, all adhesive specimens were kept in distilled, deionized water for 5 days [95, 100]. The polymer specimens became swollen in water and their final dimensions were measured. For E1 adhesive specimens, the thickness was measured ~1.60 mm, the diameter was ~3.10 mm and the hole diameter was read ~0.84 mm. For C1 adhesive specimens, the thickness was measured ~1.61 mm, the diameter was ~3.16 mm and the hole diameter was read ~1.00 mm.

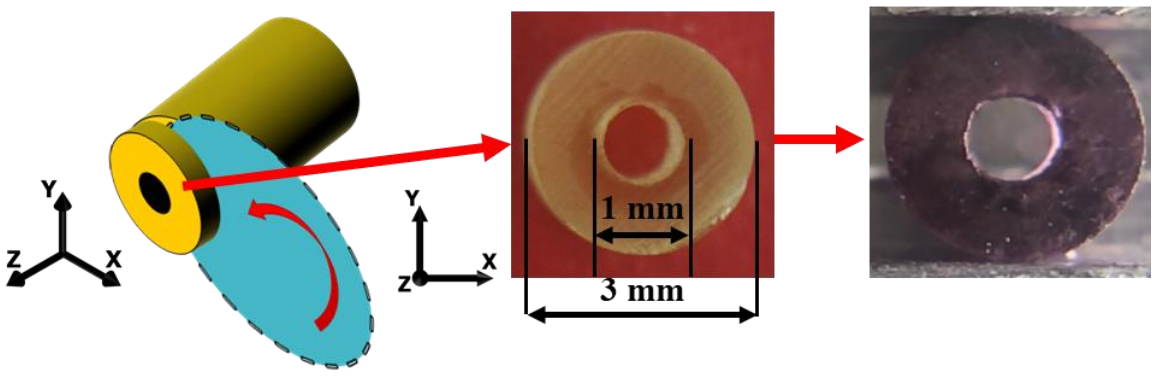

Figure 3.3: Adhesive polymer specimen that was cut into a disk specimen from a larger adhesive polymer cylinder that contains a hole in its center. All specimens were dyed with a black

permanent marker before mechanical test to reveal the fracture path. After machining, all specimens have diameter of 3 mm, thickness of 1.5 mm and hole diameter of 1 mm.

3.2.1.3 **Interfacial Specimens**

The interfacial specimens were prepared by using 20 mineralized tissue ring specimens and the adhesive resins, E1 and C1. The interfacial specimen was designed as a disk geometry of two concentric parts. The mineralized tissue ring specimens were used for the outer layer and the center inclusions were created by applying each E1 and C1 adhesive formulations separately (Figure 3.4). The mineralized tissue disk specimens were divided into two groups, where each adhesive formulation was applied to 10 disk specimens. In order to apply the adhesives, the hole surface in the mineralized tissue disk was first etched with a mixture of phosphoric acid and ethanol (60% v/v 35% H3PO4+ 40% v/v ethanol) for 10 min and then rinsed with deionized water. The resin was applied to fill the hole in the mineralized tissue disk and light-irradiated for 40 s at 23±2 °C using a commercial light source (Spectrum® 800, Dentsply, Milford, DE. Light intensity is 550 mW/cm2). Finally, the mineralized tissue - adhesive interfacial specimens were stored in 1x PBS solution (containing ~0.1 wt% sodium azide) at 37°C for 5 days.

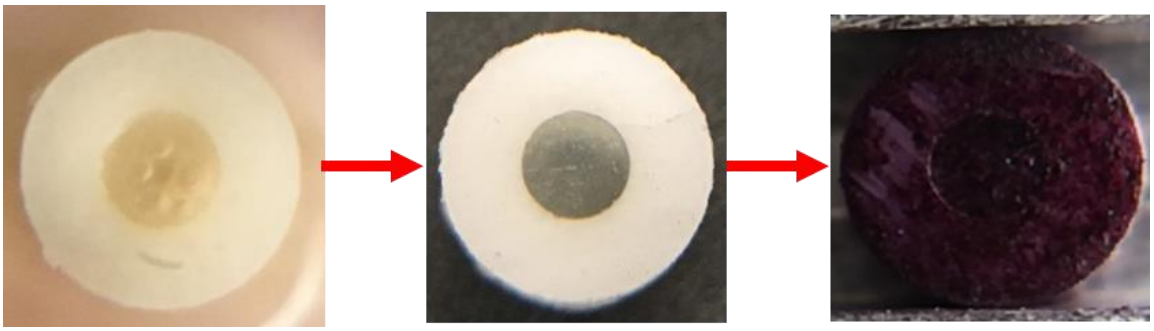

Figure 3.4: The bovine cortical bone ring specimen that is applied with the adhesive resin in the center hole in order to prepare an interfacial specimen and finally dyed with black permanent marker to create contrast for revealing the failure pattern in the mechanical test.

3.2.2 Mechanical Test

The mechanical test was conducted via Microtest stage (Microtest 200N Stage, Deben UK Ltd., Bury St Edmunds, UK) (Load cell range: 200N with the accuracy 1% of full scale range, extension range: 10 mm with the position readout accuracy of 0.1% of full scale range, standard speed range: 0.1 mm/min to 1.5 mm/min) (Figure 3.5). Two sets of specimens were tested, where two different loading rates were applied on each set. The loading rates were selected as the high loading rate of 1 mm/min and the low loading rate of 0.2 mm/min where each group consisted of 3 ring specimens made of C1 formulation, 3 ring specimens made of E1 formulation, 5 ring specimens made of the cortical bone tissue (the mineralized tissue), 5 interfacial specimens of the mineralized tissue – C1 adhesive and 5 interfacial specimens of the mineralized tissue – E1 adhesive (Figure 3.6). All specimens were kept hydrated during all procedures. They were only taken out of the hydrated conditions to perform the mechanical tests. Additionally, the test was video recorded via in-house slow-motion microscopy, 1280x720 pixels and 240 frames per second.

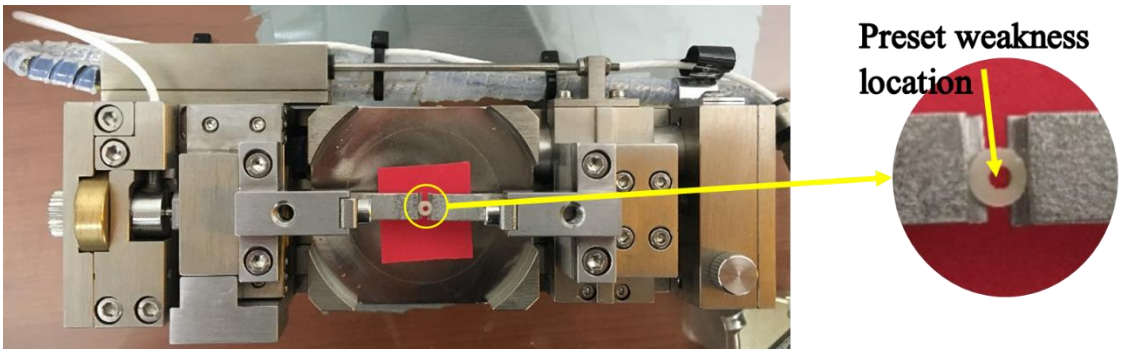

Figure 3.5: Micro-tensile test stage where the diametral compression test was performed and the close-up image of a ring specimen. The hole in the center constitutes a preset weakness location to promote failure.

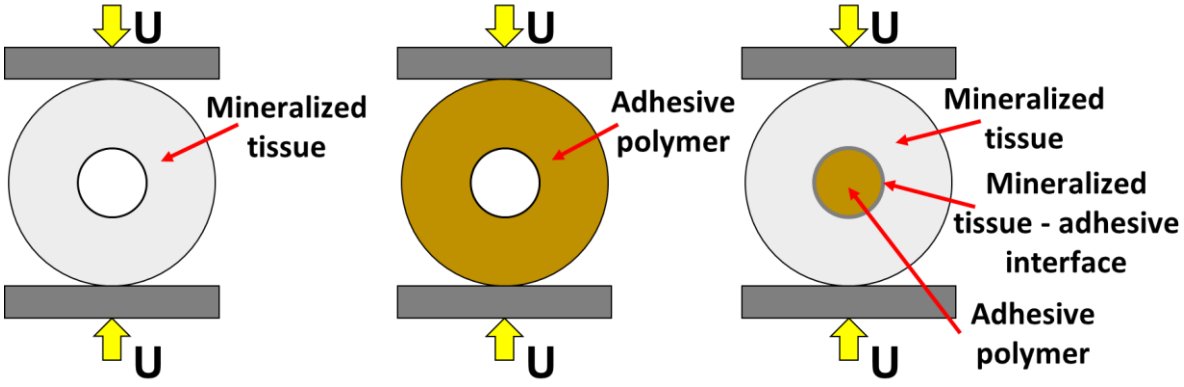

Figure 3.6: The representation of the diametral compression test of disk specimens made of the mineralized tissue and adhesive polymer and the interfacial specimen made of the mineralized tissue and adhesive to perform bond strength measurement.

3.3 Results

Mechanical tests provided the force-displacement relationships regarding the tensile nature of the mineralized tissue and polymer adhesives, C1 and E1. Moreover, the bond strength information

was obtained from the testing of the interfacial specimens of the mineralized tissue – C1 adhesive and the mineralized tissue – E1 adhesive. Additionally, deformation and failure patterns were obtained from video recordings.

3.3.1 Mineralized Tissue

From the bovine cortical bone specimens that were subject to 1 mm/min loading rate, the average peak force was read 77.61 N where the minimum peak force reading was 69.49 N and the maximum force reading was 84.11 N (Figure 3.7). The average failure displacement was 0.39 mm where the minimum failure displacement was 0.37 mm and the maximum failure displacement was 0.44 mm (see the Appendix D, Table 11.1).

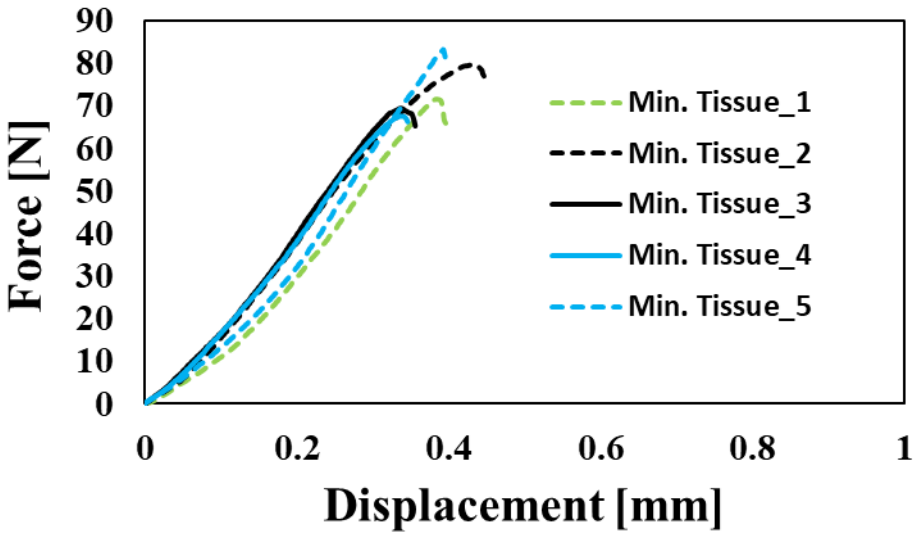

Figure 3.7: Force-displacement results obtained from the diametral compression test of the mineralized tissue ring specimens (Min. Tissue) at 1 mm/min loading rate.

As it is seen from the comparison of Figure 3.8(a) with Figure 3.8(b), the image after failure reveals that a discoloration zone emerged on the surface of the mineralized tissue specimen (circled with yellow line) at 1 mm/min loading rate. This discoloration indicates where the fracture was initiated and how it propagated. The fracture started inside out along the loading axis and propagated towards the loading surface. The quality of the image was compromised due to water film existing on the specimen' surface. This situation may potentially add to challenge of using the digital image correlation technique to study these specimens.

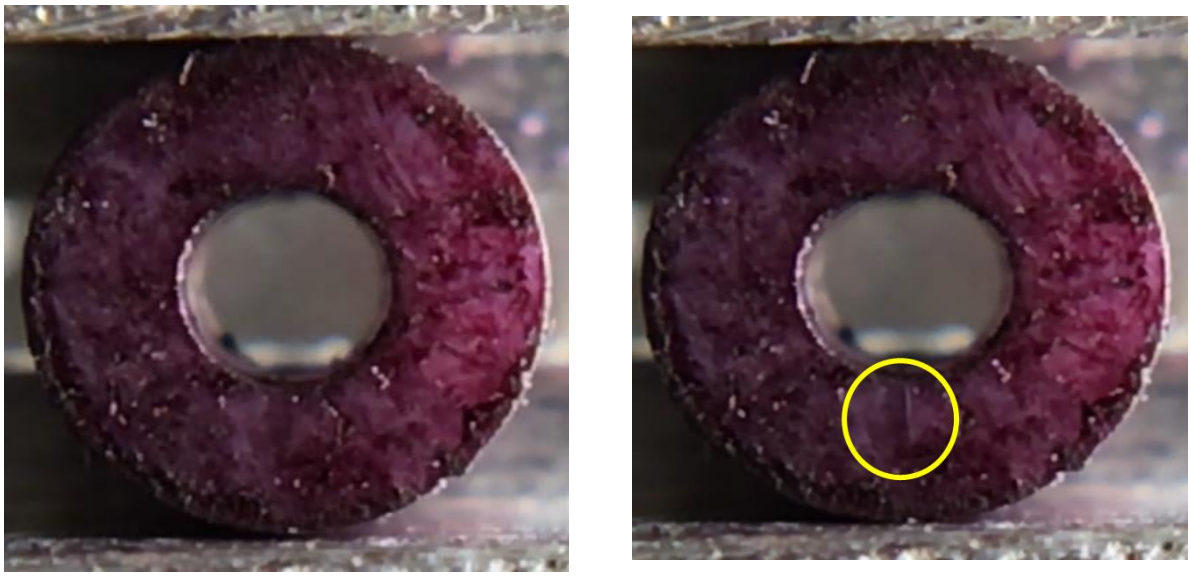

a b

Figure 3.8: Snapshots from the diametral compression test of the mineralized tissue at 1 mm/min loading rate: (a) the undeformed specimen and (b) the specimen after failure (post-failure).

For the mineralized tissue ring specimens subject to 0.2 mm/min loading rate, the average peak force yielded 51.50 N where the minimum peak force read 48.9 N and the maximum force was measured 56.44 N (Figure 3.9). Besides, the failure displacement was averaged as 0.28 mm where the minimum was 0.27 mm and the maximum was 0.31 mm. One outlier specimen was eliminated

from the results and the data were averaged by using the results of four specimens. It is observed that both the average peak force and the average failure displacement of the mineralized tissue ring specimens at 0.2 mm/min loading rate were lower compared to their average peak force and displacement at 1 mm/min loading rate, respectively (see the Appendix D, Table 11.1).

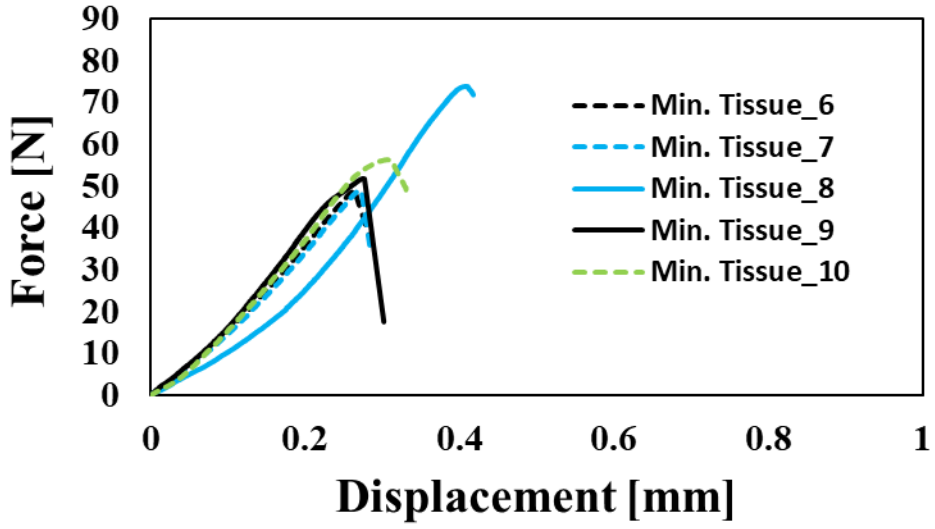

Figure 3.9: Force-displacement results obtained from the diametral compression test of the mineralized tissue ring specimens (Min. Tissue) at 0.2 mm/min loading rate.

When the mineralized tissue ring specimen was subject to the loading rate of 0.2 mm/min, the discoloration zone was observed at the same location as of 1 mm/min loading rate. The failed specimen (Figure 3.10(b)) had the fracture initiation around the hole and along the loading axis. This is clearly observed when the failed specimen's surface is compared to the intact specimen (Figure 3.10(a)). The fracture path was circled with a yellow line and it was found to be between the load surface and the hole on the loading axis. The observed fracture initiation location and the fracture path of the mineralized tissue at loading rate of 0.2 mm/min matched with the location of initiation and evolution of its fracture at 1 mm/min loading rate.

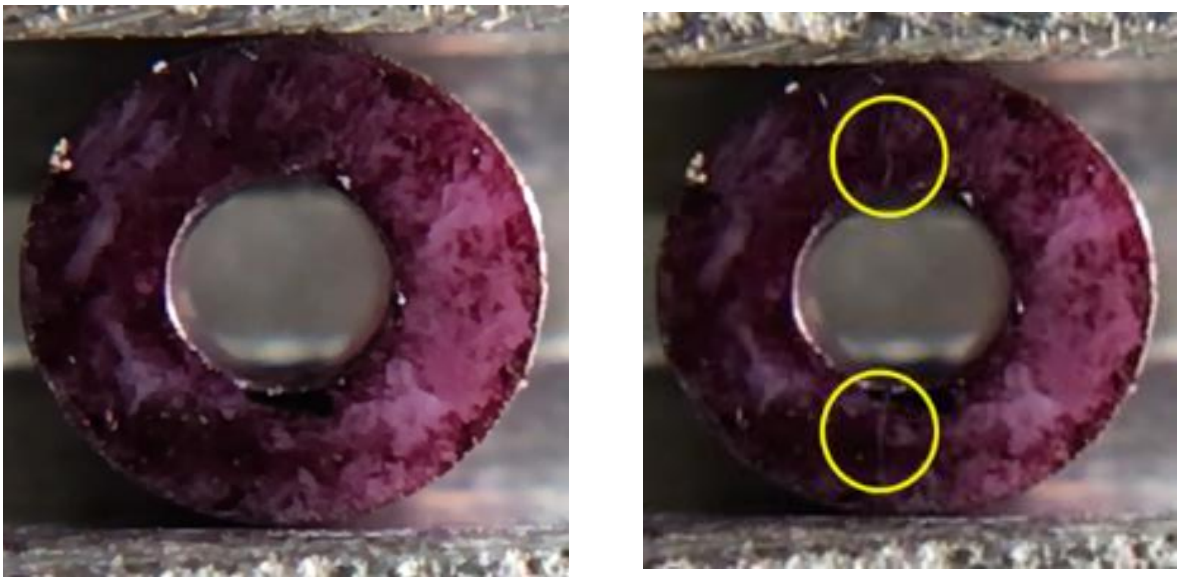

a b

Figure 3.10: Snapshots from the diametral compression test of the mineralized tissue at 0.2 mm/min loading rate: (a) the undeformed specimen and (b) the specimen after failure (post-failure).

3.3.2 Adhesive Polymers

The polymer ring specimens made of C1 formulation and tested at 1 mm/min had an average peak force of 28.50 N (Figure 3.11). The minimum peak force was measured 27.57 N and the maximum was 29.74 N. The average displacement at failure was reported as 0.52 mm where the minimum and maximum were 0.46 mm and 0.57 mm, respectively. The average failure force of C1 adhesive specimens at 1 mm/min loading rate was found to be significantly smaller than the average failure force of the mineralized tissue at both 1 mm/min and 0.2 mm/min loading rate. On the other hand, C1 adhesive specimens failed at a larger displacement at 1 mm/min loading rate comparing to the mineralized tissue specimens at both 1 mm/min and 0.2 mm/min loading rates (see the Appendix D, Table 11.1).

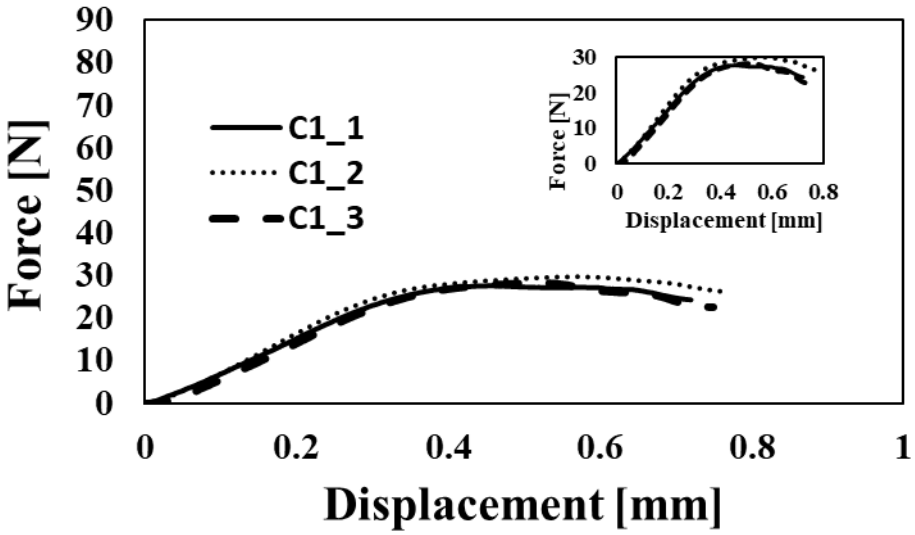

Figure 3.11: Force-displacement results obtained from the diametral compression test of C1 adhesive specimens at 1 mm/min loading rate. The inset figure provides the same force-displacement relationship with refined x- and y-axes.

The post-failure pattern (Figure 3.12(b)) of C1 adhesive ring specimen at the loading rate of 1 mm/min shows that the fracture was observed along the loading axis and it was initiated at the hole. In comparison with the undeformed specimen (Figure 3.12(a)), it is seen that the failure evolves towards the contact surfaces with the load platens. The failure pattern of C1 adhesive specimen at 1 mm/min loading rate was observed similar to the mineralized tissue specimens at both loading rates of 1 mm/min and 0.2 mm/min. Additionally, C1 adhesive specimen appears highly deformed by compression while reaching failure at 1 mm/min loading rate whereas the mineralized tissue specimens failed while the shape of the specimens is similar to their undeformed shapes at both loading rates of 1 mm/min and 0.2 mm/min. This observation is complemented by the average failure displacement of C1 adhesive specimen at 1 mm/min loading rate that is fairly

larger than the average failure displacement of the mineralized tissue at both 1 mm/min and 0.2 mm/min loading rates.

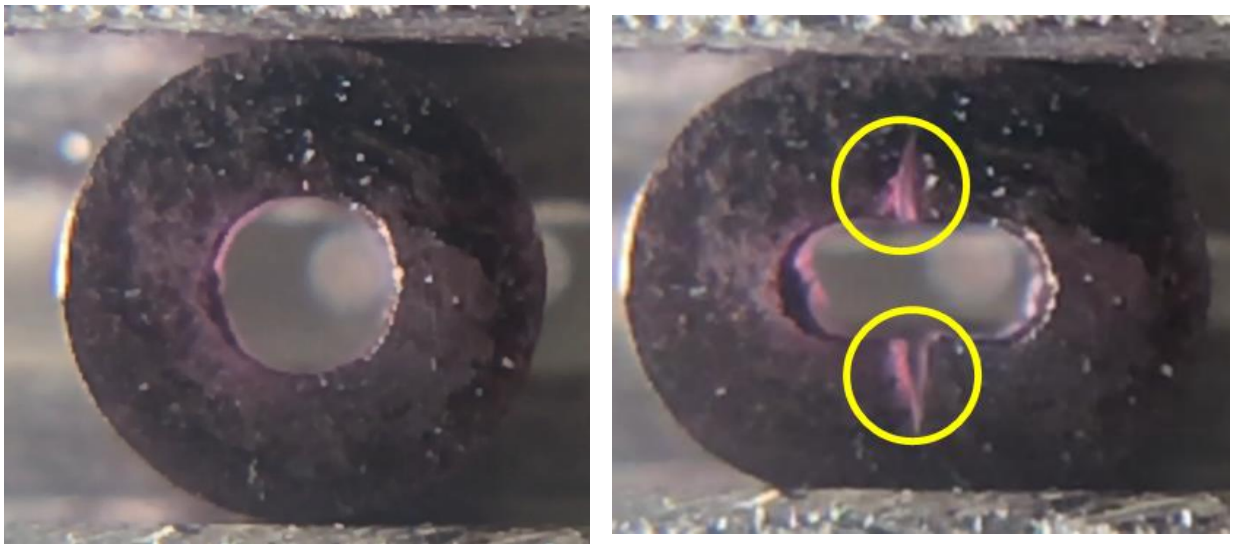

a b

Figure 3.12: Snapshots from the diametral compression test of C1 adhesive at 1 mm/min loading rate: (a) the undeformed specimen and (b) the specimen after failure (post-failure).

C1 adhesive ring specimens that were subject to 0.2 mm/min loading rate resulted a peak force average of 21.56 N (Figure 3.13). The minimum peak force was measured 21.30 N and the maximum peak force was 22.06 N. The failure displacements were averaged as 0.55 mm where their minimum and maximum were 0.46 mm and 0.71 mm, respectively. It is clear that C1 adhesive dropped the failure force significantly at 0.2 mm/min loading rate comparing to 1 mm/min loading rate. It also failed at a significantly smaller load than the mineralized tissue specimens at 0.2 mm/min. On the other hand, C1 adhesive had almost the same average failure displacement at 0.2 mm/min as 1 mm/min loading rate. However, the minimum and maximum failure displacements

at both loading rates might indicate that C1 adhesive at 0.2 mm/min yields a relatively lower failure displacement than the failure displacement at 1 mm/min (see the Appendix D, Table 11.1).

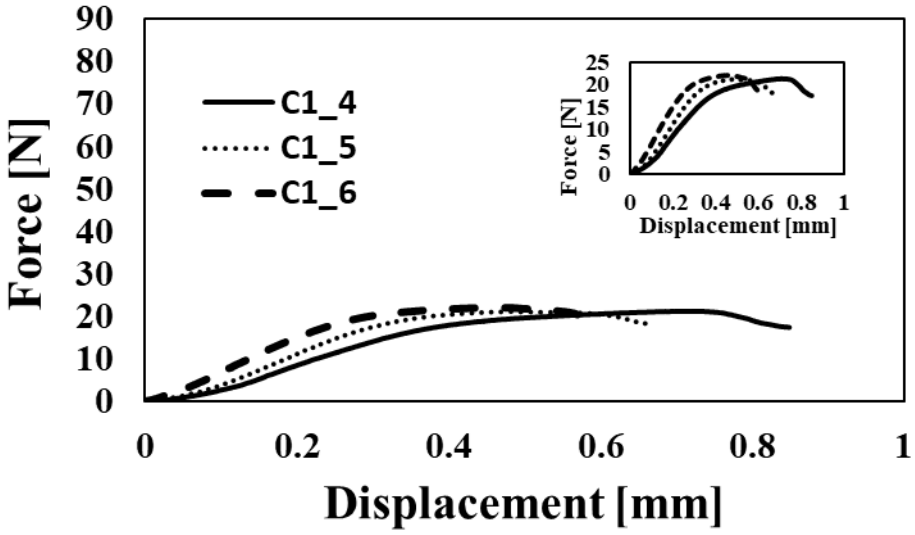

Figure 3.13: Force-displacement results obtained from the diametral compression test of C1 adhesive specimens at 0.2 mm/min loading rate. The inset figure provides the same force-displacement relationship with a refined y-axis.

The experimental snapshots of C1 adhesive ring specimens at 0.2 mm/min loading rate show that the specimen started to fail at the hole along the load axis (Figure 3.14(b)). Moreover, the orientation of the fracture path appears towards the loading surface by comparing the circled zone in (Figure 3.14(b)) to the intact specimen in (Figure 3.14(a)). The observed fracture pattern of C1 adhesive specimen at 0.2 mm/min is similar to its fracture pattern at 1 mm/min. C1 adhesive specimen underwent relatively higher deformation than the mineralized tissue at both loading rates of 1 mm/min and 0.2 mm/min before reaching the failure similar to its behavior at 1 mm/min loading rate.

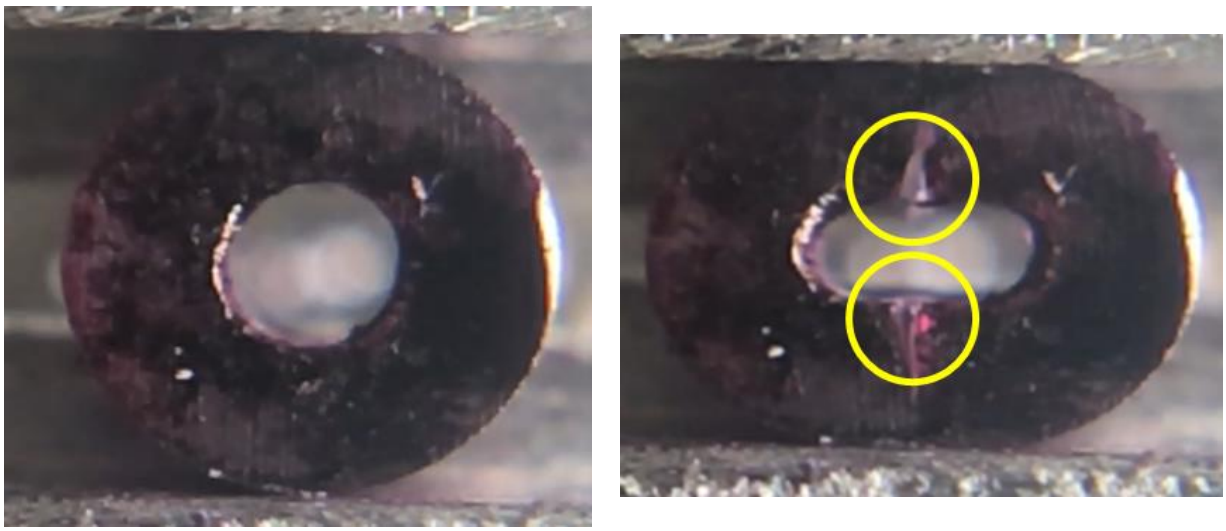

a b

Figure 3.14: Snapshots from the diametral compression test of C1 adhesive at 0.2 mm/min loading rate: (a) the undeformed specimen and (b) the specimen after failure (post-failure).

The ring specimens made of E1 formulation resulted in the average peak force of 38.63 N at 1 mm/min loading rate (Figure 3.15). The lowest peak force of E1 specimens was 35.34 N and the highest peak force was measured 41.85 N. The displacement corresponding the peak forces was averaged to be 0.34 mm where their minimum and maximum were read 0.33 mm and 0.40 mm, respectively. At 1 mm/min loading rate, E1 adhesive specimens failed at a higher load comparing to C1 adhesive and smaller load than the mineralized tissue. It is seen that the average failure displacement of E1 adhesive specimens at 1 mm/min was quite close to the average failure displacement of the mineralized tissue whereas it was found smaller than C1 adhesive specimen's failure displacement at both 1 mm/min and 0.2 mm/min (see the Appendix D, Table 11.1).

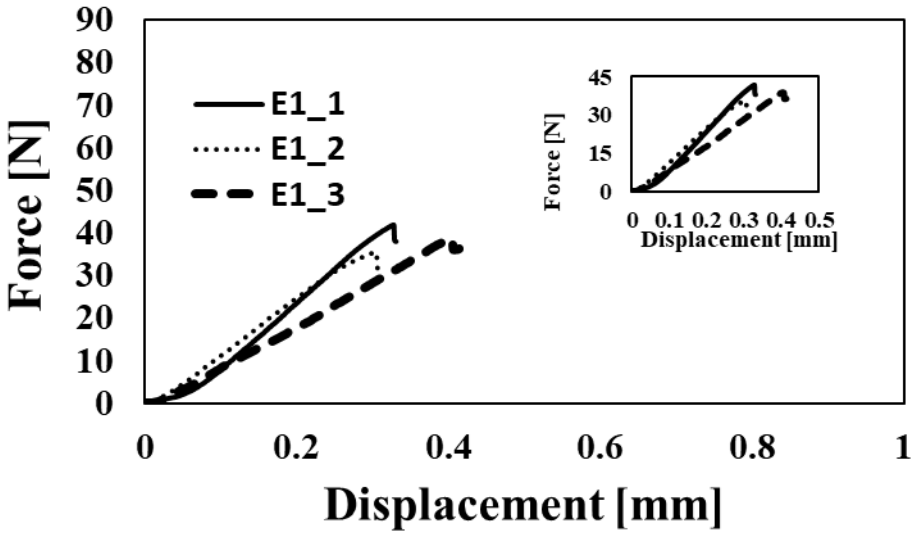

Figure 3.15: Force-displacement results obtained from the diametral compression test of E1 adhesive specimens at 1 mm/min loading rate. The inset figure provides the same force-displacement relationship with refined x- and y-axes.

E1 adhesive ring specimen started failing along the loading axis (yellow circles) (Figure 3.16(b)) at loading rate of 1 mm/min. When the intact specimen (Figure 3.16(a)) is compared to the failed specimen (Figure 3.16(b)), it is clear that the failure was initiated at the hole and propagated to the load surface following the loading axis. Similar to the mineralized tissue specimen's failure, E1 adhesive specimen at 1 mm/min loading rate reached failure while maintaining a similar shape to its undeformed shape that indicates failure after relatively low deformation. In other words, comparing to C1 adhesive specimen at both loading rates, E1 adhesive specimen at 1 mm/min undergoes quite lower deformation before failure that is also seen in the force-displacement relationships of both E1 and C1 adhesive specimens. The fracture path also appeared the same as both the mineralized tissue and C1 adhesive specimens at 1 mm/min and 0.2 mm/min loading rates.

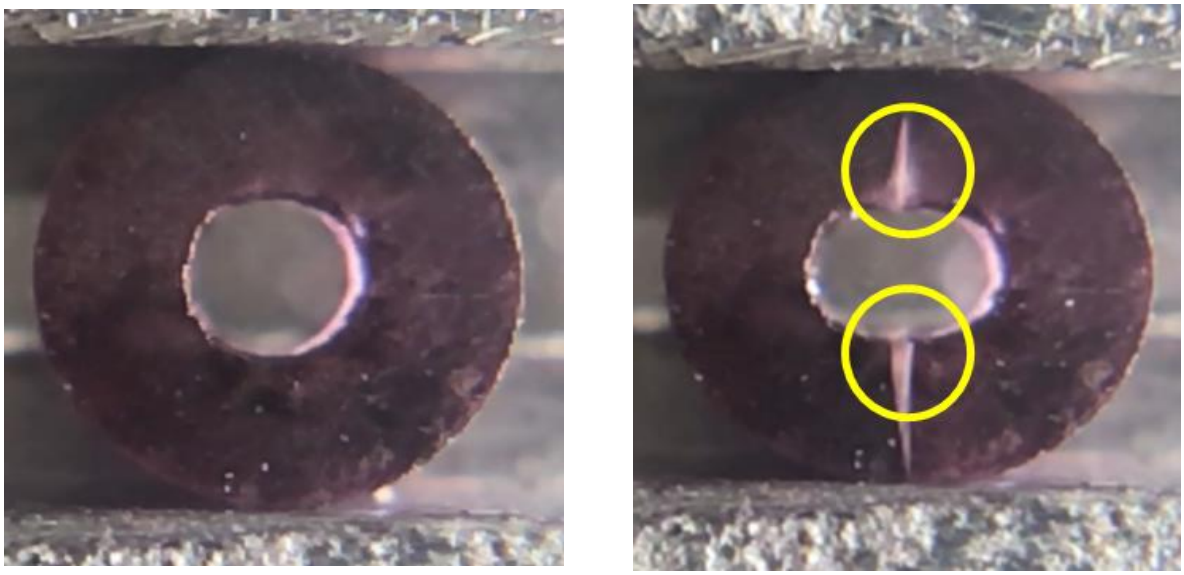

a b

Figure 3.16: Snapshots from the diametral compression test of E1 adhesive at 1 mm/min loading rate: (a) the undeformed specimen and (b) the specimen after failure (post-failure).

When E1 adhesive ring specimens were subject to 0.2 mm/min loading rate, the average peak force was measured 27.48 N (Figure 3.17). The minimum peak force was read 26.95 N and the maximum was 28.05 N. The corresponding failure displacement resulted in an average of 0.32 mm with a minimum of 0.29 mm and a maximum of 0.33 mm. Compared with their behavior at 1 mm/min, E1 adhesive specimens failed at a lower load at 0.2 mm/min. However, the average failure force of E1 adhesive at 0.2 mm/min was quite close to C1 adhesive's average failure force at 1 mm/min. In terms of the average failure displacement, E1 adhesive was on the lower side comparing to its average failure force at 1 mm/min and C1 adhesive's average failure force at both loading rates (see the Appendix D, Table 11.1).

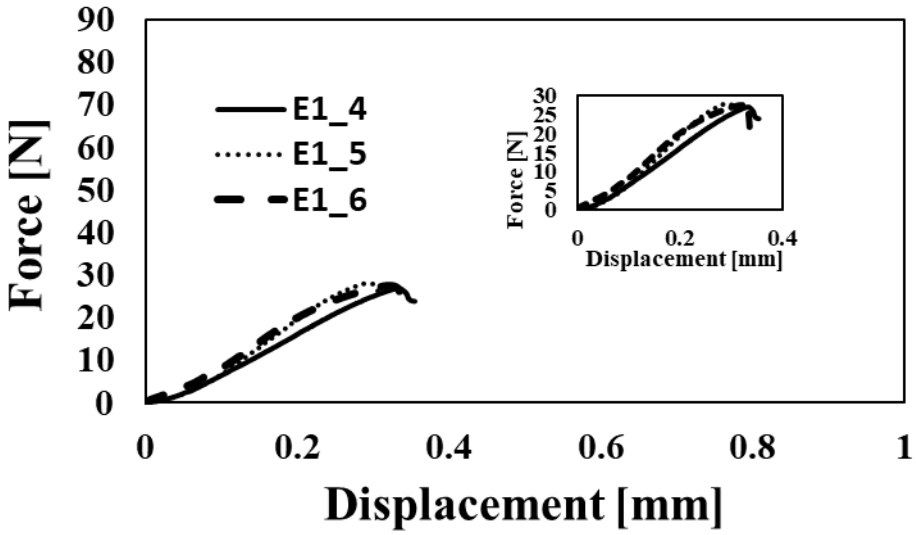

Figure 3.17: Force-displacement results obtained the from diametral compression test of E1 adhesive specimens at 0.2 mm/min loading rate. The inset figure provides the same force-displacement relationship with refined x- and y-axes.

At the loading rate of 0.2 mm/min, the fracture initiation was observed at the hole and it coincides with the loading axis (circled zone) as seen from Figure 3.18(b). After the fracture initiates at the hole, it continues on the loading axis in the direction towards the load platens. This fracture evolution is clearly seen by comparing the specimen before failure (Figure 3.18(a) and after failure Figure 3.18(b). E1 adhesive specimen followed the same fracture pattern at 0.2 mm/min as its fracture pattern at 1 mm/min loading rate. Its post-failure shape was close to its undeformed shape, as expected from the force-displacement relationship that indicates relatively low deformation while reaching the failure.

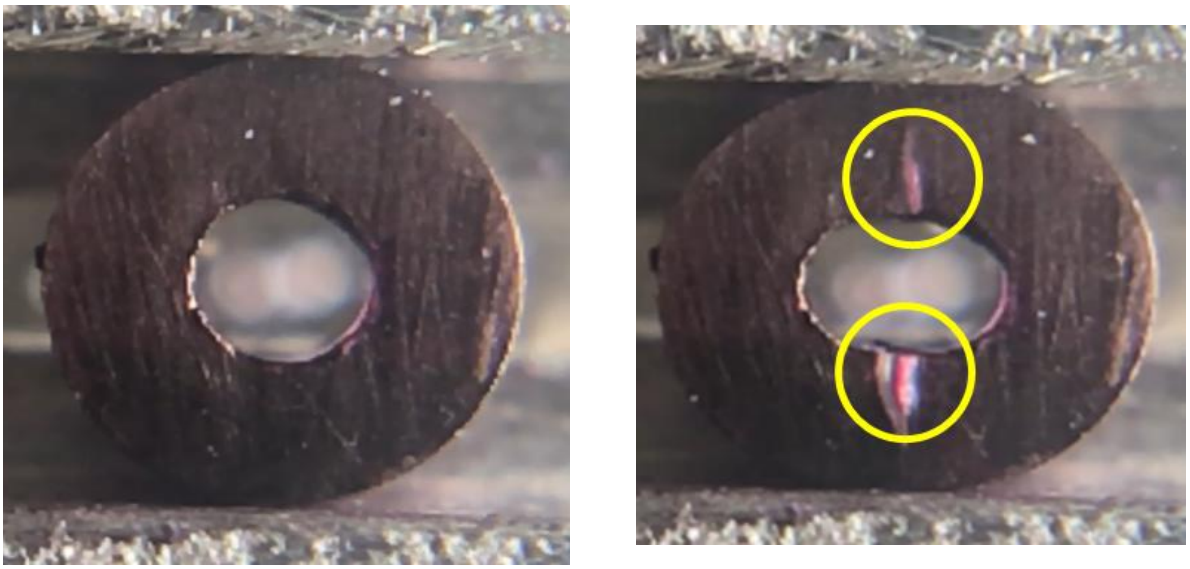

a b

Figure 3.18: Snapshots from the diametral compression test of E1 adhesive at 0.2 mm/min loading rate: (a) the undeformed specimen and (b) the specimen after failure (post-failure).

3.3.3 Interfacial Specimens

The interfacial specimens of the mineralized tissue – C1 adhesive had the average peak force of 86.67 N at 1 mm/min (Figure 3.19). Their lowest peak force was measured 70.75 N and the highest peak force was 93 N. Their failure displacements were averaged as 0.48 mm where the minimum and maximum were 0.38 mm and 0.62 mm, respectively. As it is expected, the mineralized tissue – C1 adhesive interfacial specimen failed at a higher load comparing to mineralized tissue ring specimens at 1 mm/min loading rate. Besides, the failure displacement also increased with the inclusion of C1 adhesive in the specimen compared to the mineralized tissue ring specimen. However, the average failure displacement of the mineralized tissue – C1 adhesive interfacial

specimens was smaller than C1 adhesive ring specimens' average failure displacement (see the Appendix D, Table 11.1).

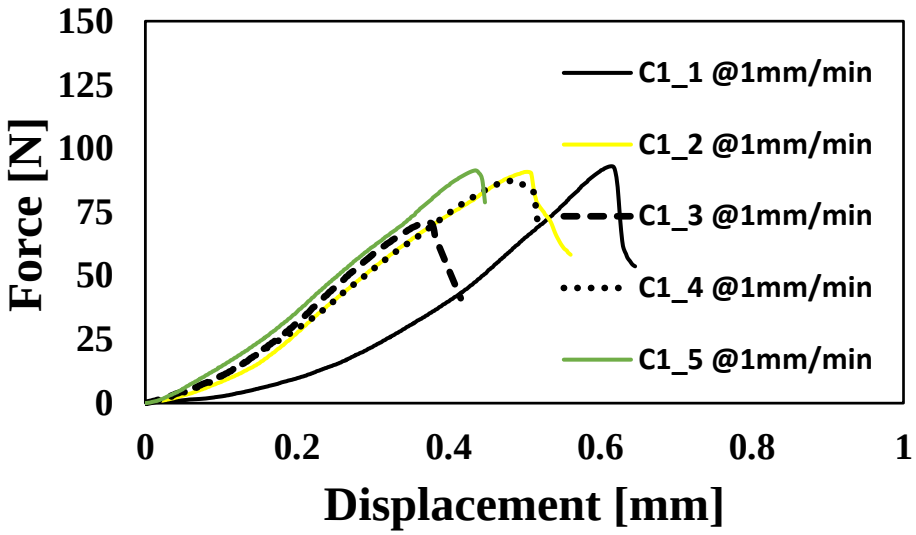

Figure 3.19: Force-displacement results obtained from the diametral compression test of the mineralized tissue – C1 adhesive interfacial specimens at 1 mm/min loading rate.

As seen from Figure 3.20, there is a discoloration zone at the interface on the transverse axis to the loading axis in yellow circle on the surface of the failed specimen (Figure 3.20(b)). When this discoloration zone is compared to the intact specimen (Figure 3.20(a)), it is observed that the failure evolves at the interface orthogonal to the loading axis. This fracture pattern of the mineralized tissue – C1 adhesive interfacial specimen was quite different from both ring specimens made of the mineralized tissue and the adhesives that was inside out from the hole along the load axis.

a b

Figure 3.20: Snapshots from the diametral compression test of the mineralized tissue – C1 adhesive interfacial specimens at 1 mm/min loading rate: (a) the undeformed specimen and (b) the specimen after failure (post-failure).

When interfacial specimens made of mineralized tissue and C1 adhesive were tested at 0.2 mm/min loading rate, the average peak force was reported to be 81.69 N with a minimum of 69.70 N and a maximum of 88.07 N (Figure 3.21). When the specimens reached their peak forces, they resulted in the displacement average as 0.41 mm. The minimum failure displacement was found to be 0.37 mm whereas the maximum one was 0.45 mm. It is clearly seen that the mineralized tissue – C1 adhesive interfacial specimens failed at both lower load and lower displacement at 0.2 mm/min than their average failure load and average failure displacement at 1 mm/min loading rate. It is also observed that the average failure force and failure displacement of the mineralized tissue – C1 adhesive specimens at 0.2 mm/min were higher than the mineralized tissue ring specimen's average failure force and displacement at 1 mm/min loading rate (see the Appendix D, Table 11.1).

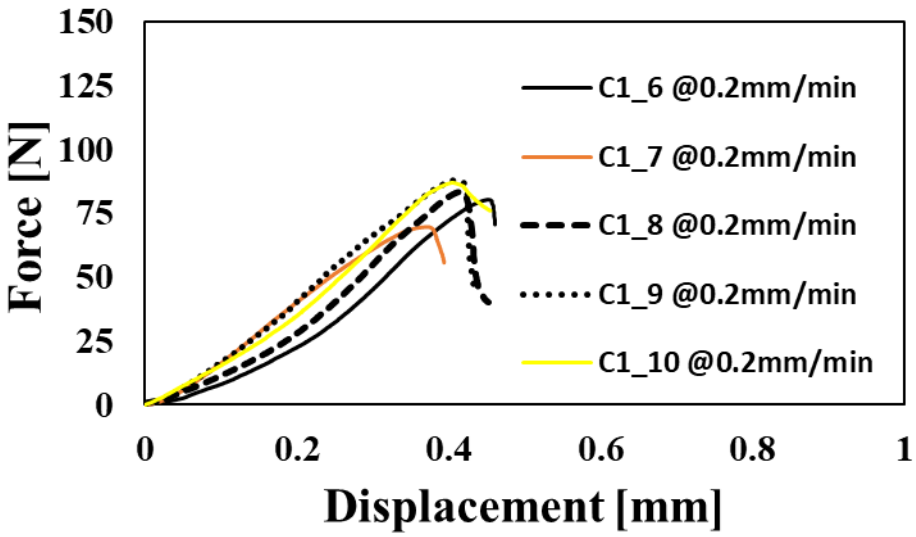

Figure 3.21: Force-displacement results obtained from the diametral compression test of the mineralized tissue – C1 adhesive interfacial specimens at 0.2 mm/min loading rate.

The experimental post-failure snapshot of the mineralized tissue – C1 interfacial specimen at 0.2 mm/min (Figure 3.22(b)) shows the separation at the interface along the axis that is transverse to the loading axis (yellow circled). The interfacial separation gets smaller towards the loading axis, indicating the propagation of the failure toward the load axis when the post-failure pattern is compared to the intact specimen (Figure 3.22(a)). The post-failure pattern of the mineralized tissue – C1 adhesive interfacial specimen at 0.2 mm/min loading rate is the same as its post-failure pattern at 1 mm/min loading rate.

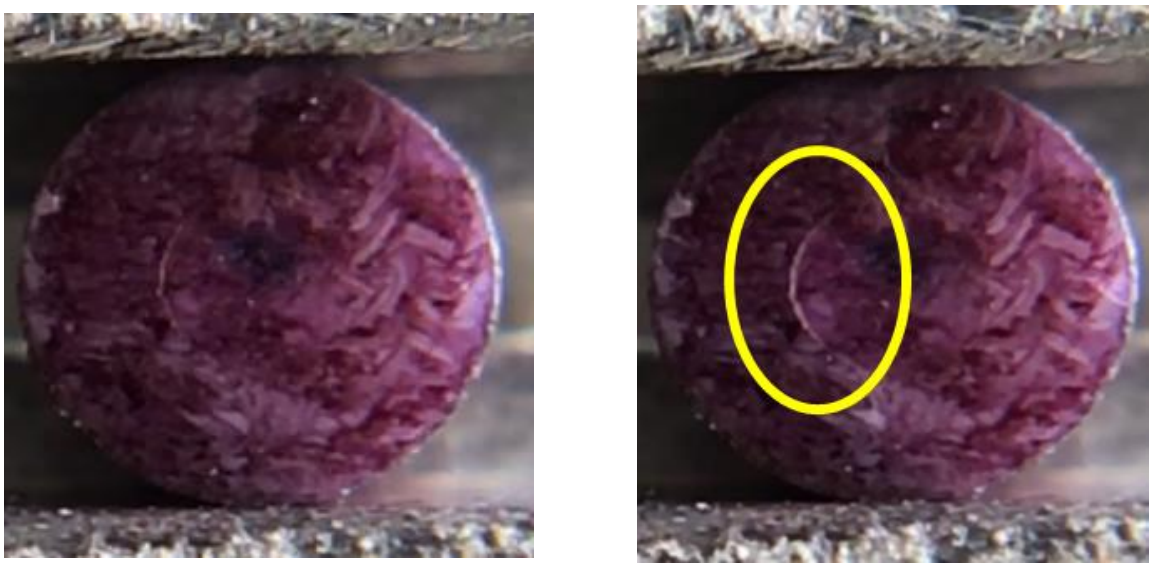

a b

Figure 3.22: Snapshots from the diametral compression test of the mineralized tissue – C1 adhesive interfacial specimens at 0.2 mm/min loading rate: (a) the undeformed specimen and (b) the specimen after failure (post-failure).

When the interfacial specimens made of the mineralized tissue and E1 adhesive were tested at 1 mm/min, they reached the average peak force of 119.72 N (Figure 3.23). The minimum peak force was read 110.23 N and the maximum peak force was found 129.16 N. The displacements corresponding to their peak forces were averaged as 0.51 mm where their lowest one was 0.48 mm and their highest one was 0.55 mm. The mineralized tissue – E1 adhesive interfacial specimens were significantly higher in the average failure load and displacement than the mineralized tissue – C1 adhesive interfacial specimens at 1 mm/min loading rate. They exhibited average failure displacement that is fairly close the average failure displacement of C1 adhesive ring specimens (see the Appendix D, Table 11.1).

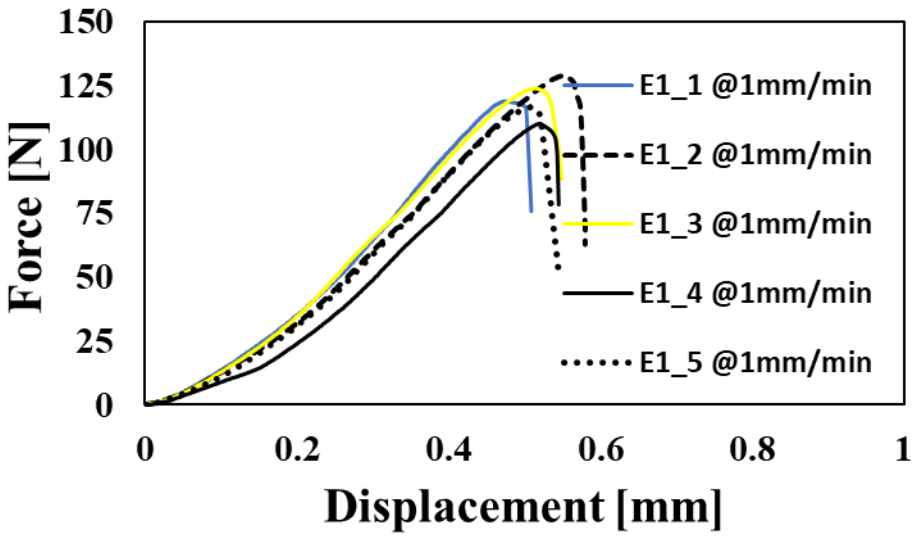

Figure 3.23: Force-displacement results obtained from the diametral compression test of the mineralized tissue – E1 adhesive interfacial specimens at 1 mm/min loading rate.

The failure initiation at the mineralized tissue – E1 adhesive interfacial specimen was observed at the interface on the transverse axis to the loading when the specimen was subject to the loading rate of 1 mm/min (Figure 3.24(b)). The discoloration zone, which indicates the failure, appears to be smaller towards the load surfaces when the undeformed specimen (Figure 3.24(a)) is compared with the failed interfacial specimen (Figure 3.24(b)). This reveals that the fracture evolves toward the loading axis. Therefore, the fracture path of the mineralized tissue – E1 adhesive interfacial specimen at 1 mm/min loading rate was the same as the mineralized tissue – C1 adhesive interfacial specimen at both loading rates of 1 mm/min and 0.2 mm/min.

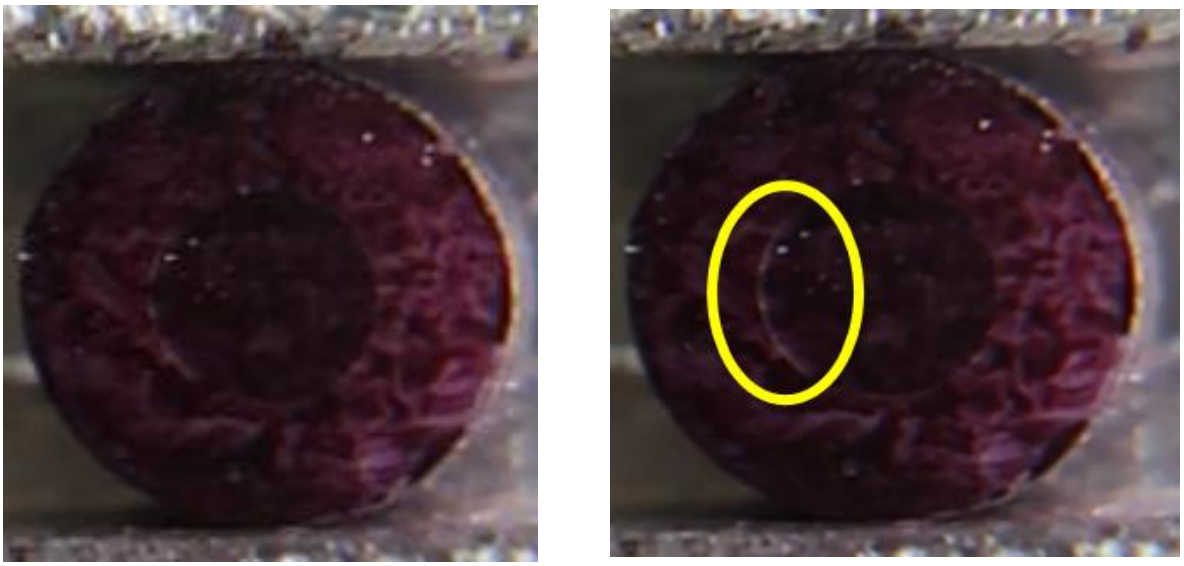

a b

Figure 3.24: Snapshots from the diametral compression test of the mineralized tissue – E1 adhesive interfacial specimens at 1 mm/min loading rate: (a) the undeformed specimen and (b) the specimen after failure (post-failure).

For the mineralized tissue – E1 adhesive interfacial specimens at 0.2 mm/min loading rate, the average failure load was found to be 103.49 N with a minimum of 93.25 N and a maximum of 112.63 N (Figure 3.25). They failed at an average displacement of 0.48 mm where the lowest failure displacement was 0.43 mm and the highest failure displacement was 0.50 mm. The mineralized tissue – E1 adhesive interfacial specimens reached failure at 0.2 mm/min loading rate at a lower load than their behavior at 1 mm/min loading rate whereas it was significantly higher than the average failure load of the mineralized tissue – C1 adhesive interfacial specimen's average failure load at 1 mm/min loading rate. Similarly, the average failure displacement of the mineralized tissue – E1 adhesive interfacial specimen at 0.2 mm/min was relatively lower than its average failure displacement at 1 mm/min loading rate. However, it was quite close to the average

failure displacement of the mineralized tissue – C1 adhesive interfacial specimen at 1 mm/min (see the Appendix D, Table 11.1).

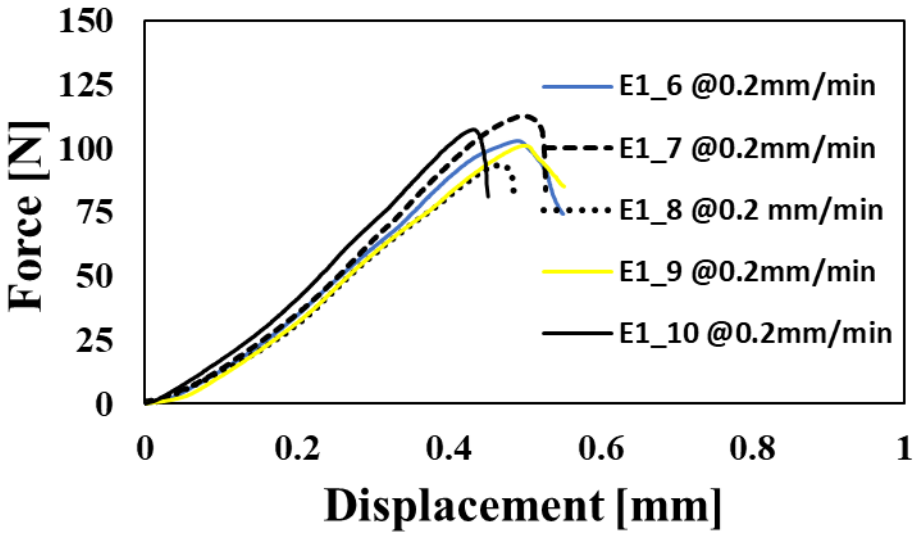

Figure 3.25: Force-displacement results obtained from the diametral compression test of the mineralized tissue – E1 adhesive interfacial specimens at 0.2 mm/min loading rate.

When the snapshots of the diametral compression test on the interfacial specimen made of the mineralized tissue – E1 adhesive are compared in terms of intact (Figure 3.26(a)) and post-failure (Figure 3.26(b)) states at 0.2 mm/min loading rate, it is observed that the specimen initiated failure at the interface along the transverse axis to the load axis. The propagation of the failure appeared in the direction towards the load axis along the interface. This failure pattern was the same as the mineralized tissue – E1 adhesive interfacial specimen at 1 mm/min loading rate and the mineralized tissue – C1 adhesive interfacial specimens at both 1 mm/min and 0.2 mm/min loading rates (see the Appendix D, Table 11.1).

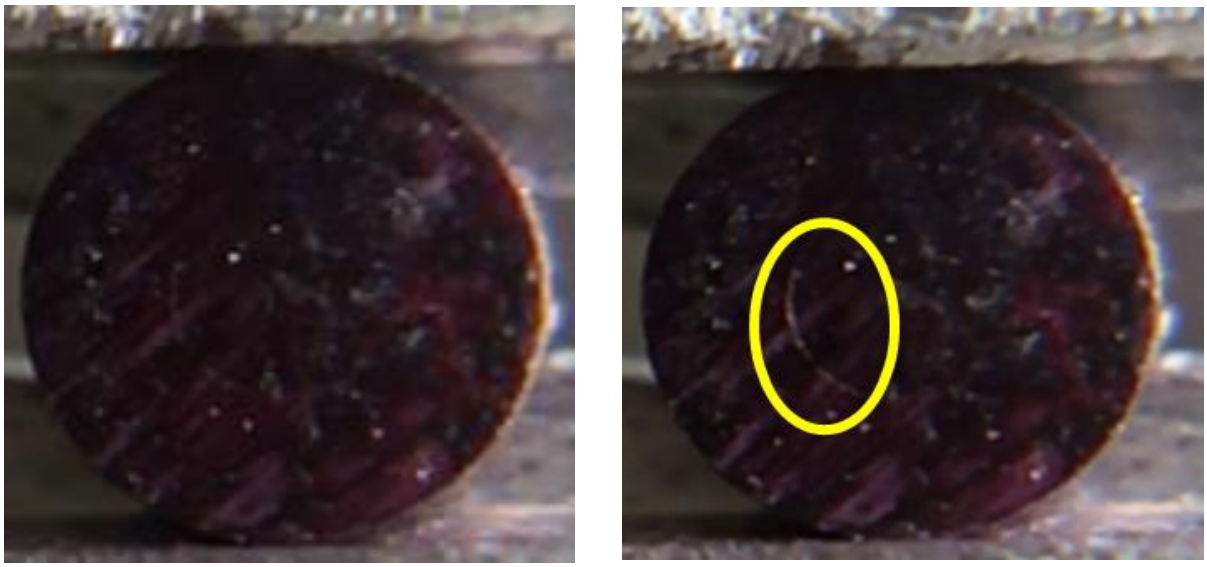

a b

Figure 3.26: Snapshots from the diametral compression test of the mineralized tissue – E1 adhesive interfacial specimens at 1 mm/min loading rate: (a) the undeformed specimen and (b) the specimen after failure (post-failure).

3.4 Discussion

It is noted that all force-displacement relationships obtained from both the ring specimens and the interfacial specimens experienced a small concave upward trend in the measurement. This type of behavior is likely due to the stiffening associated with the growing area between the surface of the specimen and the load platens [70]. As it is seen from the force-displacement curves, the hardening mechanism competes with the softening mechanism. Initially, the hardening mechanism is dominant and the specimens' response gets stiffer at each load increment. However, the softening mechanism takes over close to the yielding due the accumulation of the damage within the specimen. As the damage increases more, the specimens reach failure and eventually, they experience post-peak softening.

When the post-failure snapshots of specimens are compared to the intact shape of the specimens, it is noted that the failure pattern is the same for all ring specimens. The failure is initiated as a discoloration at hole that coincides with the diametral load axis. Afterward, the failure propagates along the diametral axis towards the loading surface while the discoloration intensifies. Eventually, the specimen experiences abrupt fracture when the specimen cannot resist more separation along the diametral axis. On the other hand, the interfacial specimens exhibit a different failure pattern than the failure pattern of ring specimens, although they have the same failure pattern when compared to each other. The failure of the interfacial specimens starts at the interface that coincides the transverse axis to the diametral load axis. It is noted that this failure or separation at the interface is observed only on one side of the interface. This behavior likely results from the randomly heterogeneous defect distribution in the mineralized tissue section of the interfacial specimens. This heterogeneous nature might cause discontinuities in the stress distribution, such as stress concentrations that will likely end up in the asymmetrical failure pattern at the interface. Moreover, it is also seen that the failure propagates in all interfacial specimens along the interface towards the intersection of the interface with the diametral load axis. This particular failure path can be devoted to the nature of the mineralized tissue section. It is already noted that the specimen fails at the hole along the loading axis when there is no inclusion in the ring specimens. In the presence of the inclusion in the center, the initial failure is shifted towards the transverse axis and grows towards the loading axis along the interface. This evolution of failure might be following the direction of a secondary failure location that is the initial failure location of the mineralized tissue ring along the loading axis.

The ring specimens were prepared to include a preset weakness location to promote and control the initial failure location. It also complements the understanding of the failure of the interfacial

specimens since the identical mineralized tissue ring specimens were used to prepare the interfacial specimens. In order to compare the reliability of the obtained information, the results obtained from the diametral compression test of the mineralized tissue ring specimen were compared to the existing data in the literature. The most comprehensive data in the literature was found about the mechanical strength values of human cortical bone [101]. It is assumed that these data will be suggesting a good approximation to the values for the bovine cortical bone specimens tested in this study. The data in the literature was reported in terms of stress. In order to enable one to one comparison, the force measurements in this study were converted into stress. To this end, the apparent tensile strength of the ring specimen was calculated by using the following equation [102-105]:

$$\sigma_t = 2P(6 + 38\bar{r}^2)/\pi Dt \tag{3.1}$$

where σ_t is the apparent tensile strength of a ring specimen, P is the measured force, $\bar{r}$ is the ratio of the hole diameter to the outer diameter, D is the outer diameter and t is the thickness of the specimen.

The average apparent tensile strength of the mineralized tissue specimens was found 112.23 MPa and 74.47 MPa at 1 mm/min and 0.2 mm/min loading rates, respectively. The apparent tensile strength calculated using (3.1) is in the range of the tensile strength reported in the literature for human cortical bones. It is noted, however, that the literature values (1) often do not report the loading rates or use rates that are different from that used in this work, and (2) have a much wider variation likely due to the natural variability of the tissue and also the uncertainty of the testing procedure [101]. The data obtained from the testing of the polymer adhesives were also calculated in terms of their apparent tensile strength. The average tensile strength of C1 and E1 adhesives at 1 mm/min loading rate was calculated as 35.11 MPa and 43.91 MPa, respectively. Moreover, C1

and E1 adhesives have an apparent tensile strength of 26.56 MPa and 31.24 MPa, respectively, at 0.2 mm/min loading rate.

Similarly, the data obtained from the testing of the interfacial specimens were converted into apparent tensile strength by using the following equation [80, 102, 106, 107]:

$$\sigma_t = 2P/\pi Dt \tag{3.2}$$

where σ_t is the apparent tensile strength of a disk specimen, *P* is the measured force, *D* is the disk diameter and *t* is the disk thickness. For the bond strength characterization, it was assumed that the apparent tensile strength is the bond strength since it was observed that the interfacial specimens reached failure at the interface. To this end, the average bond strength data for the mineralized tissue – C1 adhesive interface was calculated as 12.26 MPa and 11.56 MPa at 1 mm/min and 0.2 mm/min loading rates, respectively. On the other hand, the mineralized tissue – E1 adhesive interface resulted in the average bond strength of 16.94 MPa and 14.64 MPa at loading rates of 1 mm/min and 0.2 mm/min, respectively, which are reasonable comparing to the data in the literature from conventional bond strength characterization of dentin-adhesive interface via micro-tensile test [20, 21] and a diametral compression test on dentin-adhesive-composite interface for bond strength characterization [81]. In detail, a recent study followed a similar approach using the diametral compression test on interfacial specimens where the specimens were prepared as three sections [81]. These three sections were bovine dentin tissue as the mineralized tissue at the outer section, a bonding agent as adhesive in the middle section and restorative composite at the inclusion section. Moreover, the specimens in that study were tested in a vertical configuration whereas in this study the specimens were tested horizontal configuration. The testing configuration can potentially affect the application of the assumed boundary conditions due to the alignment of the specimen during loading. While considering these differences in the characterization, it is noted

that this data in the literature provides a benchmark range to verify the reliability of the bond strength characterization in this study.

After conducting the diametral compression test on each particular material and interfacial pair, it was seen that the higher loading rate yielded higher average failure force and displacement for all materials and interfacial pairs. This observation is due to the viscoelastic nature of both the mineralized tissue and the polymer adhesive materials where the viscoelastic material stiffens with the increasing loading rate (see the Appendix D, Table 11.1).

When C1 adhesive and E1 adhesive are compared in terms of their failure load at both 1 mm/min and 0.2 mm/min loading rates, it is seen that E1 adhesive's failure load is higher than C1 adhesive at both loading rate. This finding can be explained by the mechanical response of amorphous polymer that is strongly affected by the crosslinking density [108]. E1 adhesive polymer has higher crosslinking density due to the further contribution of the self-strengthening reaction [91-94], reflecting to the increase in the failure load. However, the higher crosslinking density is also why E1 adhesive specimens failed at a lower displacement compared to the C1 adhesive specimens. This phenomenon is suggested by a molecular dynamics simulation study where more strain concentrations emerged from a higher crosslinking density [108]. Eventually, the specimen fails in a more brittle manner with the increased strain concentrations, which is observed by comparing brittle failure of E1 adhesive, whose crosslinking density is higher than C1 adhesive that failed more ductile. Moreover, it is observed that E1 adhesive increased its failure load at the higher loading rate significantly higher than that for the C1 adhesive (see the Appendix D, Table 11.1). This behavior of E1 adhesive is due to the relaxation of pedant side chains and dynamic hydrogen bonds where the increasing loading rate requires a shorter process for dissociation of reversible cross-links [109]. In the bond strength measurement, it is observed that the mineralized tissue –

E1 adhesive interface yields significantly higher bond strength than the mineralized tissue – C1 adhesive interface at both 1 mm/min and 0.2 mm/min loading rates (see the Appendix D, Table 11.1). This superior mechanical strength of the mineralized tissue – E1 adhesive can be addressed by the hydrolyzed MPS in E1 adhesive. The hydrolyzed MPS contains three silanol groups whereas C1 adhesive has no silanol groups and has less amount of hydrogen bond donor/acceptor [95]. A condensation reaction between the silanol and hydroxyl groups of collagen might lead to the formation of covalent bonds. This will drop the polymer/collagen chain mobility and inhibit the plastic flow while being deformed. Moreover, the theoretical density of polymer and polymer/collagen hybrid materials is determined by the crosslinker content. The chain reorganization possibility diminishes with higher crosslinking density [110, 111] and this reflects to higher stiffness [112, 113]. The hybrid networks also stiffen since the motion of the side chain can also be hindered by more hydrogen bonds such as silanol-silanol, silanol-hydroxyl and silanol-collagen, etc.) [114].

3.5 Summary and Conclusions

In this study, the bovine cortical bone tissue – dental adhesive interface and its components were experimentally investigated. The purpose of these investigations was to inform the design of dental restorative materials using a reliable measurement of mechanical properties. Due to compositional similarities and accessibility, the bovine cortical bone tissue was preferred as a surrogate material for human dentin. The diametral compression test was performed in to reveal the tensile nature of the mineralized tissue (the cortical bone) and the adhesive polymers, as well as the bond strength of the mineralized tissue – adhesive interface. Two different adhesive formulations were

investigated during this study. The formulations differ only by means of the γ-methacryloxypropyl trimethoxysilane (MPS) they contain. While the experimental (E1) formulation contained MPS, the control (C1) formulation did not contain MPS.

MPS was reported to provide self-strengthening characteristics to the adhesives. After performing the tests at two different loading rates, the tensile strength of the materials and the bond strength of the interfacial material systems were evaluated. The rate-dependent nature was clearly observed for the mineralized tissue, adhesive polymers and the interfacial material systems. The tensile strength of the bovine cortical bone tissue and the bond strength of the mineralized tissue – adhesive interface obtained from the diametral compression test were found to be relatively repeatable and in good agreement with the literature. The experimental post-failure snapshots revealed failure initiation locations and paths of failure evolution in both single material and interfacial testing. Particularly, the failure initiation at the interfacial testing was observed at the interface. It suggests that the testing is informative about the bonding characteristics. Additionally, the self-strengthening adhesive, E1, was found to be more superior to C1 adhesive in terms of both its tensile nature and its bonding to the mineralized tissue (see the Appendix D, Table 11.1). Moreover, E1 adhesive was observed to be more brittle in tensile nature compared to C1 adhesive. The difference in the mechanical behavior of E1 and C1 adhesives was mainly linked to the properties of E1 adhesive. These properties include a higher crosslinking density, more hydrogen bonds and lower chain mobility than C1 adhesive. It is noted that the mechanical test technique selected in this study effectively eliminated the drawbacks inherent to the conventional tensile testing. However, the physical experiment alone may not necessarily deliver the true mechanics underlying the tensile nature and bond mechanics. A deeper understanding of the true tensile nature and bonding characteristics of these material systems can be established through the assistance of

advanced techniques such as finite element analysis and digital image correlation. These complementary methods may reveal stress and strain distribution on the domain of interest. The hybrid layer is one of the domains where the deformation and failure mechanisms can be investigated thoroughly.

CHAPTER 4

PARAMETRIC STUDY FOR COMPUTATIONAL ANALYSIS OF THE DIAMETRAL COMPRESSION TEST

4.1 Introduction

The developed granular micromechanics nonlinear material model was successfully demonstrated as a promising model with its capability to capture the rate dependent nonlinear mechanical behavior in Chapter 2. This nonlinear material model's performance needs to be examined before starting a systematic computational characterization study. This examination is aiming at evaluation of the rate dependent damage and failure mechanisms of the mineralized tissue, the adhesive polymer and the interfacial material systems as experimentally characterized in Chapter 3. In this chapter, the nonlinear material model's numerical accuracy and computational time were investigated in the mineralized tissue's diametral compression test simulations. After optimizing the model's numerical accuracy and computational time, the developed computational framework was used to simulate the rate dependent mechanical behavior of the mineralized tissue and an adhesive polymer. The studied material model parameters were estimated based on a recent study [70].

4.2 Computational Analysis

The finite element (FE) simulations were performed via the commercial FE code, Abaqus (Simulia/ABAQUS V 6.13-3, Dassault Systémes, RI, USA). This commercial FE code was

coupled with visual Fortran composer (Intel, Santa Clara, CA) to implement the developed nonlinear material model into FE analyses, as presented in Chapter 2. Accordingly, the material model was formatted as a user-defined nonlinear material model (UMAT). The FE models were created based on the application of the diametral compression test of the bovine femur cortical bone tissue (the mineralized tissue) based on a recent study (Figure 4.1(b)) [70].

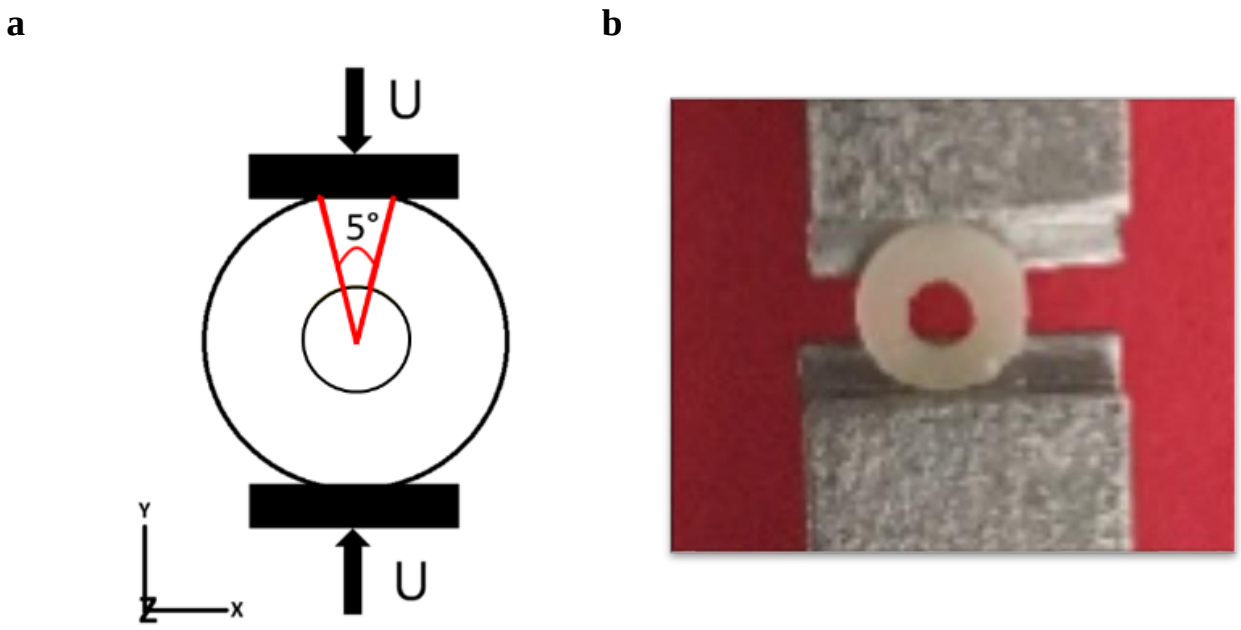

Figure 4.1: (a) Representation of the diametral compression test considered in the finite element model and (b) the physical diametral compression test setup [70].

Five different FE models were generated. The first model was created to investigate the material model's numerical accuracy in a boundary value problem. In this model, the ring specimen's geometry was prepared with an outer diameter of 1 mm. The ratio of the outer diameter to the inner diameter was selected as 3. The thickness was set 0.01 and one single element was assigned in the

z-direction (along with the thickness of the ring specimen). Moreover, the displacement of all nodes was set to zero in the z-direction. Thus, a plain-strain-type condition was applied to ease the experimental conditions and decrease the computational effort. Additionally, only one-fourth of the ring specimen was used for the simulations (Figure 4.1(a)). Therefore, the symmetric boundary conditions were assigned on x-z and y-z planes (Figure 4.2(a)). 4 node linear tetrahedral elements were used to mesh the geometry. The model has 2280 degrees of freedom. The experimental loading conditions were simplified by applying a displacement load in the negative y-direction. The load surface was set as an arc of 2.5° from the center of the geometry (Figure 4.2(b)). The applied loading rate was assigned to be 1 mm/min. Five different simulations were simulated with this model by varying the time incrementation size. The time incrementation sizes were 0.00025 min, 0.0005 min, 0.001 min, 0.0025 min and 0.005 min. Moreover, three more simulations were performed to demonstrate the rate dependent capability of the material model. These three simulations used the loading rates of 0.2 mm/min, 0.5 mm/min and 1 mm/min. Their time incrementation was set 0.0025 min. The material model parameters were assigned for the bovine cortical bone tissue, as presented in Chapter 2 [70] (see the Appendix C, Table 10.1).

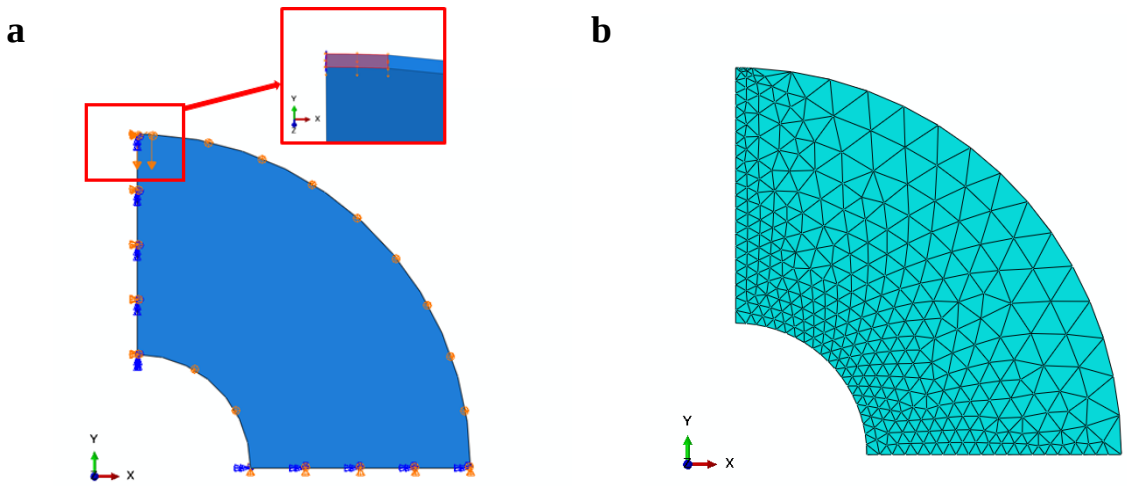

Figure 4.2: Finite element model of the diametral compression test specimen with (a) the boundary conditions and (b) the meshed geometry.

In the second FE model, the geometry was created in consideration of a three-dimensional model. A 0.6 mm thick disk was prepared with a diameter of 3 mm and a hole diameter of 1 mm by following the experimental specimen's dimensions [70]. This model only contained one-eighth of the geometry as the symmetric boundary conditions were applied on the xy, xz and yz planes (Figure 4.3(a)). The geometry was meshed with 4 node linear tetrahedral elements. The model contained 7083 degrees of freedom (Figure 4.3(b)). The experimental loading was simulated by applying a displacement with a loading rate of 0.2 mm/min. This load was applied in the negative y-direction. The load surface was generated as an arc of 2.5°, whose center was the specimen's center. The time incrementation size was assigned as 0.0025 min. The mineralized tissue's nonlinear material model parameters were selected after calibration against the experimental data [70] (see the Appendix C, Table 10.2).

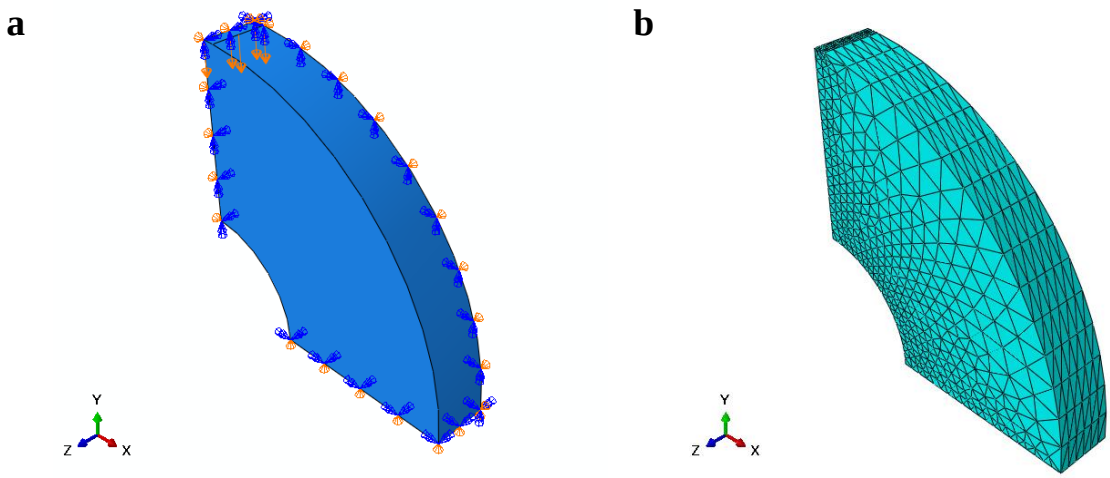

Figure 4.3: Three-dimensional finite element model of the diametral compression test of the 0.6 mm thick ring specimen with (a) the boundary conditions and (b) the meshed geometry.

The third and fourth FE models were prepared to investigate the diametral compression test of the mineralized tissue with a larger thickness. A 1.5 mm thick disk geometry was created with a diameter of 3 mm. The third model had a full disk geometry (Figure 4.4(a)). In the fourth model, a hole was introduced in the center (Figure 4.5(a)). The hole had a diameter of 1 mm. Both models had the symmetric boundary conditions on xy, xz and yz planes since only one-eighth of their geometries were included in the models. Both geometries were meshed by using 4 node linear tetrahedral elements. The disk model had 3270 degrees of freedom (Figure 4.4(b)) and the ring model contained 2955 degrees of freedom (Figure 4.5(b)). In these models, the time incrementation size was selected 0.0025 min. Three simulations were performed with each model. These simulations were performed at the loading rates of 0.2 mm/min, 0.5 mm/min and 1 mm/min. The same material model parameters were assigned as the second FE model (see the Appendix C, Table 10.2).

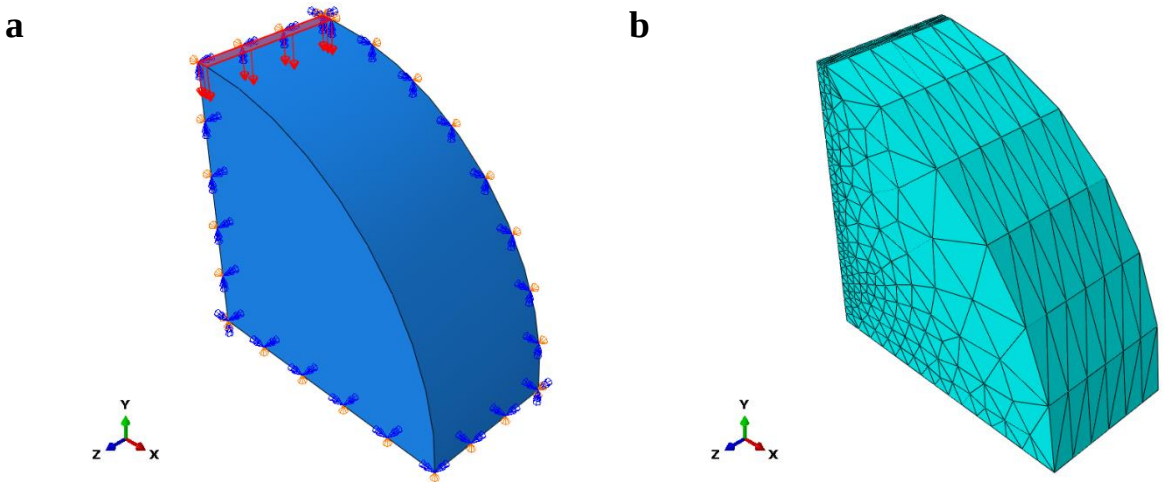

Figure 4.4: Three-dimensional finite element model of the diametral compression test of the 1.5 mm thick full disk specimen with (a) the boundary conditions and (b) the meshed geometry.

For the fifth FE model, the same model was used as the fourth FE model. This model was created to simulate the behavior of an adhesive polymer. Three different loading rates were applied. These loading rates were 0.2 mm/min, 0.5 mm/min and 1 mm/min. The material model parameters were assigned by speculating the adhesive polymer's mechanical behavior. The adhesive's micro-scale normal and shear stiffnesses were assumed to be 10% of the bovine cortical bone tissue used in the second FE model (see the Appendix C, Table 10.2).

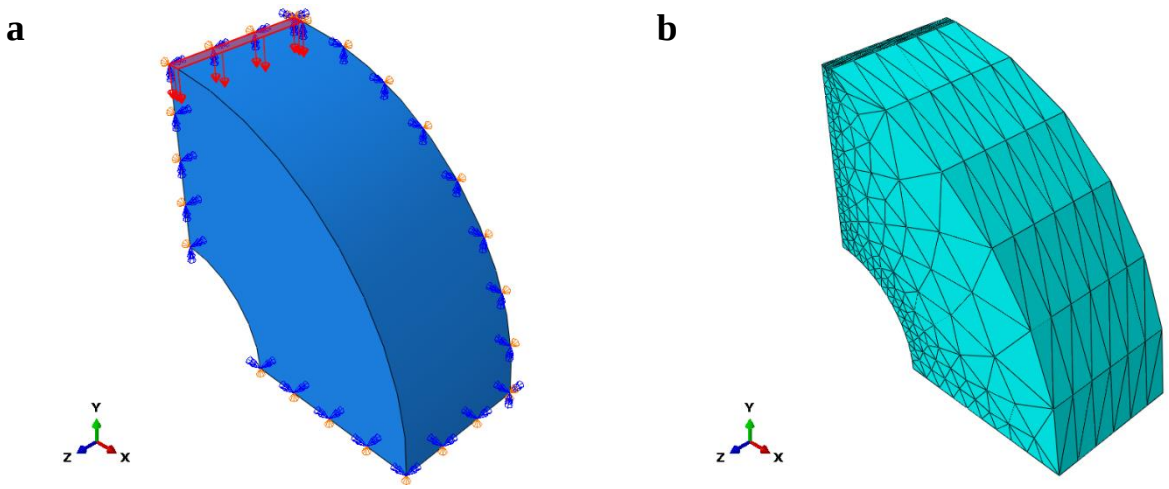

Figure 4.5: Three-dimensional finite element model of the diametral compression of the 1.5 mm thick ring specimen with (a) the boundary conditions and (b) the meshed geometry.

4.3 Results and Discussion

The model's numerical accuracy was investigated by using the force-displacement results of the simulations with the plain strain type conditions. These simulations had the same loading rate. They were performed with different time incrementation sizes. These time incrementation sizes varied between 0.00025 min and 0.005 min. The force-displacement results were obtained from the simulations to evaluate the model's numerical accuracy (Figure 4.6). In general, the simulations were capable of capturing the typical trends in a nonlinear force-displacement relationship. In detail, all the curves consisted of an initial linear trend, a pre-peak softening regime and a post-peak softening regime. It was observed that the results approximated each other with decreasing time incrementation size.

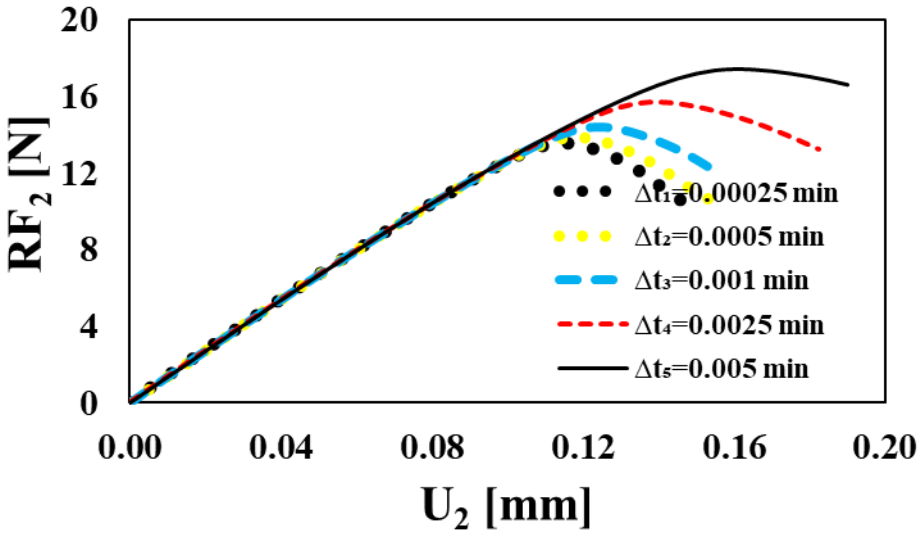

Figure 4.6: Force-displacement relationships obtained from the diametral compression test simulations with different time incrementation sizes, Δt. (RF_2: the reaction force in the loading direction and U_2: displacements in the loading direction)

The results appeared to converge to a solution with the decreasing time incrementation size. An error evaluation was done by using the peak reaction force (RF_{2_p}) and the peak displacement ($-U_{2_p}$). These values were determined for each case from the simulated force-displacement relationships. Subsequently, L_2 norms of the peak displacement and the peak reaction force were computed for error evaluation as the following:

$$L_{2_{U_{2p}}} = \frac{\left(U^0_{2\,p} - U_{2_p}\right)^2}{\left(U^0_{2\,p}\right)^2}$$

$$L_{2_{RF_{2p}}} = \frac{\left(RF^0_{2\,p} - RF_{2_p}\right)^2}{\left(RF^0_{2\,p}\right)^2} \qquad (4.1)$$

where $U_{2_p}^0$ and $RF_{2_p}^0$ are the peak reaction force and the peak displacement, respectively, of the simulation solved with the minimum time incrementation size that is 0.00025 min. In Figure 4.7, the L_2 norm of the peak displacement and time incrementation size relationship was shown. The time incrementation sizes were normalized by the initial retardation time, $\tau_{n\delta}(0)$ as shown in Chapter 2.

In Figure 4.7, it was observed that the error in the peak displacement went up with the increase in the time incrementation size. The error appeared reasonable up to 0.0025 min. Particularly, the error increased from 0.05 to 0.16 when the time incrementation size increased from 0.0025 min to 0.005 min.

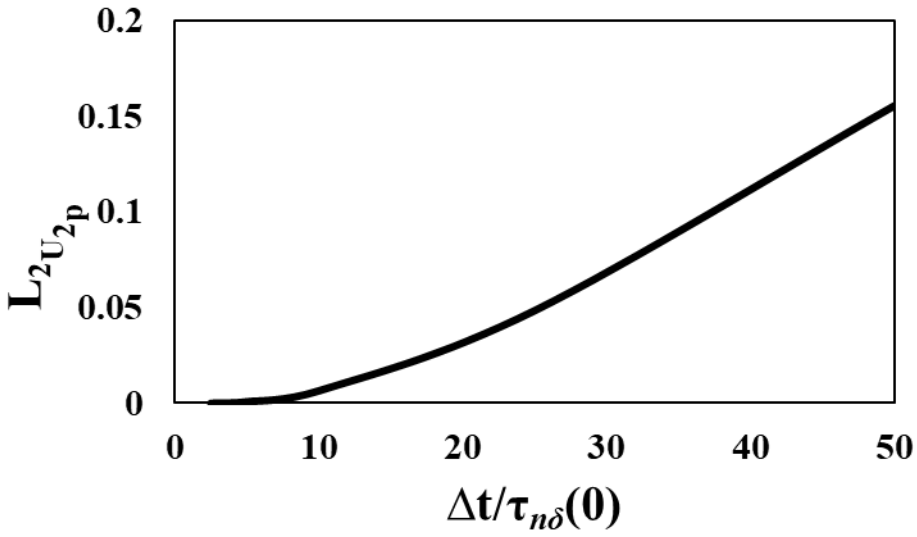

Figure 4.7: The error of peak displacement in the diametral compression simulation with respect to the normalized time incrementation size.

Figure 4.8 suggested that the solution diverged from the true solution and the error in peak force was increased when the time incrementation size was increased. The error was observed as 0.03

at 0.0025 min. This error was lower than the error in the displacement at the same time incrementation size. Afterward, the error increased to 0.08 when the time incrementation size increased to 0.005 min.

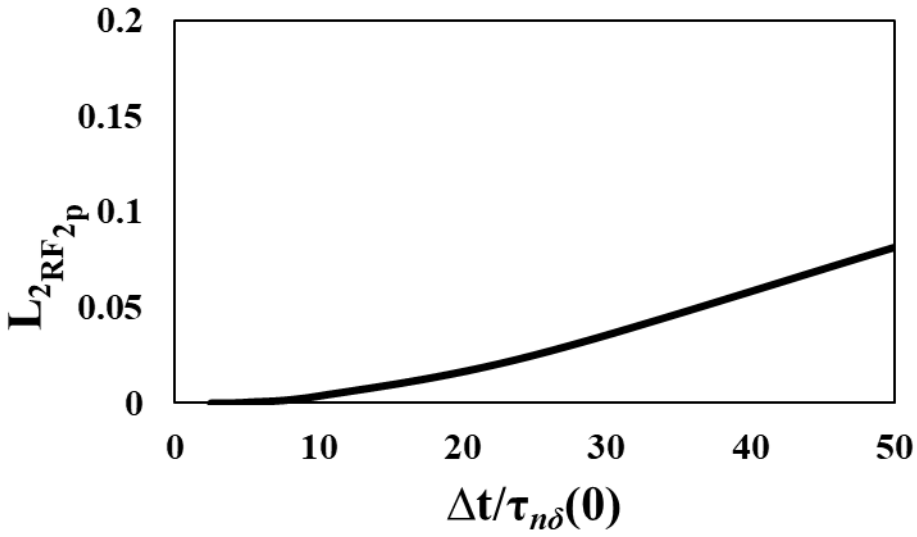

Figure 4.8: The error of peak reaction force in the diametral compression test simulation with respect to the normalized time incrementation size.

In addition to the error analysis, the simulation's computational time reported for each time incrementation size (Figure 4.9). This data showed that the computational demand significantly drops with larger incrementation sizes. Regarding the error, the largest time incrementation size resulted in solutions with the largest error. Therefore, 0.0025 min was found to optimize both numerical accuracy and computational time.

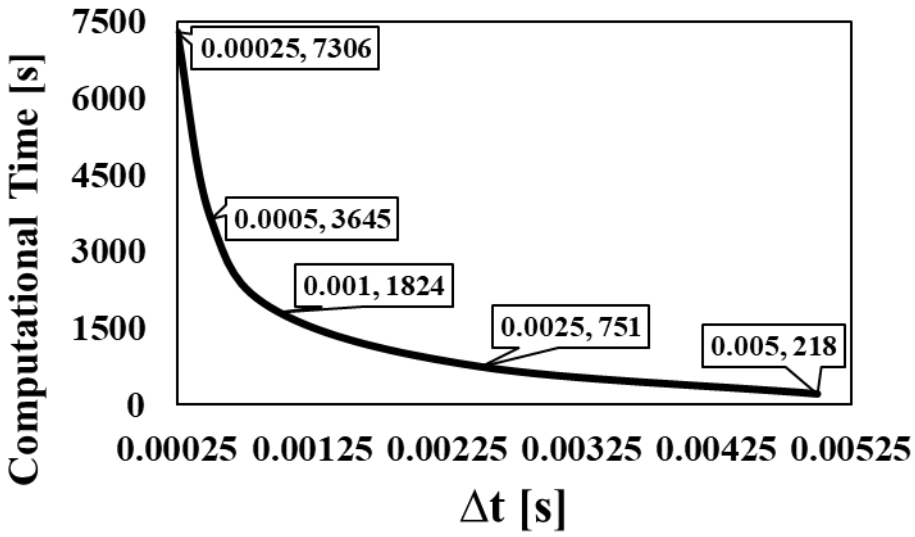

Figure 4.9: The computational time for running the diametral compression test simulations with respect to the time incrementation size.

The time incrementation size of 0.0025 min was used for demonstrating the material model's rate dependent capability in this boundary value problem. Three different simulations were done at different loading rates. These loading rates were selected as 0.2 mm/min, 0.5 mm/min and 1 mm/min. The highest force peak was observed at high loading rate, whereas the lowest force peak was at the lowest loading rate. At 1 mm/min, the peak force was read as 15.71 N at a displacement of 0.14 mm in the high load rate case. The load rate of 0.5 mm/min resulted in the peak force of 14.39 N at a displacement of 0.12 mm. In the case of 0.2 mm/min, the peak force was predicted to be 13.37 N at a displacement of 0.11 mm. These results showed that the material model successfully captured the rate dependent mechanical behavior in the diametral compression test simulations.

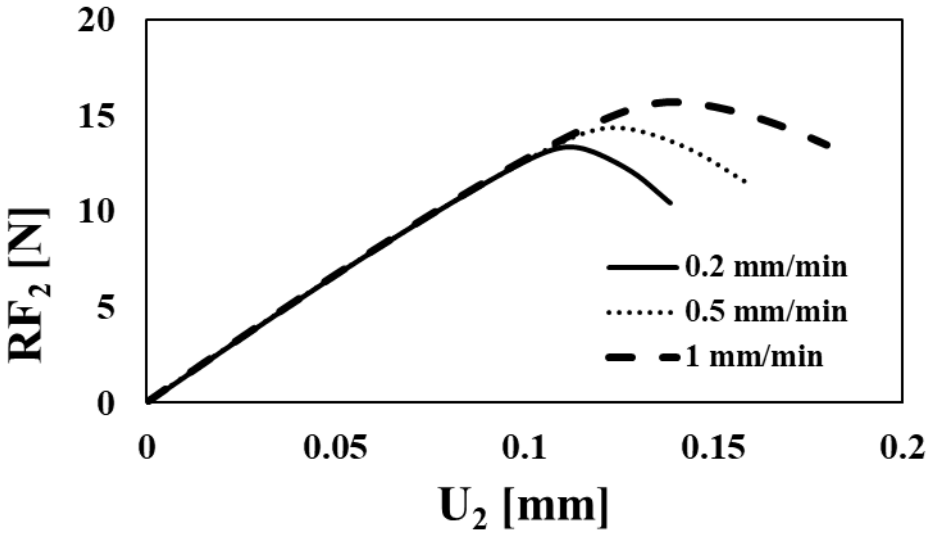

Figure 4.10: Reaction force-displacement relationships in diametral compression test at loading rates of 0.2 mm/min, 0.5 mm/min and 1 mm/min.

Moreover, the simulated force-displacement results were obtained from the 3D FE model with the experimental specimen's dimensions. These results were compared to the experimental force-displacement relationship from the mineralized tissue's physical experiment [70] (Figure 4.11(a)). The diametral compression test's 3D FE model with the calibrated mineralized tissue material model parameters captured the overall mechanical behavior well. In detail, the experimental peak force was 17.34 N at a displacement of 0.174 mm and the simulation predicted the peak force as 17.09 N at a displacement of 0.158 mm. While capturing the overall trend in the force-displacement relationship relatively successful, there was a slight offset in the initial behavior. This offset might be possibly resulted from the stiffening with the increasing contact area between the specimen and load platens in the physical experiment that was not accounted for in the FE model.

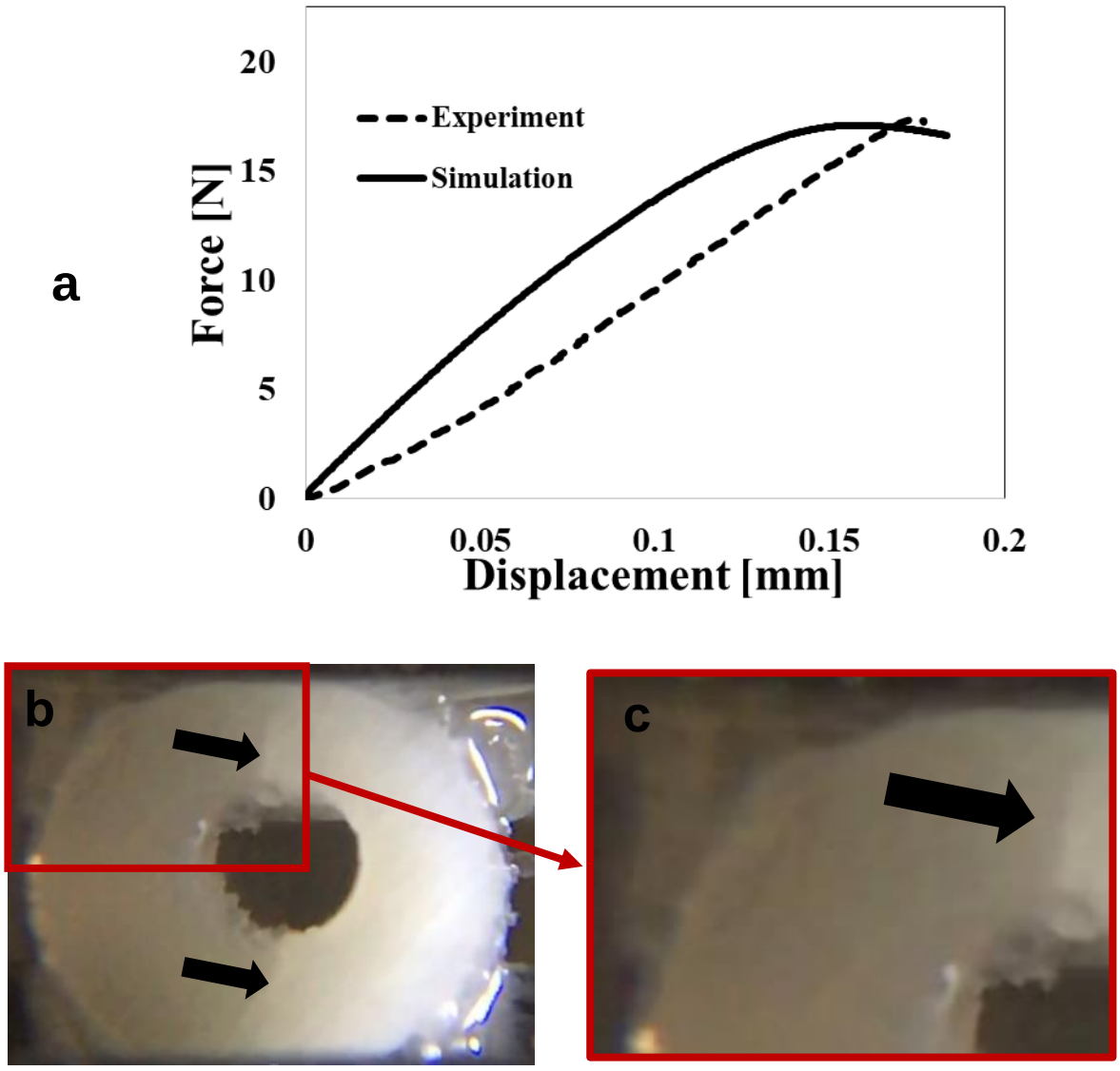

Figure 4.11: Experimental observations from the application of diametral compression test on the mineralized tissue: a) Force-displacement relationship obtained from the physical experiment vs. the results obtained from the simulation with the calibrated nonlinear material properties, b) Failure evolution within the specimen observed in the physical experiment and c) Close-up image indicating the location of the failure within the specimen [70].

Furthermore, the 3D FE simulation results were post-processed into the octahedral normal and the octahedral shear strain maps. These maps informed the local volume change and local distortion,

respectively. In Figure 4.12(a) and Figure 4.12(b), these maps were presented at a post-failure displacement. The grey areas belonged to the locations exceeding the fixed color bar values. The color bar of each map was fixed at the failure displacement. The failure was predicted to initiate and evolve along with the loading axis starting inside out from the hole in the center. This observation successfully matched the experimental failure snapshots. The experimental failure began as a discoloration zone along with the loading axis starting from the hole in the center while the microcracks developed with the increase in the load (Figure 4.11(b) and Figure 4.11(c)).

a

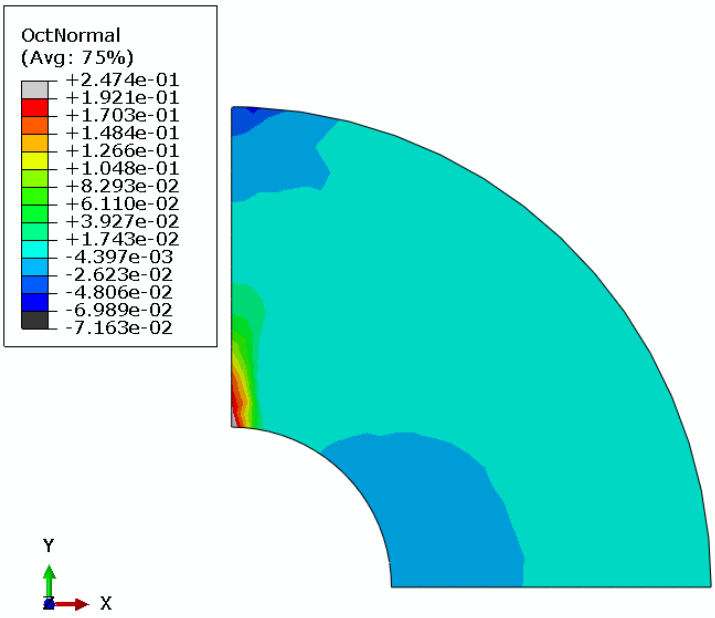

b

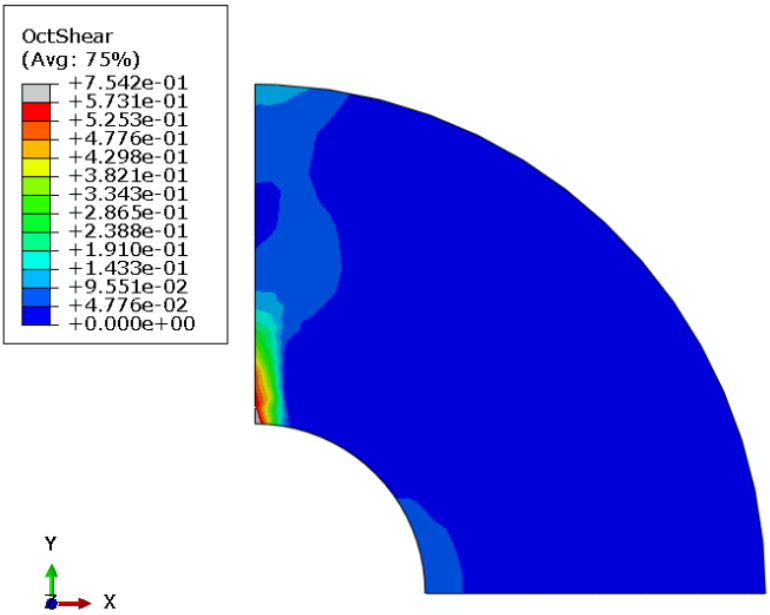

Figure 4.12: a) Local volume change and b) Local distortion maps from the simulation of diametral compression test on the mineralized tissue.

Moreover, the simulation data was further post-processed in to present the material model's capability to capture the 3D nature of the loading. This investigations revealed the strain paths within the specimen. The elements from seven critical locations were selected and designated, as it is shown in Figure 4.13(a). The relationship between octahedral normal strain and octahedral shear strain at each selected element was given in Figure 4.13(b). The presented relationships revealed that a dilatational behavior dominated the elements within the vicinity of failure zone such as Element 1 and Element 2. The elements along the transverse axis to the loading axis and within hole's proximity, such as Element 7 and Element 6, experienced a contraction behavior. Similarly, Element 4, which was located between loading and the transverse axes, exhibited a contraction only behavior. On the other hand, it was observed that the elements along the loading and its transverse axes, and in the proximity of the outer edge such as Element 3 and Element 5

initially experienced a contraction behavior, which was later followed by a dilatational behavior. These observations clearly showed that every point within the specimen experienced a different load path. The material model captured the contraction to dilatation behavior, which is not captured in linear elastic fracture mechanics.

a

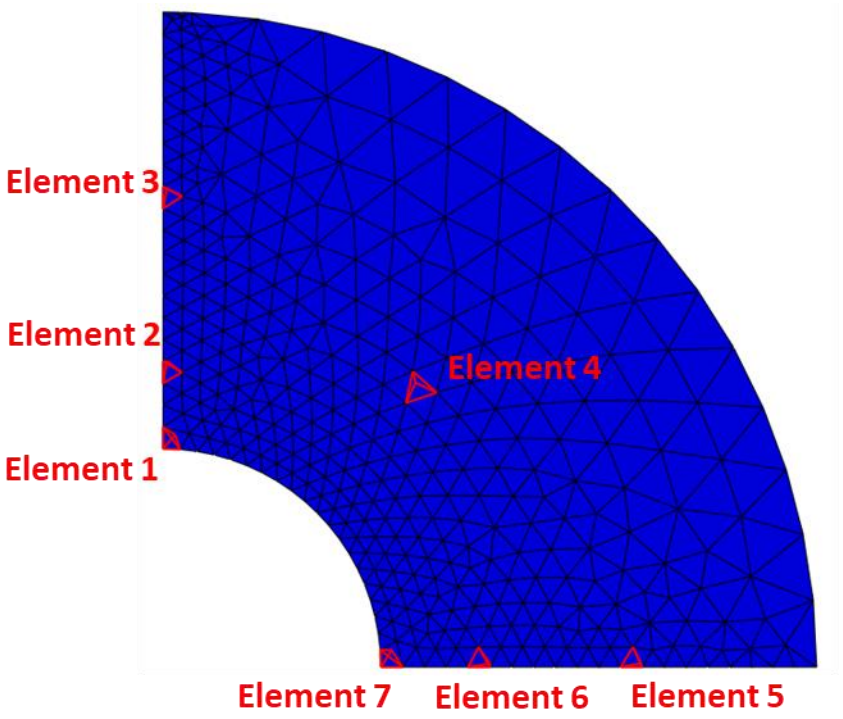

b

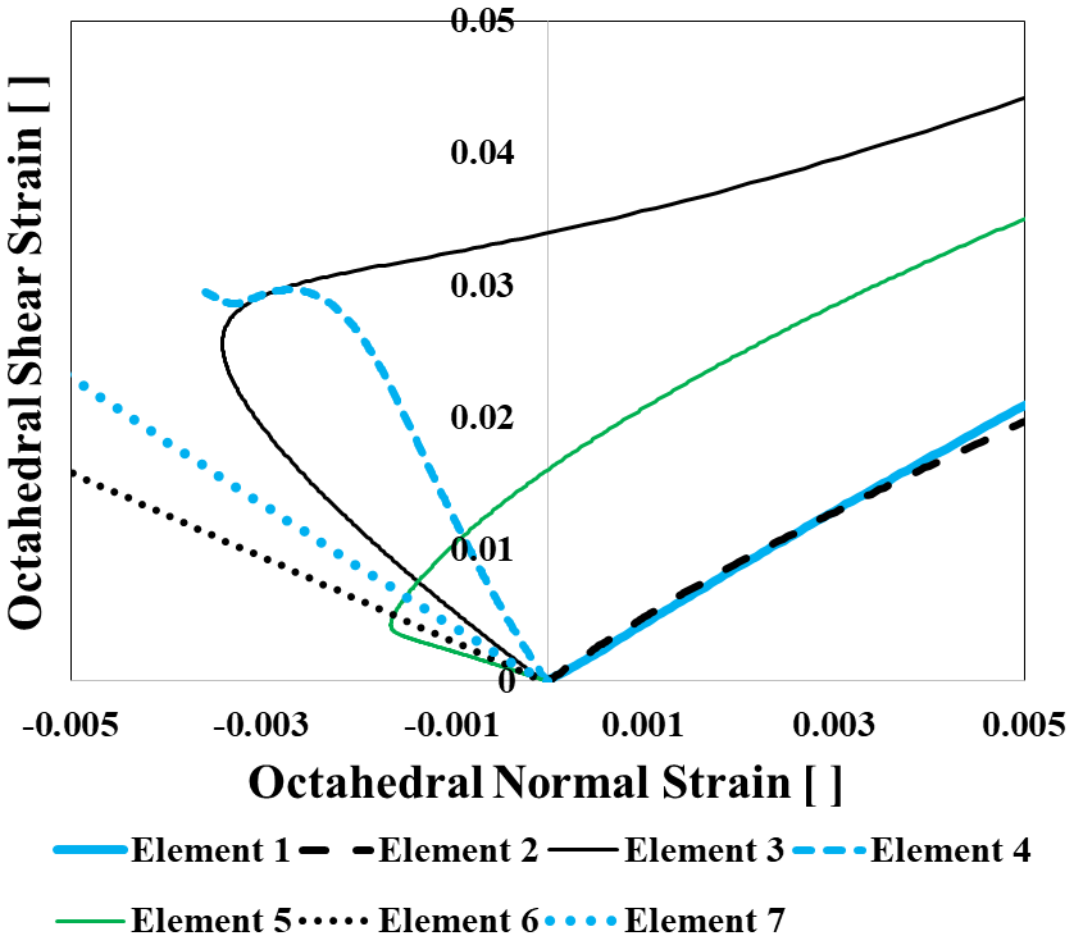

Figure 4.13: a) Elements selected at critical locations within the specimen and b) Strain path evaluation at the selected elements in terms of the relationship between octahedral normal and octahedral shear strains.

It was assumed that a thicker specimen than 0.6 mm might be more convenient in specimen preparation. Therefore, a diametral compression test model was created with a 1.5 mm thick full disk specimen. This model used a geometry without a hole in the center to evaluate the central hole's effect on the failure mechanism. The mineralized tissue's calibrated material model parameters were assigned to this model. Three simulations were performed at different loading rates. These load rates were selected as 0.2 mm/min, 0.5 mm/min and 1 mm/min. The simulated

force-displacement relationships (Figure 4.14) predicted that the mineralized tissue full disk specimen's peak force is 105.62 N, 109.27 N and 113.89 at 0.2 mm/min, 0.5 mm/min and 1 mm/min, respectively. Moreover, the specimen failed at a displacement of 0.26 mm, 0.28 mm and 0.30 mm at the loading rates of 0.2 mm/min, 0.5 mm/min and 1 mm/min, respectively. The mineralized tissue full disk specimen significantly increased its peak force and peak displacement with increasing loading rate.

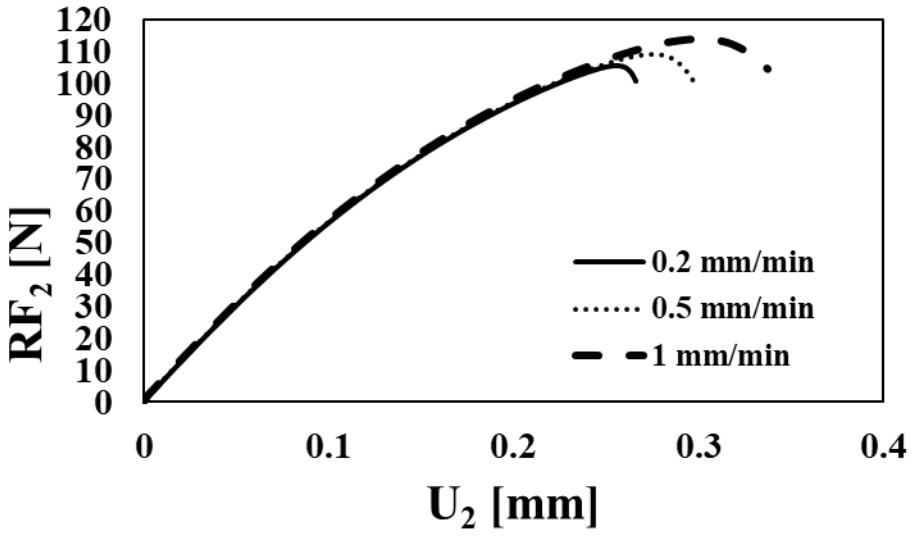

Figure 4.14: The predicted force-displacement relationship of the mineralized tissue full disk specimen at 0.2 mm/min, 0.5 mm/min and 1 mm/min.

Moreover, a 1.5 mm thick mineralized tissue ring specimen's mechanical test was simulated at 0.2 mm/min, 0.5 mm/min and 1 mm/min. This specimen's force-displacement relationships were obtained from the simulations (Figure 4.15). The ring specimen's peak force was predicted to be 39.19 N, 42.77 N and 47.21 N at 0.2 mm/min, 0.5 mm/min and 1 mm/min, respectively. The

specimen reached failure at a displacement of 0.12 mm, 0.14 mm and 0.16 mm at the loading rates of 0.2 mm/min, 0.5 mm/min and 1 mm/min, respectively. It was observed that the mineralized tissue ring specimen failed at significantly lower loads and displacements compared to the full disk mineralized tissue disk specimen at all loading rates.

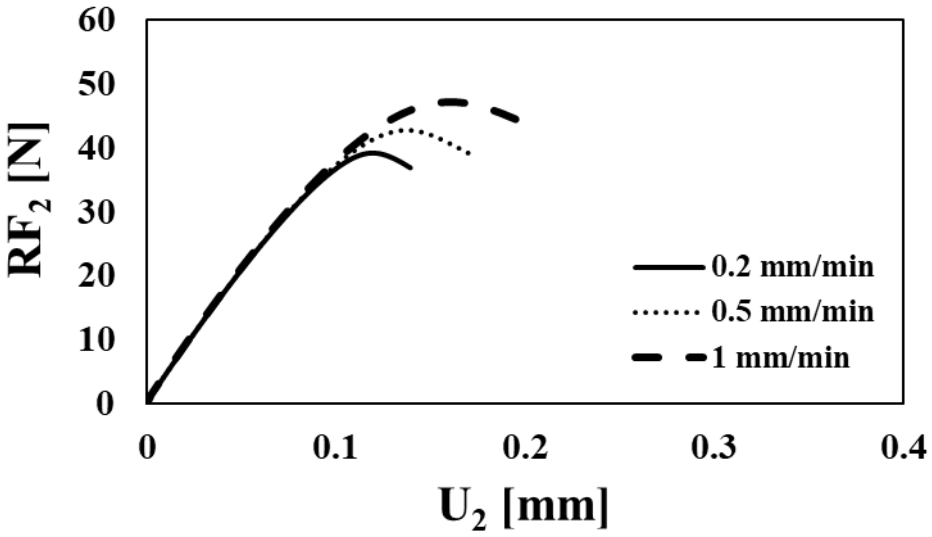

Figure 4.15: The predicted force-displacement relationship of the mineralized tissue ring specimen at 0.2 mm/min, 0.5 mm/min and 1 mm/min.

The same 3 mm thick ring model was used to predict a hypothetical polymer adhesive's behavior. The same set of material model parameters were taken into account. It was assumed that only the micro-scale normal and shear stiffnesses become 10% of the mineralized tissue's calibrated parameters for modeling the adhesive polymer. The simulations were created at 0.2 mm/min, 0.5 mm/min and 1 mm/min. The adhesive polymer ring specimen's force-displacement relationships (Figure 4.16) suggested that this specimen fails at a force of 4.97 N, 5.97 N and 7.03 N at 0.2

mm/min, 0.5 mm/min and 1 mm/min, respectively. Moreover, it was found that the specimen fails at a displacement of 0.18 mm, 0.23 mm and 0.26 mm at the loading rates of 0.2 mm/min, 0.5 mm/min and 1 mm/min, respectively. It was seen that the adhesive polymer specimen's failure load is significantly smaller than the mineralized tissue ring specimen at each loading rate. Moreover, it was observed that the adhesive polymer specimen's failure displacement is larger than the mineralized tissue ring specimen.

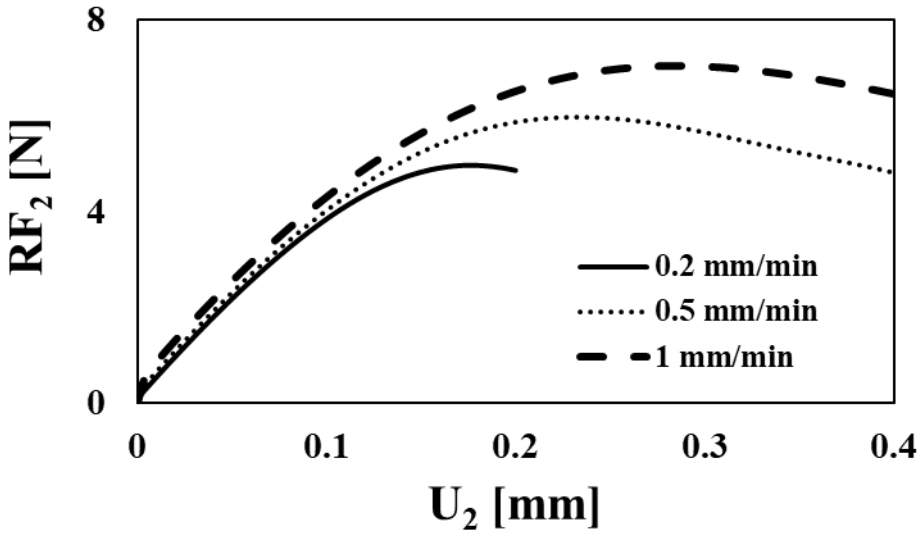

Figure 4.16: The predicted force-displacement relationship of the adhesive polymer ring specimen at 0.2 mm/min, 0.5 mm/min and 1 mm/min.

The local failure (Figure 4.17(a)) and local distortion (Figure 4.17(b)) maps were generated from the full disk mineralized tissue specimen's FE results at all loading rates. The color bar of each map was fixed at the corresponding failure displacement and the maps were advanced the same amount of displacement to a post-failure displacement. The grey colored zones indicated the failed

locations. It was found that the dilatational behavior preceded the distortion at each loading rate. The failure was observed along the loading axis, starting from the specimen's center. This observation was the same for all loading rates. Moreover, it was observed that failure grew larger at higher loading rates. This observation indicated a brittle manner of failure.

a **b**

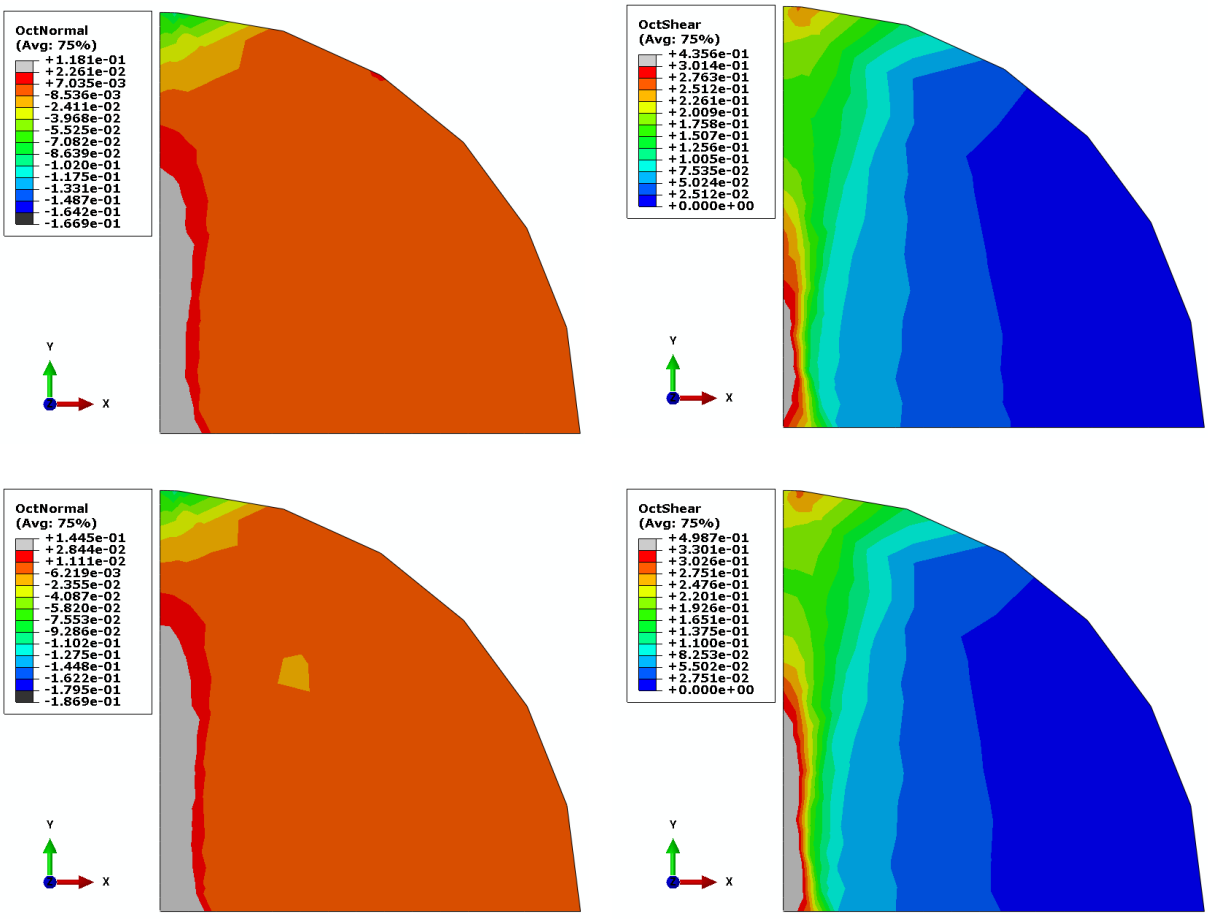

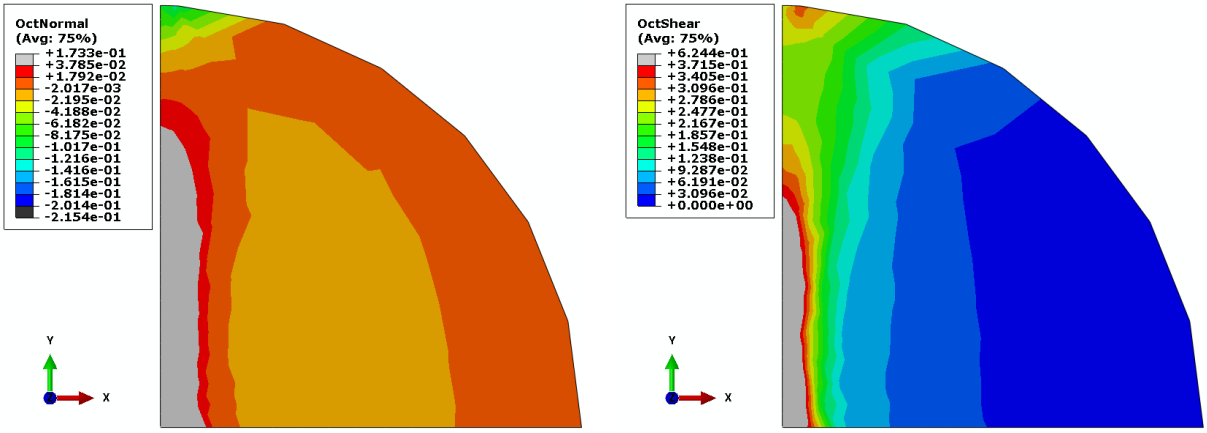

Figure 4.17: (a) Local volume change and (b) local distortion maps of the mineralized tissue full disk specimen at 0.2 mm/min (the first row), 0.5 mm/min (the second row) and 1 mm/min (the third row) loading rates.

Similarly, the mineralized tissue ring specimen's results were used to create the local failure (Figure 4.18(a)) and local distortion (Figure 4.18(b)) maps. The maps were thresholded at the corresponding failure displacements at each loading rate. The maps progressed to a post-failure displacement keeping the difference the same as the full disk specimen. The grey colored zones revealed the failure. The failure was at the hole along the loading axis at each loading rate. It was observed that the failure zone was slightly larger at higher loading rates. The full disk specimen was found to fail in a more brittle manner compared to the ring specimen.

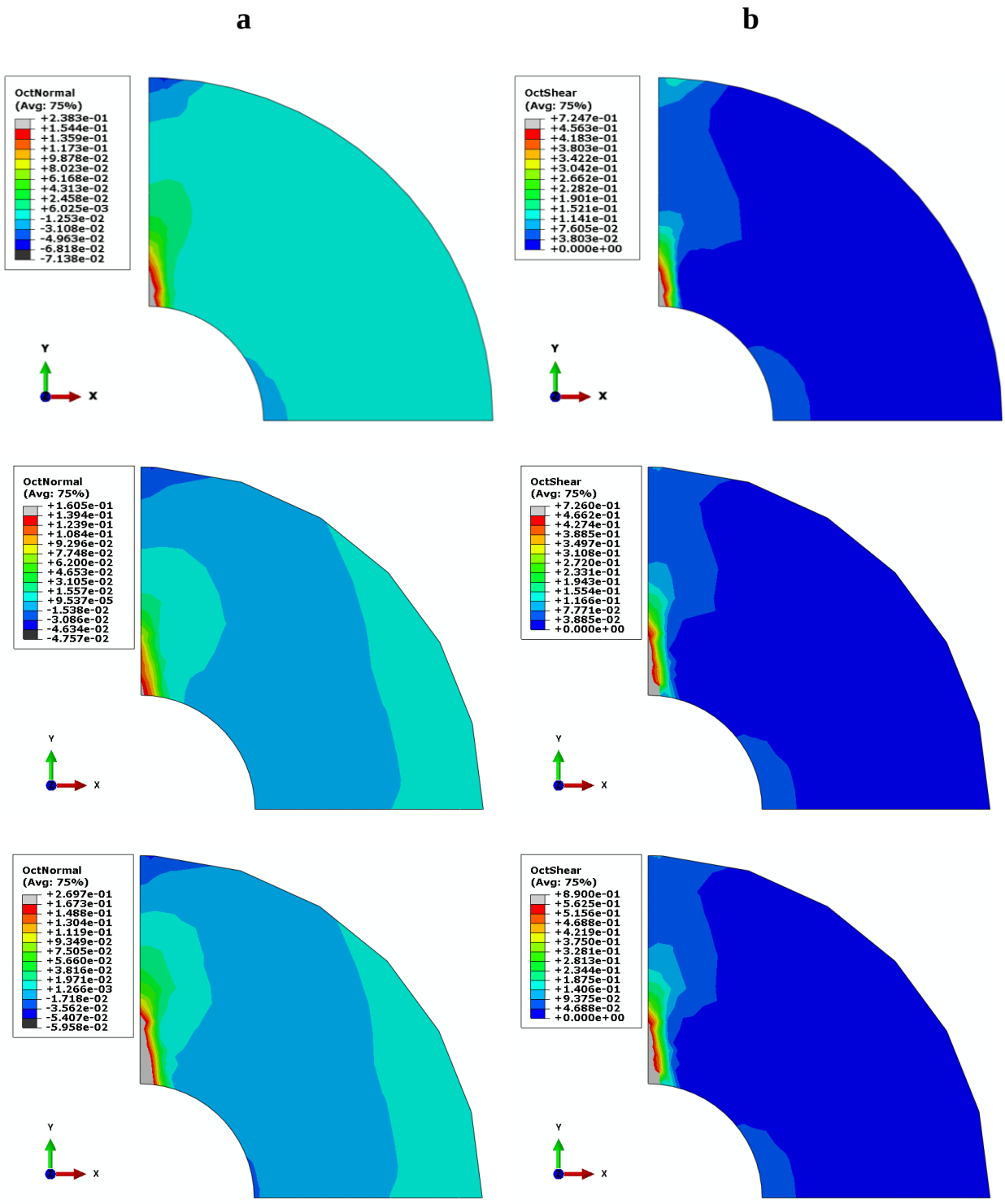

Figure 4.18: (a) Local volume change and (b) local distortion maps of the mineralized tissue ring specimen at 0.2 mm/min (the first row), 0.5 mm/min (the second row) and 1 mm/min (the third row) loading rates.

The adhesive polymer ring specimen's simulations were used to post-process the local failure (Figure 4.19(a)) and local distortion (Figure 4.19(b)) distributions at all loading rates. A post-failure displacement was found by keeping the same amount of displacement from the failure displacement as the mineralized tissue maps. The local volume change and local distortion distributions were fixed by their color bar at the failure displacements. After the maps progressed to the post-failure displacement, a grey color appeared on the distributions. The grey colored zones indicated the failure. The failure was observed at the same location with the mineralized tissue ring specimen. The failure's size was predicted to be larger than the mineralized tissue. Moreover, the failure became bigger with the increase in the loading rate.

a b

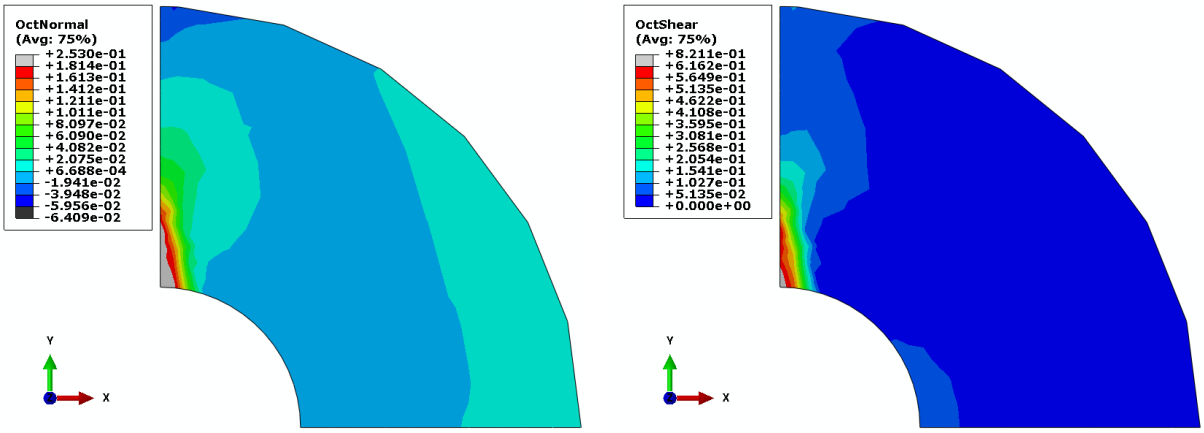

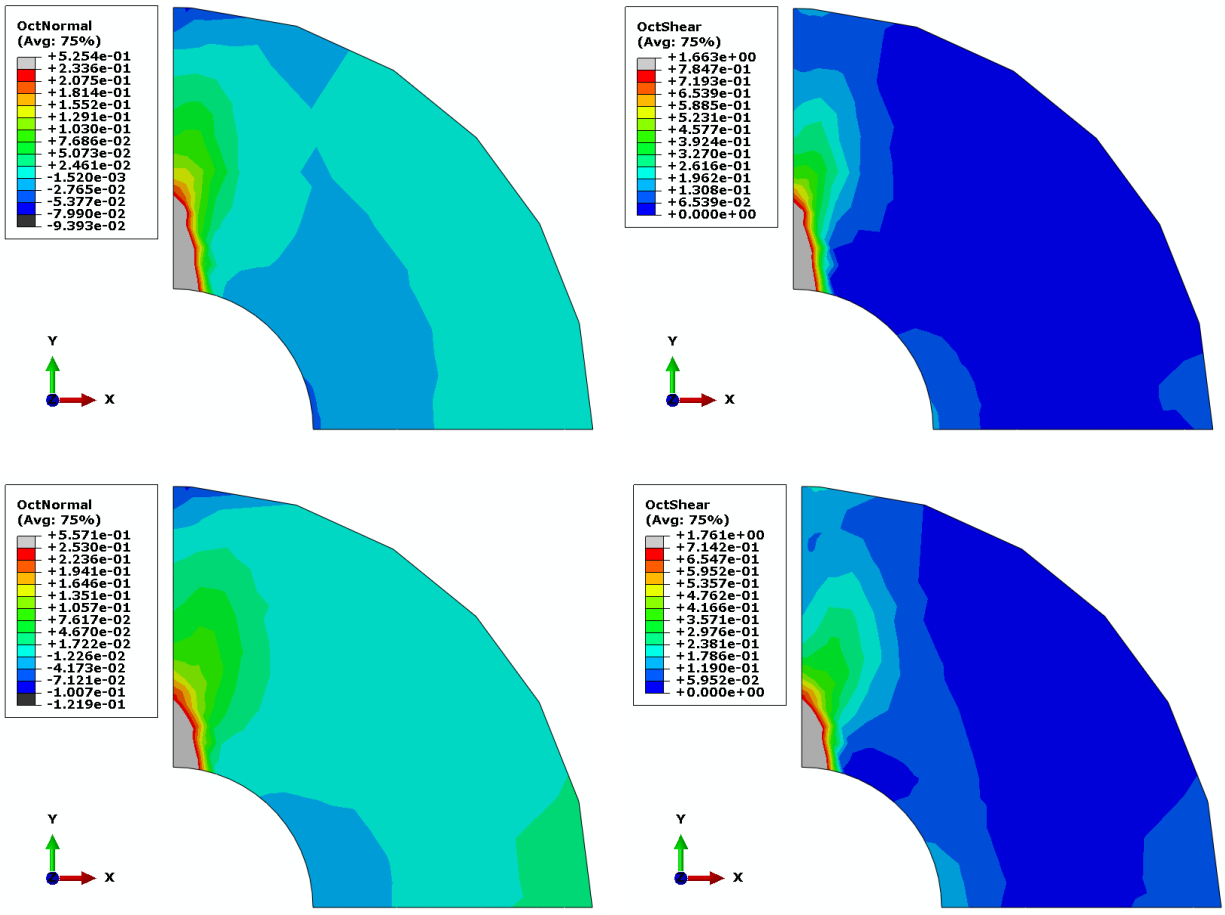

Figure 4.19: (a) Local volume change and (b) local distortion maps of the adhesive polymer ring specimen at 0.2 mm/min (the first row), 0.5 mm/min (the second row) and 1 mm/min (the third row) loading rates.

4.4 Summary and Conclusion

In this chapter, the developed nonlinear material model's accuracy was studied in a boundary value problem. The diametral compression test of the mineralized tissue was modeled as the boundary value problem. The numerical accuracy was evaluated with respect to the time incrementation size in the solution. It was concluded that the computational time significantly increases to approximate the true solution. Therefore, a time incrementation size of 0.0025 mm/min was selected to optimize the numerical accuracy and computational time. After determining the time incrementation size,

the material model's rate dependent capability was demonstrated in the same FE model. Three different loading rates were simulated. The results showed a significant increase in the failure force and the failure displacement at higher loading rates. It was seen that the rate dependent behavior was captured well in the FE simulations. A three-dimensional FE simulation was performed to calibrate and investigate the diametral compression test failure of the mineralized tissue from a recent study. The material model parameters were successfully calibrated. The simulations with the calibrated parameters suggested the same failure initiation location and evolution path as the physical experiments in the recent study. Moreover, the simulations revealed that every point within the specimen experiences a different load path. Furthermore, a 1.5 mm disk model was created to evaluate the difference in the failure in the presence of a hole. It was predicted that the full disk fails at higher loads and it is more brittle than the ring specimen. It was concluded that the ring specimen enables a more controlled failure mechanism to observe the failure's initiation as well as its propagation. Due to the full disk specimen's highly brittle nature, the specimen might fail quickly. Therefore, it might be difficult to capture the disk specimen's failure in the physical experiments. Finally, a polymer adhesive ring specimen was simulated in the same model with speculated material model parameters. This simulation suggested a similar failure pattern to the mineralized tissue ring specimen. It was predicted that the polymer adhesive specimen fails at a significantly lower failure load than the mineralized tissue. It was concluded that the generated computational framework could represent the mineralized tissue and a polymer adhesive's mechanical behavior. This study considered the experimental results at a single loading rate. In the future, the material model parameters need to be calibrated and validated at two different loading rates to capture the true rate dependent nature.

CHAPTER 5

PREDICTION OF RATE-DEPENDENT TENSILE DAMAGE AND FAILURE OF THE MINERALIZED TISSUE AND ADHESIVE POLYMERS: CALIBRATION, VALIDATION AND PREDICTION

5.1 Introduction

Experimental characterization methods provide limited information about the bond mechanics at the mineralized tissue - adhesive interface. Mathematical modeling provides information such as stress and strain distributions at the interface. This information is critical to understand the mechanical behavior of the hybrid layer stated in Chapter 3. The experimental data for the behavior of the mineralized tissue, adhesive polymers and the interfacial specimens were presented in Chapter 3. A finite element (FE) model can simulate the interfacial specimen's diametral compression test (Figure 5.1). This model can consist of three sections: (i) the mineralized tissue, (ii) the adhesive polymer, and (iii) the hybrid layer. Material model parameters of the mineralized tissue and the adhesive polymer need to be known to characterize the hybrid layer's mechanical properties. In this chapter, FE simulations are performed to calibrate and validate the nonlinear material model parameters of the mineralized tissue, the control adhesive polymer and the experimental adhesive polymer against the experimental data generated in Chapter 3. Furthermore, their damage and failure mechanisms are predicted at the experimental and clinical loading rates.

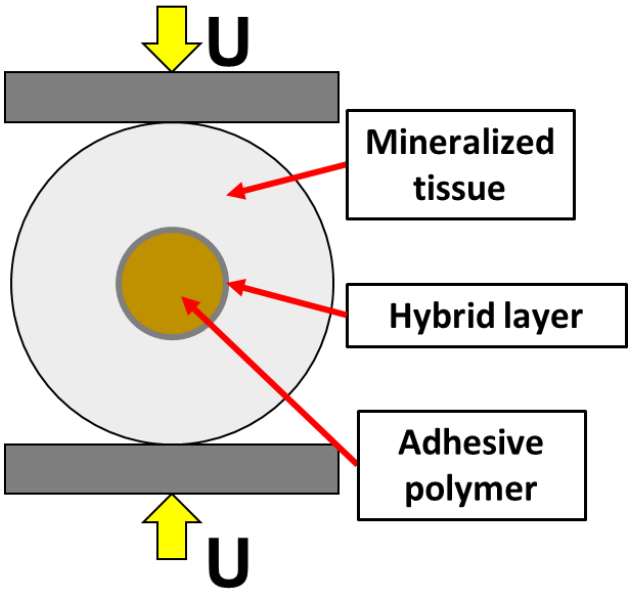

Figure 5.1: A schematic representing the diametral compression test to characterize the hybrid layer mechanical properties via computational analysis.

5.2 Materials and Methods

The simulations were created by using the commercial finite element analysis software, Abaqus (Simulia/ABAQUS V 6.13-3, Dassault Systémes, RI, USA). Abaqus was linked with visual Fortran composer (Intel, Santa Clara, CA). This link enabled the implementation of the developed granular micromechanics nonlinear material model into finite element analysis as presented in Chapter 2. The material model was prepared in user-defined nonlinear material (UMAT) format to interact with the commercial finite element analysis code. The finite element simulations were improved with the nonlinear model implementation to capture materials' rate-dependent behavior with damage and plasticity. Four different finite element models were created. Three of those were prepared for modeling the diametral compression test of the mineralized tissue, the control adhesive (C1) polymer and the experimental adhesive (E1) polymer. All these models' geometries

were created based on their average dimensions in the physical tests presented in Chapter 3. The fourth model was prepared for the single patch test to simulate these materials' pure tensile nature. The first model was created for the mineralized tissue. Its geometry was generated as a 1.5 mm thick disk with a diameter of 3 mm and a hole diameter of 1 mm. The second model was prepared for the C1 polymer. Its geometry was created considering a thickness of 1.61 mm, a diameter of 3.16 mm, and a hole diameter of 1 mm. The third model was generated for the E1 polymer. Its geometry was prepared with a thickness of 1.60 mm, a diameter of 3.10 mm, and a hole diameter of 0.84 mm. Only one-eighth of their geometry was used in all these three models (Figure 5.2(a)) and the symmetric type boundary conditions were applied on the planes xy, xz and yz (Figure 5.2(b)). The mesh was created using 8 node linear hexahedral elements. In all three models, the number of degrees of freedom was 5187 (Figure 5.2(c)). To simulate the experimental loading conditions, the load was applied as displacement in negative y-direction along the thickness of the disk. The load surface was created an arc of 2.5° whose center is the disk center. Lastly, the single element patch test was created with a cubic geometry. This cube had a side length of 1 mm and the mesh was done with one 8 node linear hexahedral element. Except for the nodes on y-z surface, displacements were fixed in all directions to all the nodes. A displacement load was applied on the nodes on the y-z surface and their displacements were fixed to zero in y- and z-directions. This displacement load was in the positive x-direction. In all four finite element models, three different loading rates were applied. For the diametral compression test models, these three loading rates refer to calibration and validation of material properties and prediction of materials' behavior at the clinical loading condition [21, 115-118]. In detail, a loading rate of 1 mm/min was assigned to calibrate material model parameters for each material. The model parameters were calibrated against the experimental force-displacement data presented in Chapter 3. Secondly, a loading rate

of 0.2 mm was applied for validating the calibrated material model parameters. The validation was done against the experimental force-displacement data from Chapter 3. Lastly, the simulations were done at 3.5 mm/min loading rate to predict the materials' behavior at clinical loading rates. Moreover, the single patch test was conducted at all three loading rates to simulate materials' behavior under true uniaxial tensile loading. Three different sets of nonlinear material model parameters were assigned for each material and these sets of parameters were kept the same for calibration, validation and prediction. Furthermore, single patch tests were performed with each set of material model parameters. The assigned nonlinear material model parameters are presented in the Appendix (see the Appendix C, Table 10.3).

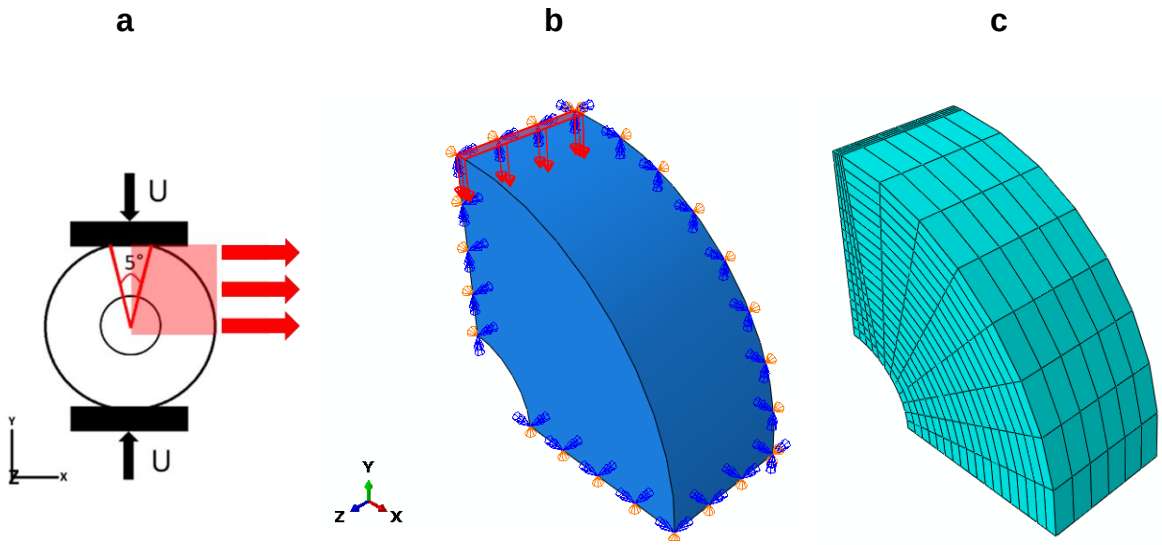

Figure 5.2: (a) Diametral compression test representation considered in finite element model, (b) the boundary conditions and (c) the meshed geometry generated in finite element model for the experimental adhesive polymer.

5.3 Results and Discussion

This section presents the computational investigation on the damage and failure of the mineralized tissue, the C1 polymer and the E1 polymer. Initially, each material's nonlinear material model parameters were calibrated against the measured force-displacement data at 1 mm/min loading rate. After the calibration, each set of nonlinear material model parameters were validated against the experimental force-displacement relationships at 0.2 mm/min. Finally, several predictions were performed by using each material's calibrated and validated. These predictions include the mechanical behavior at the clinical loading rate of 3.5 mm/min. The local distortion and the local volume change distributions were presented within the specimens at each loading rate. For this purpose, the FE results were post-processed to obtain the octahedral shear and the octahedral normal strains. The octahedral shear and normal strains indicate the local distortion and volume change, respectively. Moreover, each specimen's failure initiation location was investigated in terms of their local stress-strain relationships. Based on these relationships, each specimen's local toughness was evaluated at each loading rate. Finally, each material's pure uniaxial tensile stress-strain relationships were predicted by using their calibrated and validated material model parameters in the single patch tests. These single patch test simulations revealed the pure tensile behavior and the toughness at each loading rate.

5.3.1 Mineralized Tissue

The diametral compression test of the mineralized tissue ring specimen was performed by using the FE model prepared for the mineralized tissue ring specimen. The loading rate was 1 mm/min. The predicted force-displacement relationship was obtained from the nodes where the loading was

applied. Figure 5.3 compares the predicted force-displacement relationship to the experimental force-displacement curve of a mineralized tissue ring specimen presented in Chapter 3. This comparison was made over different sets of nonlinear material model parameters to approximate the experimental behavior. In Figure 5.3, the results from the best approximation were presented. The selected material model parameters achieved the calibration of the mineralized tissue's nonlinear material model parameters. The failure force in the experiment was measured 71.60 N. The simulation predicted the failure force as 72.73 N. Moreover, the specimen failed at 0.38 mm in the test. The FE analysis predicted the failure displacement as 0.43 mm.

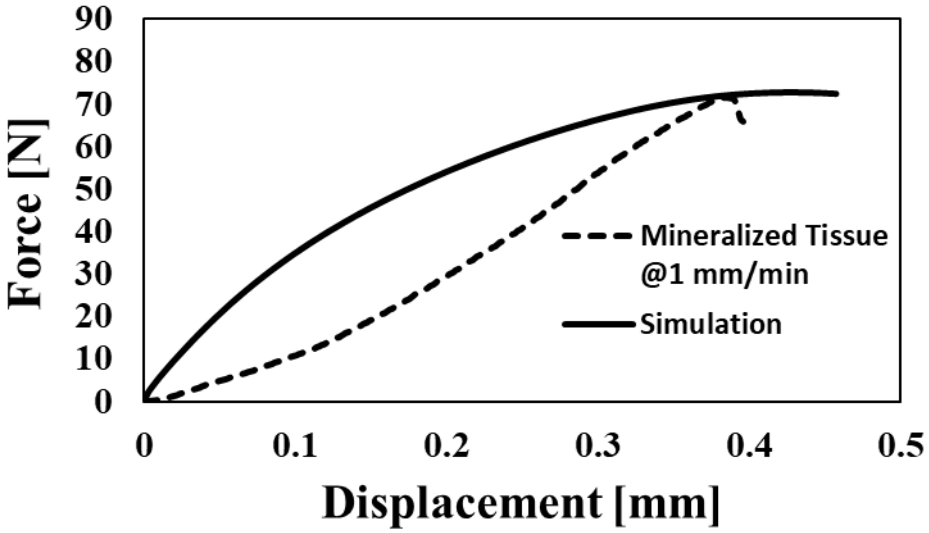

Figure 5.3: Calibration of the material model parameters for the mineralized tissue: Comparison of the simulated force-displacement relationship to the experimental force-displacement relationship of the mineralized tissue at 1 mm/min loading rate.

After the calibration of the nonlinear model parameters, the simulation was conducted at 0.2 mm/min loading rate. The material model parameters were kept the same as the 1 mm/min loading

rate. The predicted force-displacement relationship was compared to the measured force-displacement relationship in Chapter 3 (Figure 5.4). This comparison revealed if the calibrated material model parameters could capture the rate dependent mechanical behavior. In the physical test, the failure force was read 56.44 N. The simulation computed the failure force as 56.34 N. The experimental failure displacement was 0.31 mm. The FE simulation found the failure displacement as 0.26 mm. Hence, the calibrated material model parameters of the mineralized tissue were validated to represent the mineralized tissue.

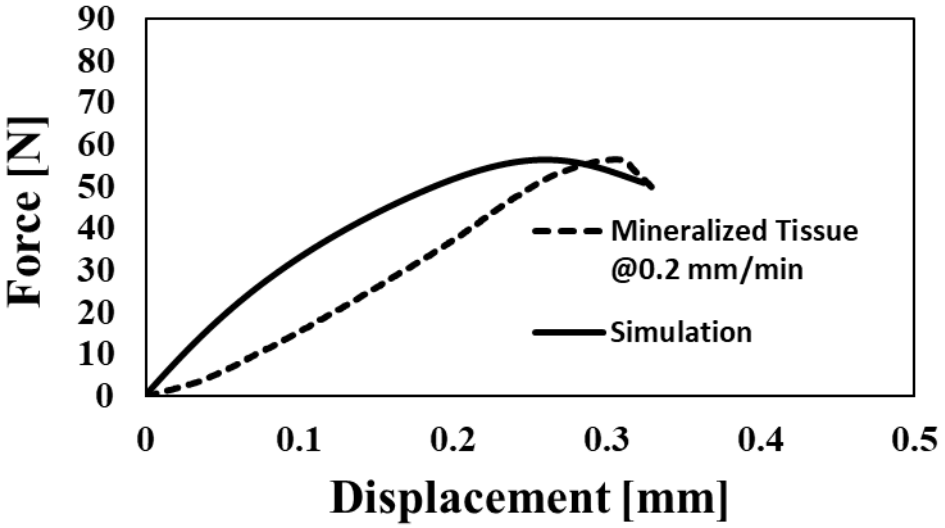

Figure 5.4: Validation of the material model parameters for the mineralized tissue: Comparison of the simulated force-displacement relationship to the experimental force-displacement relationship of the mineralized tissue at 0.2 mm/min loading rate.

The local distortion and local volume change maps were created from the FE results of the test at 1 mm/min loading rate. These maps were compared to the experimental failure pattern presented in Chapter 3 (Figure 5.5(a)). In Figure 5.5(c) and Figure 5.5(e), the maps were color thresholded

with their peak values close to the failure displacement (δ_f) and progressed to a selected displacement at post-failure regime ($\delta_{p\text{-}f}$) (Figure 5.5(b)). The difference between δ_f and $\delta_{p\text{-}f}$ was assigned 0.05 mm. The grey colored zones in Figure 5.5(d) and Figure 5.5(f) indicated the evolutions of local distortion and volume change beyond failure, respectively. The post-failure experimental snapshot shows the fracture zone. It is circled with a yellow line. It was observed that the failure was initiated at the hole along the loading axis. Following the loading axis, the fracture propagated towards the load surface. The FE simulation predicted that the highest distortion and volume change was experienced at the hole along the loading axis (Figure 5.5(c) and Figure 5.5(e)). The highest volume change was observed in the form of dilatation. The dilatation indicates volume expansion at the failure location. The post-failure local volume change and local distortion maps predicted the fracture evolution. The predicted fracture evolution was observed towards the load application surface along the loading axis.

a

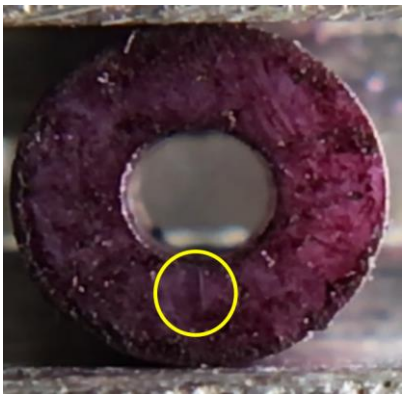

b

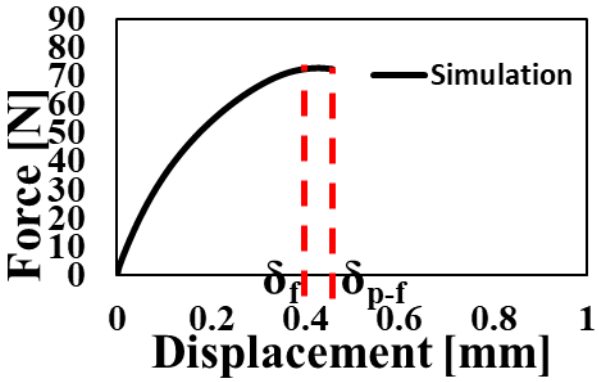

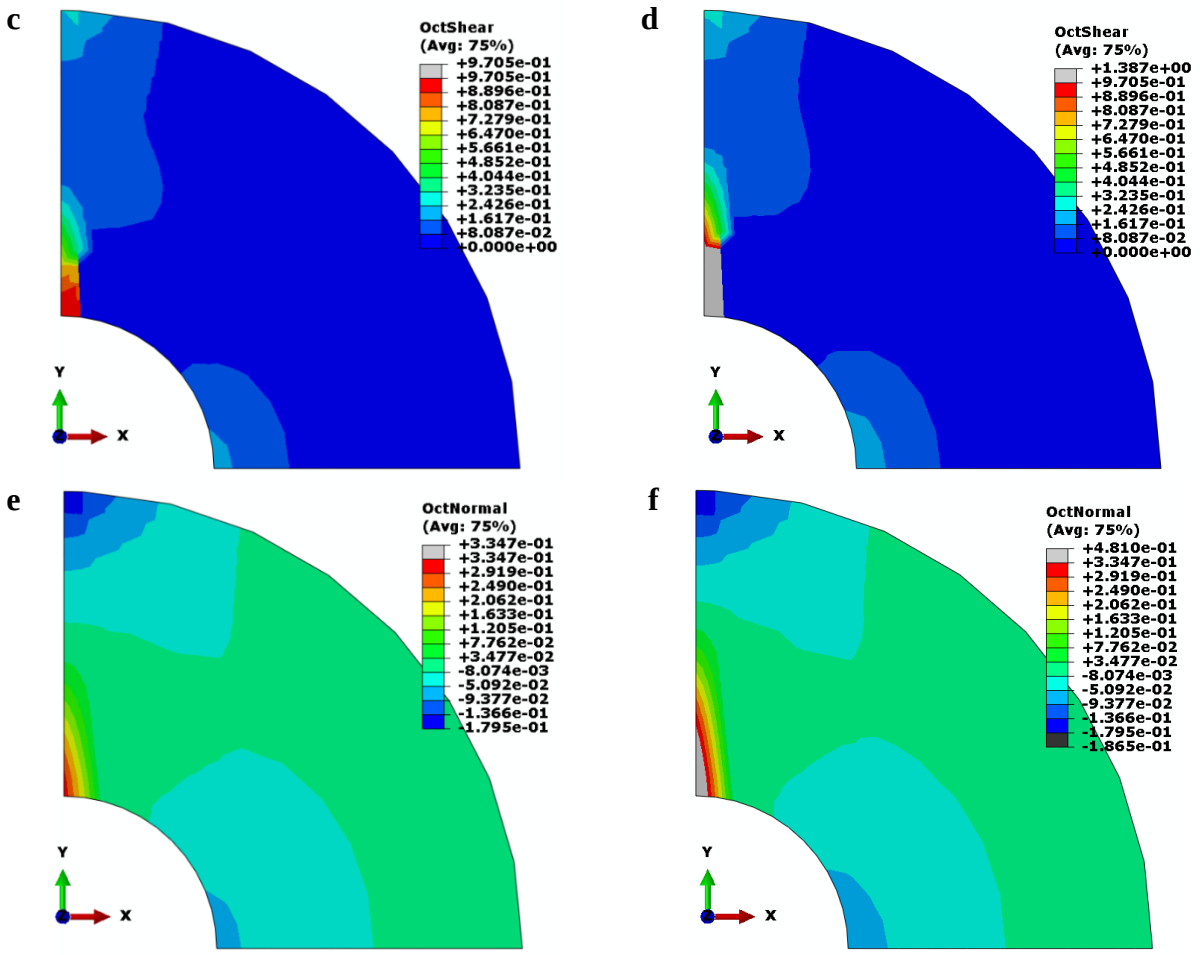

Figure 5.5: Failure analysis of the mineralized tissue at 1 mm/min loading rate: (a) Post-failure snapshot from the experiment, (b) Force-displacement relationship from the simulation (δ_f: failure displacement, $\delta_{p\text{-}f}$: post-failure displacement), (c and d) Local volume change maps at failure and post-failure, respectively and (e and f) Local distortion maps at failure and post-failure, respectively.

Similarly, the strain maps of local distortion and local volume change were generated from the FE results of the test at the loading rate of 0.2 mm/min. The post-failure pattern in Chapter 3 was used for the comparison the physical experiment (Figure 5.6(a)). Both local distortion and volume change maps were thresholded at the failure displacement (δ_f) (Figure 5.6(c) and Figure 5.6(e)). The maps progressed a displacement of 0.05 mm more from δ_f to predict the local distortion and

volume change distributions at a post-failure displacement ($\delta_{p\text{-}f}$) (Figure 5.6(d) and Figure 5.6(f)). In the physical experiment, the specimen initiated to fail at around the hole following the loading axis. Subsequently, the failure grew into a fracture following a path towards the load surface along the loading axis. In the local volume change map, high dilatational strains were observed around the hole coinciding with the loading axis. This observation suggests volume expansion. Moreover, the local distortion map captured the highest distortion in the same location. The grey area in both maps suggested the evolution of failure towards the load surface at the loading axis. It is also seen that the post-failure maps at 0.2 mm/min loading rate grew a larger grey area comparing to the 1 mm/min loading rate.

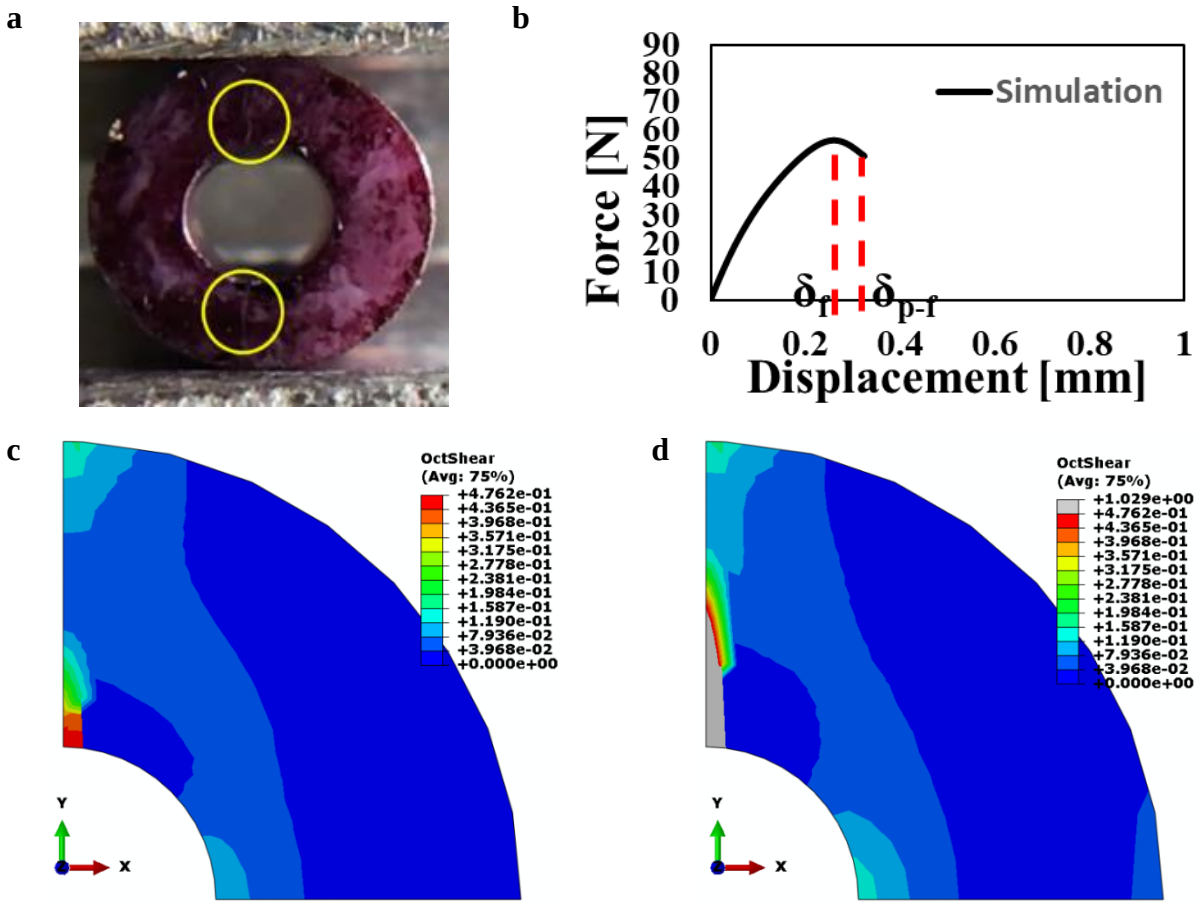

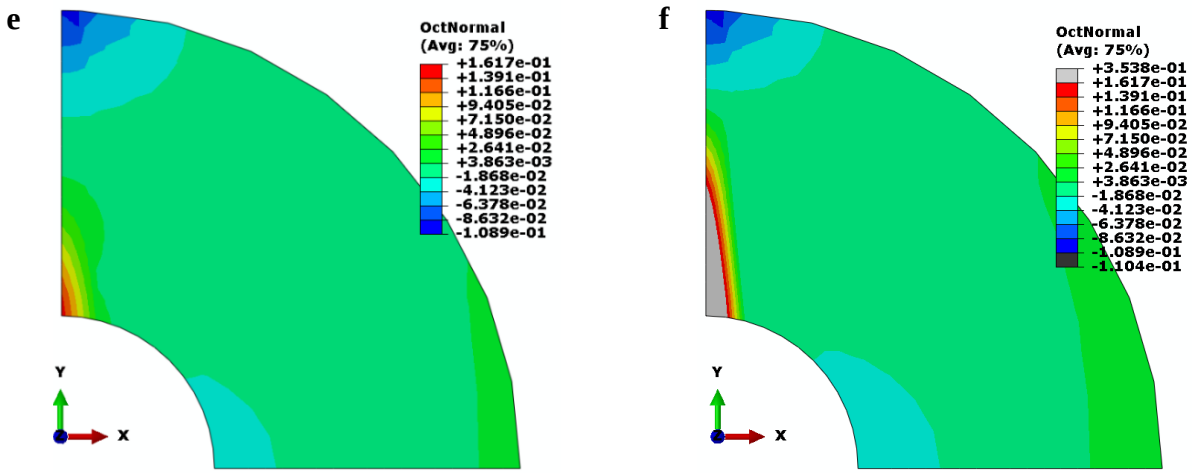

Figure 5.6: Failure analysis of the mineralized tissue at 0.2 mm/min loading rate: (a) Post-failure snapshot from the experiment, (b) Force-displacement relationship from the simulation (δ_f: failure displacement, $\delta_{p\text{-}f}$: post-failure displacement), (c and d) Local volume change maps at failure and post-failure, respectively and (e and f) Local distortion maps at failure and post-failure, respectively.

The mineralized tissue's mechanical behavior was simulated at the clinical loading rate of 3.5 mm/min. This simulation suggested that the mineralized tissue fails at a load of 96.71 N and a displacement of 0.74 mm (Figure 5.7(a)). The local volume change and distortion maps were post-processed from this simulation. They were thresholded at the failure displacement (δ_f) (Figure 5.7(c) and Figure 5.7(e)) and advanced to a post-failure displacement ($\delta_{p\text{-}f}$) (Figure 5.7(d) and Figure 5.7(f)). It is seen that the highest distortion and volume change were both observed at the hole along the loading axis. The volume change was observed in dilatation mode. These observations predicted the failure initiation in the same location as the 1 mm/min and 0.2 mm/min loading rates. Moreover, the failure path was observed along the load axis towards the load application surface. The predicted behavior also showed that the fracture zone at the clinical loading rate was smaller compared to both loading rates of 1 mm/min and 0.2 mm/min.

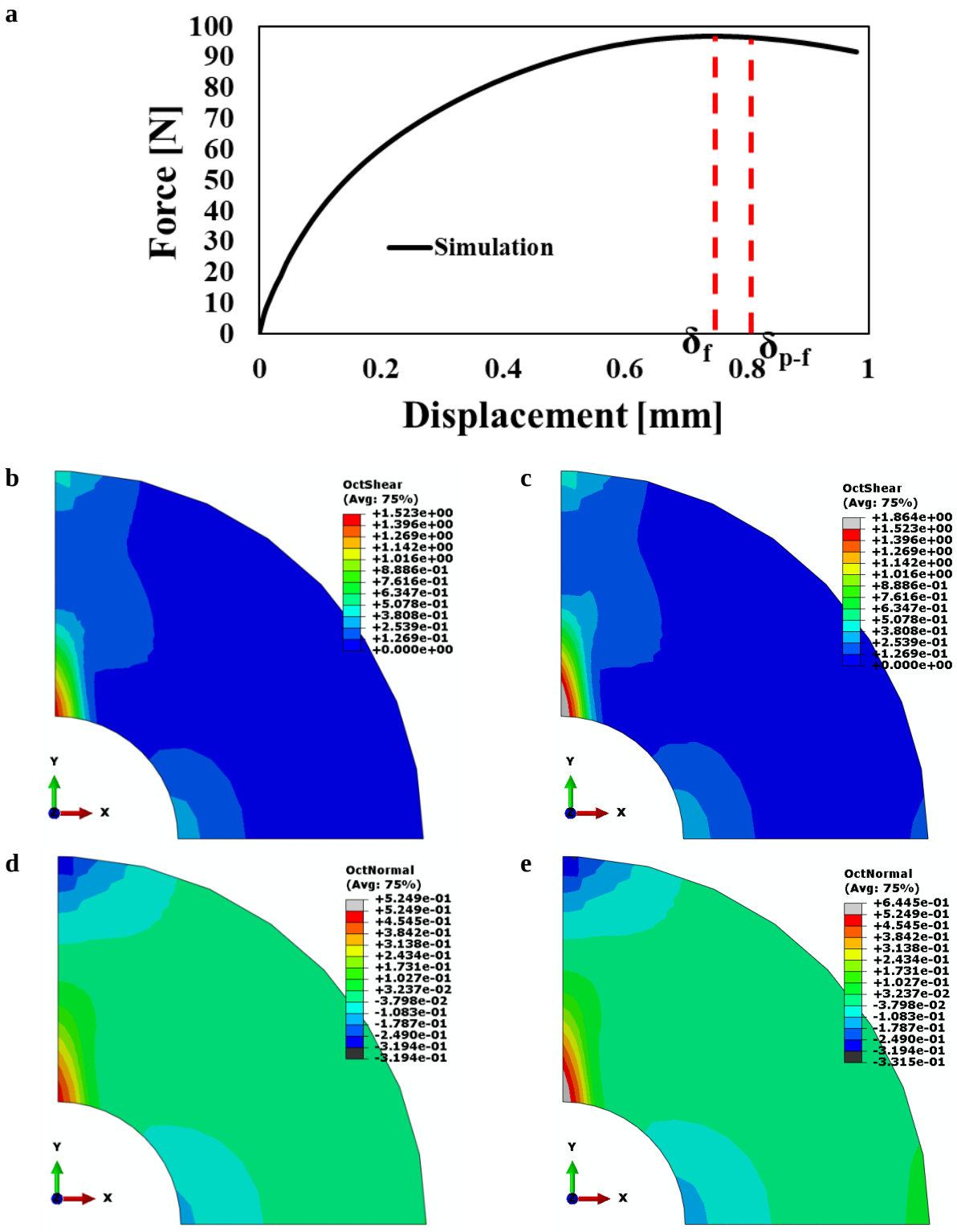

Figure 5.7: Failure analysis of the mineralized tissue at 3.5 mm/min loading rate: (a) Force-displacement relationship from the simulation (δ_f: failure displacement, $\delta_{p\text{-}f}$: post-failure

displacement), (b and c) Local volume change maps at failure and post-failure, respectively and (d and e) Local distortion maps at failure and post-failure, respectively.

The local distortion and volume change maps suggested a difference in failure evolution at different loading rates. Thus, a quantitative evaluation of the failure propagation was performed. For this purpose, the maximum principal stress and maximum principal strain were extracted from the FE results at each loading rate (Figure 5.9). These stress and strain data were taken from the element that was at the failure initiation location (Figure 5.8). The obtained data also predicted the mineralized tissue's local failure behavior in the diametral compression mode at each loading rate. The mineralized tissue's failure stress and strain were predicted as 36.58 MPa and 0.067 at 0.2 mm/min loading rate. When the mineralized tissue was subject to 1 mm/min, the stress and strain at failure were observed as 41.40 MPa and 0.075, respectively. Moreover, the simulation at the clinical loading rate showed that the mineralized tissue's failure stress and strain went up to 53.13 MPa and 0.083, respectively. It is clear that the mineralized tissue failed at larger stress and strain when the loading rate was increased.

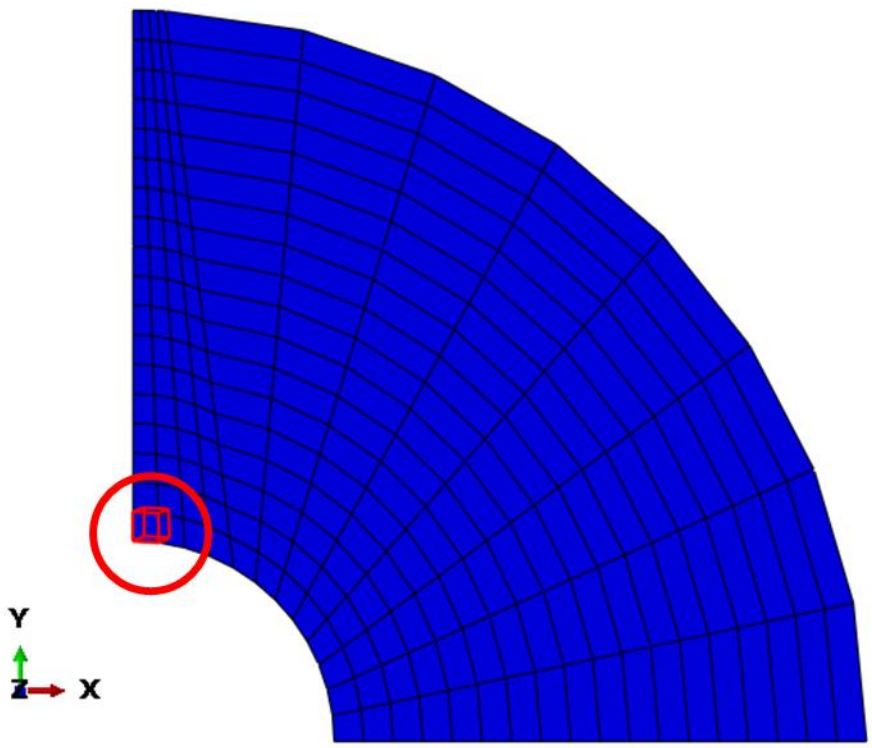

Figure 5.8: Failure initiation location in a ring specimen. The element that fails the first during the loading. This location is the same for all materials at all loading rates.

These stress-strain relationships also revealed how the mineralized tissue resisted fracture at different loading rates. The toughness was calculated to quantify this behavior. It was obtained by calculating the area under the stress-strain curve up to the failure strain. These areas are designated in Fig 5.8 as I, II, and III, corresponding to 0.2 mm/min, 1 mm/min, and 3.5 mm/min loading rates. The mineralized tissue's toughness was predicted 1.81 MPa, 2.35 MPa, and 3.38 MPa at loading rates of 0.2 mm/min, 1 mm/min, and 3.5 mm/min, respectively. It was observed that the mineralized tissue's toughness went up with the increase in loading rate.

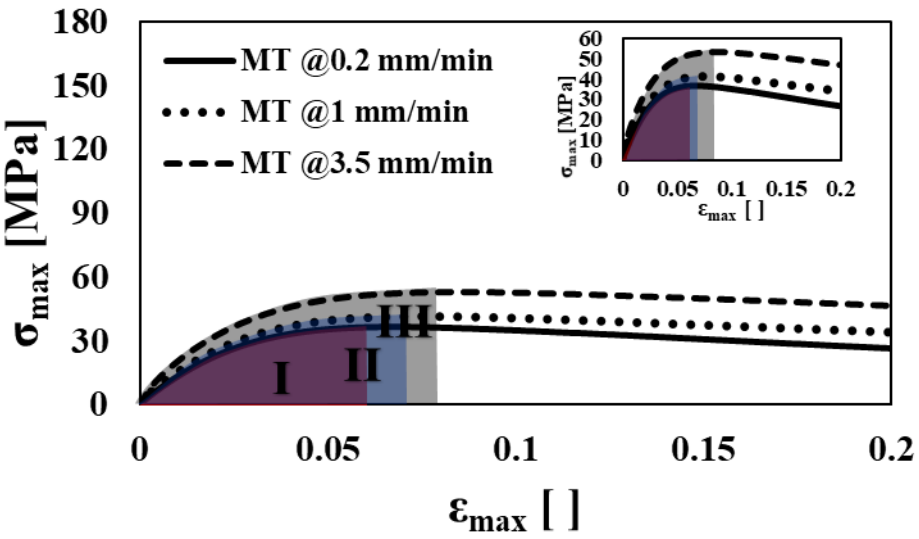

Figure 5.9: Stress-strain behavior of the mineralized tissue (MT) at failure initiation location at 0.2, 1 and 3.5 mm/min loading rates. Stress and strain values are presented in terms of maximum principal stress and maximum principal strain. I, II, and III indicate the area under each curve up to the corresponding failure strain. The inset figure provides the same stress-strain relationship with a refined y-axis.

It is noted that the diametral compression load provides an indirect tensile action. Therefore, the material point at the failure initiation may be exposed to a mixed loading mode. This loading exposure can compromise the failure stress and strain values of the material. Therefore, a uniaxial tensile test simulation can predict the mineralized tissue's true tensile nature. Accordingly, a single patch test was performed with the mineralized tissue's nonlinear material model parameters. The stress and strain results were obtained at different loading rates and the toughness was calculated for each loading rate (I, II and III) (Figure 5.10). These simulations predicted that the mineralized tissue's failure stress and strain were 44.44 MPa and 0.059 at 0.2 mm/min, 79.51 MPa and 0.063 at 1 mm/min, and 176.96 MPa and 0.091 at 3.5 mm/min, respectively. The mineralized tissue's toughness under uniaxial tension was predicted as 1.96 MPa, 3.68 MPa and 11.08 MPa at loading

rates of 0.2 mm/min, 1 mm/min and 3.5 mm/min, respectively. The failure stress and toughness under diametral compression load were observed significantly lower than the uniaxial tensile load. The single patch test results showed that the diametral compression test might report lower tensile properties than the mineralized tissue's true tensile behavior.

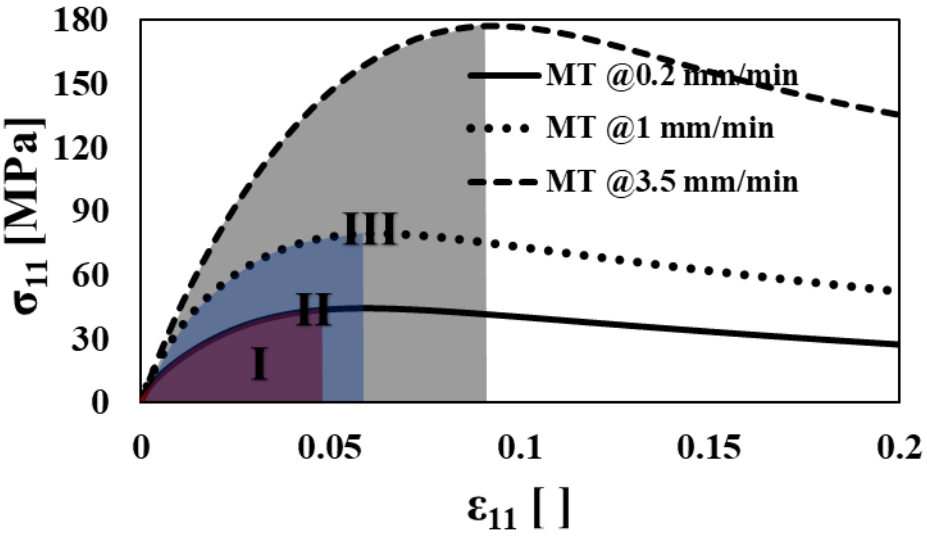

Figure 5.10: Stress-strain behavior of the mineralized tissue (MT) at uniaxial tensile loading at 0.2, 1 and 3.5 mm/min loading rates. I, II and III indicate the area under each curve up to the corresponding failure strain.

5.3.2 Control Adhesive (C1) Polymer

FE model of the control adhesive (C1) polymer was used to simulate the diametral compression test of the C1 polymer ring specimen. The force-displacement relationship was predicted at 1 mm/min loading rate. The simulated relationship was compared to a C1 polymer ring specimen's experimental force-displacement relationship at 1 mm/min loading rate from Chapter 3. Figure 5.11 shows the simulation results with the selected set of material model parameters for the C1

polymer. FE simulation results overlapped well with experimental results. Therefore, the material model parameters were calibrated for the C1 polymer. The test measured the failure force and displacement as 28.19 N and 0.52 mm, respectively. The FE simulation predicted that the C1 polymer specimen failed at a load of 26.39 N and a displacement of 0.56 mm.

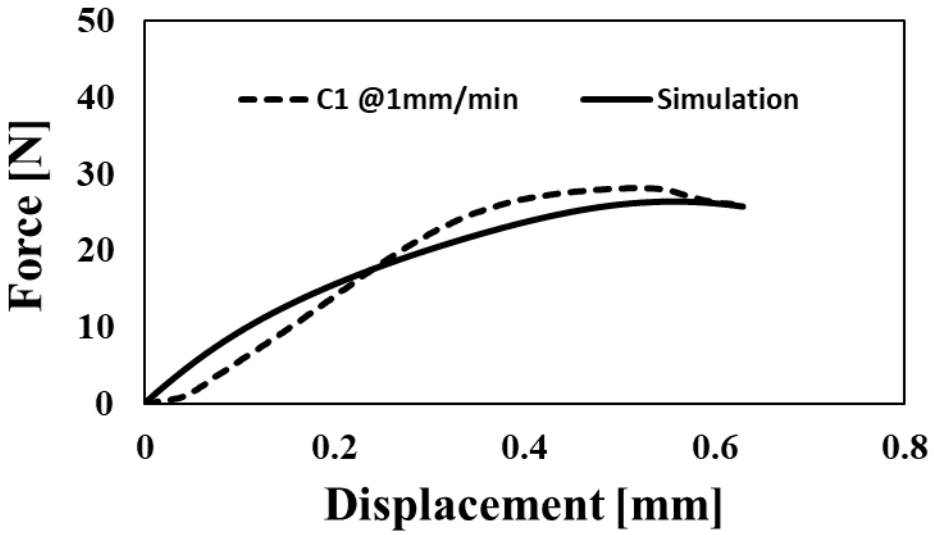

Figure 5.11: Calibration of the material model parameters for the C1 adhesive: Comparison of the simulated force-displacement relationship to the experimental force-displacement relationship of the C1 adhesive at 1 mm/min loading rate.

To validate the material model parameters for the C1 polymer, a simulation was performed at 0.2 mm/min with the calibrated model parameters. The force-displacement relationship obtained from this simulation was compared to the experimental relationship presented in Chapter 3 (Figure 5.12). It was observed that the calibrated model parameters resulted in similar results with the experimental results at 0.2 mm/min loading rate. Hence, C1 polymer's material model parameters were validated. The experiment measured that the C1 polymer failed at a force of 22.06 N and a

displacement of 0.46 mm. The simulation suggested that the failure force was 23.04 N and the failure displacement was 0.42 mm.

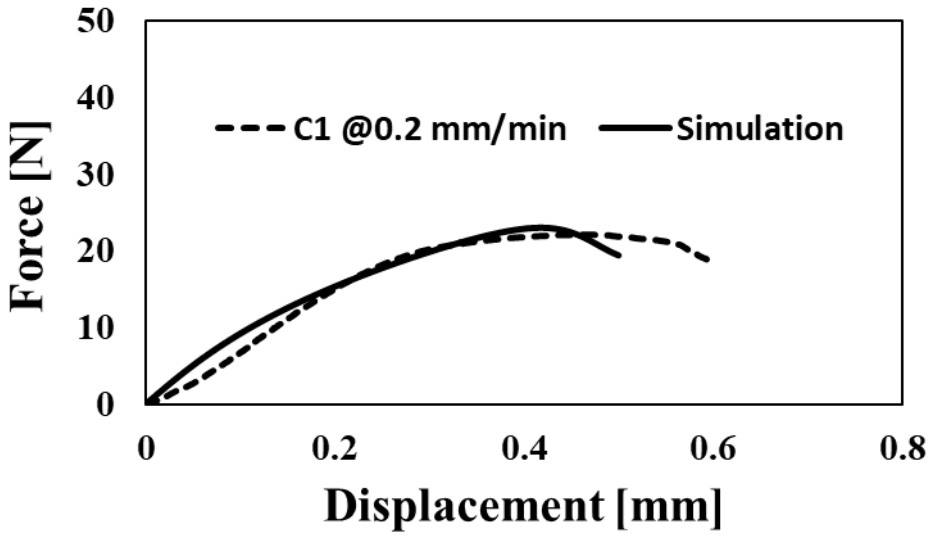

Figure 5.12: Validation of the material model parameters for the C1 adhesive: Comparison of the simulated force-displacement relationship to the experimental force-displacement relationship of the C1 adhesive at 0.2 mm/min loading rate.

FE results of the C1 polymer were post-processed to generate the local distortion and volume change maps at 1 mm/min. The failure of the C1 polymer was investigated by comparing these maps against the experimental post-failure pattern of the C1 polymer at 1 mm/min from Chapter 3 (Figure 5.13(a)). The color bars of the local distortion and the volume change maps were fixed at the failure displacement (δ_f) (Figure 5.13(c) and Figure 5.13(e)). To reveal the failure evolution, the local distortion and volume change maps were also obtained from a post-failure displacement ($\delta_{p\text{-}f}$) (Figure 5.13(d) and Figure 5.13(f)). $\delta_{p\text{-}f}$ was selected 0.05 mm more than δ_f (Figure 5.13(b)). The experimental snapshot shows that the failure began at the hole along the loading axis and it

propagated towards the load application location following the same axis. In the simulation, the highest distortion and volume change were found at the hole along the load axis at failure. The highest distortion suggested a volume expansion at the failure location. The grey area in post-failure maps showed the evolution of failure. It is seen that the failure propagated toward the load surface following the load axis.

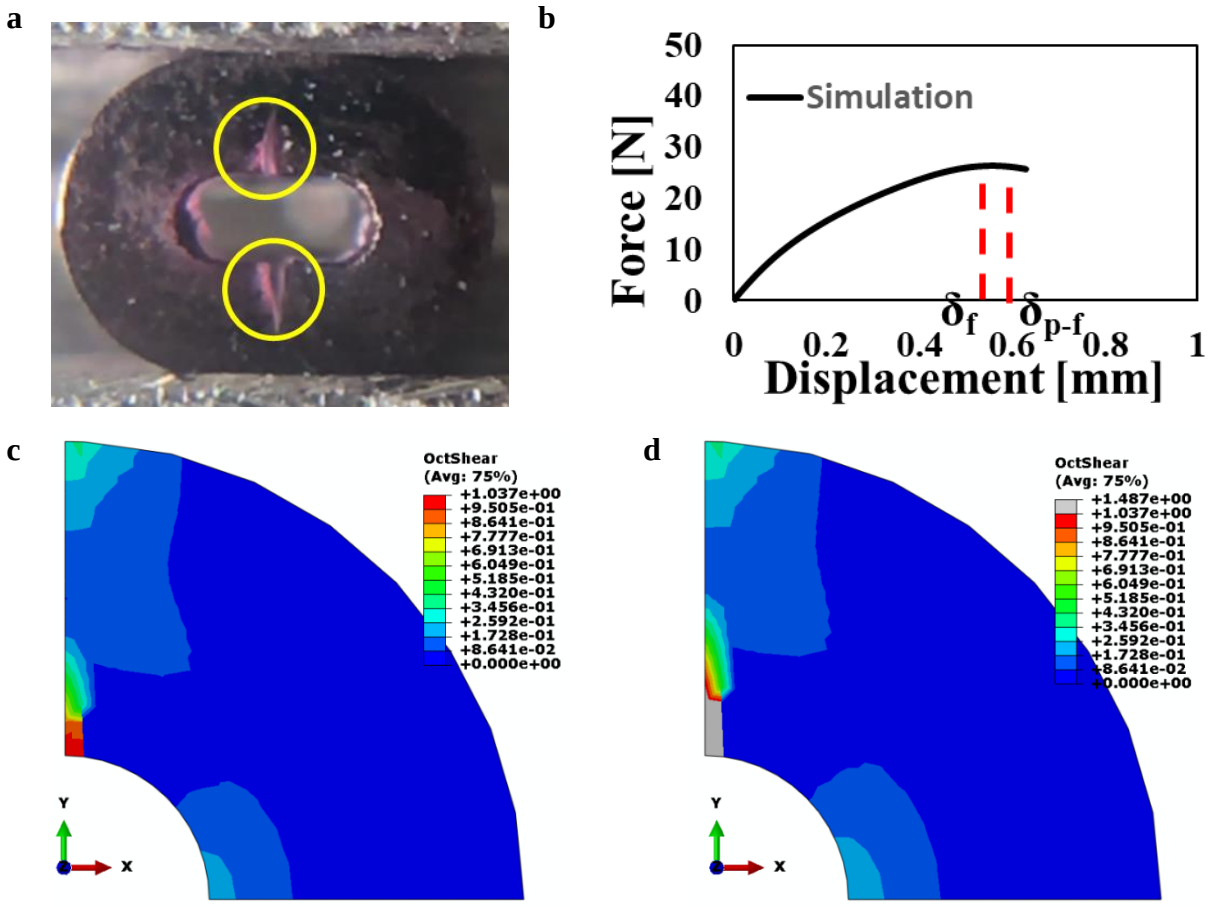

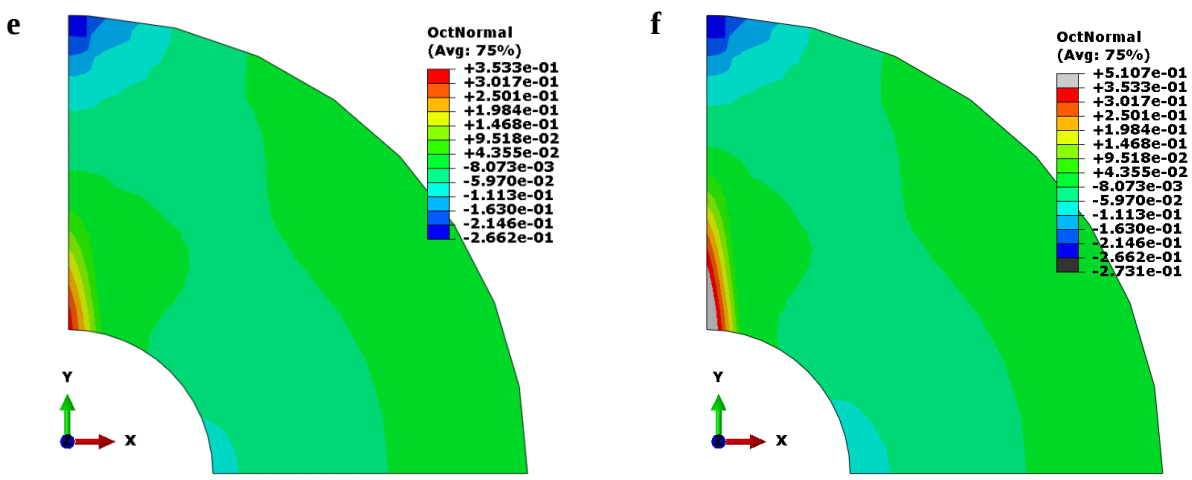

Figure 5.13: Failure analysis of the C1 polymer at 1 mm/min loading rate: (a) Post-failure snapshot from the experiment, (b) Force-displacement relationship from the simulation (δ_f: failure displacement, $\delta_{p\text{-}f}$: post-failure displacement), (c and d) Local volume change maps at failure and post-failure, respectively and (e and f) Local distortion maps at failure and post-failure, respectively.

The local distortion and volume change maps were also created from the simulation results at 0.2 mm/min. These maps were used to investigate the failure of the C1 polymer in comparison with its post-failure image presented in Chapter 3 (Figure 5.14(a)). The failure displacement (δ_f) and a post-failure displacement ($\delta_{p\text{-}f}$) were determined from the predicted force-displacement relationship (Figure 5.14(b)). A difference of 0.05 mm was kept between δ_f and $\delta_{p\text{-}f}$. The strain maps were thresholded at δ_f and they were progressed to $\delta_{p\text{-}f}$. The maps at δ_f revealed the distribution of local distortion and volume change at failure (Figure 5.14(f) and Figure 5.14(e)). The maps at $\delta_{p\text{-}f}$ showed that the failure evolution (Figure 5.14(d) and Figure 5.14(g)). The mechanical test showed the failure of the C1 polymer was initiated and propagated inside out from the hole along the loading axis. The local distortion and volume change maps at the failure predicted that the largest distortion and volume change was at the same location as the experiment.

The post-failure maps suggested that the failure propagated towards the load application surface following the same path as the experiment. It is also observed that the failed area was larger at 0.2 mm/min compared to 1 mm/min.

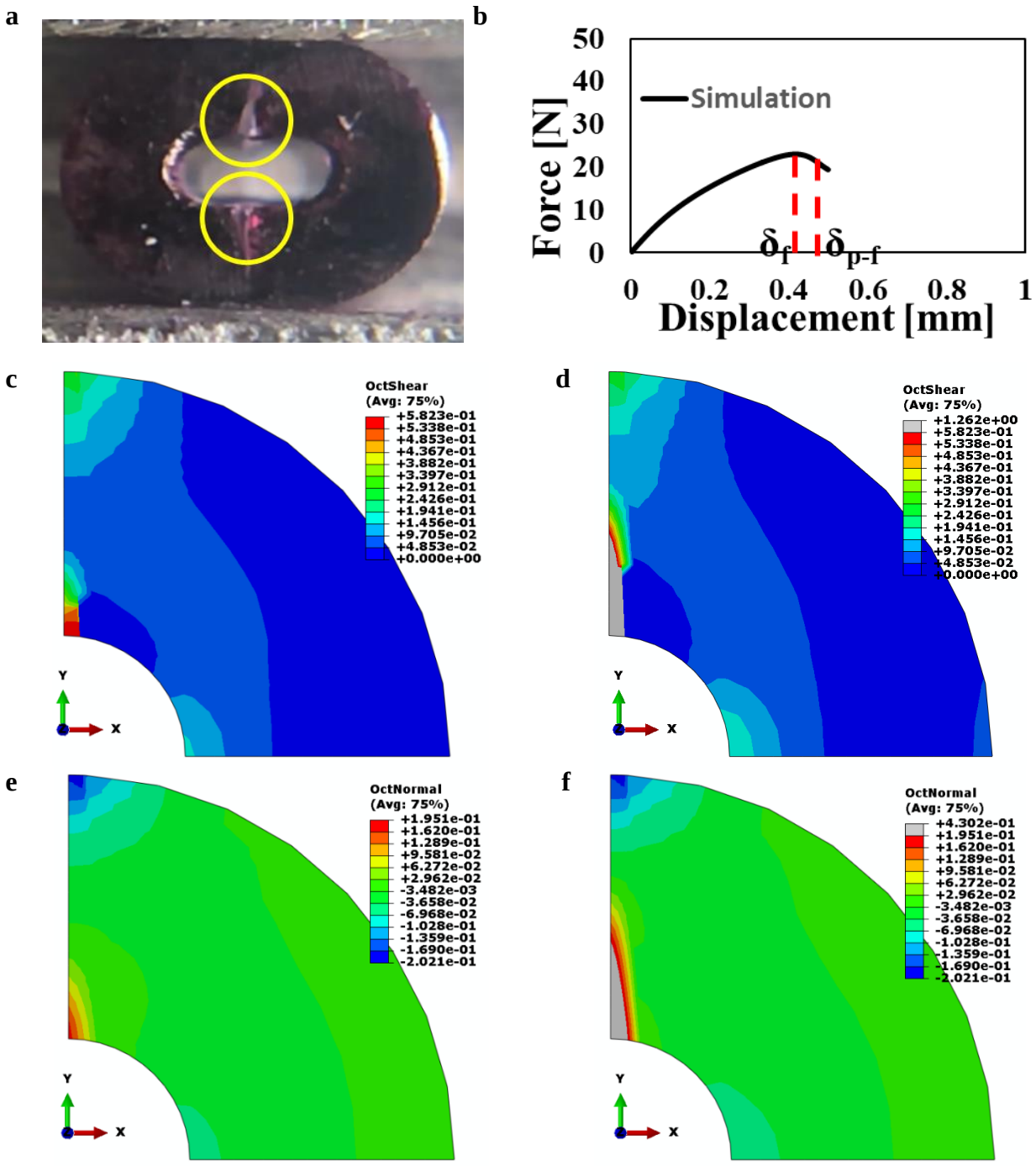

Figure 5.14: Failure analysis of the C1 polymer at 0.2 mm/min loading rate: (a) Post-failure snapshot from the experiment, (b) Force-displacement relationship from the simulation (δ_f: failure displacement, $\delta_{p\text{-}f}$: post-failure displacement), (c and d) Local volume change maps at failure and post-failure, respectively and (e and f) Local distortion maps at failure and post-failure, respectively.

The calibrated and validated material model parameters of the C1 polymer were used to simulate this polymer's clinical mechanical performance. A loading rate of 3.5 mm/min was applied. The FE simulation suggested that the C1 polymer can bear loads up to 32.86 N and fails at a displacement of 0.87 mm under the clinical loading condition. The local distortion and volume change were also assessed for this simulation. They were thresholded with their color bars at the failure displacement (δ_f). The predicted force-displacement relationship was used to find δ_f and a past-failure displacement ($\delta_{p\text{-}f}$) (Figure 5.15(a)). The maps at failure suggested that the location at the hole along the loading axis has the highest local distortion and volume change in dilatation mode (Figure 5.15(b) and Figure 5.15(d)). Additionally, the failure propagation was found to be towards the load surface along the load axis. The size of the failed zone was predicted to be significantly smaller than 0.2 mm/min and about the same as 1 mm/min.

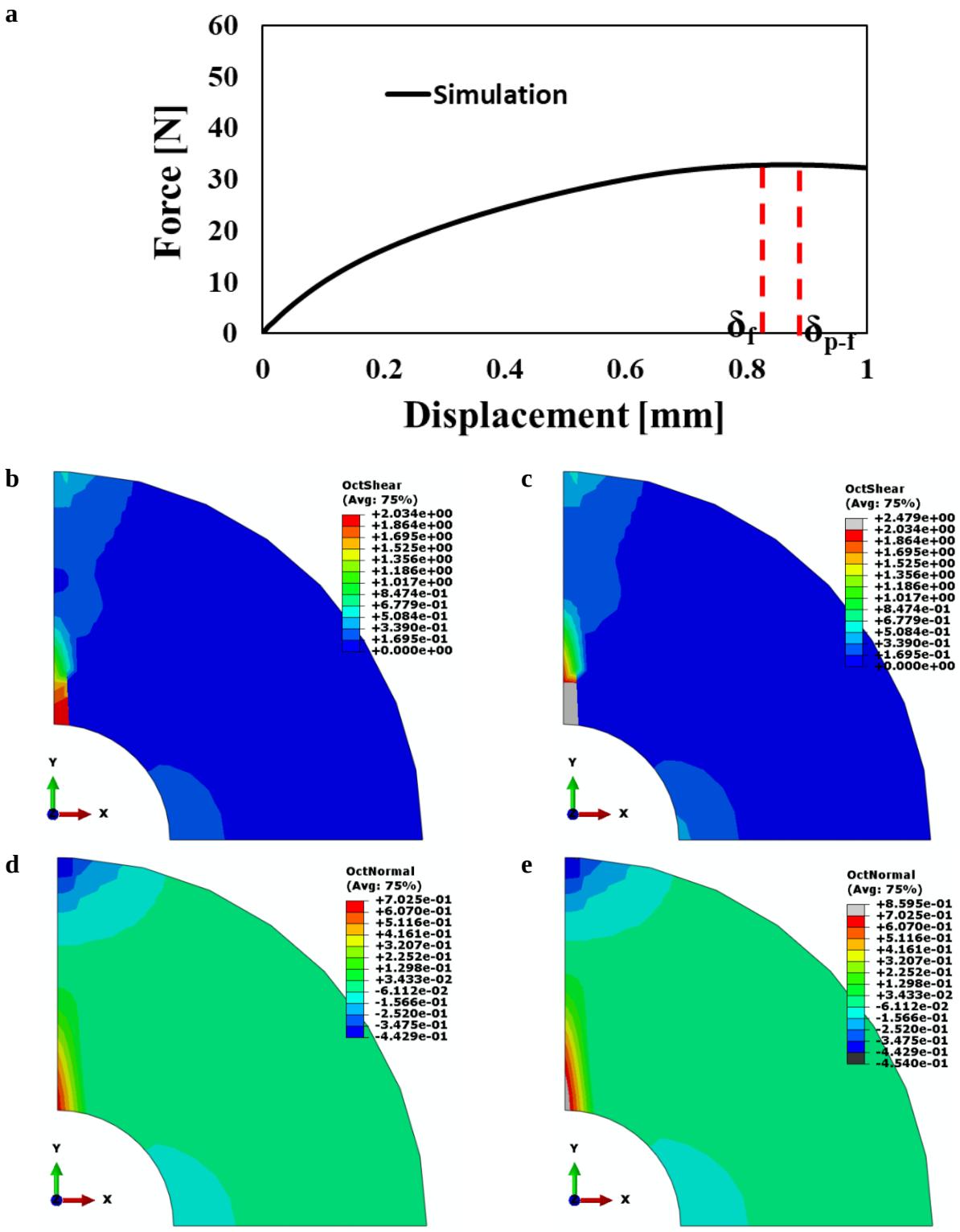

Figure 5.15: Failure analysis of the C1 polymer at 3.5 mm/min loading rate: (a) Force-displacement relationship from the simulation (δ_f: failure displacement, δ_{p-f}: post-failure

displacement), (b and c) Local volume change maps at failure and post-failure, respectively and (d and e) Local distortion maps at failure and post-failure, respectively.

To investigate the rate dependent failure evolution, the maximum principal stress and strains were obtained from the failure initiation element at each loading rate (Figure 5.8 and Figure 5.16). The stress-strain data suggested that the C1 polymer failed at a stress of 14.46 MPa and a strain of 0.097 at 0.2 mm/min. It had a failure stress of 15.12 MPa and a failure strain of 0.103 at 1 mm/min. When it was subject to 3.5 mm/min, it failed at a stress of 16.79 MPa and a strain of 0.113. Moreover, the toughness of the C1 polymer was predicted by using the areas I, II and III, which are under the stress-strain curve up to the failure strain. C1 polymer's toughness was suggested 0.99 MPa, 1.13 MPa and 1.4 MPa at 0.2 mm/min, 1 mm/min and 3.5 mm/min, respectively.

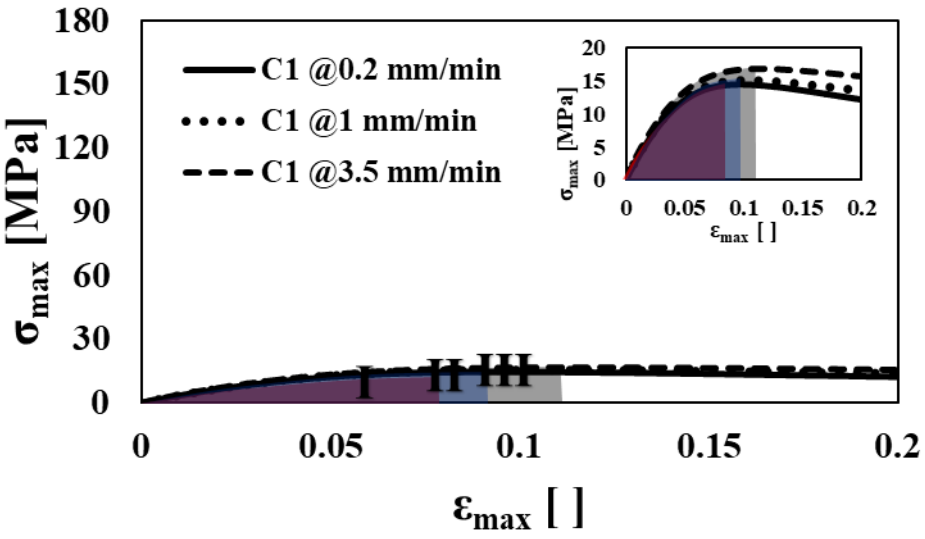

Figure 5.16: Stress-strain behavior of the C1 polymer at failure initiation location at 0.2, 1 and 3.5 mm/min loading rates. Stress and strain values are presented in terms of maximum principal stress and maximum principal strain. I, II and III indicate the area under each curve up to the

corresponding failure strain. The inset figure provides the same stress-strain relationship with a refined y-axis.

Finally, the single patch test was performed with C1 polymer's calibrated and validated material model parameters. These simulations were made at each loading rate. The stress-strain results from the simulations (Figure 5.17) were compared to the results from the failure initiation element at the diametral compression test simulations. The single patch test simulations predicted that the C1 polymer fails at a stress of 15.637 MPa and a strain of 0.090 at 0.2 mm/min, a stress of 20.23 MPa and a strain of 0.093 at 1 mm/min and a stress of 34.41 MPa and a strain of 0.118 at 3.5 mm/min. These predictions indicate C1 polymer's behavior under uniaxial tensile loading. C1 polymer's toughness was also predicted under pure tensile loading at different loading rates by using the areas I, II and III. The toughness of C1 polymer was suggested to be 0.99 MPa, 1.34 MPa and 2.87 MPa at 0.2 mm/min, 1 mm/min and 3.5 mm/min, respectively. It is observed that the diametral compression test simulation provided a similar toughness as the uniaxial tensile loading simulation. However, the toughness obtained from the diametral compression test simulation was significantly lower compared to the uniaxial tensile loading simulation at 1 mm/min and 3.5 mm/min.

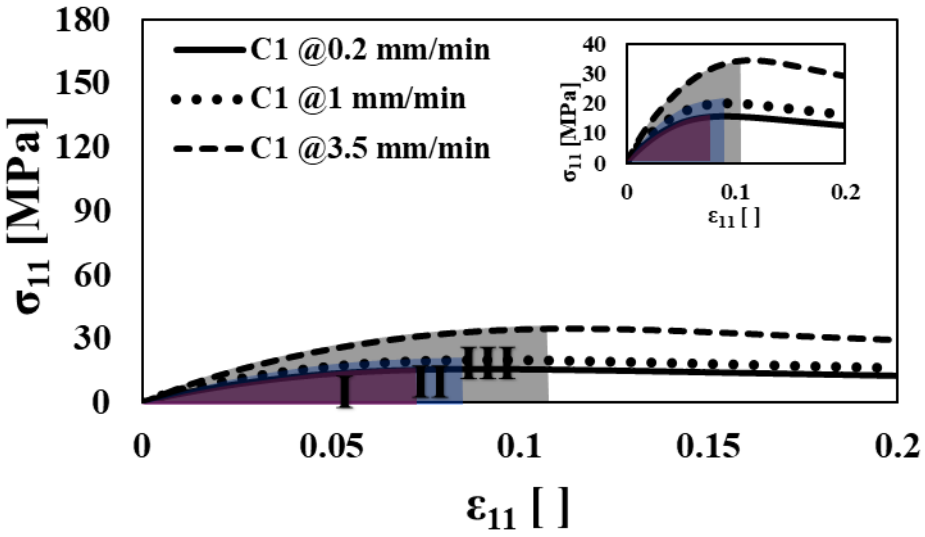

Figure 5.17: Stress-strain behavior of the C1 polymer at uniaxial tensile loading at 0.2, 1 and 3.5 mm/min loading rates. I, II and III indicate the area under each curve up to the corresponding failure strain. The inset figure provides the same stress-strain relationship with a refined y-axis.

5.3.3 Experimental Adhesive (E1) Polymer

The experimental adhesive (E1) polymer's failure and damage were investigated by running the diametral compression test FE simulations. A simulation was prepared for predicting E1 polymer ring specimen's mechanical behavior at 1 mm/min loading rate. The material model parameters were selected to approximate the experimental force-displacement relationship obtained from an E1 polymer specimen in Chapter 3. In Figure 5.18, the predicted force-displacement relationship is in good agreement with the experimental results. This observation suggests that the assigned material model parameters were calibrated for the E1 polymer. In the physical test, the E1 polymer specimen failed at a load of 38.70 N and a displacement of 0.40 mm. The FE simulation predicted

that the E1 polymer specimen's failure load was 37.40 N and its failure displacement was 0.42 mm.

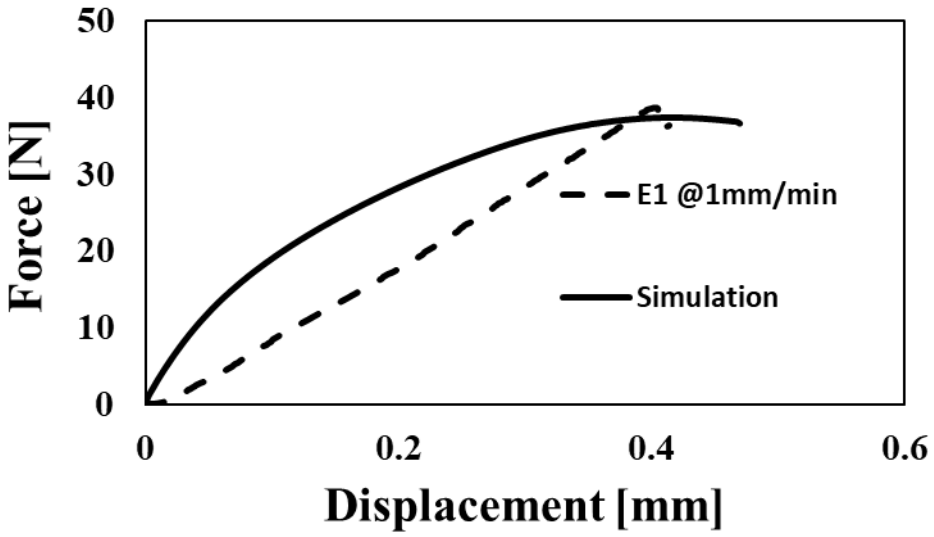

Figure 5.18: Calibration of the material model parameters for E1 adhesive: Comparison of the simulated force-displacement relationship to the experimental force-displacement relationship of E1 adhesive at 1 mm/min loading rate.

The assigned material model parameters were kept the same and another simulation was performed at 0.2 mm/min. This simulation was compared against an E1 polymer's experimental results at 0.2 mm/min in Chapter 3 (Figure 5.19). This comparison validated the calibrated set of material model parameters to represent the E1 polymer as the simulated results exhibited good approximation with the experimental results. The mechanical test read the failure load of the E1 polymer as 28.05 N and the failure displacement as 0.30 mm. The simulation predicted that the E1 polymer specimen failed at a load of 29.62 N and a displacement of 0.25 mm.

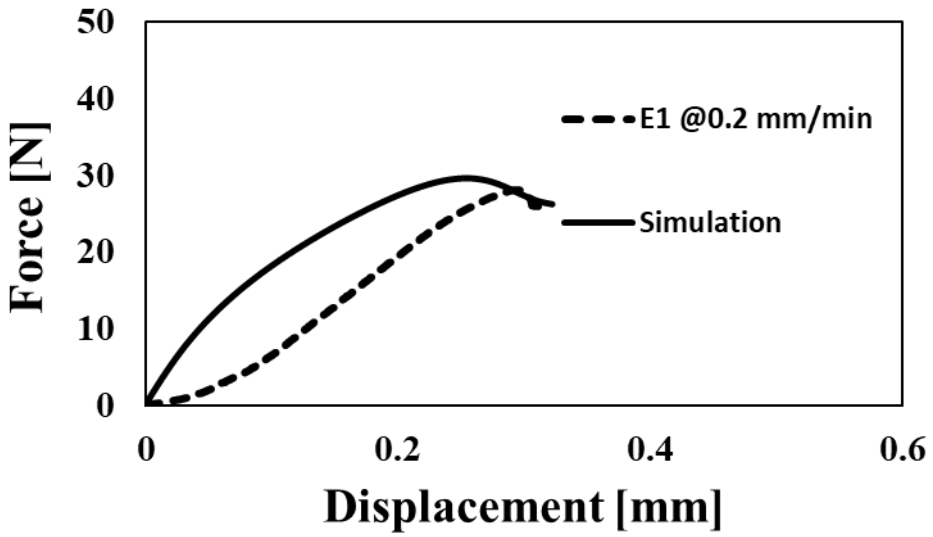

Figure 5.19: Validation of the material model parameters for the E1 adhesive: Comparison of the simulated force-displacement relationship to the experimental force-displacement relationship of the E1 adhesive at 0.2 mm/min loading rate.

The local distortion and volume change maps were created with the data obtained from the simulation at 1 mm/min. The failure displacement (δ_f) and a post-failure displacement ($\delta_{p\text{-}f}$) were selected from the predicted force-displacement relationship (Figure 5.20(b)). The color bars of local volume change and distortion maps were fixed at δ_f (Figure 5.20(c) and Figure 5.20(e)). When the maps were advanced to $\delta_{p\text{-}f}$, a grey colored zone appeared to reveal the failed locations (Figure 5.20(d) and Figure 5.20(f)). $\delta_{p\text{-}f}$ was selected by applying an additional displacement of 0.05 mm after δ_f. The predicted failure initiation location and failure evolution path agreed well with the experimental fracture pattern in Chapter 3 (Figure 5.20(a)). In both cases, the failure began at the hole along the loading axis and propagated towards the load surface along the load axis.

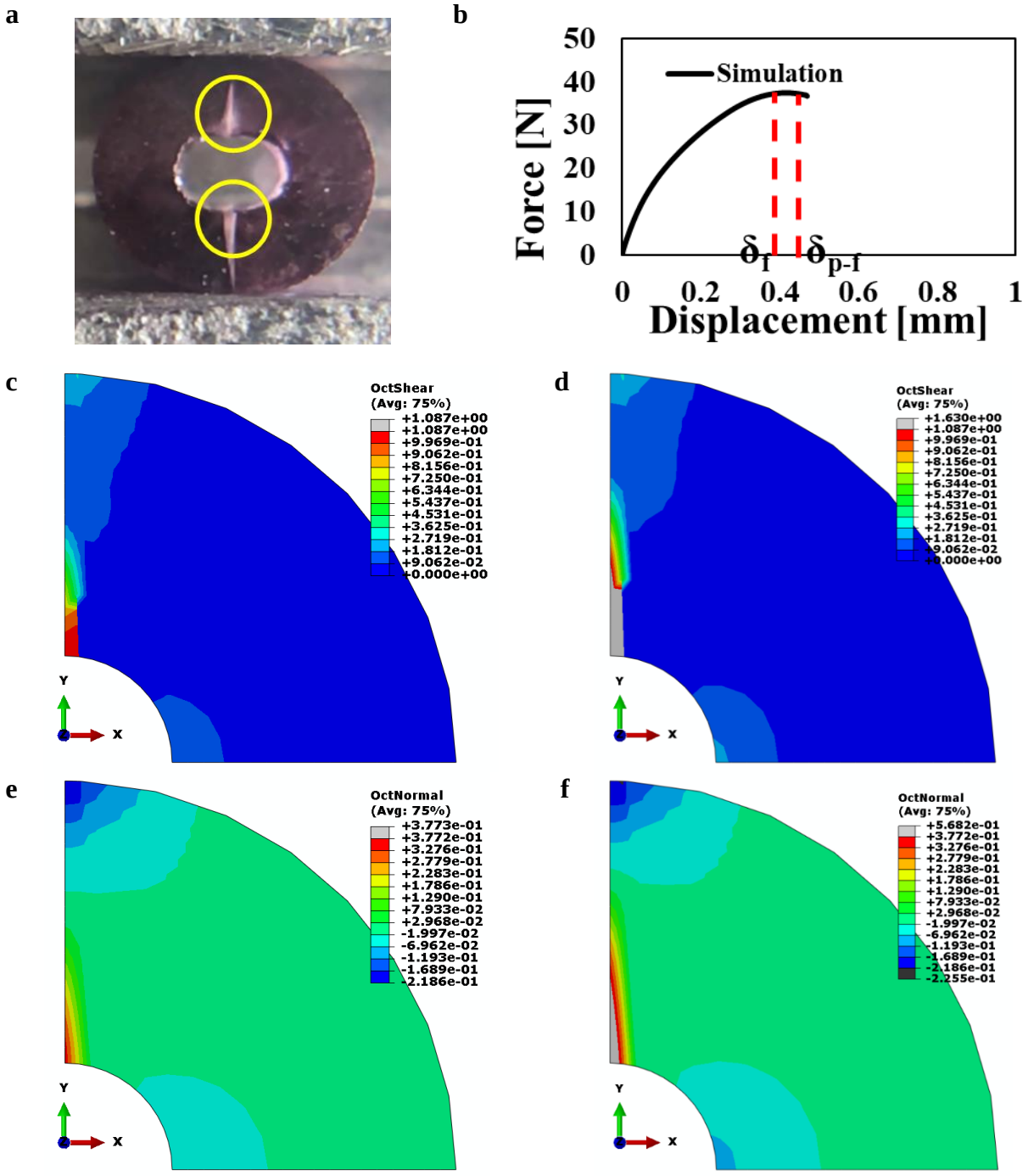

Figure 5.20: Failure analysis of the E1 polymer at 1 mm/min loading rate: (a) Post-failure snapshot from the experiment, (b) Force-displacement relationship from the simulation (δ_f: failure displacement, $\delta_{p\text{-}f}$: post-failure displacement), (c and d) Local volume change maps at failure and post-failure, respectively and (e and f) Local distortion maps at failure and post-failure, respectively.

The local distortion and volume change maps at 0.2 mm/min were also created. They were compared to the experimental failure in Chapter 3 (Figure 5.21(a)). The difference between displacement failure (δ_f) and the post-failure displacement ($\delta_{p\text{-}f}$) was selected as 0.05 mm. The simulated force-displacement curve was used to find δ_f and $\delta_{p\text{-}f}$ (Figure 5.21(b)). The color bars of local distortion and volume change maps were thresholded at δ_f. (Figure 5.21(c) and Figure 5.21(e)). The maps at $\delta_{p\text{-}f}$ showed a grey colored zone as an indication of failure. The failed zone in both maps was found at the loading axis. Moreover, the highest distortion and volume change were observed at the hole along the loading axis. These observations indicate that the simulated failure pattern matched well with the experimental post-failure pattern. Additionally, the failed zone in the E1 polymer was predicted larger than the C1 polymer at 0.2 mm/min.

a

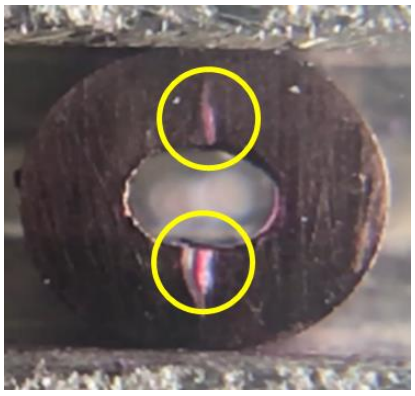

b

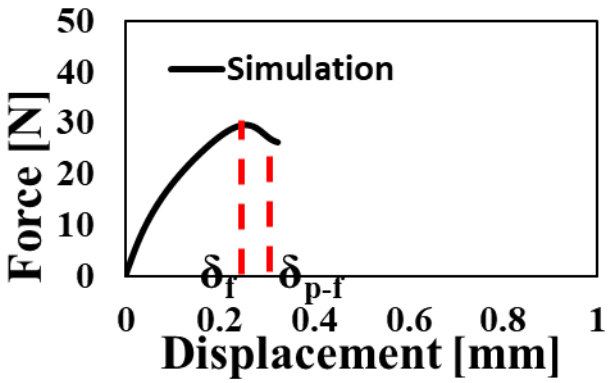

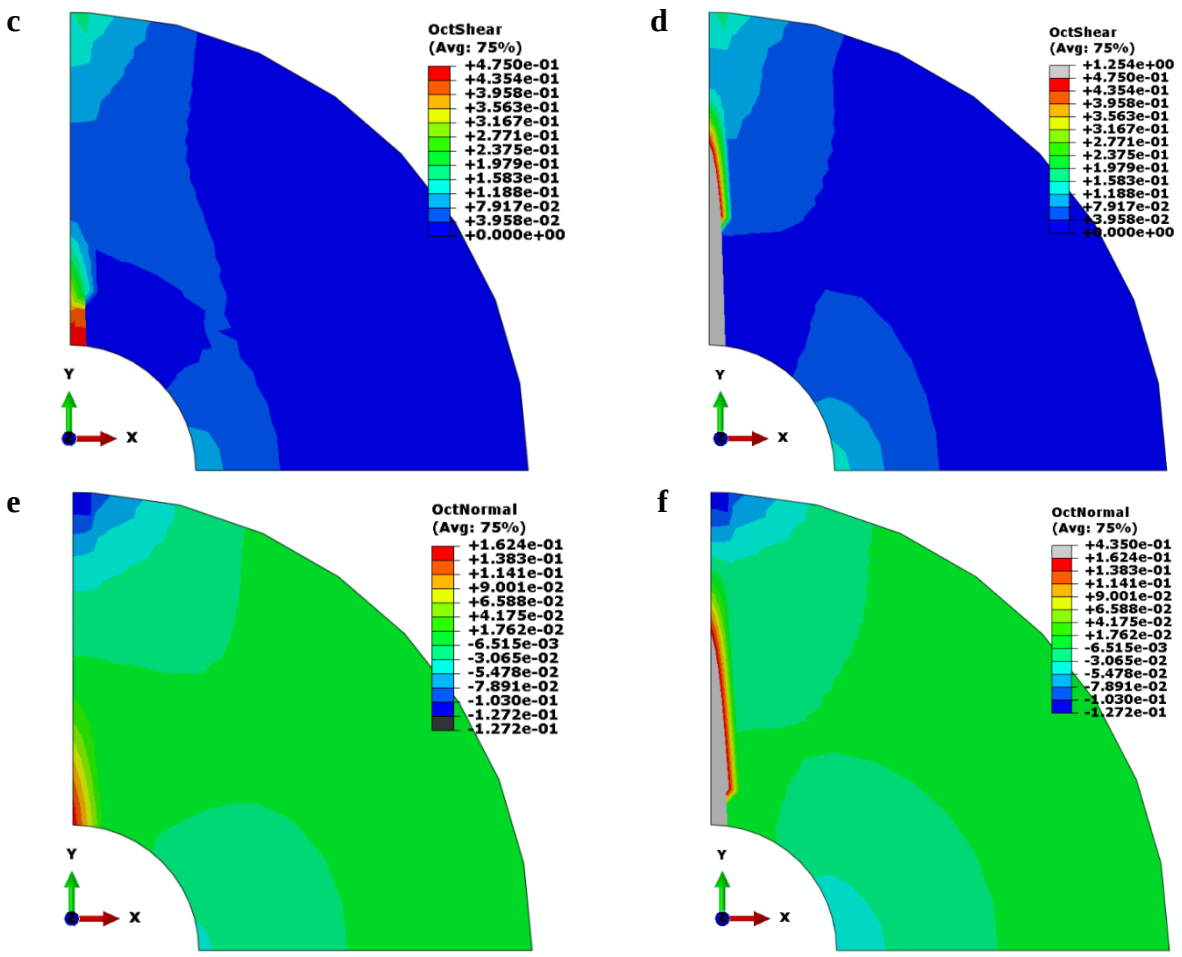

Figure 5.21: Failure analysis of the E1 polymer at 0.2 mm/min loading rate: (a) Post-failure snapshot from the experiment, (b) Force-displacement relationship from the simulation (δ_f: failure displacement, $\delta_{p\text{-}f}$: post-failure displacement), (c and d) Local volume change maps at failure and post-failure, respectively and (e and f) Local distortion maps at failure and post-failure, respectively.

To predict E1 polymer's clinical mechanical performance, a simulation was performed at 3.5 mm/min. The calibrated and validated material model parameters were used for this simulation. It was predicted that the E1 polymer fails at clinical conditions when the load is 49.79 N and the displacement is 0.74 mm (Figure 5.22(a)). The local distortion and volume change maps were also derived from this simulation. Their color bars were fixed at the failure displacement (δ_f) and a

post-failure displacement ($\delta_{p\text{-}f}$) (Figure 5.22(b) and Figure 5.22(d)). These displacements were determined from the predicted force-displacement curve by maintaining a difference of 0.05 mm between them. The failed locations were revealed by progressing to $\delta_{p\text{-}f}$ in both maps. The maps suggested that the failure starts at the hole along the loading axis and propagates towards the loading surface following the same axis (Figure 5.22(c) and Figure 5.22(e)). It was observed that the failed area size is smaller than the predictions at 0.2 mm/min and 1 mm/min.

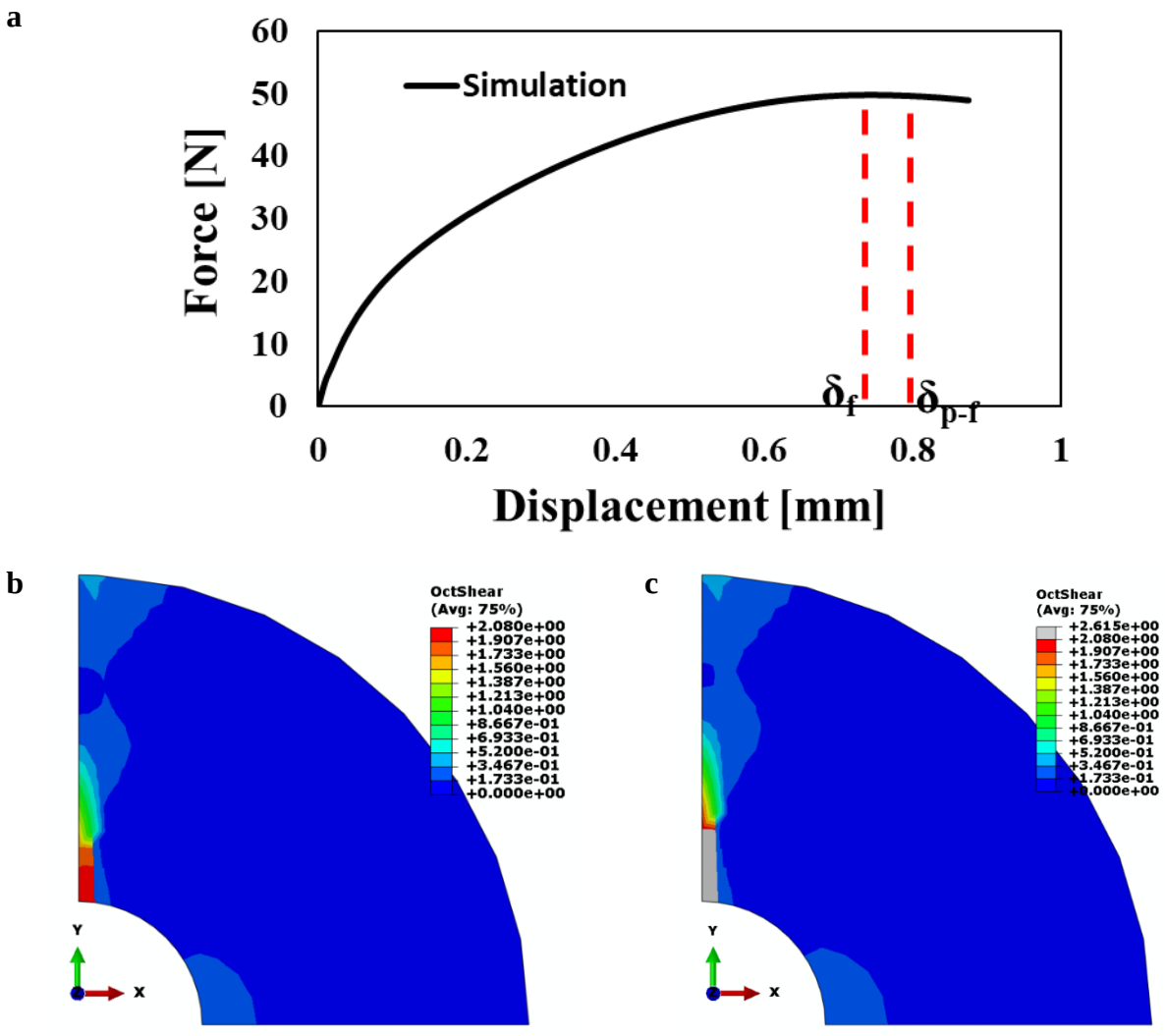

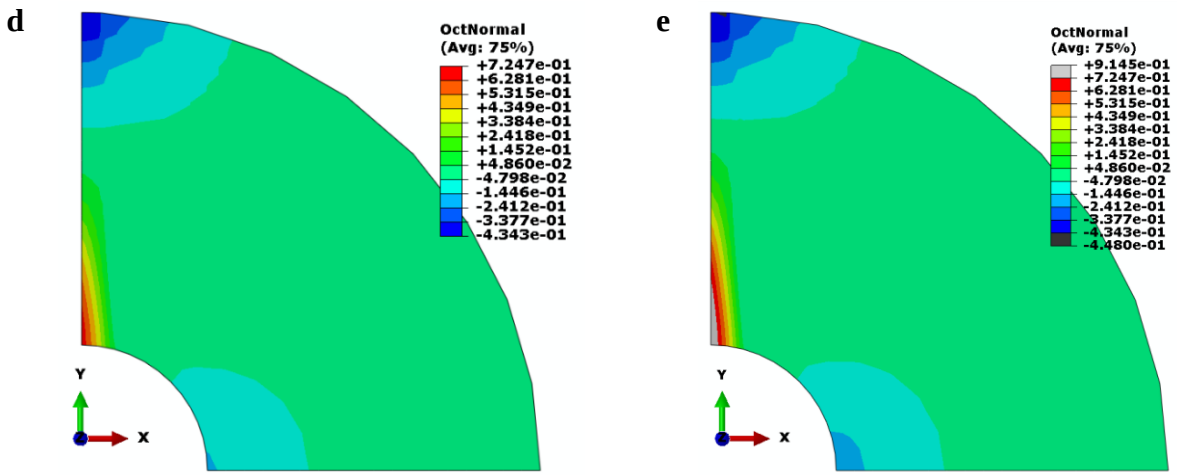

Figure 5.22: Failure analysis of the E1 polymer at 3.5 mm/min loading rate: (a) Force-displacement relationship from the simulation (δ_f: failure displacement, $\delta_{p\text{-}f}$: post-failure displacement), (b and c) Local volume change maps at failure and post-failure, respectively and (d and e) Local distortion maps at failure and post-failure, respectively.

The failure patterns at all loading rates revealed a rate dependent failure pattern. To investigate this behavior, the maximum principal stress and strain were derived from the initial failure location of the E1 polymer specimen (Figure 5.8 and Figure 5.23). These relationships showed that E1 polymer's failure stress was 15.35 MPa, 16.75 MPa and 20.18 MPa at the loading rates of 0.2 mm/min, 1 mm/min and 3.5 mm/min, respectively. Its failure strain was predicted as 0.051, 0.055 and 0.064 at 0.2 mm/min, 1 mm/min and 3.5 mm/min, respectively. Additionally, E1 polymer's toughness was calculated considering the areas I, II and III. These areas are under the stress-strain curves up to the failure strains. The simulations predicted that E1 polymer's toughness was 0.57 MPa, 0.69 MPa and 1.00 MPa at the loading rates of 0.2 mm/min, 1 mm/min and 3.5 mm/min, respectively.

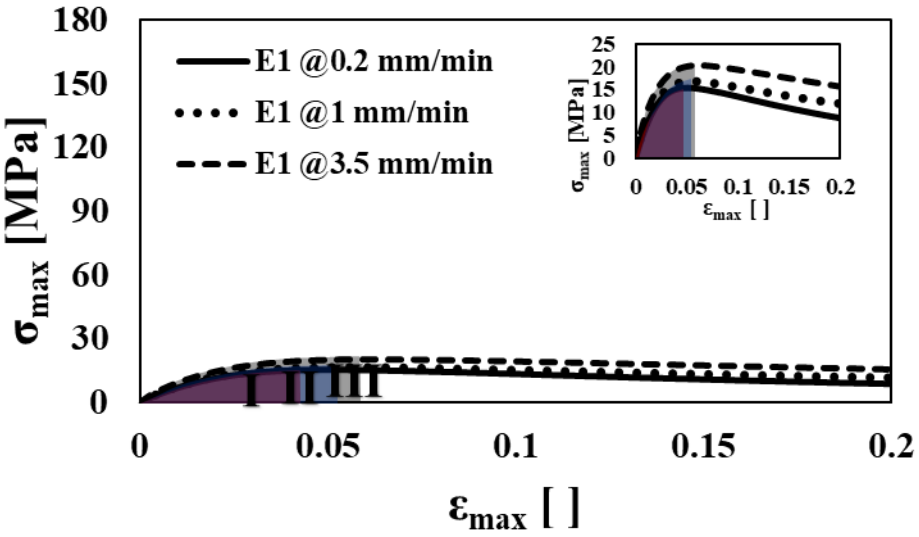

Figure 5.23: Stress-strain behavior of the E1 polymer at failure initiation location at 0.2, 1 and 3.5 mm/min loading rates. Stress and strain values are presented in terms of maximum principal stress and maximum principal strain. I, II and III indicate the area under each curve up to the corresponding failure strain. The inset figure provides the same stress-strain relationship with a refined y-axis.

To predict the true tensile nature of the E1 polymer, three single patch tests were simulated. These tests used the calibrated and validated material model parameters for the E1 polymer. The simulated uniaxial tensile stress-strain results (Figure 5.24) predicted that the E1 polymer has a failure stress of 18.18 MPa, 30.37 MPa and 65.07 MPa at 0.2 mm/min, 1 mm/min and 3.5 mm/min, respectively. Moreover, the E1 polymer fails at strain of 0.046, 0.048 and 0.073 at 0.2 mm/min, 1 mm/min and 3.5 mm/min, respectively. After calculating the areas I, II and III, the toughness of the E1 polymer was found 0.62 MPa, 1.06 MPa and 3.36 MPa at 0.2 mm/min, 1 mm/min and 3.5 mm/min, respectively. E1 polymer's failure stress and toughness were significantly lower in diametral compression test than the pure tensile loading simulation.

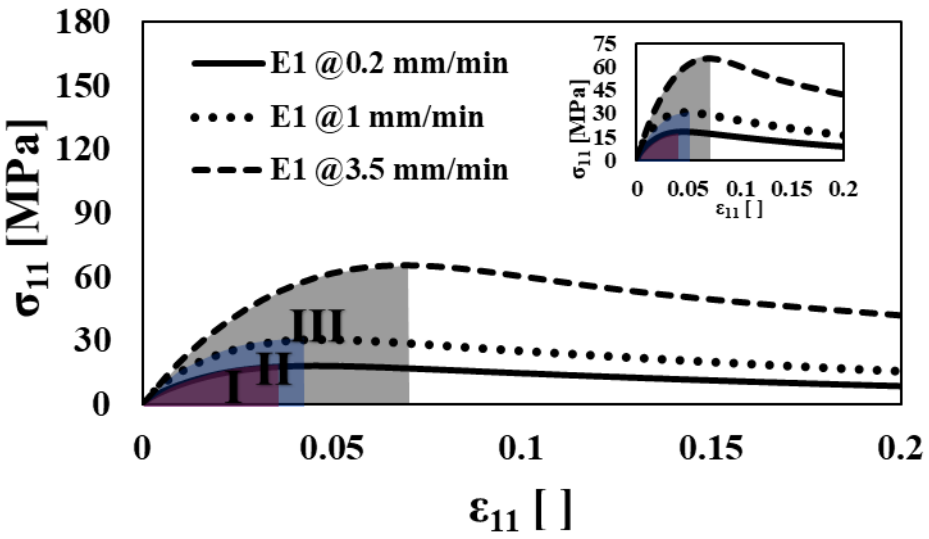

Figure 5.24: Stress-strain behavior of the E1 polymer at uniaxial tensile loading at 0.2, 1 and 3.5 mm/min loading rates. I, II and III indicate the area under each curve up to the corresponding failure strain. The inset figure provides the same stress-strain relationship with a refined y-axis.

5.4 Summary and Conclusions

In this study, FE simulations were performed to calibrate and validate the granular micromechanics material model parameters of the mineralized tissue, the C1 adhesive polymer and the E1 adhesive polymer. For this purpose, each material's model parameters were calibrated and validated against the experimental data shown in Chapter 3. It is concluded that the granular micromechanics material model is capable of capturing the rate dependent nature of the mineralized tissue and the adhesive polymers. In general, the simulation predicted the failure initiation location and failure evolution paths of each material in a reliable fashion. For this evaluation, the predicted failure locations were compared to the experimental post-failure snapshots in Chapter 3. After validation and calibration, the FE models were used to predict the information not directly accessible with physical experiments. The mechanical behavior of the mineralized tissue and the adhesive polymers were predicted with the calibrated and validated material properties. The predictions

suggested that the materials grow more resistant against fracture with an increase in the loading rate. It was predicted that the E1 polymer can bear higher stresses than the C1 polymer at all loading rates. This prediction was supported in Chapter 3. The E1 adhesive has a higher crosslinking density than the C1 adhesive due to the contribution of self-strengthening reaction. This higher crosslinking strongly affects the mechanical response of the polymer. However, the simulations suggested that E1 polymer's toughness is significantly lower than the C1 polymer. This prediction can be linked to the brittle nature of E1 adhesive, as it was explained in Chapter 3. The high crosslinking density results in strain concentration. The increased amount of strain concentrations in the polymer leads to the failure at lower displacements. Moreover, the simulations suggested that the diametral compression test results in lower stress and toughness for materials. This information was revealed by simulating uniaxial tensile tests and comparing them to the failure initiation element's behavior in the diametral compression tests. This difference can be devoted to the mechanism where different locations undergo different loading modes in the specimen under the diametral compression load. In the studied FE models, the load application was simplified by eliminating the load platens. In the future, these simulations can be improved by introducing the load platens into the model. It might capture the initial stiffening in the force-displacement relationships.

CHAPTER 6

PREDICTION OF BOND MECHANICS AT THE MINERALIZED TISSUE – ADHESIVE INTERFACE: CALIBRATION, VALIDATION AND PREDICTION

6.1 Introduction

The hybrid layer's mechanical behavior is critical for understanding the bond mechanics at the mineralized tissue – adhesive interface. This chapter combines the mathematical modeling studies in Chapter 2, Chapter 4 and Chapter 5 with the experimental work in Chapter 3. The combination of these studies enables the computational characterization of the hybrid layer's mechanical behavior. In Chapter 5, the nonlinear material model parameters were calibrated and validated for the mineralized tissue, the C1 polymer and the E1 polymer. In this chapter, finite element (FE) analyses are conducted for the calibration and validation of the C1 and the E1 hybrid layer's nonlinear material model parameters against the data from the interfacial experiments presented in Chapter 3. The failure and damage of these hybrid layers were evaluated at the loading rates in the experiments and in the clinical conditions [21, 115-118]. Moreover, the mechanical performance of these hybrid layers were predicted under remineralization and degradation conditions.

6.2 Computational Analyses

The finite element (FE) simulations were performed via the commercial FE code, Abaqus (Simulia/ABAQUS V 6.13-3, Dassault Systémes, RI, USA). To enable the implementation of the developed granular micromechanics nonlinear material model into FE, Abaqus was coupled with visual Fortran composer (Intel, Santa Clara, CA) as stated in Chapter 2. This material model was written in Fortran by following the format for user-defined nonlinear material (UMAT). This formatting was required to couple the commercial FE software and the material model. After implementing the nonlinear material model, the FE simulations were enhanced to capture rate-dependent nonlinear mechanical behavior with damage and plasticity. Five FE models were generated. Two of these models were created to model the diametral compression test of the interfacial specimens presented in Chapter 3. These interfacial specimens were prepared with material pairs of the mineralized tissue – control adhesive (C1) and the mineralized tissue – experimental adhesive (E1). The other two models were created for predicting the behavior of the mineralized tissue – E1 adhesive specimen under two additional conditions. These conditions were the remineralization and degradation of the mineralized tissue – E1 adhesive hybrid layer. In these four models, the same geometry was used. It was created based on the average dimensions in the interfacial mechanical tests covered in Chapter 3. In detail, the geometry was a 1.52 mm thick disk having a diameter of 3.04 mm. This disk was partitioned into three concentric sections to represent the interfacial material system (Figure 6.1(a)). The inner section had a diameter of 0.98 mm and the intermediate section had a thickness of 50 μm. The intermediate section represented the hybrid layer, and its dimension was speculated. The FE models considered the one-eighth of the geometry and had the symmetric boundary conditions on xy, xz and yz planes (Figure 6.1(b)). 8 node linear hexahedral elements were used for the mesh. Each model had 7854 degrees of freedom (Figure

6.1(c)). Moreover, the experimental loading was simulated by applying a displacement in the negative y-direction. The load was uniformly set on a surface along the thickness starting from the yz plane. It followed the path of an arc. This arc was 2.5° and concentric with the disk center. At last, the single element patch test model was generated. This model's geometry was a cube whose side length is 1 mm. Its mesh was created with one 8 node linear hexahedral element. All nodes were fixed with no displacements in all directions except for the nodes on y-z surface. These nodes were subject to a displacement load in the positive x-direction while they were restricted to be zero in terms of displacements in the y- and z-directions. Three different loading rates were assigned for all the created FE models. In the FE models for the diametral compression test, these loading rates were used to perform the calibration and validation of the hybrid layers' material properties and predict hybrid layers' mechanical behavior at clinical loading. Material model parameters for each hybrid layer material were calibrated against the experimental force-displacement relationship at 1 mm/min loading rate presented in Chapter 3. Therefore, these models were subject to the loading rate of 1 mm/min. Subsequently, the calibrated material model parameters were validated against the experimental data at 0.2 mm/min loading rate. Hence, the second applied loading rate was 0.2 mm/min in the FE models. Furthermore, the simulations of the clinical conditions were performed by applying the clinical loading rate of 3.5 mm/min [21, 115-118]. Finally, all three loading rates were applied in the single patch test to inform the hybrid layer materials' mechanical behavior under pure uniaxial tensile loading. In the diametral compression test's FE models, the outer layer was assigned with the calibrated and validated material model parameters of the mineralized tissue in Chapter 5 (see the Appendix C, Table 10.3). In the simulations of the mineralized tissue – C1 adhesive specimens, the inner section was assigned with the calibrated and validated material model parameters of the C1 adhesive polymer in Chapter 5.

Similarly, the diametral compression test of the mineralized tissue – E1 adhesive specimens used the calibrated and validated material model parameters of the E1 adhesive polymer in Chapter 5 for the inner section. Finally, two different sets of material model parameters were assigned to the intermediate section to fulfill the calibration and validation of each hybrid layer's material model parameters. E1 hybrid layer's micro-scale normal and shear stiffness were assumed to increase by 10% to model the remineralized E1 hybrid layer. For the degradation, E1 hybrid layer's micro-scale normal and shear stiffness were assumed to decrease by 10%. All the assigned material model parameters are listed in the Appendix (see the Appendix C, Table 10.4).

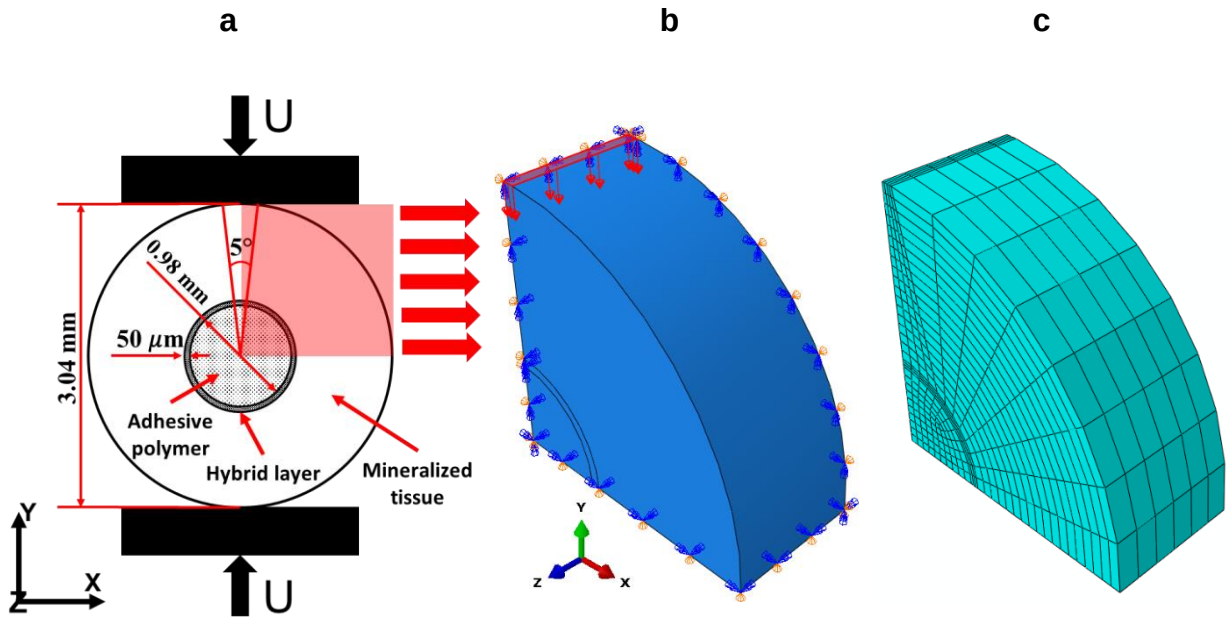

Figure 6.1: (a) Representation of the bond strength test considered in the finite element model, (b) the boundary conditions and (c) the meshed geometry generated in three-dimensional finite element models.

6.3 Results and Discussion

This section covers computational characterization of the bond mechanics at the mineralized tissue – C1 adhesive interface and the mineralized tissue – E1 adhesive interface. The nonlinear material model parameters were calibrated for the hybrid layer of C1 adhesive and the hybrid layer of E1 adhesive against the data obtained from the interfacial mechanical tests at 1 mm/min presented in Chapter 3. Subsequently, the calibrated hybrid layer materials' nonlinear material model parameters were validated against the interfacial experimental data at 0.2 mm/min. Moreover, each hybrid layer' clinical mechanical performance was predicted with their calibrated and validated model parameters. Additionally, the hybrid layers' mechanical behaviors were predicted at a clinical loading rate of 3.5 mm/min [21, 115-118]. The local distortion and local volume change maps were created by computing the octahedral shear and octahedral normal strains, respectively. These maps were used to predict the failure initiation and evolution at the interface. Furthermore, single patch test simulations were performed to reveal the hybrid layer materials' uniaxial tensile behavior. The local stress-strain and the toughness were evaluated for each material. Finally, the mechanical behaviors of the mineralized E1 hybrid layer and the degraded E1 hybrid layer were predictited with a simulated interfacial diametral compression test and a uniaxial tensile load simulation.

6.3.1 Mineralized Tissue – Control Adhesive (C1) Interface

The mineralized tissue – C1 interface FE model simulated the diametral compression test of the interfacial specimen made of the mineralized tissue and the C1 adhesive. The force and displacement data were extracted from the nodes in the load surface. The first simulation was

performed at a loading rate of 1 mm/min. The predicted force-displacement curve was compared to an experimental force-displacement data presented in Chapter 3. The material model parameters of the C1 hybrid layer were selected when the simulated results approximated the experimental results the most (Figure 6.2). This approximation ensured the calibration of C1 hybrid layer's material model parameters. In the experiment, the mineralized tissue – C1 interfacial specimen failed at a force of 90.83 N and a displacement of 0.50 mm. The simulation predicted that this interfacial specimen had a failure force of 91.34 N and a failure displacement of 0.5 mm.

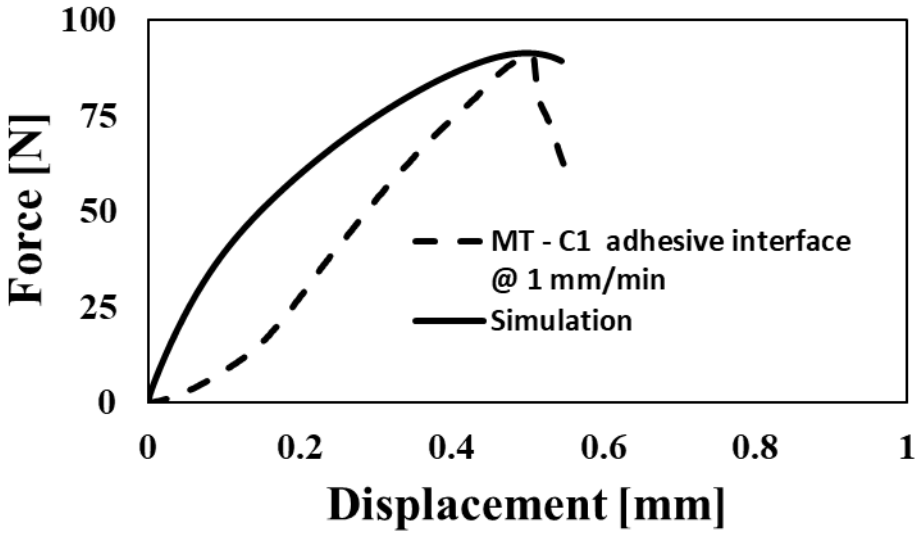

Figure 6.2: Calibration of the material model parameters for the mineralized tissue (MT) – C1 adhesive hybrid layer: Comparison of the simulated force-displacement relationship to the experimental force-displacement relationship of the mineralized tissue (MT) – C1 adhesive interface at 1 mm/min loading rate.

The calibrated set of material model parameters were used for a simulation at a 0.2 mm/min loading rate. This simulation was performed to validate the material model's capability to capture

C1 hybrid layer's rate dependent mechanical behavior. The simulated force and displacement relationship was compared to the experimental results of a mineralized tissue – C1 adhesive interfacial specimen presented in Chapter 3. It was observed that the calibrated material model parameters were able to approximate the experimental mechanical behavior (Figure 6.3). Thus, C1 hybrid layer's material model parameters were validated to capture its rate dependent mechanical behavior. The experiment on the mineralized tissue – C1 adhesive interfacial specimen measured the failure load as 69.70 N and the failure displacement as 0.37 mm. The simulation found that the failure force was 75.90 N and the failure displacement was 0.35 mm.

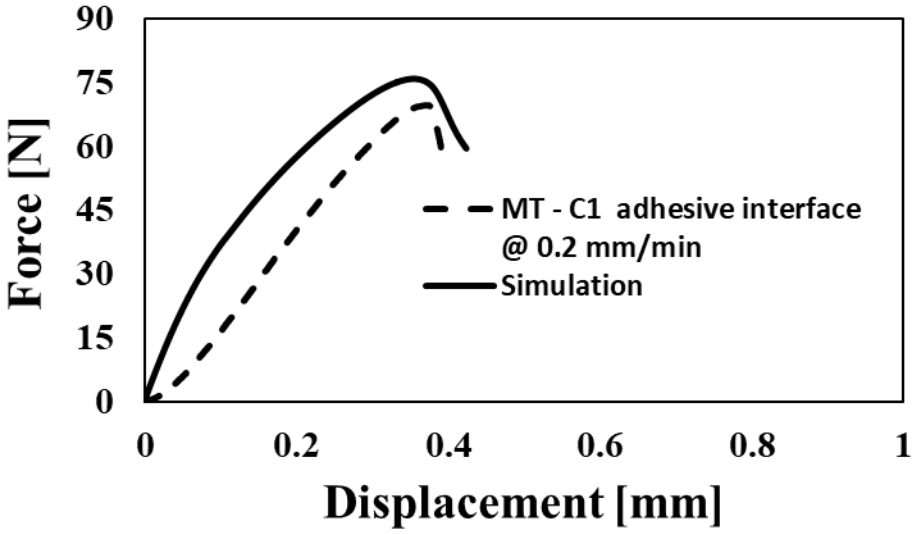

Figure 6.3: Validation of the material model parameters for the mineralized tissue (MT) – C1 adhesive hybrid layer: Comparison of the simulated force-displacement relationship to the experimental force-displacement relationship of the mineralized tissue (MT) – C1 adhesive interface at 0.2 mm/min loading rate.

The FE simulation at 1 mm/min was used to generate the local distortion and local volume change maps. The generated maps were checked against the experimental post-failure pattern of the

mineralized tissue – C1 adhesive interfacial specimen at 1 mm/min presented in Chapter 3 (Figure 6.4). The color bar of each map was fixed close to the failure displacement (δ_f) (Figure 6.4(c) and Figure 6.4(e)). Subsequently, the maps were advanced to a post-failure displacement ($\delta_{p\text{-}f}$) (Figure 6.4(d) and Figure 6.4(f)). $\delta_{p\text{-}f}$ was selected 0.05 mm more than δ_f (Figure 6.4(b)). The grey area in the distortion map at $\delta_{p\text{-}f}$ indicated the failed locations. The experimental post-failure snapshot shows that the failure was initiated at the interface along the transverse axis to the loading axis. Local volume change and distortion maps suggested the initial failure was at the same location as the experimental pattern. They also predicted a subsequent failure at the interface along the loading axis. The initial failure was predicted to evolve along with the interface toward the load axis. The local volume change map suggested that the initial failure was in dilatation mode (grey colored) and the subsequent failure was in contraction mode (black colored). The initial failure location was predicted between the hybrid layer and the C1 polymer. The subsequent failure was observed between the mineralized tissue and the C1 hybrid layer. Moreover, it was predicted that the mineralized tissue initiated a larger volume change next to the failed hybrid layer along the load axis. This volume change was found in dilatation mode.

a

b

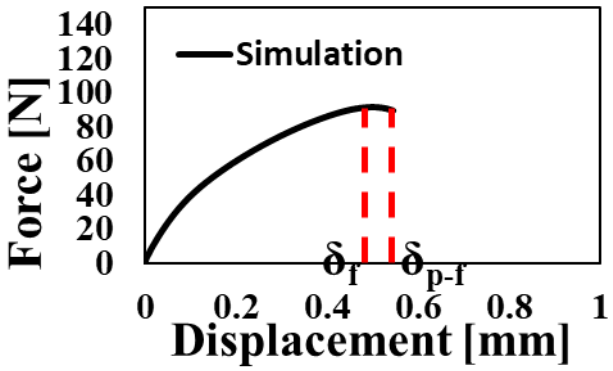

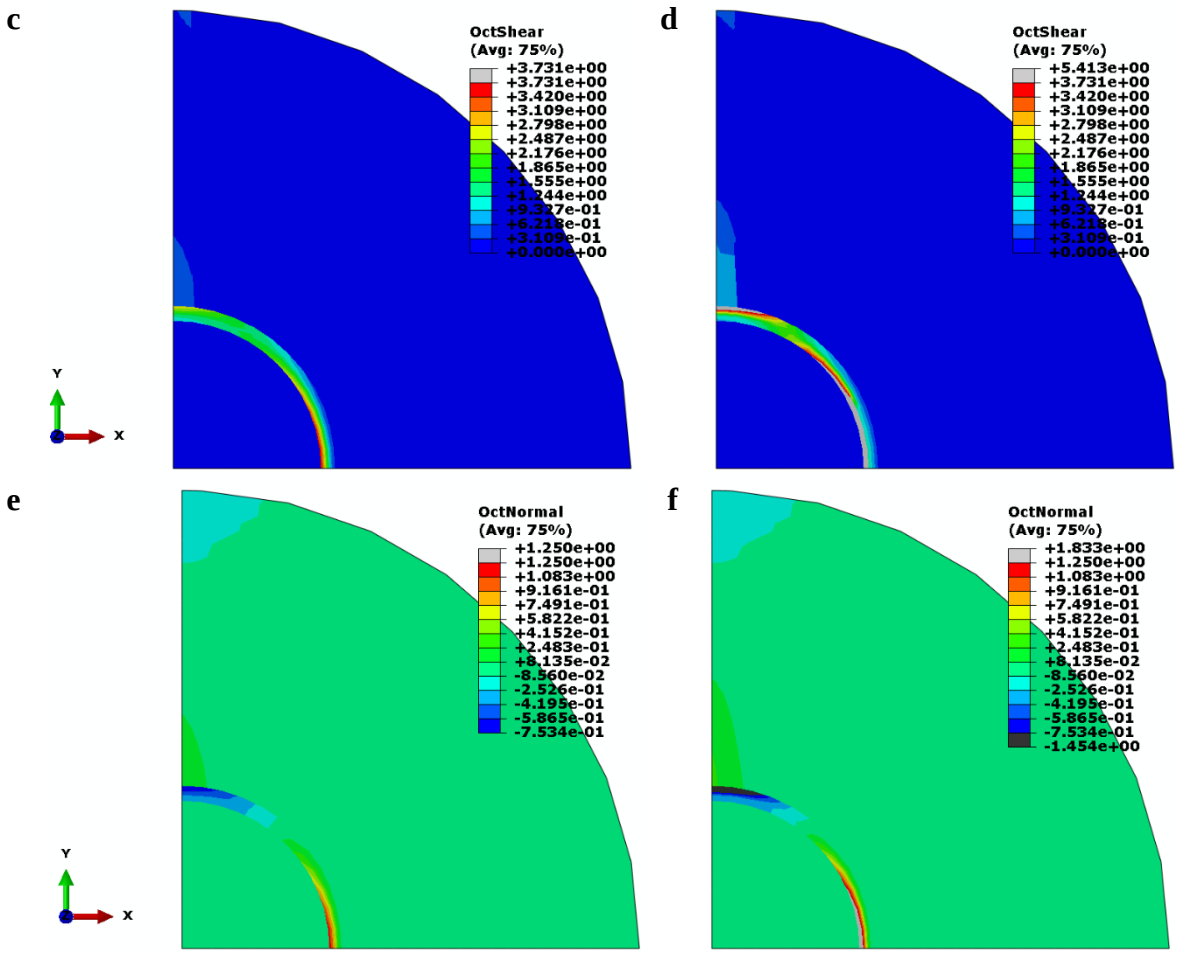

Figure 6.4: Failure analysis of the mineralized tissue - C1 adhesive interface at 1 mm/min loading rate: (a) Post-failure snapshot from the experiment, (b) Force-displacement relationship from the simulation (δ_f: failure displacement, $\delta_{p\text{-}f}$: post-failure displacement), (c and d) Local volume change maps at failure and post-failure, respectively and (e and f) Local distortion maps at failure and post-failure, respectively.

Similarly, the FE results at 0.2 mm/min were post-processed to obtain the local distortion and volume change distributions. These distributions were evaluated against the experimental post-failure snapshot of a mineralized tissue – C1 adhesive interfacial specimen at 0.2 mm/min shown in Chapter 3 (Figure 6.5(a)). The local distortion and volume change maps were presented with a color bar fixed at a displacement close to failure (δ_f) (Figure 6.5(c) and Figure 6.5(e)). After

applying an additional displacement of 0.05 mm (Figure 6.5(b)), these distributions were presented at a post-failure displacement ($\delta_{p\text{-}f}$) (Figure 6.5(d) and Figure 6.5(f)). The grey color revealed the failed locations in post-failure distortion distributions. The experiment observed that the failure was initiated at the interface along the transverse axis to the loading. The simulation suggested the same failure initiation location. This failure was suggested to be in dilatation mode (grey colored) in the volume change map. Additionally, the simulation showed a subsequent failure location. This location was predicted to be at the interface along the loading axis. This failure's mode was predicted as a contraction (black colored) in the volume change map. The initial failure was found between the C1 polymer and the hybrid layer. The second failure was observed between the mineralized tissue and the hybrid layer. Moreover, the predictions showed that the mineralized tissue experienced dilatation next to the second failure location along the loading axis. Both failure locations were found larger in size compared to the loading rate of 1 mm/min.

a

b

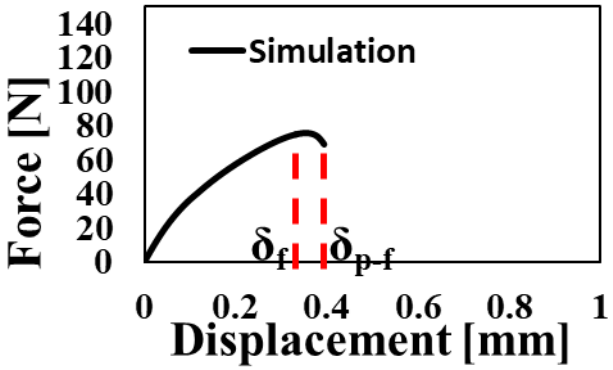

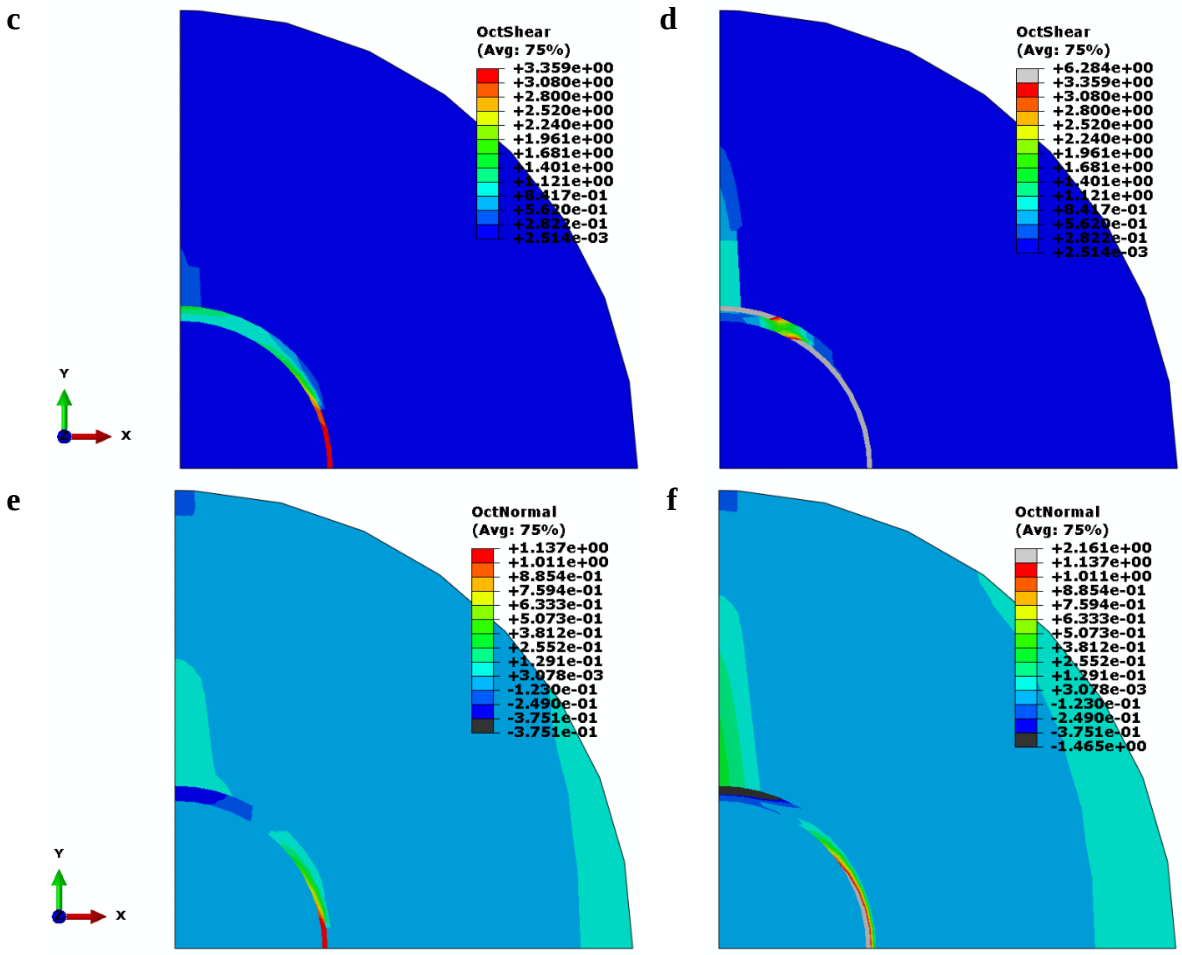

Figure 6.5: Failure analysis of the mineralized tissue - C1 adhesive interface at 0.2 mm/min loading rate: (a) Post-failure snapshot from the experiment, (b) Force-displacement relationship from the simulation (δ_f: failure displacement, $\delta_{p\text{-}f}$: post-failure displacement), (c and d) Local volume change maps at failure and post-failure, respectively and (e and f) Local distortion maps at failure and post-failure, respectively.

The diametral compression test of the mineralized tissue – C1 adhesive interfacial specimen was simulated at the clinical loading rate of 3.5 mm/min. The simulated force-displacement relationship suggested that this interfacial specimen fails at a load of 112.65 N and a displacement of 0.77 mm (Figure 6.6(a)). This specimen was predicted to fail in a brittle manner without post-peak softening. This simulation's local volume change and distortion maps were thresholded at a

displacement close to failure ($\delta_{b\text{-}f}$) (Figure 6.6(b) and Figure 6.6(d)) and advanced to the failure displacement (δ_f) (Figure 6.6(c) and Figure 6.6(e)). The difference between these displacements was assigned 0.05 mm. The gray area in the distortion map suggested that the failure is initiated at the interface along the loading axis's transverse direction. A second failure location was found at the interface along the loading axis. The initial failure appeared between the hybrid layer and the C1 polymer. It experienced a dilatation (grey colored) behavior in volume change. The second failure was between the hybrid layer and the mineralized tissue. It was found in contraction (black colored) mode in volume change. Moreover, the mineralized tissue experienced a higher dilatation next to the second failure along the loading axis. The size of the failed location was found significantly smaller than 0.2 mm/min.

a

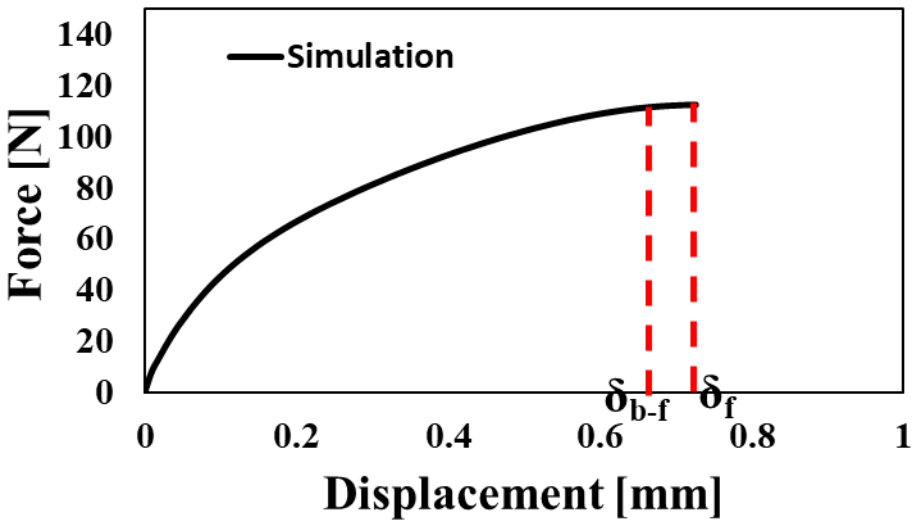

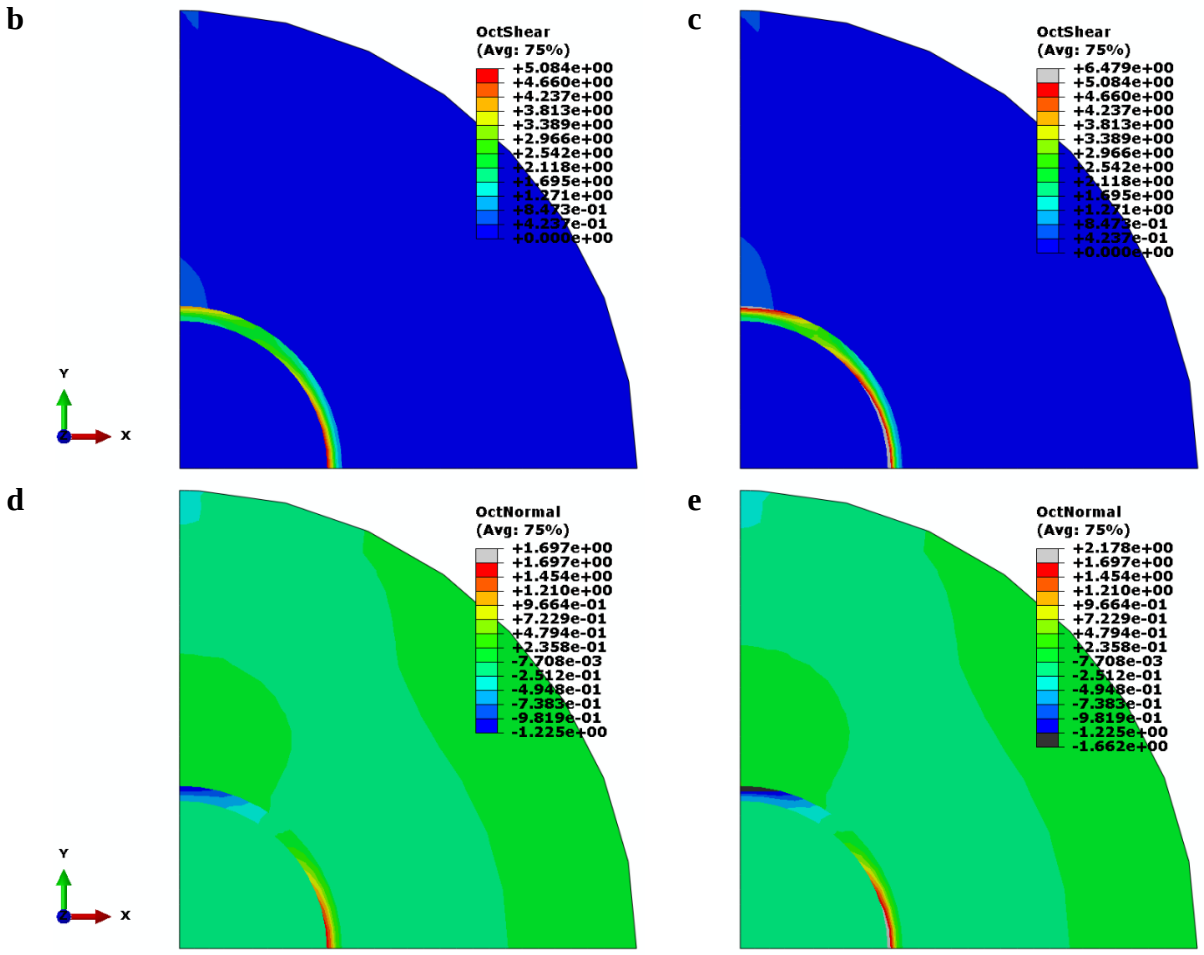

Figure 6.6: Failure analysis of the mineralized tissue - C1 adhesive interface at 3.5 mm/min loading rate: (a) Force-displacement relationship from the simulation ($\delta_{b\text{-}f}$: pre-failure displacement, δ_f: failure displacement), (b and c) Local volume change maps at pre-failure and failure, respectively and (d and e) Local distortion maps at pre-failure and failure, respectively.

The size of the failed locations was observed to shrink with the increasing loading rate. This observation was investigated by using the initial local failure. The maximum principal stress - maximum principal strain relationship (Figure 6.8) was obtained from the failure initiation location in the simulations (Figure 6.7). The local stress-strain relationship showed that the C1 hybrid layer failed at a stress of 3.13 MPa and a strain of 0.062 at 0.2 mm/min. It was predicted that C1 hybrid layer's failure was at a stress of 3.81 MPa and a strain of 0.077 when the interfacial specimen was

subject to a 1 mm/min loading rate. C1 hybrid layers' failure at the clinical loading rate was predicted at a stress of 5.38 MPa and a strain of 0.115. It was seen that the failure stress significantly increased at a 3.5 mm/min loading rate.

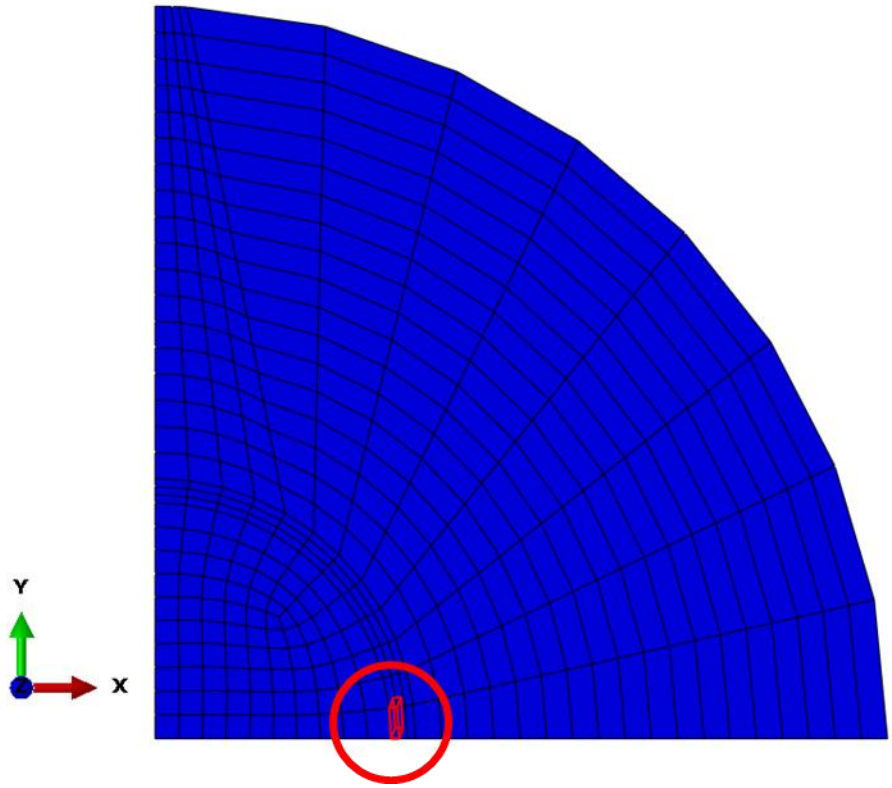

Figure 6.7: Failure initiation location in the interfacial specimen. The element that fails the first during the loading. This location is the same for all material pairs at all loading rates.

The areas under the stress-strain curves (I, II and III) were calculated to determine the C1 hybrid layer's toughness at each loading rates. These areas were considered up to the failure strains. Toughness of the C1 hybrid layer was predicted to be 0.14 MPa, 0.22 MPa and 0.48 MPa at the loading rates of 0.2 mm/min, 1 mm/min, and 3.5 mm/min, respectively. It was observed that C1 hybrid layer's toughness went up with the increasing loading rate.

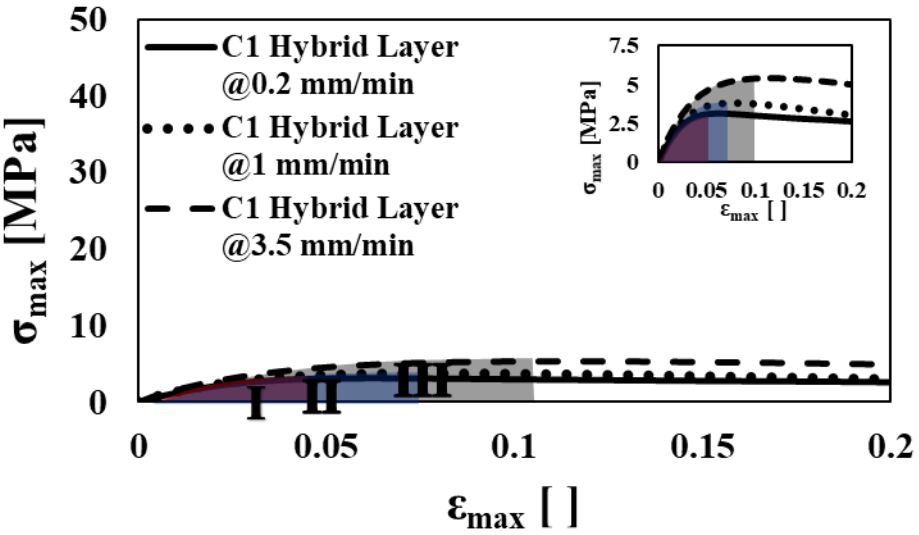

Figure 6.8: Stress-strain behavior of the C1 hybrid layer at failure initiation location at 0.2, 1 and 3.5 mm/min loading rates. Stress and strain values are presented in terms of maximum principal stress and maximum principal strain. I, II and III indicate the area under each curve up to the corresponding failure strain. The inset figure provides the same stress-strain relationship with a refined y-axis.

A uniaxial tensile simulation was performed by using the single patch test model, since the diametral compression test results in a mixed loading mode at the failure location. This simulation was conducted to reveal the true tensile nature of the C1 hybrid layer. After performing the simulation at loading rates of 0.2 mm/min, 1 mm/min and 3.5 mm/min, the stress-strain results were obtained (Figure 6.9). The C1 hybrid layer was predicted to fail at a stress of 3.42 MPa and a strain of 0.049 at 0.2 mm/min. At 1 mm/min, the predicted failure was at a stress of 5.18 MPa and a strain of 0.050. When the loading was 3.5 mm/min, C1 hybrid layer's failure stress was 10.41 MPa and its failure strain was 0.073. Moreover, C1 hybrid layer's uniaxial tensile toughness was predicted to be 0.12 MPa, 0.19 MPa and 0.54 MPa at 0.2 mm/min, 1 mm/min, and 3.5

mm/min, respectively. The uniaxial test simulation showed that the diametral compression test resulted in similar failure characteristics comparing to pure tensile behavior.

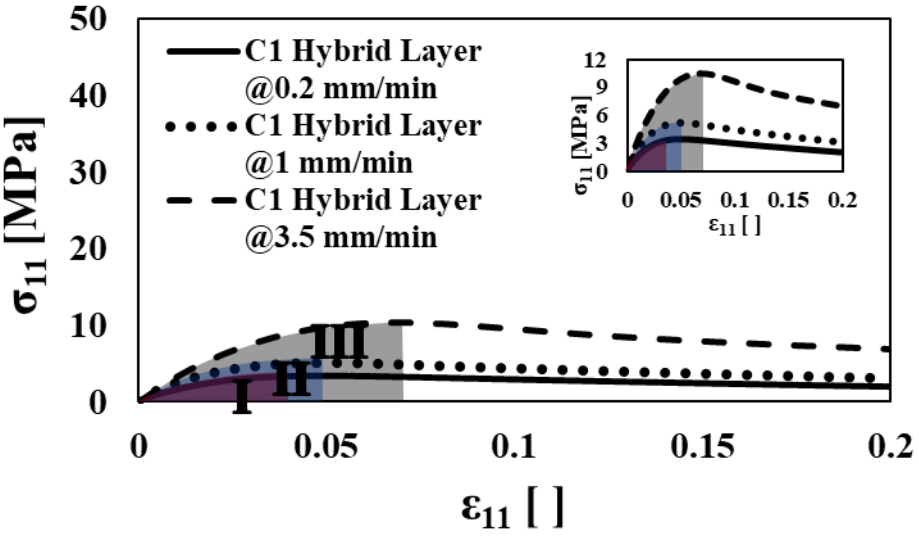

Figure 6.9: Stress-strain behavior of the C1 hybrid layer at uniaxial tensile loading at 0.2, 1 and 3.5 mm/min. I, II and III indicate the area under each curve up to the corresponding failure strain. The inset figure provides the same stress-strain relationship with a refined y-axis.

6.3.2 Mineralized Tissue – Experimental Adhesive (E1) Interface

The diametral compression test of the mineralized tissue – E1 interfacial specimen was simulated with the FE model prepared for the mineralized tissue – E1 interface. A simulation was run at 1 mm/min loading rate. The simulated force-displacement data was checked against the experimental mechanical behavior of a mineralized tissue – E1 interfacial specimen at 1 mm/min loading rate shown in Chapter 3 (Figure 6.10). This comparison suggested that the simulated and the experimental behavior matched. Thus, the selected set of material model parameters was

calibrated. The experiment read the failure force as 110.23 N and the failure displacement as 0.52 mm. In the simulation, the mineralized tissue – E1 interfacial specimen failed at a force of 107.06 N and a displacement of 0.57 mm.

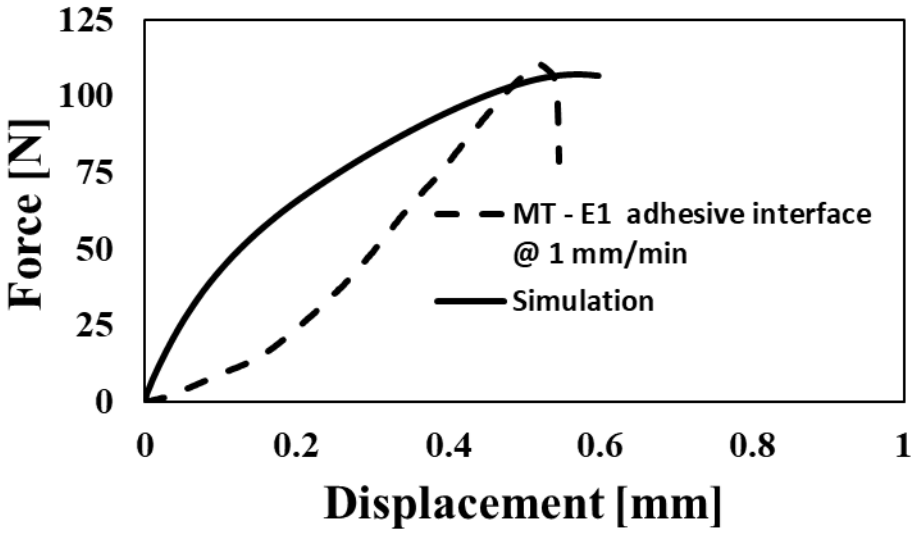

Figure 6.10: Calibration of the material model parameters for the mineralized tissue (MT) – E1 adhesive hybrid layer: Comparison of the simulated force-displacement relationship to the experimental force-displacement relationship of the mineralized tissue (MT) – E1 adhesive interface at 1 mm/min loading rate.

A second simulation was performed by keeping the material model parameters the same. A loading rate of 0.2 mm/min was applied. The simulated force-displacement relationship was compared to the experimental data of a mineralized tissue – E1 interfacial specimen presented in Chapter 3 (Figure 6.11). It was observed that the simulated behavior approximated the experimental data. This approximation showed that the calibrated material model parameters were validated to represent the E1 hybrid layer's rate dependent mechanical behavior. The mineralized tissue – E1

interfacial specimen failed at a force of 93.25 N and a displacement of 0.47 mm in the experiment. The simulation predicted that the failure was at a load of 89.82 N and a displacement of 0.41 mm.

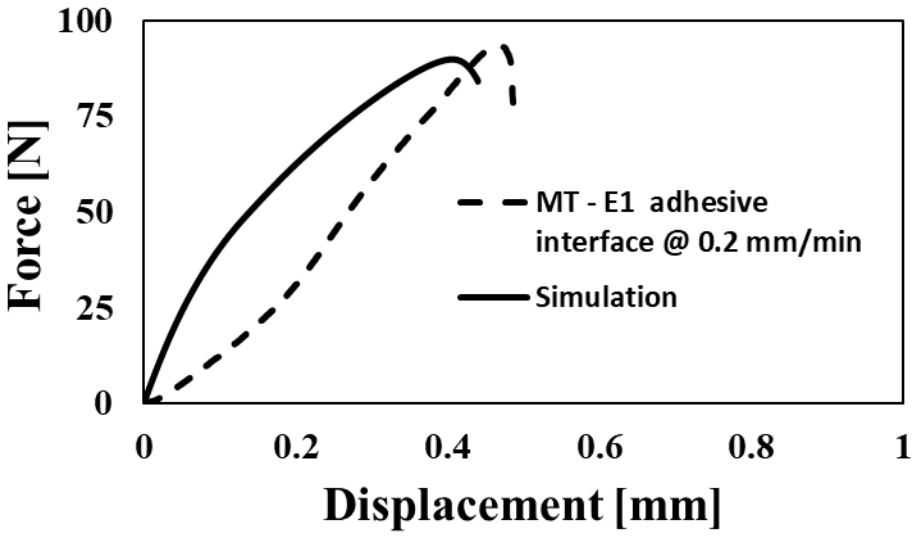

Figure 6.11: Validation of the material model parameters for the mineralized tissue (MT) – E1 adhesive hybrid layer: Comparison of the simulated force-displacement relationship to the experimental force-displacement relationship of the mineralized tissue (MT) – E1 adhesive interface at 0.2 mm/min loading rate.

The simulation results at 1 mm/min were post-processed to create the local distortion and volume change maps. These maps were compared to a mineralized tissue – E1 interfacial specimen's failure pattern at 1 mm/min loading rate presented in Chapter 3 (Figure 6.12(a)). The local distortion and volume change maps were thresholded at a displacement close to the failure (δ_f) (Figure 6.12(c) and Figure 6.12(e)). A post-failure displacement ($\delta_{p\text{-}f}$) was selected 0.05 mm far from δ_f (Figure 6.12(b)). When the maps progressed to $\delta_{p\text{-}f}$, a grey and a black color appeared to show the failed locations (Figure 6.12(d) and Figure 6.12(f)). The failure pattern was initiated at

the interface along the transverse axis to the loading in the mechanical test. The simulation suggested an initial failure location at the same location. Moreover, this failure location was predicted to be between the hybrid layer and the E1 polymer. The simulation also suggested a subsequent failure location at the interface along the loading axis. This failure location was found between the mineralized tissue and the hybrid layer. The initial failure location experienced dilatational behavior (grey colored) and the subsequent location was under contraction (black colored) in the volume change map. The mineralized tissue next to the subsequent location was predicted to undergo dilatational volume change along the loading axis. This volume change zone was predicted to be smaller than the mineralized tissue – C1 interfacial specimen at 1 mm/min. In general, the size of the failed locations was appeared similar to the mineralized tissue – C1 interfacial specimen at a 1 mm/min loading rate.

a

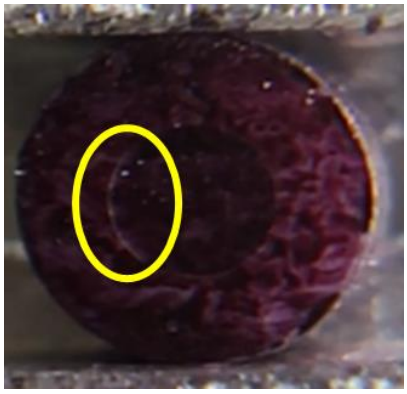

b

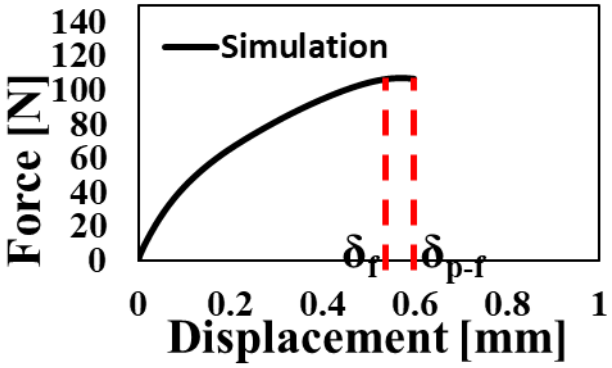

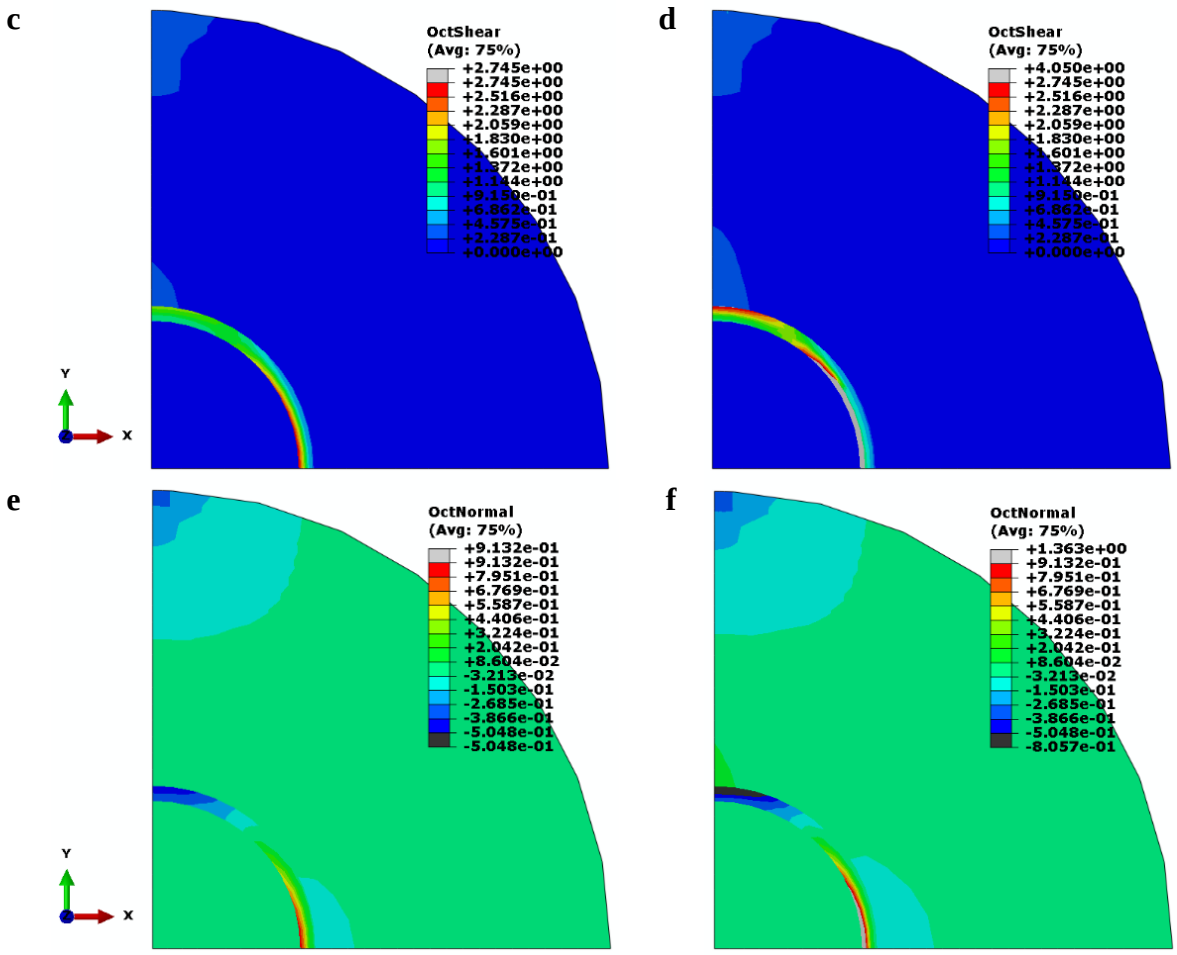

Figure 6.12: Failure analysis of the mineralized tissue - E1 adhesive interface at 1 mm/min loading rate: (a) Post-failure snapshot from the experiment, (b) Force-displacement relationship from the simulation (δ_f: failure displacement, $\delta_{p\text{-}f}$: post-failure displacement), (c and d) Local volume change maps at failure and post-failure, respectively and (e and f) Local distortion maps at failure and post-failure, respectively.

A similar analysis was done by using the FE results at a 0.2 mm/min loading rate. The simulated force-displacement data was used to determine a displacement close to the failure (δ_f). The color bars of local distortion and local volume change maps were fixed at δ_f (Figure 6.13(c) and Figure 6.13(e)). A displacement of 0.05 mm was added to δ_f to find a post-failure displacement ($\delta_{p\text{-}f}$)

(Figure 6.13(b)). The distortion and volume change maps were advanced to $\delta_{p\text{-}f}$ (Figure 6.13(d) and Figure 6.13(f)). A grey and a black color appeared on the post-failure maps. The grey colored zones indicated the failed locations in distortion maps. The created local distortion and volume change maps were compared to the experimental failure snapshot of a mineralized tissue – E1 adhesive interfacial specimen at 0.2 mm/min presented in Chapter 3 (Figure 6.13(a)). The failure in the experiment was observed at the interface along the transverse axis to the load axis. The simulation predicted the initial failure at the same location as the experiment. This prediction also suggested that this failure was between the E1 polymer and the hybrid layer. Furthermore, the simulation suggested a subsequent failure location. This failure location was seen at the interface along the load axis. It is also predicted that this failure was between the mineralized tissue and the hybrid layer. Moreover, the initial failure was found in dilatation mode (grey colored) and the subsequent failure was in contraction (black colored). It was also observed that the mineralized tissue grew higher dilatational volume change above the second failure location along the loading axis. This dilatational zone was found smaller than the mineralized tissue – C1 interfacial specimen at the same loading rate. The overall size of the failure locations was found similar to the mineralized tissue – C1 interfacial specimen.

a

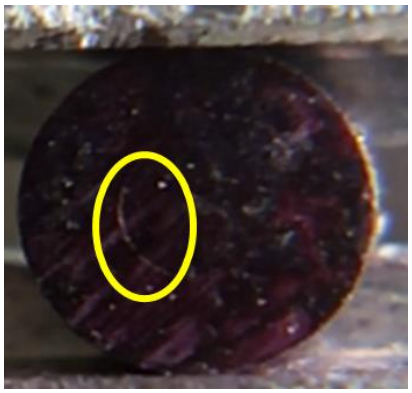

b

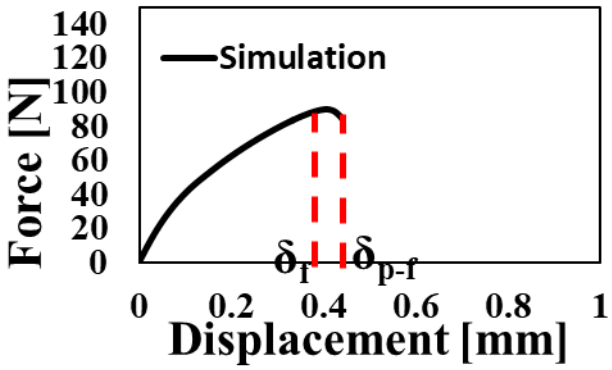

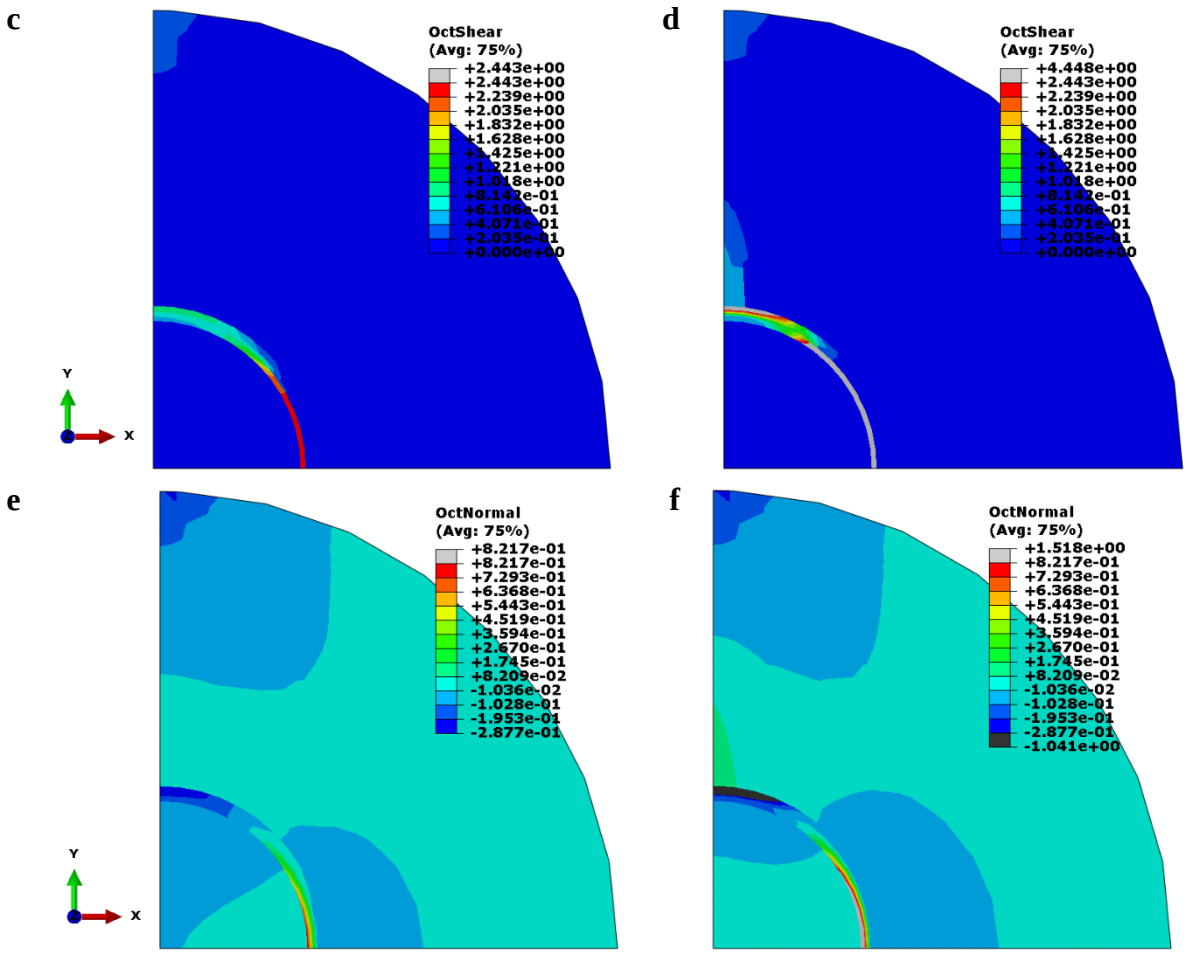

Figure 6.13: Failure analysis of the mineralized tissue - E1 adhesive interface at 0.2 mm/min loading rate: (a) Post-failure snapshot from the experiment, (b) Force-displacement relationship from the simulation (δ_f: failure displacement, $\delta_{p\text{-}f}$: post-failure displacement), (c and d) Local volume change maps at failure and post-failure, respectively and (e and f) Local distortion maps at failure and post-failure, respectively.

The calibrated and validated material model parameters of the E1 hybrid layer was used to simulate the mechanical behavior of the mineralized tissue – E1 interfacial specimen at the clinical loading rate of 3.5 mm/min. The simulated results predicted that this interfacial specimen's failure load is 134.31 N and its failure displacement is 0.77 mm (Figure 6.14(a)). Since the specimen fails without a post-peak softening, the generated local distortion and volume change maps were fixed at a

displacement close to failure ($\delta_{b\text{-}f}$) (Figure 6.14(b) and Figure 6.14(d)). A displacement of 0.05 mm was kept between $\delta_{b\text{-}f}$ and the failure displacement (δ_f) (Figure 6.14(c) and Figure 6.14(e)). The grey colored locations in the distortion map suggested the failed locations. The initial failure was observed mainly at the interface along the transverse axis to the loading axis. A small subsequent failure was also observed at the interface along the loading axis. The initial failure exhibits dilatational behavior (grey colored) and the subsequent failure is under contraction (black colored) in the volume change map. The overall failed locations were predicted to be smaller than the mineralized tissue – C1 interfacial specimen.

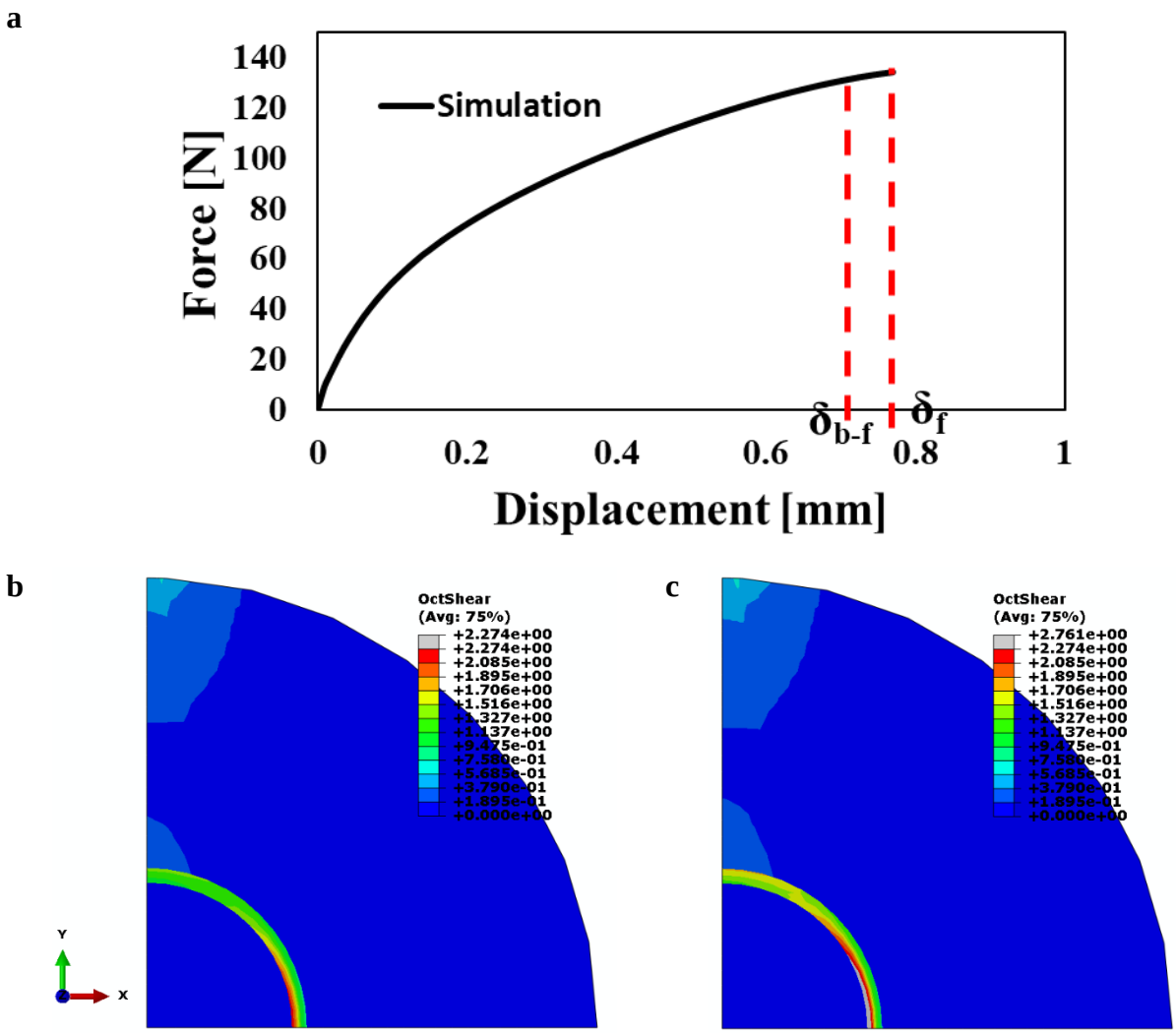

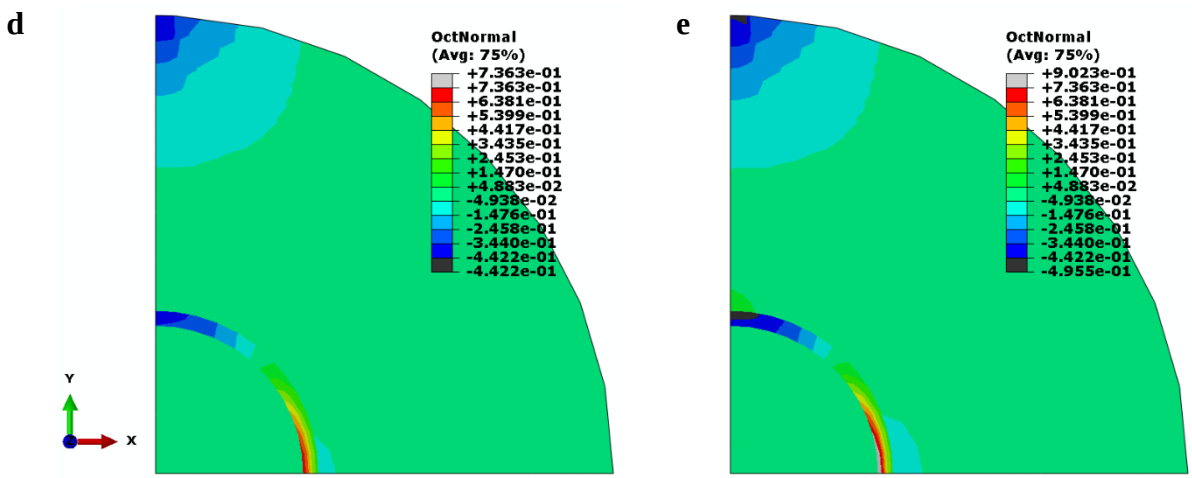

Figure 6.14: Failure analysis of the mineralized tissue - E1 adhesive interface at 3.5 mm/min loading rate: (a) Force-displacement relationship from the simulation ($\delta_{b\text{-}f}$: pre-failure displacement, δ_f: failure displacement), (b and c) Local volume change maps at pre-failure and failure, respectively and (d and e) Local distortion maps at pre-failure and failure, respectively.

The rate dependent failure of the mineralized tissue – E1 specimens were investigated by obtaining the maximum principal stress and strain relationships at the initial failure location (Figure 6.7) in the simulations. These local stress-strain relationships (Figure 6.15) suggested that the E1 hybrid layer failed at a stress of 5.08 MPa and a strain of 0.047 at 0.2 mm/min. The E1 hybrid layer had a failure stress of 6.95 MPa and a failure strain of 0.071 when the loading rate was 1 mm/min. Moreover, the hybrid layer failed at a stress of 10.20 MPa and a strain of 0.108 at 3.5 mm/min. The areas under each curve up to their failure represent the toughness (I, II and III). Toughness of the E1 hybrid layer was computed to be 0.20 MPa, 0.40 MPa and 1.09 MPa at loading rates of 0.2 mm/min, 1 mm/min and 3.5 mm/min, respectively. Toughness of the E1 hybrid layer was found significantly higher than the C1 hybrid layer at all loading rates.

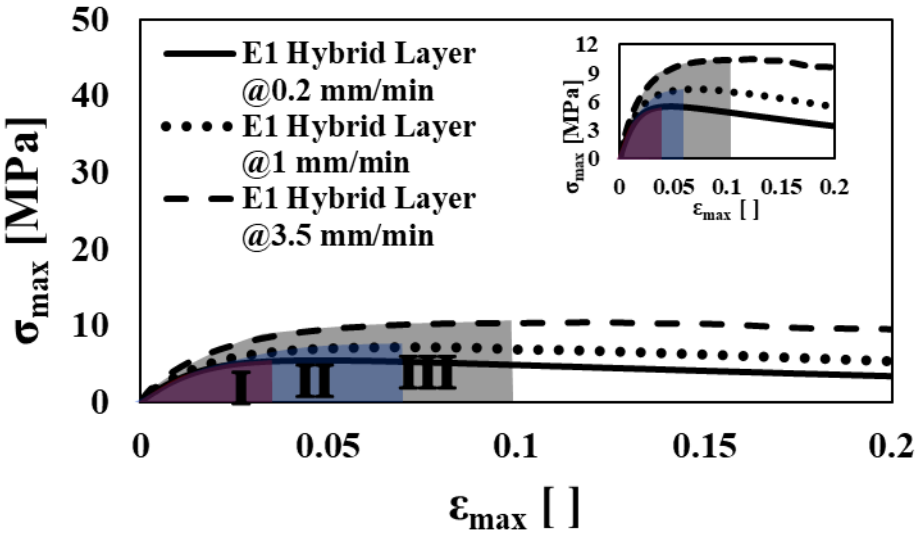

Figure 6.15: Stress-strain behavior of the E1 hybrid layer at failure initiation location at 0.2, 1 and 3.5 mm/min loading rates. Stress and strain values are presented in terms of maximum principal stress and maximum principal strain. I, II and III indicate the area under each curve up to the corresponding failure strain. The inset figure provides the same stress-strain relationship with a refined y-axis.

The calibrated and validated material model parameters for the E1 hybrid layer were used in a single patch test. Uniaxial tensile test simulations were performed at 0.2 mm/min, 1 mm/min and 3.5 mm/min loading rates. These simulations were created to evaluate the true tensile nature of the E1 hybrid layer (Figure 6.16). The E1 hybrid layer failed at a stress of 7.91 MPa and a strain of 0.028 at 0.2 mm/min. The failure at 1 mm/min was predicted at a stress of 18.53 MPa and a strain of 0.038 at 1 mm/min. When the loading rate was 3.5 mm/min, E1 hybrid layer had a failure stress of 44.64 MPa and a failure strain of 0.073. Moreover, the toughness at each loading rate was calculated from the areas I, II and III. E1 hybrid layer's toughness under uniaxial tensile mode was predicted to be 0.16 MPa, 0.50 MPa and 2.24 MPa at 0.2 mm/min, 1 mm/min and 3.5 mm/min loading rates, respectively. These results suggested that the diametral compression test provided

reasonable results for the tensile nature at 0.2 mm/min and 1 mm/min. It was seen that the predicted clinical uniaxial tensile performance is significantly higher than the interfacial diametral compression test simulations. E1 hybrid layer's uniaxial tensile mechanical performance was predicted to be superior to the C1 hybrid layer at all loading rates.

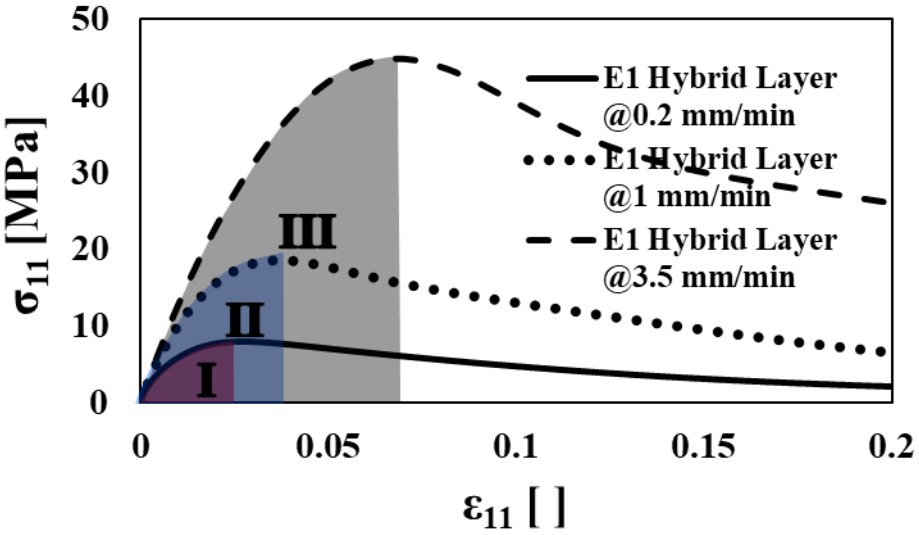

Figure 6.16: Stress-strain behavior of the E1 hybrid layer at 0.2, 1 and 3.5 mm/min. I, II and III indicate the area under each curve up to the corresponding failure strain.

6.3.3 Mineralized Tissue – Experimental Adhesive (E1) Interface with Remineralized and Weakened Hybrid Layer

In this section, the FE model of the mineralized tissue – E1 interface was used to simulate the interfacial specimen's mechanical behavior under two different considerations. These considerations are the remineralization and the degradation at the E1 hybrid layer. The mineralization is known to increase the hybrid layer's strength whereas the degradation weakens

the hybrid layer [119]. The material model parameters of the E1 hybrid layer were modified to investigate these two aspects. The micro-scale normal and shear stiffness parameters of the E1 hybrid layer were assumed to increase by 10% to represent the remineralized E1 hybrid layer. Moreover, the micro-scale normal and shear stiffnesses of the E1 hybrid layer were assumed to decrease by 10% to model the weakened E1 hybrid layer. The force-displacement relationships were obtained from each hybrid layer's diametral compression test simulations. These relationships were compared to the behavior of the E1 hybrid layer (Figure 6.17). It was observed that the remineralization significantly increased the failure load of the hybrid layer at 0.2 mm/min. The degradation significantly decreased the failure load of the hybrid layer at 0.2 mm/min. At the higher loading rates, it was observed that the behaviors under remineralization and degradation were almost the same as the normal interfacial specimen.

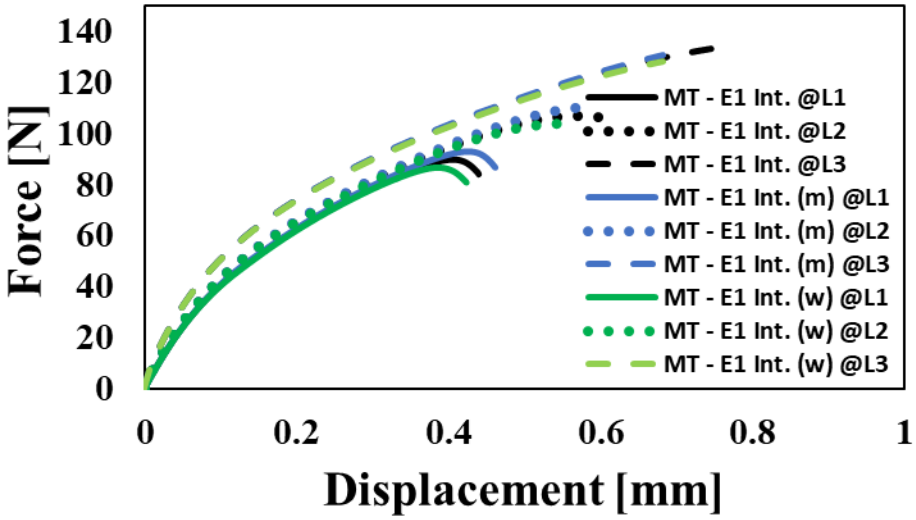

Figure 6.17: Force-displacement relationships from simulations: The mineralized tissue – E1 adhesive interface (MT – E1 Int.) is compared to the mineralized tissue – E1 adhesive interface with the remineralized hybrid layer (MT – E1 Int. (m)) and the mineralized tissue – E1 adhesive

interface with the weakened hybrid layer (MT – E1 Int. (w)) at loading rates of L1 = 0.2 mm/min, L2 = 1 mm/min and L3 = 3.5 mm/min. (m: remineralized and w: weakened)

These simulated results were post-processed to generate the local distortion and local volume change maps. The color bars of these maps at 0.2 mm/min were fixed at a displacement close to the failure (δ_f) (Figure 6.18(b), Figure 6.18(d), Figure 6.19(b) and Figure 6.19(d)). A post-failure displacement ($\delta_{p\text{-}f}$) was found by adding a displacement of 0.05 mm to δ_f (Figure 6.18(a) and Figure 6.19(a)). The post-failure local distortion and volume change maps were presented at $\delta_{p\text{-}f}$ (Figure 6.18(c), Figure 6.18(e), Figure 6.19(c) and Figure 6.19(e)). The grey colored areas in the distortion maps suggested the failure locations. The failure locations were found similar to each other in the simulations with the E1 hybrid layer, the mineralized E1 hybrid layer and the weakened hybrid layer. In all the simulations, the initial failure was predicted to be at the interface along the transverse axis to the loading axis. Moreover, a second failure was observed at the interface along the loading axis. The initial failure underwent a dilatiation (grey colored) in volume change maps. The second failure was found in contraction (black colored) in volume change. The mineralized tissue was observed to experience dilatation next to the second failure along the loading axis.

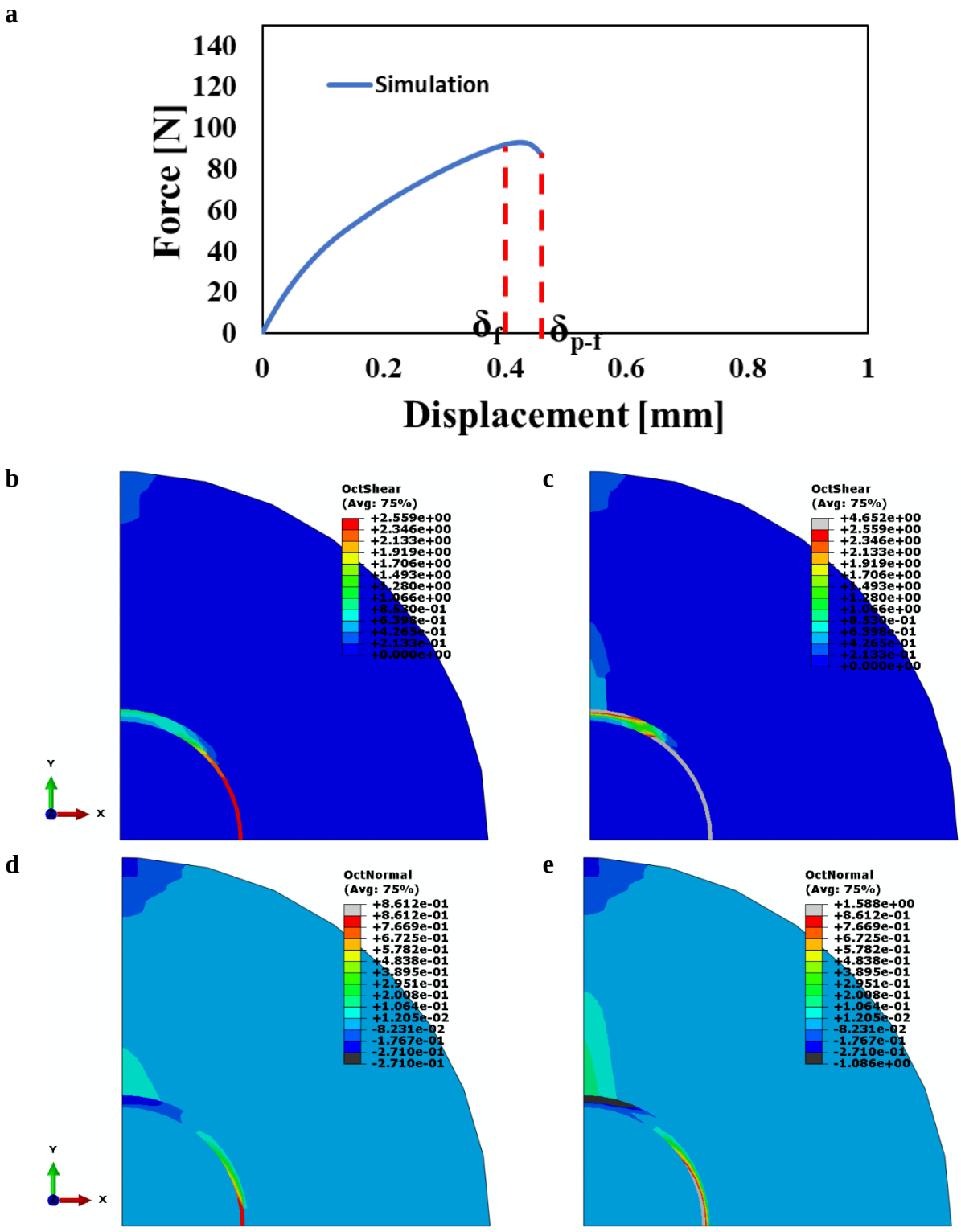

Figure 6.18: Failure analysis of the mineralized tissue – E1 adhesive interface with the remineralized hybrid layer at 0.2 mm/min loading rate: (a) Force-displacement relationship from

the simulation (δ_f: failure displacement, δ_{p-f}: post-failure displacement), (b and c) Local volume change maps at failure and post-failure, respectively and (d and e) Local distortion maps at failure and post-failure, respectively.

a

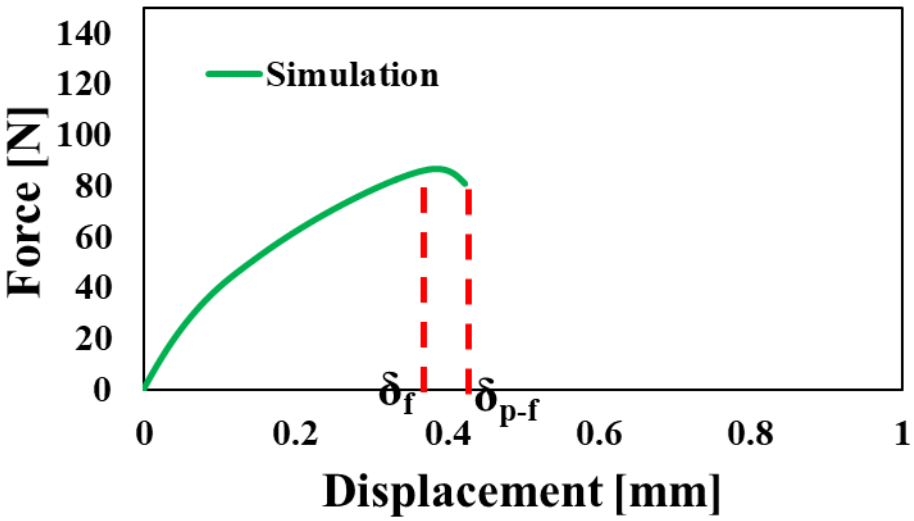

b

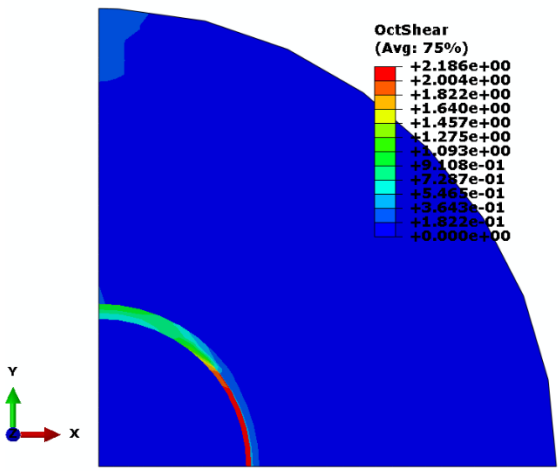

c

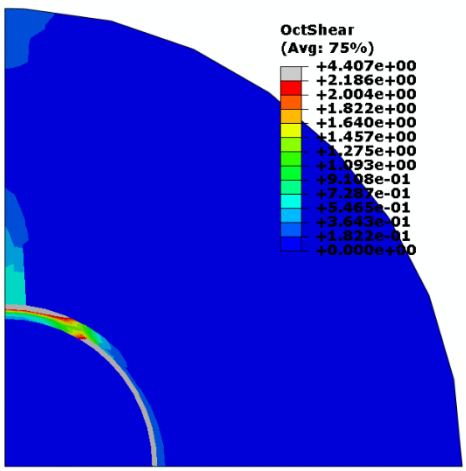

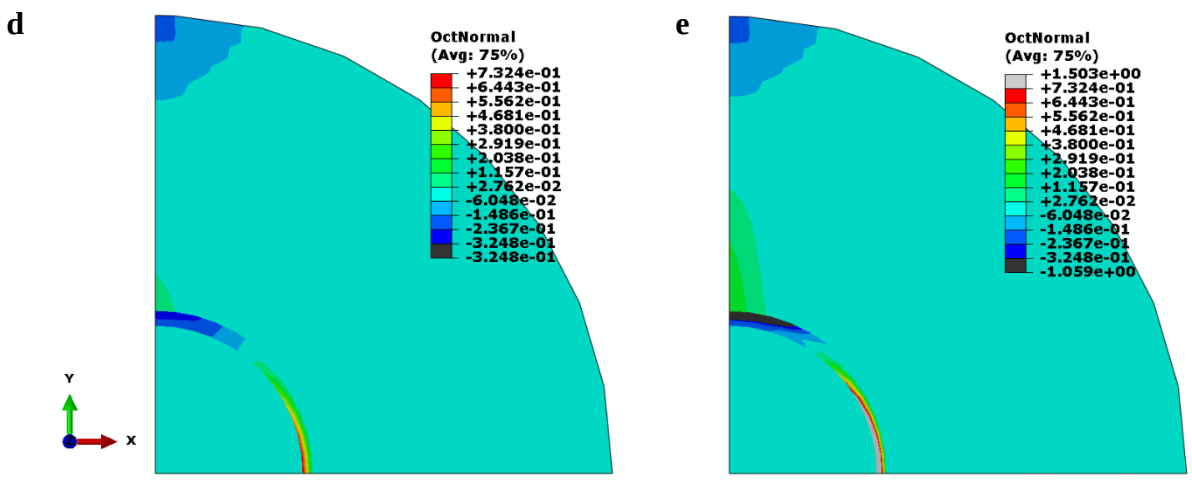

Figure 6.19: Failure analysis of the mineralized tissue – E1 adhesive interface with the weakened hybrid layer at 0.2 mm/min loading rate: (a) Force-displacement relationship from the simulation (δ_f: failure displacement, $\delta_{p\text{-}f}$: post-failure displacement), (b and c) Local volume change maps at failure and post-failure, respectively and (d and e) Local distortion maps at failure and post-failure, respectively.

The local failure and volume change maps at 1 mm/min were fixed at a displacement close to the failure ($\delta_{b\text{-}f}$) (Figure 6.20(b), Figure 6.20(d), Figure 6.21(b) and Figure 6.21(d)). A displacement of 0.05 mm was maintained between $\delta_{b\text{-}f}$ and the failure displacement (δ_f) (Figure 6.20(a) and Figure 6.21(a)). The post-failure maps were shown at δ_f (Figure 6.20(c), Figure 6.20(e), Figure 6.21(c) and Figure 6.21(e)). In local distortion maps, grey areas showed the failure locations. Similar failure patterns were observed for the E1 hybrid layer, the mineralized E1 hybrid layer and the weakened hybrid layer. The failure was initated at the interface along the transverse axis to the load axis. A subsequent failure was observed at the interface along the load axis. The initial failure was predicted to exhibit dilatational (grey colored) volume change. Moreover, the second failure was predicted to experience contraction (black colored).

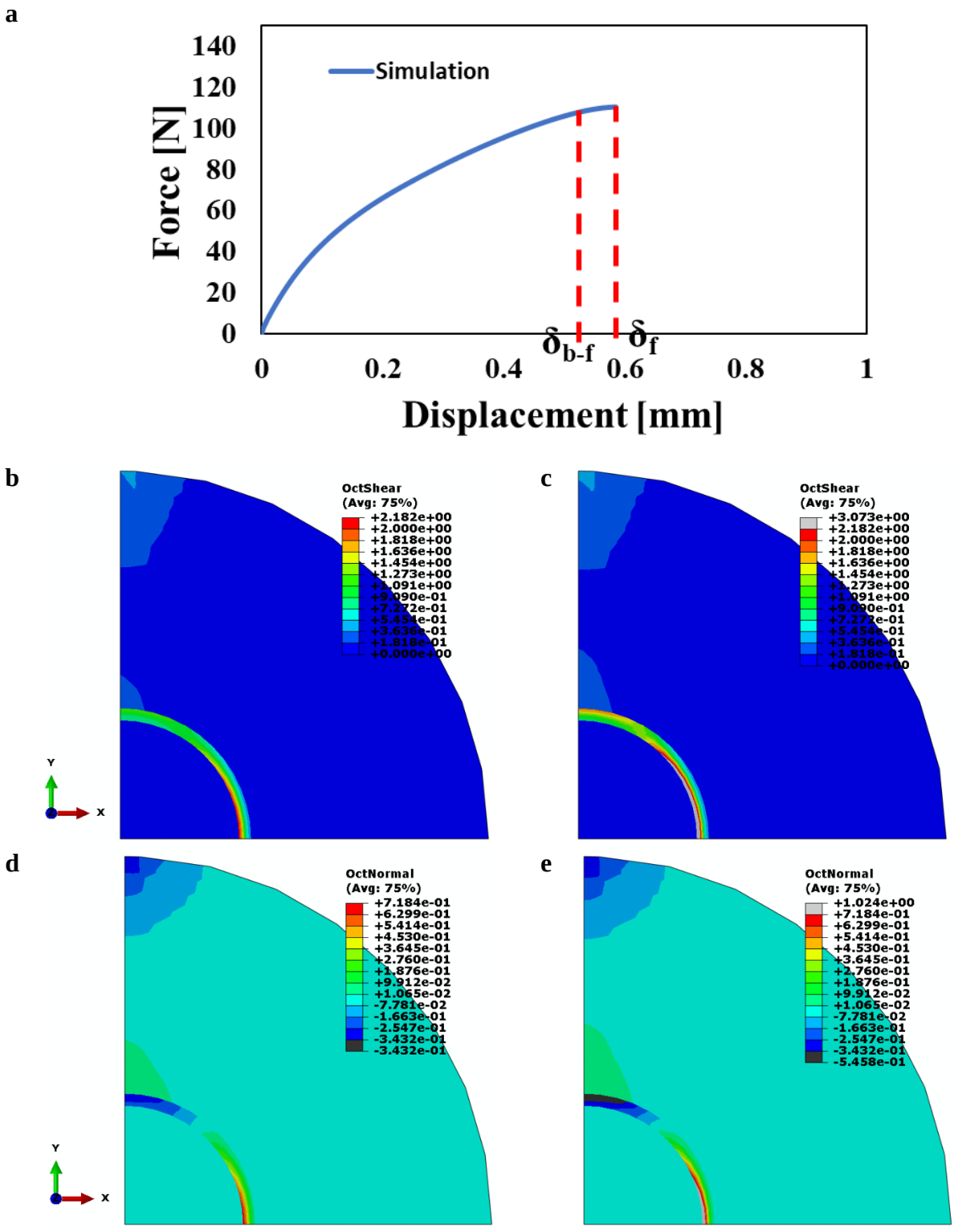

Figure 6.20: Failure analysis of the mineralized tissue – E1 adhesive interface with the remineralized hybrid layer at 1 mm/min loading rate: (a) Force-displacement relationship from

the simulation (δ_{b-f}: pre-failure displacement, δ_f: failure displacement), (b and c) Local volume change maps at pre-failure and failure, respectively and (d and e) Local distortion maps at pre-failure and failure, respectively.

a

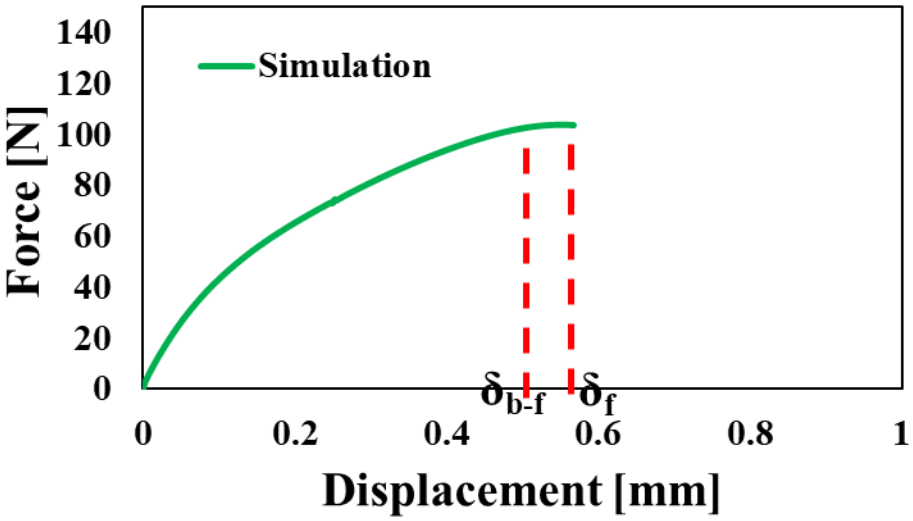

b

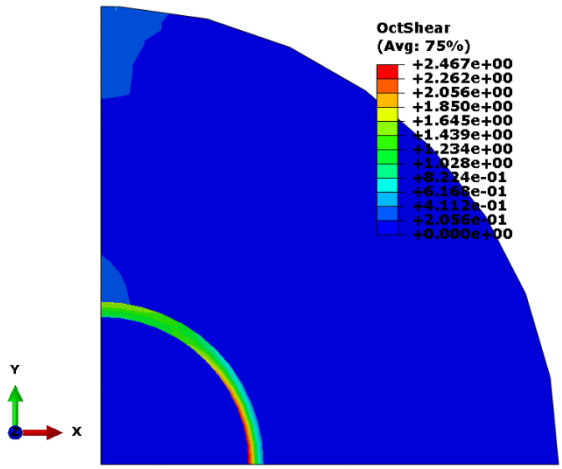

c

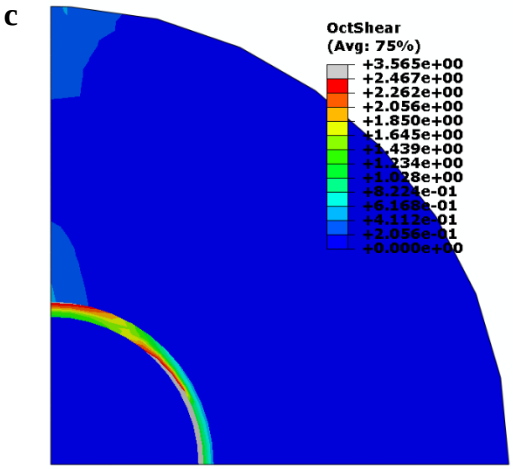

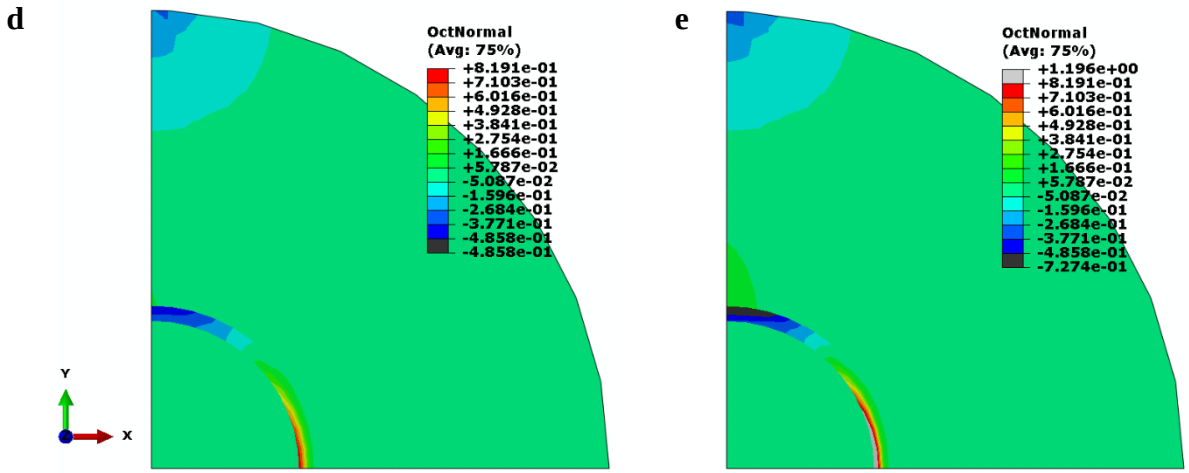

Figure 6.21: Failure analysis of the mineralized tissue – E1 adhesive interface with the weakened hybrid layer at 1 mm/min loading rate: (a) Force-displacement relationship from the simulation ($\delta_{b\text{-}f}$: pre-failure displacement, δ_f: post-failure displacement), (b and c) Local volume change maps at pre-failure and failure, respectively and (d and e) Local distortion maps at pre-failure and failure, respectively.

Local failure and volume change distributions were obtained from the simulations at the clinical loading rate of 3.5 mm/min. These distributions were thresholded at a displacement close to the failure ($\delta_{b\text{-}f}$) (Figure 6.22(b), Figure 6.22(d), Figure 6.23(b) and Figure 6.23(d)). $\delta_{b\text{-}f}$ was selected 0.05 mm before the failure displacement (δ_f) (Figure 6.22(a) and Figure 6.23(a)). The post-failure distributions were presented at δ_f (Figure 6.22(c), Figure 6.22(e), Figure 6.23(c) and Figure 6.23(e)). The local distortion distributions suggested that grey are the failure locations. The simulations resulted in similar failure patterns for the E1 hybrid layer, the remineralized E1 hybrid layer and the weakened hybrid layer. In detail, initial failure was at the interface along the transverse axis to the loading axis. Afterward, a second failure appeared at the interface along the loading axis. The volume change distributions revealed that the initial failure was in dilatational mode (grey colored) and the second failure was in contraction (black colored).

a

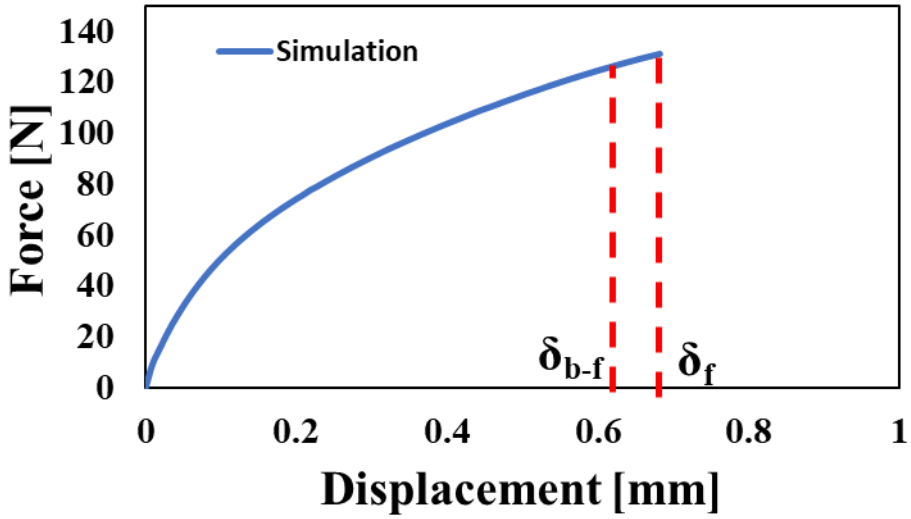
Simulation
Force [N]
140
120
100
80
60
40
20
0
0
0.2
0.4
0.6
0.8
1
Displacement [mm]
δb-f
δf

b

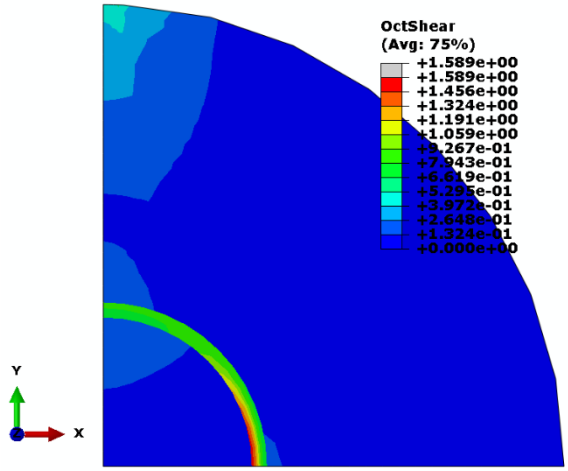
OctShear
(Avg: 75%)
+1.589e+00
+1.589e+00
+1.456e+00
+1.324e+00
+1.191e+00
+1.059e+00
+9.267e-01
+7.943e-01
+6.619e-01
+5.295e-01
+3.972e-01
+2.648e-01
+1.324e-01
+0.000e+00
Y
X

c

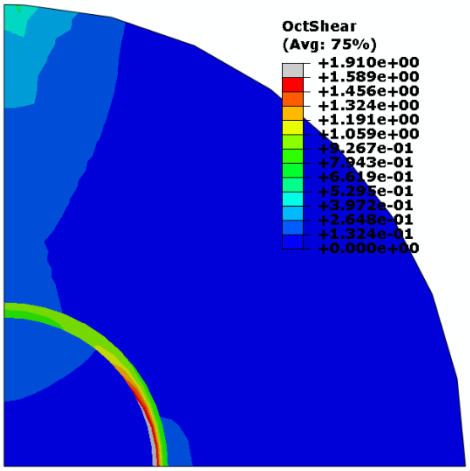
OctShear
(Avg: 75%)
+1.910e+00
+1.589e+00
+1.456e+00
+1.324e+00
+1.191e+00
+1.059e+00
+9.267e-01
+7.943e-01
+6.619e-01
+5.295e-01
+3.972e-01
+2.648e-01
+1.324e-01
+0.000e+00

d

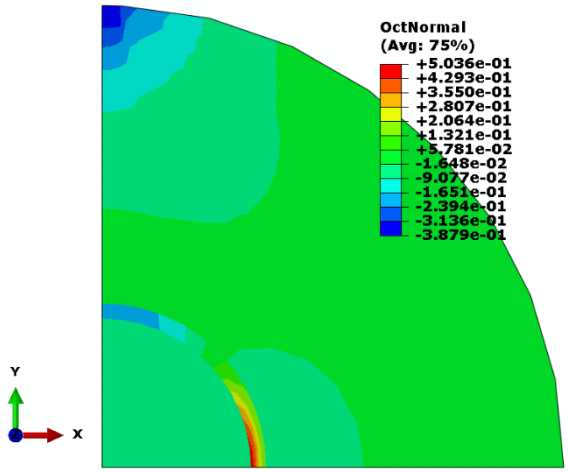
OctNormal
(Avg: 75%)
+5.036e-01
+4.293e-01
+3.550e-01
+2.807e-01
+2.064e-01
+1.321e-01
+5.781e-02
-1.648e-02
-9.077e-02
-1.651e-01
-2.394e-01
-3.136e-01
-3.879e-01
Y
X

e

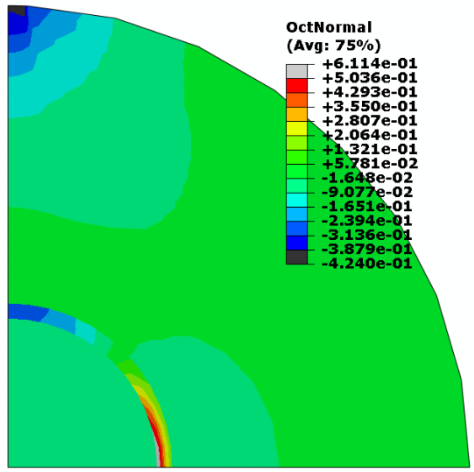
OctNormal
(Avg: 75%)
+6.114e-01
+5.036e-01
+4.293e-01
+3.550e-01
+2.807e-01
+2.064e-01
+1.321e-01
+5.781e-02
-1.648e-02
-9.077e-02
-1.651e-01
-2.394e-01
-3.136e-01
-3.879e-01
-4.240e-01

Figure 6.22: Failure analysis of the mineralized tissue – E1 adhesive interface with remineralized hybrid layer at 3.5 mm/min loading rate: (a) Force-displacement relationship from the simulation ($\delta_{b\text{-}f}$: pre-failure displacement, δ_f: failure displacement), (b and c) Local volume change maps at pre-failure and failure, respectively and (d and e) Local distortion maps at pre-failure and failure, respectively.

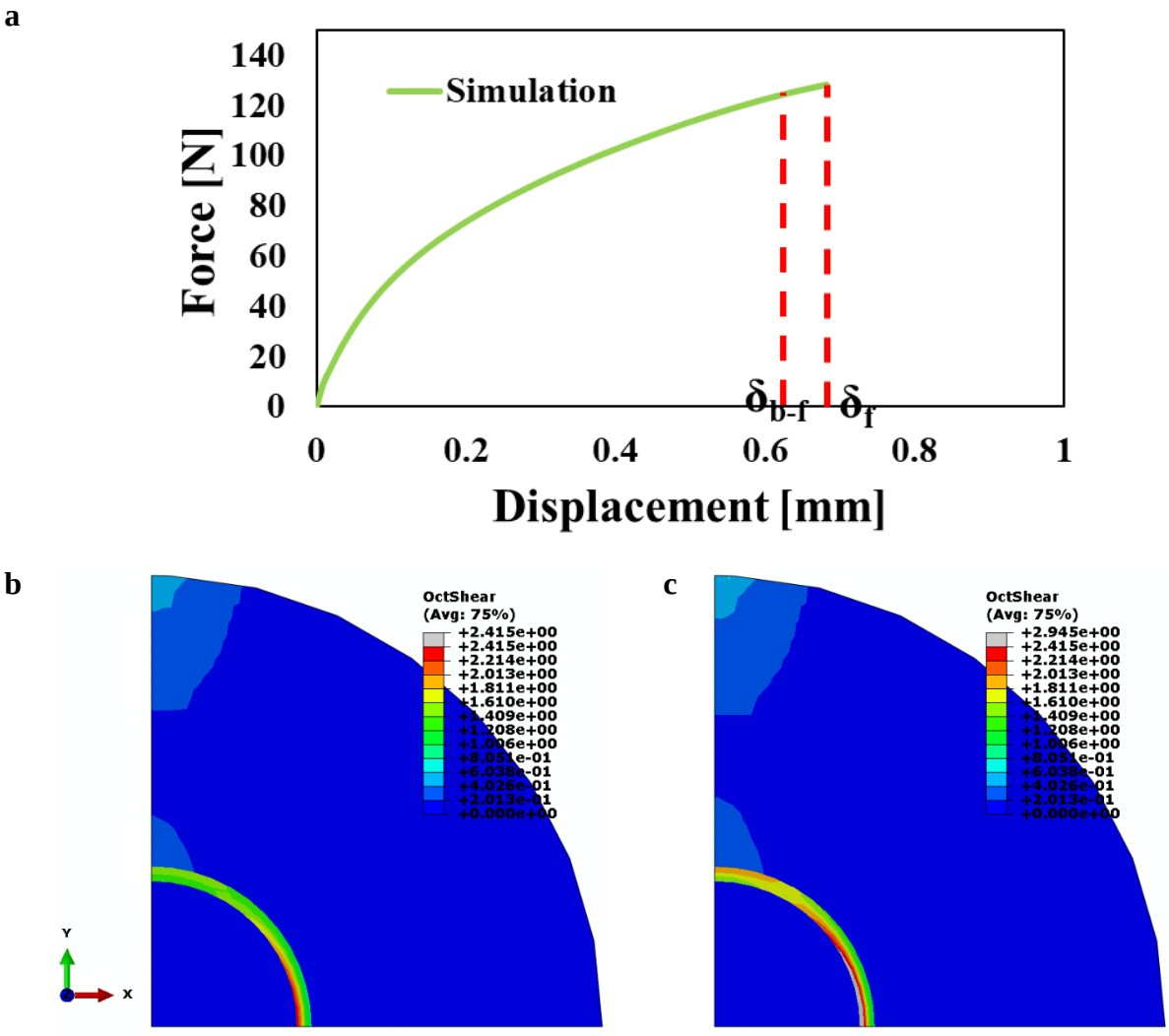

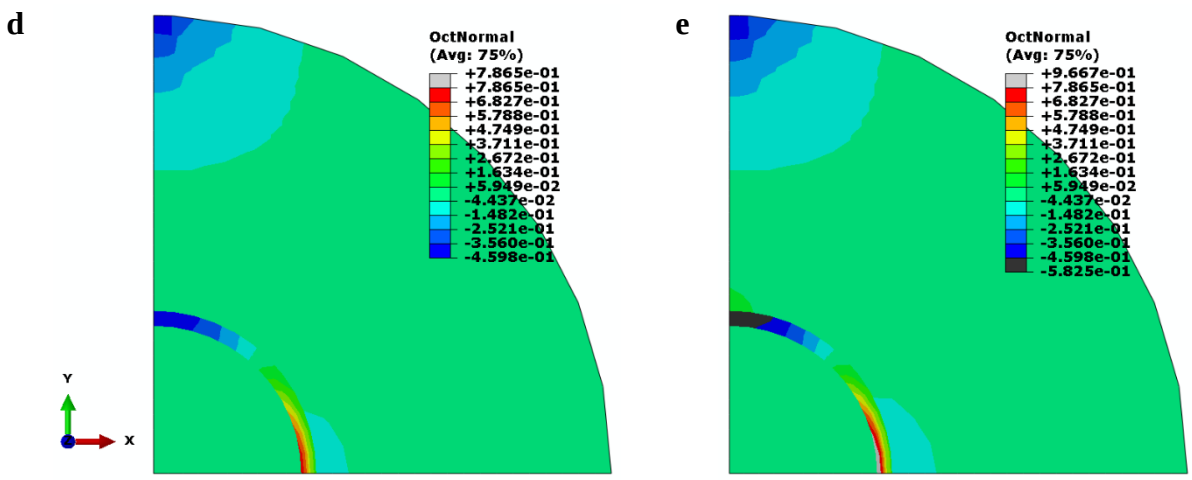

Figure 6.23: Failure analysis of the mineralized tissue – E1 adhesive interface with weakened hybrid layer at 3.5 mm/min loading rate: (a) Force-displacement relationship from the simulation ($\delta_{b\text{-}f}$: pre-failure displacement, δ_f: failure displacement), (b and c) Local volume change maps at pre-failure and failure, respectively and (d and e) Local distortion maps at pre-failure and failure, respectively.

The local failure in these simulations was investigated by deriving their maximum principal stress and strain relationship at the failure initiation elements at all loading rates. The local stress-strain relationships showed that failure stress and strain were almost the same in both the mineralized and weakened hybrid layers (Figure 6.24 and Figure 6.25). Moreover, the toughness was computed from areas I, II and III. The remineralized hybrid layer has the toughness of 0.22 MPa, 0.43 MPa and 0.94 MPa at 0.2 mm/min, 1 mm/min and 3.5 mm/min, respectively. The weakened hybrid layer's toughness was predicted 0.18 MPa, 0.39 MPa and 0.90 MPa at 0.2 mm/min, 1 mm/min and 3.5 mm/min, respectively. These data showed that the hybrid layer's behavior was similar to each other under the normal, remineralized and weakening conditions.

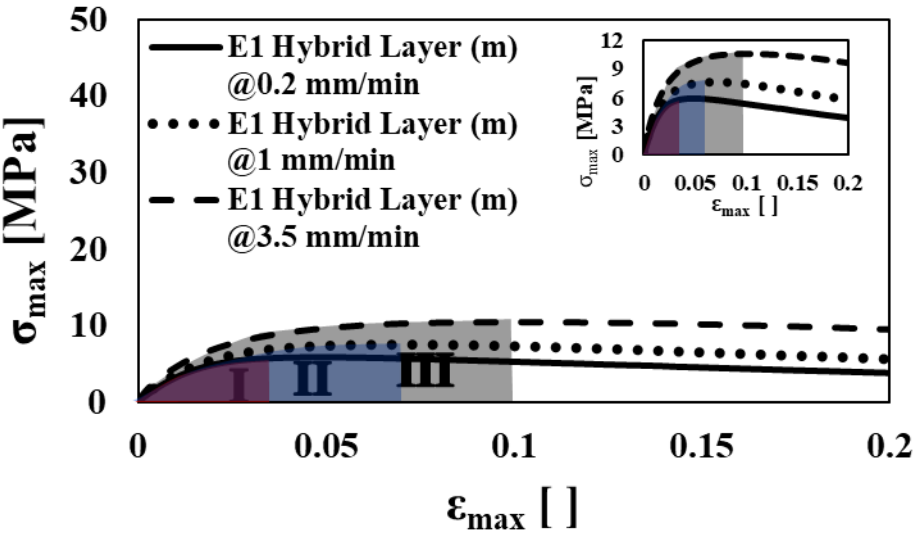

Figure 6.24: Stress-strain behavior of the remineralized E1 hybrid layer at failure initiation location at 0.2, 1 and 3.5 mm/min loading rates. Stress and strain values are presented in terms of maximum principal stress and maximum principal strain. I, II and III indicate the area under each curve up to the corresponding failure strain. The inset figure provides the same stress-strain relationship with a refined y-axis. (m: remineralized)

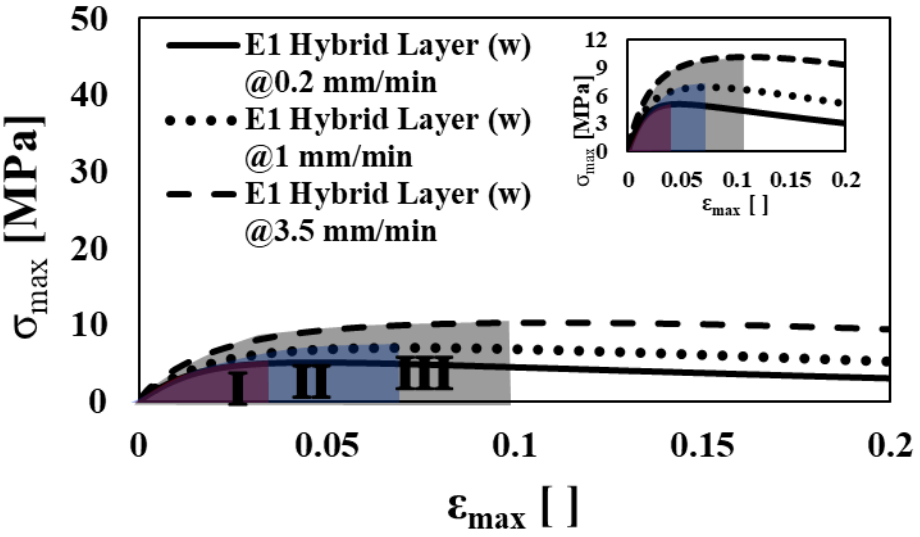

Figure 6.25: Stress-strain behavior of the weakened E1 hybrid layer at failure initiation location at 0.2, 1 and 3.5 mm/min loading rates. Stress and strain values are presented in terms of maximum principal stress and maximum principal strain. I, II and III indicate the area under

each curve up to the corresponding failure strain. The inset figure provides the same stress-strain relationship with a refined y-axis. (w: weakened)

The uniaxial tensile behavior of the remineralized E1 hybrid layer and the weakened E1 hybrid layer were simulated by using the single patch test model. These simulations were performed at 0.2 mm/min, 1 mm/min and 3.5 mm/min loading rates. The simulations revealed the tensile nature difference due to remineralization and degradation (Figure 6.26 and Figure 6.27). The remineralized hybrid layer was predicted to fail at a failure stress of 8.42 MPa, 19.22 MPa and 46.23 MPa and a failure strain of 0.027, 0.035 and 0.064 at 0.2 mm/min, 1 mm/min and 3.5 mm/min loading rates, respectively. The weakened hybrid layer had a failure stress of 7.40 MPa, 17.80 MPa and 43.25 MPa, and a failure strain of 0.028, 0.036 and 0.073 at loading rates of 0.2 mm/min, 1 mm/min and 3.5 mm/min, respectively. Moreover, these hybrid layer's toughness was computed from the areas I, II and III. Toughness of the remineralized hybrid layer was 0.17 MPa, 0.47 MPa and 1.94 MPa at 0.2 mm/min, 1 mm/min and 3.5 mm/min, respectively. The simulations suggested that the weakened hybrid layer had the toughness of 0.15 MPa, 0.47 MPa and 2.11 MPa at loading rates of 0.2 mm/min, 1 mm/min and 3.5 mm/min, respectively. These simulated data predicted a slight increase in the E1 hybrid layer's mechanical performance in the remineralization condition. Moreover, it was seen that the E1 hybrid layer slightly decreases its mechanical performance in the degradation conditions.

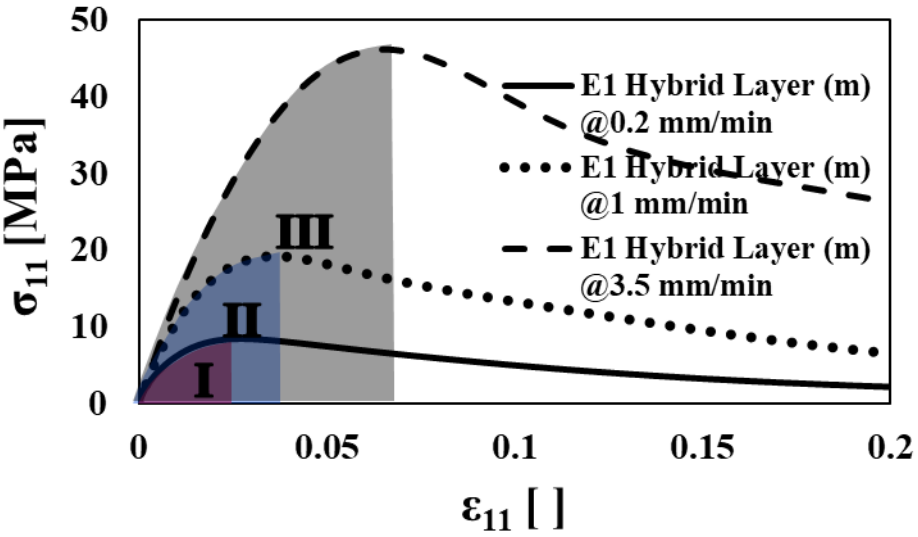

Figure 6.26: Stress-strain behavior of the remineralized E1 hybrid layer at uniaxial tensile loading at 0.2, 1 and 3.5 mm/min. I, II and III indicate the area under each curve up to the corresponding failure strain. The inset figure provides the same stress-strain relationship with a refined y-axis. (m: remineralized)

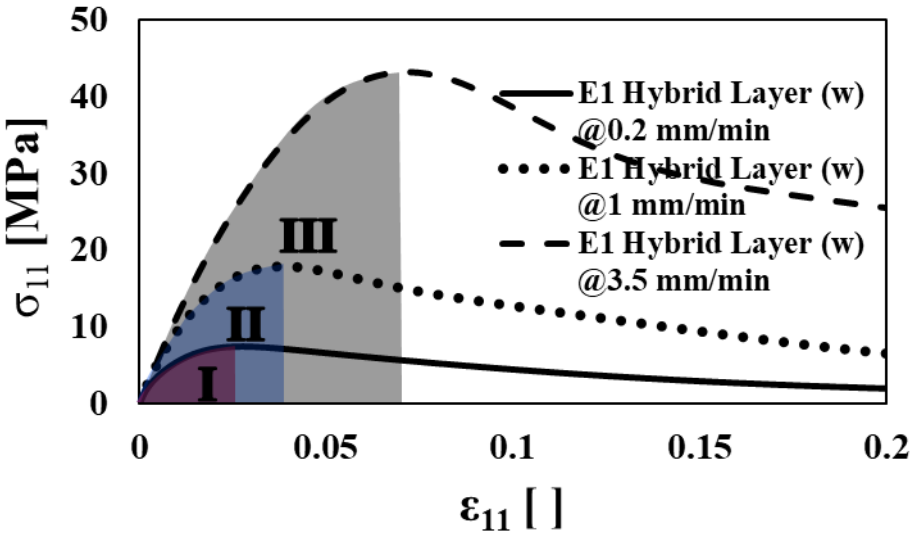

Figure 6.27: Stress-strain behavior of the weakened E1 hybrid layer at uniaxial tensile loading at 0.2, 1 and 3.5 mm/min. I, II and III indicate the area under each curve up to the corresponding failure strain. The inset figure provides the same stress-strain relationship with a refined y-axis. (w: weakened)

6.4 Summary and Conclusion

Interfacial FE models were created by using the material model parameters of the mineralized tissue, the C1 polymer and the E1 polymer determined in Chapter 5. The C1 and the E1 hybrid layers' nonlinear material model parameters were calibrated and validated against the experimental data presented in Chapter 3. The studied material model parameters represented the overall mechanical behavior of the hybrid layer materials. The simulations captured the initial and secondary failure locations in the interfacial testing. The initial failure was successfully predicted at the actual location observed in the physical experiments. The simulations also suggested a subsequent failure location, which was not accessible by the physical experiments. The subsequent failure location was observed to trigger strain concentrations within the intact mineralized tissue. It is concluded that a local failure within the hybrid layer might not compromise the overall interfacial behavior. However, this local failure in the hybrid layer affects the stress distributions in the intact mineralized tissue, such as high dilatations. Thus, a patient treated using these adhesives might experience discomfort even before the dental restoration fails. Moreover, the interfacial diametral compression test was found to provide reasonable tensile properties for hybrid layer materials' tensile behavior at low loading rates. However, the simulations found that the interfacial diametral compression test is not suggestive for these materials' pure tensile behavior at the clinical loading rate. Furthermore, the E1 hybrid layer was predicted to have superior mechanical performance compared to the C1 hybrid layer. Finally, the simulations suggested that

the remineralization significantly improve the E1 hybrid layer's mechanical performance at low loading rates. Similarly, the degradation was found to decrease the mechanical performance of the E1 hybrid layer at low loading rates. In this study, the remineralized and degraded hybrid layers' material model parameters were speculated. In the future, the interfacial specimen can be tested in the remineralization and the degradation conditions. These experimental data can provide the calibration and validation of the material model parameters for the remineralized and degraded hybrid layers. Moreover, the hybrid layer's thickness was speculated in the studied FE models. This thickness can be studied to improve the reliability of these simulations.

CHAPTER 7

SUMMARY, CONCLUSIONS AND FUTURE DIRECTIONS

7.1 Summary

This study presents a framework for characterization of the bond strength at the mineralized tissue – adhesive interface. This framework was built upon the correlation between physical experimentations and mathematical modeling. Mathematical modeling was provided by developing a rate dependent nonlinear granular micromechanics with damage and plasticity. The developed material model was implemented into a commercial finite element (FE) analysis code. The diametral compression test was used to improve repeatability in experimental data. The tensile mechanical behavior of the mineralized tissue and the adhesive polymers, as well as the bond strength at the mineralized tissue – adhesive interface were characterized. Two different adhesive formulations were used to investigate the effect of the self-strengthening property. The material model was optimized for the numerical accuracy and the computational time in the FE simulations of the diametral compression test. Material model parameters were calibrated and validated against the experimental data. Mechanical performance of the materials was simulated under the clinical loading conditions. FE simulations predicted the uniaxial tensile behavior of each material under all of the studied loading rates. Finally, the mechanical performance of the mineralized tissue – adhesive interface was predicted under the remineralization and degradation conditions.

7.2 Conclusions

The material model captured the nonlinear rate dependent mechanical behavior of the materials. The initial linear regime as well as the pre-peak and the post-peak softening were successfully simulated in the stress-stress relationships. The simulations were able to capture the strengthening in the materials' mechanical behavior with the increasing loading rate. The diametral compression test lowered the variations in the tensile testing of the mineralized tissue and the polymer adhesives as well as the bond strength testing of the mineralized tissue adhesive interface. The self-strengthening property significantly improved the mechanical behavior of the adhesive polymer and the mineralized tissue – adhesive interface based on the mechanical testing observations. The diametral compression test FE models successfully captured the nonlinear rate dependent mechanical response monitored in the experiments. The diametral compression test simulations concluded that the self-strengthening property increased the adhesive polymer's strength, whereas it diminished the adhesive polymer's toughness. The diametral compressive load was predicted to yield lower tensile properties for a single material system compared to the uniaxial tensile loading. In the interfacial simulations, the diametral compression test was concluded to provide the uniaxial tensile properties of the hybrid layer materials. The self-strengthening provided superior mechanical properties to the hybrid layer. In general, the failure was predicted to initiate between the hybrid layer and the adhesive polymer. It was concluded that the interface might not fail with the initiation of local failures. However, the stress distributions within the mineralized tissue are affected by the local failures at the interface. Therefore, a patient might have discomfort even when the dental restoration is intact. The simulations also suggested that the assumed remineralization would slightly improve the hybrid layer's mechanical performance, whereas the degradation slightly lowers the hybrid layer's mechanical performance.

7.3 Future Directions

In the current study, the diametral compression test FE models were simplified by eliminating the load platens in the physical experiments. Therefore, the simulations were not able to capture the initial contact stiffening behavior in the force-displacement curves. In the future, the contact between the disk specimen and the load platens can be included in the FE models.

This study modeled the interfacial specimen in three material sections. The hybrid layer was assumed to be a single section. In the future, the hybrid layer can be modeled as multiple sections to approximate the true nature of the mineralized tissue – adhesive interface.

In the FE models, the hybrid layer thickness was assumed to be 50 micrometers. In the future, the hybrid layer thickness can be studied for each formulation. The FE models can be updated with the studied hybrid layer thickness.

In the physical experimentations, an in-house built video recording system was used with limited imaging capabilities. In the future, digital image correlation can be used as an advanced technique to provide field measurements.

This study roughly estimated the remineralization effect in the material properties. The mineralization effect was only accounted for the hybrid layer material at a certain amount of stiffening. In the future, the models can be improved with the experimental data from remineralization studies.

Similarly, the degradation effect was roughly estimated in the material properties. It was only accounted for the hybrid layer material at a certain amount of weakening. In the future, the model parameters can be updated with the experimental data from degradation studies.

In this study, two adhesive formulations were investigated. The material model parameters for each formulation were selected by means of the MPS monomer's presence. In the future, the self-

strengthening effect can be modeled by creating a correlation between the weight percentage of the MPS in the adhesive formulation and the material model parameters. Therefore, the developed characterization framework can be used on a third adhesive formulation with a different MPS weight percentage.

This study used the bovine femur cortical bone tissue as a surrogate material for the human dentin. In the future, this characterization framework may benefit the utilization of the human dentin to inform the dental restorative design.

APPENDIX A: MATLAB CODE FOR GRANULAR MICROMECHANICS BASED NONLINEAR MATERIAL MODEL

This appendix presents the Matlab code of the developed granular micromechanics nonlinear material model. This code simulates the material behavior for a single material point.

```
format long;
tic;


%% Material model parameters assigned (Mineralized tissue in Chapter 5)
GA=1.80E-01;
GB=2.67E-04;
GC=5.14E-02;
GD=5.03E-04;
GR=2;
L0=0.01;
Np=10^9;
Galpha1=10.5;
Galpha2=7;
Ga_M=0.0000265;
Ga_D=0.0012;


%% Parameters E1 and G1
GE1=2.3*GA;
GG1=2.3*GC;
%% Viscosity and plasticity parameters
Gmu_n0=7.25E-04;
Gmu_w0=7.25E-04;
GMst=2*GA*GB*GR/pi/exp(1);
GNst=GA/GMst;
GB_mu=4;
betaPL=0;
GMst_mu=2*Gmu_n0*GB*GB_mu*GR/pi/exp(1);
GNst_mu=Gmu_n0/GMst_mu;


% Direction Cosines
All = xlsread('nstxi.xlsx','nstxi','A1:J218');

% Local normal unit vector components
```

```
n1=All(:,1);
n2=All(:,2);
n3=All(:,3);
n=[n1,n2,n3];

% Local length components of branch vector
l=L0*n;
l1=l(:,1);
l2=l(:,2);
l3=l(:,3);

% Local first tangential unit vector components
s1=All(:,4);
s2=All(:,5);
s3=All(:,6);
s=[s1,s2,s3];

% Local second tangential unit vector components
t1=All(:,7);
t2=All(:,8);
t3=All(:,9);
t=[t1,t2,t3];

% Distribution Fuction
xi=All(:,10);

%  Number of all directions
nctc=length(xi);

%  Time related parameters

Time_total=1;
DTIME=0.0025;
Time=0:DTIME:Time_total;
seps=length(Time);

% Applied load
de11=(load/100)/(seps-1);
de22=0;
de33=0;
de23=0;
de13=0;
de12=0;
de32=0;
de31=0;
de21=0;

% Stress values at all increments
Sig11_all=zeros(1,seps);
Sig22_all=zeros(1,seps);
Sig33_all=zeros(1,seps);
```

```
Sig23_all=zeros(1,seps);
Sig13_all=zeros(1,seps);
Sig12_all=zeros(1,seps);
Sig31_all=zeros(1,seps);
Sig32_all=zeros(1,seps);
Sig21_all=zeros(1,seps);

MeanStress_all=zeros(1,seps);
% Rate of inter-granular forces in global coordinates at all increments
Fd1_all=zeros(nctc,seps);
Fd2_all=zeros(nctc,seps);
Fd3_all=zeros(nctc,seps);

% Inter-granular forces in global coordinates (predictor step)
Fp1=zeros(nctc,seps);
Fp2=zeros(nctc,seps);
Fp3=zeros(nctc,seps);

% Displacement rate in global coordinates
Dt1all=zeros(nctc,1);
Dt2all=zeros(nctc,1);
Dt3all=zeros(nctc,1);

Dt1_all=zeros(nctc,seps);
Dt2_all=zeros(nctc,seps);
Dt3_all=zeros(nctc,seps);

% Normal and shear forces in local coordinates (predictor step)
Fpn=zeros(nctc,seps);
Fps=zeros(nctc,seps);
Fpt=zeros(nctc,seps);
Fpw=zeros(nctc,seps);
visc1=zeros(nctc,seps);
vis1=zeros(nctc,seps);
vis12=zeros(nctc,seps);
visc2=zeros(nctc,seps);
vis2=zeros(nctc,seps);
vis22=zeros(nctc,seps);
visc3=zeros(nctc,seps);
vis3=zeros(nctc,seps);
vis32=zeros(nctc,seps);
E2plot=zeros(nctc,seps);
MUnplot=zeros(nctc,seps);
Gknplot=zeros(nctc,seps);

Cn=zeros(nctc,seps);
Cw=zeros(nctc,seps);
Pn=zeros(nctc,seps);
Pw=zeros(nctc,seps);
Qn=zeros(nctc,seps);
Qw=zeros(nctc,seps);
```

```
fgln=zeros(nctc,seps);
fglw=zeros(nctc,seps);

% Displacement rate in local coordinates
Dt1alln=zeros(nctc,seps);
Dt1alls=zeros(nctc,seps);
Dt1allt=zeros(nctc,seps);
Dt1allw=zeros(nctc,seps);


Ckijprev=zeros(3*nctc,3);
Pij=zeros(3*nctc,3);
Qij=zeros(3*nctc,3);
DVij=zeros(3*nctc,3);
Ckij=zeros(3*nctc,3);
Ckij1=zeros(nctc,3);
Ckij2=zeros(nctc,3);
Ckij3=zeros(nctc,3);
DnMaxT=zeros(nctc,seps);
DnMaxC=zeros(nctc,seps);
DwMax=zeros(nctc,seps);
FnMaxT=zeros(nctc,seps);
FnMaxC=zeros(nctc,seps);
FwMax=zeros(nctc,seps);
Gmuij=zeros(3*nctc,3);

% Strain at each increment (from applied strain rate)
Eps_11=zeros(seps,1);
Eps_22=zeros(seps,1);
Eps_33=zeros(seps,1);
Eps_23=zeros(seps,1);
Eps_13=zeros(seps,1);
Eps_12=zeros(seps,1);
Eps_31=zeros(seps,1);
Eps_32=zeros(seps,1);
Eps_21=zeros(seps,1);


% Processing for each increment
for i=2:seps


% Loading
Eps_11(i,1)=(i-1)*de11;
Eps_22(i,1)=(i-1)*de22;
Eps_33(i,1)=(i-1)*de33;
Eps_23(i,1)=(i-1)*de23;
Eps_13(i,1)=(i-1)*de13;
Eps_12(i,1)=(i-1)*de12;
Eps_31(i,1)=(i-1)*de31;
```

```
Eps_32(i,1)=(i-1)*de32;
Eps_21(i,1)=(i-1)*de21;

MeanStress_all(1,i)=-((Sig11_all(1,i-1)+Sig22_all(1,i-1)+Sig33_all(1,i-1))/3);

Galpha3=Ga_D*abs(MeanStress_all(1,i));
GMst=2*GA*GB*GR/pi/exp(1);
GMst=GMst*(1+Ga_M*MeanStress_all(1,i));

%% Displacement rate calculation

Dt1=L0*(Eps_11(i)*n1+Eps_12(i)*n2+Eps_13(i)*n3);
Dt2=L0*(Eps_21(i)*n1+Eps_22(i)*n2+Eps_23(i)*n3);
Dt3=L0*(Eps_31(i)*n1+Eps_32(i)*n2+Eps_33(i)*n3);

Dt1all(1:nctc)=Dt1;
Dt2all(1:nctc)=Dt2;
Dt3all(1:nctc)=Dt3;

Dt1_all(1:nctc,i)=Dt1all;
Dt2_all(1:nctc,i)=Dt2all;
Dt3_all(1:nctc,i)=Dt3all;


Dt1alln(1:nctc,i)=Dt1all(1:nctc).*n1...
+Dt2all(1:nctc).*n2...
+Dt3all(1:nctc).*n3;



Dt1alls(1:nctc,i)=Dt1all(1:nctc).*s1...
+Dt2all(1:nctc).*s2...
+Dt3all(1:nctc).*s3;



Dt1allt(1:nctc,i)=Dt1all(1:nctc).*t1...
+Dt2all(1:nctc).*t2...
+Dt3all(1:nctc).*t3;

Dt1allw(1:nctc,i)=sqrt(Dt1alls(1:nctc,i).^2+Dt1allt(1:nctc,i).^2);


%Calculation of each direction
for j=1:nctc


% UpdateDeltaMax
   if Dt1alln(j,i)>=0
      if Dt1alln(j,i)>DnMaxT(j,i-1)
         DnMaxT(j,i)=Dt1alln(j,i);
```

```
        else
            DnMaxT(j,i)=DnMaxT(j,i-1);
        end
    else
        if Dt1alln(j,i)<DnMaxC(j,i-1)
            DnMaxC(j,i)=Dt1alln(j,i);
        else
            DnMaxC(j,i)=DnMaxC(j,i-1);
        end
    end

    if Dt1allw(j,i)>DwMax(j,i-1)
        DwMax(j,i)=Dt1allw(j,i);
    else
        DwMax(j,i)=DwMax(j,i-1);
    end


%% Tension-Normal
    if Dt1alln(j,i)>=0

        DMod=GD;
        if Dt1alln(j,i)==DnMaxT(j,i)
            E2=GA*exp(-(Dt1alln(j,i-1)-Fpn(j,i-1)/GE1)/GB);
            MUn=Gmu_n0*exp(-(Dt1alln(j,i-1)-Fpn(j,i-1)/GE1)/GB_mu/GB);
             if Dt1alln(j,i-1)==0
                E2=GA*exp(-(Dt1alln(j,i-1)-Fpn(j,i-1)/GE1)/GB)*(1-(Dt1alln(j,i-1)-Fpn(j,i-1)/GE1)/GB);
                MUn=Gmu_n0*exp(-((Dt1alln(j,i-1)-Fpn(j,i-1)/GE1)/GB_mu/GB))*(1-(Dt1alln(j,i-1)-
Fpn(j,i-1)/GE1)/GB_mu/GB);
             end
        else %Unloading
            E2=GA*exp(-(DnMaxT(j,i-1)-FnMaxT(j,i-1)/GE1)/GB);
            MUn=Gmu_n0*exp(-((DnMaxT(j,i-1)-FnMaxT(j,i-1)/GE1)/GB_mu/GB));
        end
    end

    %% Compression-Normal
    if Dt1alln(j,i)<0
        if Dt1alln(j,i)==DnMaxC(j,i)
         if Dt1alln(j,i-1)==0
            E2=GMst*GNst;
            MUn=GMst_mu*GNst_mu;
         else
            E2=GMst*atan(GNst*(Dt1alln(j,i-1)-Fpn(j,i-1)/GE1))/Dt1alln(j,i-1);
            MUn=GMst_mu*atan(GNst_mu*(Dt1alln(j,i-1)-Fpn(j,i-1)/GE1/GB_mu))/Dt1alln(j,i-1);
         end
        else %Unloading
        if DnMaxC(j,i-1)==0
            E2=GMst*GNst;
            MUn=GMst_mu*GNst_mu;
        else
```

```
            E2=GMst*atan(GNst*(DnMaxC(j,i-1)-FnMaxC(j,i-1)/GE1))/(DnMaxC(j,i-1));
            MUn=GMst_mu*atan(GNst_mu*(DnMaxC(j,i-1)-FnMaxC(j,i-1)/GE1/GB_mu))/DnMaxC(j,i-1);
        end
        end

        if Dt1alln(j,i-1)>GD*(1-Galpha1)/Galpha2
            DMod=GD-Galpha2*Dt1alln(j,i-1);
        else
            DMod=Galpha1*GD+(GD*(1-Galpha1)/Galpha2-Dt1alln(j,i-1))*Galpha3;
        end
    end
    % Shear
     if Dt1allw(j,i)==DwMax(j,i)
        G2=GC*exp(-abs(Dt1allw(j,i-1)-Fpw(j,i-1)/GG1)/DMod);
        MUw=Gmu_w0*exp(-abs(Dt1allw(j,i-1)-Fpw(j,i-1)/GG1)/GB_mu/DMod);
     else %Unloading
        G2=GC*exp(-abs(DwMax(j,i-1)-FwMax(j,i-1)/GG1)/DMod)/(1-betaPL);
        MUw=Gmu_w0*exp(-abs(DwMax(j,i-1)-FwMax(j,i-1)/GG1)/GB_mu/DMod)/(1-betaPL);
     end


%Local stiffness
    Gkn=GE1*E2/(GE1+E2);
    Gkw=GG1*G2/(GG1+G2);
    Gks=Gkw;
    Gkt=Gkw;

%Local viscosity
    Gmun=GE1*MUn/(GE1+E2);
    Gmuw=GG1*MUw/(GG1+G2);

%Local relaxation
    Gzetan=MUn/(GE1+E2);
    Gzetaw=MUw/(GG1+G2);

%Micro-scale force components
    denomn=DTIME+Gzetan;
    denomw=DTIME+Gzetaw;
    Pn(j,i)=-Gmun/denomn;
    Pw(j,i)=-Gmuw/denomw;
    Cn(j,i)=(Gkn*DTIME)/denomn-Pn(j,i);
    Cw(j,i)=(Gkw*DTIME)/denomw-Pw(j,i);
    Qn(j,i)=Gzetan/denomn;
    Qw(j,i)=Gzetaw/denomw;
    fgln(j,i)=Cn(j,i)*Dt1alln(j,i)+Pn(j,i)*Dt1alln(j,i-1)+Qn(j,i)*fgln(j,i-1);
    fglw(j,i)=Cw(j,i)*Dt1allw(j,i)+Pw(j,i)*Dt1allw(j,i-1)+Qw(j,i)*fglw(j,i-1);
    Ckijprev(3*j-2,1)=Cn(j,i)*n1(j)*n1(j)+Cw(j,i)*s1(j)*s1(j)+Cw(j,i)*t1(j)*t1(j);
    Ckijprev(3*j-1,2)=Cn(j,i)*n2(j)*n2(j)+Cw(j,i)*s2(j)*s2(j)+Cw(j,i)*t2(j)*t2(j);
    Ckijprev(3*j,3)=Cn(j,i)*n3(j)*n3(j)+Cw(j,i)*s3(j)*s3(j)+Cw(j,i)*t3(j)*t3(j);
    Ckijprev(3*j-2,2)=Cn(j,i)*n1(j)*n2(j)+Cw(j,i)*s1(j)*s2(j)+Cw(j,i)*t1(j)*t2(j);
    Ckijprev(3*j-2,3)=Cn(j,i)*n1(j)*n3(j)+Cw(j,i)*s1(j)*s3(j)+Cw(j,i)*t1(j)*t3(j);
```

```
Ckijprev(3*j-1,3)=Cn(j,i)*n2(j)*n3(j)+Cw(j,i)*s2(j)*s3(j)+Cw(j,i)*t2(j)*t3(j);
Ckijprev(3*j-1,1)=Ckijprev(3*j-2,2);
Ckijprev(3*j-0,1)=Ckijprev(3*j-2,3);
Ckijprev(3*j-0,2)=Ckijprev(3*j-1,3);
Pij(3*j-2,1)=Pn(j,i)*n1(j)*n1(j)+Pw(j,i)*s1(j)*s1(j)+Pw(j,i)*t1(j)*t1(j);
Pij(3*j-1,2)=Pn(j,i)*n2(j)*n2(j)+Pw(j,i)*s2(j)*s2(j)+Pw(j,i)*t2(j)*t2(j);
Pij(3*j,3)=Pn(j,i)*n3(j)*n3(j)+Pw(j,i)*s3(j)*s3(j)+Pw(j,i)*t3(j)*t3(j);
Pij(3*j-2,2)=Pn(j,i)*n1(j)*n2(j)+Pw(j,i)*s1(j)*s2(j)+Pw(j,i)*t1(j)*t2(j);
Pij(3*j-2,3)=Pn(j,i)*n1(j)*n3(j)+Pw(j,i)*s1(j)*s3(j)+Pw(j,i)*t1(j)*t3(j);
Pij(3*j-1,3)=Pn(j,i)*n2(j)*n3(j)+Pw(j,i)*s2(j)*s3(j)+Pw(j,i)*t2(j)*t3(j);
Pij(3*j-1,1)=Pij(3*j-2,2);
Pij(3*j-0,1)=Pij(3*j-2,3);
Pij(3*j-0,2)=Pij(3*j-1,3);
Qij(3*j-2,1)=Qn(j,i)*n1(j)*n1(j)+Qw(j,i)*s1(j)*s1(j)+Qw(j,i)*t1(j)*t1(j);
Qij(3*j-1,2)=Qn(j,i)*n2(j)*n2(j)+Qw(j,i)*s2(j)*s2(j)+Qw(j,i)*t2(j)*t2(j);
Qij(3*j,3)=Qn(j,i)*n3(j)*n3(j)+Qw(j,i)*s3(j)*s3(j)+Qw(j,i)*t3(j)*t3(j);
Qij(3*j-2,2)=Qn(j,i)*n1(j)*n2(j)+Qw(j,i)*s1(j)*s2(j)+Qw(j,i)*t1(j)*t2(j);
Qij(3*j-2,3)=Qn(j,i)*n1(j)*n3(j)+Qw(j,i)*s1(j)*s3(j)+Qw(j,i)*t1(j)*t3(j);
Qij(3*j-1,3)=Qn(j,i)*n2(j)*n3(j)+Qw(j,i)*s2(j)*s3(j)+Qw(j,i)*t2(j)*t3(j);
Qij(3*j-1,1)=Qij(3*j-2,2);
Qij(3*j-0,1)=Qij(3*j-2,3);
Qij(3*j-0,2)=Qij(3*j-1,3);

fc1=Ckijprev(3*j-2,1)*Dt1_all(j,i)+Ckijprev(3*j-2,2)*Dt2_all(j,i)+Ckijprev(3*j-2,3)*Dt3_all(j,i);
fp1=Pij(3*j-2,1)*Dt1_all(j,i-1)+Pij(3*j-2,2)*Dt2_all(j,i-1)+Pij(3*j-2,3)*Dt3_all(j,i-1);
fq1=Qij(3*j-2,1)*Fp1(j,i-1)+Qij(3*j-2,2)*Fp2(j,i-1)+Qij(3*j-2,3)*Fp3(j,i-1);
Fp1(j,i)=(fc1+fp1+fq1);
fc2=Ckijprev(3*j-1,1)*Dt1_all(j,i)+Ckijprev(3*j-1,2)*Dt2_all(j,i)+Ckijprev(3*j-1,3)*Dt3_all(j,i);
fp2=Pij(3*j-1,1)*Dt1_all(j,i-1)+Pij(3*j-1,2)*Dt2_all(j,i-1)+Pij(3*j-1,3)*Dt3_all(j,i-1);
fq2=Qij(3*j-1,1)*Fp1(j,i-1)+Qij(3*j-1,2)*Fp2(j,i-1)+Qij(3*j-1,3)*Fp3(j,i-1);
Fp2(j,i)=(fc2+fp2+fq2);
fc3=Ckijprev(3*j,1)*Dt1_all(j,i)+Ckijprev(3*j,2)*Dt2_all(j,i)+Ckijprev(3*j,3)*Dt3_all(j,i);
fp3=Pij(3*j,1)*Dt1_all(j,i-1)+Pij(3*j,2)*Dt2_all(j,i-1)+Pij(3*j,3)*Dt3_all(j,i-1);
fq3=Qij(3*j,1)*Fp1(j,i-1)+Qij(3*j,2)*Fp2(j,i-1)+Qij(3*j,3)*Fp3(j,i-1);
Fp3(j,i)=(fc3+fp3+fq3);

visc1(j,i)=fc1*n1(j)+fc2*n2(j)+fc3*n3(j);
viscs=fc1*s1(j)+fc2*s2(j)+fc3*s3(j);
visct=fc1*t1(j)+fc2*t2(j)+fc3*t3(j);
vis1(j,i)=sqrt(viscs^2+visct^2);

visc2(j,i)=fp1*n1(j)+fp2*n2(j)+fp3*n3(j);
visc1s=fp1*s1(j)+fp2*s2(j)+fp3*s3(j);
visc1t=fp1*t1(j)+fp2*t2(j)+fp3*t3(j);
vis2(j,i)=sqrt(visc1s^2+visc1t^2);

visc3(j,i)=fq1*n1(j)+fq2*n2(j)+fq3*n3(j);
visc2s=fq1*s1(j)+fq2*s2(j)+fq3*s3(j);
visc2t=fq1*t1(j)+fq2*t2(j)+fq3*t3(j);
vis3(j,i)=sqrt(visc2s^2+visc2t^2);
```

```
%Micro-scale forces in local coordinates

Fpn(j,i)=Fp1(j,i)*n1(j)+Fp2(j,i)*n2(j)+Fp3(j,i)*n3(j);
Fps(j,i)=Fp1(j,i)*s1(j)+Fp2(j,i)*s2(j)+Fp3(j,i)*s3(j);
Fpt(j,i)=Fp1(j,i)*t1(j)+Fp2(j,i)*t2(j)+Fp3(j,i)*t3(j);
Fpw(j,i)=sqrt(Fps(j,i)^2+Fpt(j,i)^2);

% UpdateFMax

if Fpn(j,i)>=0
   if Fpn(j,i)>FnMaxT(j,i-1)
      FnMaxT(j,i)=Fpn(j,i);
   else
      FnMaxT(j,i)=FnMaxT(j,i-1);
   end
else
   if Fpn(j,i)<FnMaxC(j,i-1)
      FnMaxC(j,i)=Fpn(j,i);
   else
      FnMaxC(j,i)=FnMaxC(j,i-1);
   end
end

if Fpw(j,i)>FwMax(j,i-1)
   FwMax(j,i)=Fpw(j,i);
else
   FwMax(j,i)=FwMax(j,i-1);
end


% Local force rates
   dfn=Fpn(j,i)-Fpn(j,i-1);
   dfs=Fps(j,i)-Fps(j,i-1);
   dft=Fpt(j,i)-Fpt(j,i-1);
   dfw=sqrt(dfs^2+dft^2);

   ddn=Dt1alln(j,i)-Dt1alln(j,i-1);
   dds=Dt1alls(j,i)-Dt1alls(j,i-1);
   ddt=Dt1allt(j,i)-Dt1allt(j,i-1);
   ddw=sqrt(dds^2+ddt^2);


   Ckij(3*j-2,1)=Ckijprev(3*j-2,1);
   Ckij(3*j-1,2)=Ckijprev(3*j-1,2);
   Ckij(3*j,3)=Ckijprev(3*j,3);
   Ckij(3*j-2,2)=Ckijprev(3*j-2,2);
   Ckij(3*j-2,3)=Ckijprev(3*j-2,3);
   Ckij(3*j-1,3)=Ckijprev(3*j-1,3);
   Ckij(3*j-1,1)=Ckij(3*j-2,2);
   Ckij(3*j-0,1)=Ckij(3*j-2,3);
   Ckij(3*j-0,2)=Ckij(3*j-1,3);
```

```
    Ckij1(j,:)=Ckij(3*j-2,:);
    Ckij2(j,:)=Ckij(3*j-1,:);
    Ckij3(j,:)=Ckij(3*j,:);

end

F1=Fp1(:,i);
F2=Fp2(:,i);
F3=Fp3(:,i);

%% Voigt notation 81 elements to 21  (Stiffness Matrix)
[C_ijkl]=CalcCijkl(Ckij1, Ckij2, Ckij3, n1, n2, n3, L0, Np, xi);
NS=C_ijkl(1:3,4:6)+C_ijkl(1:3,7:9);
SN=C_ijkl(4:6,1:3)+C_ijkl(7:9,1:3);
SS=C_ijkl(4:6,4:6)+C_ijkl(4:6,7:9)+C_ijkl(7:9,4:6)+C_ijkl(7:9,7:9);
C_ijkl_6x6new(1:3,1:3)=C_ijkl(1:3,1:3);
C_ijkl_6x6new(1:3,4:6)=NS;
C_ijkl_6x6new(4:6,1:3)=SN;
C_ijkl_6x6new(4:6,4:6)=SS;

C_ijkl_6x6=C_ijkl_6x6new;
Cijkl_6x6(1:6,6*i-5:i*6)=C_ijkl_6x6new;
det_C(1,i)=det(C_ijkl_6x6new);

%Stress
[Sij]=CalcSij(F1, F2, F3, n1, n2, n3, L0, Np, xi);

Sig_11=Sij(1);
Sig_22=Sij(5);
Sig_33=Sij(9);
Sig_23=(Sij(6)+Sij(8))/2;
Sig_13=(Sij(3)+Sij(7))/2;
Sig_12=(Sij(2)+Sij(4))/2;

Sig11_all(1,i)=Sig_11;
Sig22_all(1,i)=Sig_22;
Sig33_all(1,i)=Sig_33;
Sig23_all(1,i)=Sig_23;
Sig13_all(1,i)=Sig_13;
Sig12_all(1,i)=Sig_12;

i
end

toc;

%Plot stress-strain in 11 direction
a=10;
b=10;
c=2;
```

```
d=5;
e=5;

figure
plot(Eps_11(1:i),Sig11_all(1:i),'LineWidth',c,'MarkerFaceColor',[0 0 0]);

xlabel('\epsilon_1_1 ','fontsize',a);
ylabel('\sigma_1_1 (MPa)','fontsize',a);
set(gca,'fontsize',b);

%Mark the failure stress and strain in the figure
str={max(Sig11_all),...
Eps_11(Sig11_all==max(Sig11_all))};
text(Eps_11(Sig11_all==max(Sig11_all)),max(Sig11_all),str)



%Stress function
function [Sij]=CalcSij(F1, F2, F3, n1, n2, n3, L0, Np, xi)

S11=L0*Np*(sum(xi.*n1.*F1));
S12=L0*Np*(sum(xi.*n2.*F1));
S13=L0*Np*(sum(xi.*n3.*F1));
S21=L0*Np*(sum(xi.*n1.*F2));
S22=L0*Np*(sum(xi.*n2.*F2));
S23=L0*Np*(sum(xi.*n3.*F2));
S31=L0*Np*(sum(xi.*n1.*F3));
S32=L0*Np*(sum(xi.*n2.*F3));
S33=L0*Np*(sum(xi.*n3.*F3));

Sij=[S11; S12; S13; S21; S22; S23; S31; S32; S33];

%Stiffness matrix function
function [C_ijkl]=CalcCijkl(Ckij1, Ckij2, Ckij3, n1, n2, n3, L0, Np, xi)

C1111=L0^2*Np*(sum(xi.*(n1.*n1.*Ckij1(:,1))));
C1122=L0^2*Np*(sum(xi.*(n1.*n2.*Ckij1(:,2))));
C1133=L0^2*Np*(sum(xi.*(n1.*n3.*Ckij1(:,3))));
C1123=L0^2*Np*(sum(xi.*(n1.*n3.*Ckij1(:,2))));
C1131=L0^2*Np*(sum(xi.*(n1.*n1.*Ckij1(:,3))));
C1112=L0^2*Np*(sum(xi.*(n1.*n2.*Ckij1(:,1))));
C1132=L0^2*Np*(sum(xi.*(n1.*n2.*Ckij1(:,3))));
C1113=L0^2*Np*(sum(xi.*(n1.*n3.*Ckij1(:,1))));
C1121=L0^2*Np*(sum(xi.*(n1.*n1.*Ckij1(:,2))));
C2211=L0^2*Np*(sum(xi.*(n2.*n1.*Ckij2(:,1))));
C2222=L0^2*Np*(sum(xi.*(n2.*n2.*Ckij2(:,2))));
C2233=L0^2*Np*(sum(xi.*(n2.*n3.*Ckij2(:,3))));
C2223=L0^2*Np*(sum(xi.*(n2.*n3.*Ckij2(:,2))));
C2231=L0^2*Np*(sum(xi.*(n2.*n1.*Ckij2(:,3))));
C2212=L0^2*Np*(sum(xi.*(n2.*n2.*Ckij2(:,1))));
C2232=L0^2*Np*(sum(xi.*(n2.*n2.*Ckij2(:,3))));
```

```
C2213=L0^2*Np*(sum(xi.*(n2.*n3.*Ckij2(:,1))));
C2221=L0^2*Np*(sum(xi.*(n2.*n1.*Ckij2(:,2))));
C3311=L0^2*Np*(sum(xi.*(n3.*n1.*Ckij3(:,1))));
C3322=L0^2*Np*(sum(xi.*(n3.*n2.*Ckij3(:,2))));
C3333=L0^2*Np*(sum(xi.*(n3.*n3.*Ckij3(:,3))));
C3323=L0^2*Np*(sum(xi.*(n3.*n3.*Ckij3(:,2))));
C3331=L0^2*Np*(sum(xi.*(n3.*n1.*Ckij3(:,3))));
C3312=L0^2*Np*(sum(xi.*(n3.*n2.*Ckij3(:,1))));
C3332=L0^2*Np*(sum(xi.*(n3.*n2.*Ckij3(:,3))));
C3313=L0^2*Np*(sum(xi.*(n3.*n3.*Ckij3(:,1))));
C3321=L0^2*Np*(sum(xi.*(n3.*n1.*Ckij3(:,2))));
C2311=L0^2*Np*(sum(xi.*(n3.*n1.*Ckij2(:,1))));
C2322=L0^2*Np*(sum(xi.*(n3.*n2.*Ckij2(:,2))));
C2333=L0^2*Np*(sum(xi.*(n3.*n3.*Ckij2(:,3))));
C2323=L0^2*Np*(sum(xi.*(n3.*n3.*Ckij2(:,2))));
C2331=L0^2*Np*(sum(xi.*(n3.*n1.*Ckij2(:,3))));
C2312=L0^2*Np*(sum(xi.*(n3.*n2.*Ckij2(:,1))));
C2332=L0^2*Np*(sum(xi.*(n3.*n2.*Ckij2(:,3))));
C2313=L0^2*Np*(sum(xi.*(n3.*n3.*Ckij2(:,1))));
C2321=L0^2*Np*(sum(xi.*(n3.*n1.*Ckij2(:,2))));
C3111=L0^2*Np*(sum(xi.*(n1.*n1.*Ckij3(:,1))));
C3122=L0^2*Np*(sum(xi.*(n1.*n2.*Ckij3(:,2))));
C3133=L0^2*Np*(sum(xi.*(n1.*n3.*Ckij3(:,3))));
C3123=L0^2*Np*(sum(xi.*(n1.*n3.*Ckij3(:,2))));
C3131=L0^2*Np*(sum(xi.*(n1.*n1.*Ckij3(:,3))));
C3112=L0^2*Np*(sum(xi.*(n1.*n2.*Ckij3(:,1))));
C3132=L0^2*Np*(sum(xi.*(n1.*n2.*Ckij3(:,3))));
C3113=L0^2*Np*(sum(xi.*(n1.*n3.*Ckij3(:,1))));
C3121=L0^2*Np*(sum(xi.*(n1.*n1.*Ckij3(:,2))));
C1211=L0^2*Np*(sum(xi.*(n2.*n1.*Ckij1(:,1))));
C1222=L0^2*Np*(sum(xi.*(n2.*n2.*Ckij1(:,2))));
C1233=L0^2*Np*(sum(xi.*(n2.*n3.*Ckij1(:,3))));
C1223=L0^2*Np*(sum(xi.*(n2.*n3.*Ckij1(:,2))));
C1231=L0^2*Np*(sum(xi.*(n2.*n1.*Ckij1(:,3))));
C1212=L0^2*Np*(sum(xi.*(n2.*n2.*Ckij1(:,1))));
C1232=L0^2*Np*(sum(xi.*(n2.*n2.*Ckij1(:,3))));
C1213=L0^2*Np*(sum(xi.*(n2.*n3.*Ckij1(:,1))));
C1221=L0^2*Np*(sum(xi.*(n2.*n1.*Ckij1(:,2))));
C3211=L0^2*Np*(sum(xi.*(n2.*n1.*Ckij3(:,1))));
C3222=L0^2*Np*(sum(xi.*(n2.*n2.*Ckij3(:,2))));
C3233=L0^2*Np*(sum(xi.*(n2.*n3.*Ckij3(:,3))));
C3223=L0^2*Np*(sum(xi.*(n2.*n3.*Ckij3(:,2))));
C3231=L0^2*Np*(sum(xi.*(n2.*n1.*Ckij3(:,3))));
C3212=L0^2*Np*(sum(xi.*(n2.*n2.*Ckij3(:,1))));
C3232=L0^2*Np*(sum(xi.*(n2.*n2.*Ckij3(:,3))));
C3213=L0^2*Np*(sum(xi.*(n2.*n3.*Ckij3(:,1))));
C3221=L0^2*Np*(sum(xi.*(n2.*n1.*Ckij3(:,2))));
C1311=L0^2*Np*(sum(xi.*(n3.*n1.*Ckij1(:,1))));
C1322=L0^2*Np*(sum(xi.*(n3.*n2.*Ckij1(:,2))));
C1333=L0^2*Np*(sum(xi.*(n3.*n3.*Ckij1(:,3))));
C1323=L0^2*Np*(sum(xi.*(n3.*n3.*Ckij1(:,2))));
```

```
C1331=L0^2*Np*(sum(xi.*(n3.*n1.*Ckij1(:,3))));
C1312=L0^2*Np*(sum(xi.*(n3.*n2.*Ckij1(:,1))));
C1332=L0^2*Np*(sum(xi.*(n3.*n2.*Ckij1(:,3))));
C1313=L0^2*Np*(sum(xi.*(n3.*n3.*Ckij1(:,1))));
C1321=L0^2*Np*(sum(xi.*(n3.*n1.*Ckij1(:,2))));
C2111=L0^2*Np*(sum(xi.*(n1.*n1.*Ckij2(:,1))));
C2122=L0^2*Np*(sum(xi.*(n1.*n2.*Ckij2(:,2))));
C2133=L0^2*Np*(sum(xi.*(n1.*n3.*Ckij2(:,3))));
C2123=L0^2*Np*(sum(xi.*(n1.*n3.*Ckij2(:,2))));
C2131=L0^2*Np*(sum(xi.*(n1.*n1.*Ckij2(:,3))));
C2112=L0^2*Np*(sum(xi.*(n1.*n2.*Ckij2(:,1))));
C2132=L0^2*Np*(sum(xi.*(n1.*n2.*Ckij2(:,3))));
C2113=L0^2*Np*(sum(xi.*(n1.*n3.*Ckij2(:,1))));
C2121=L0^2*Np*(sum(xi.*(n1.*n1.*Ckij2(:,2))));
C_ijkl=[C1111 C1122 C1133 C1123 C1113 C1112 C1132 C1131 C1121;
    C2211 C2222 C2233 C2223 C2213 C2212 C2232 C2231 C2221;
    C3311 C3322 C3333 C3323 C3313 C3312 C3332 C3331 C3321;
    C2311 C2322 C2333 C2323 C2313 C2312 C2332 C2331 C2321;
    C1311 C1322 C1333 C1323 C1313 C1312 C1332 C1331 C1321;
    C1211 C1222 C1233 C1223 C1213 C1212 C1232 C1231 C1221;
    C3211 C3222 C3233 C3223 C3213 C3212 C3232 C3231 C3221;
    C3111 C3122 C3133 C3123 C3113 C3112 C3132 C3131 C3121;
    C2111 C2122 C2133 C2123 C2113 C2112 C2132 C2131 C2121];
```

APPENDIX B: FORTRAN CODE FOR USER-DEFINED MATERIAL MODEL (UMAT) OF GRANULAR MICROMECHANICS BASED NONLINEAR MATERIAL MODEL

This appendix presents the Fortran code of the developed granular micromechanics nonlinear material model. This Fortran code is called to the commercial FE code, Abaqus, to run FE simulations with the developed nonlinear material model.

```
C ======================================================================
C ============================ U M A T ================================
C ======================================================================
C  **********************************************************************
C  *   Granular Micromechanics User Defined Nonlinear Material Model  *
C  **********************************************************************


SUBROUTINE UMAT(STRESS,STATEV,DDSDDE,SSE,SPD,SCD,
     1 RPL,DDSDDT,DRPLDE,DRPLDT,
     2 STRAN,DSTRAN,TIME,DTIME,TEMP,DTEMP,PREDEF,DPRED,CMNAME,
     3 NDI,NSHR,NTENS,NSTATV,PROPS,NPROPS,COORDS,DROT,PNEWDT,
     4 CELENT,DFGRD0,DFGRD1,NOEL,NPT,LAYER,KSPT,KSTEP,KINC)

      INCLUDE 'ABA_PARAM.INC'

      CHARACTER*8 CMNAME

      real*8 STRESS(NTENS),STATEV(NSTATV),
     + DDSDDE(NTENS,NTENS),DDSDDT(NTENS),DRPLDE(NTENS),
     + STRAN(NTENS),DSTRAN(NTENS),TIME(2),PREDEF(1),DPRED(1),
     + PROPS(NPROPS),COORDS(3),DROT(3,3),DFGRD0(3,3),DFGRD1(3,3)

      real*8 Cijkl(3,3,3,3)
      real*8 Strain(NTENS)

      real*8 Gkij(654,3),fi(218,3),deli(218,3),Kij(3,3),Sij(3,3),
     + deln(218),dels(218),delt(218),delw(218),Gkijprev(654,3)

      real*8 Gmuij(654,3),Qij(654,3)
```

```
      real*8 Gn(218,3),Gs(218,3),Gt(218,3),Gxi(218)

      real*8 DnMaxT(218),DnMaxC(218),DwMax(218)
      real*8 DnMaxTprev(218),DnMaxCprev(218),DwMaxprev(218)

      real*8 fnprev(218),fwprev(218),fsprev(218),ftprev(218),
     + dnprev(218),dsprev(218),dtprev(218),dwprev(218),
     + diprev(218,3),fiprev(218,3),fn(218),fw(218),GMeanSt(1),
     + fs(218),ft(218),DelV(218),Gkw(218)

      real*8 FnMaxT(218),FnMaxC(218),FwMax(218),GMstprev(1)
      real*8 FnMaxTprev(218),FnMaxCprev(218),FwMaxprev(218)

      real*8 GE2, GMUn, Dmod, betaPL, G2, GMUw, Gkn, Gks, Gkt,
     + Ggmun, Ggmuw, Gzetan, Gzetaw, Gdenomn, Gdenomw, GPn, GPw,
     + GCn, GCw, GQn, GQw

      real*8 PI

      real*8 vis1, vis12, vis2, vis22, vis3, vis32

      real*8 GA, GB, GC, GD, GR, GL, GNp, Galpha1, Galpha2,
     + Ga_M, Ga_D, GMst, GNst, GB_mu, Gmu_n0, Gmu_w0, GE1, GG1, GMst_mu,
     + GNst_mu

      COMMON/MatProp/ GA, GB, GC, GD, GR, GL, GNp, Galpha1, Galpha2,
     + Ga_M, Ga_D, GMst, GNst, GB_mu, Gmu_n0, Gmu_w0, GE1, GG1, GMst_mu,
     + GNst_mu

C --- SET IPT = WHICH POINT/NODE FOR WHICH TO WRITE VALUES
      IPT = 1

      CALL KMATERIAL_PROP(PROPS, NPROPS)

C     DEFINE PI
      PI=4.0*ATAN(1.0)

C     UPDATE STRAIN VALUES
      do i=1, 6
         Strain(i)=STRAN(i)+DSTRAN(i)
      end do

C     GENERATE STATE VARIABLES MAX DISPLACEMENT, MAX FORCE, FORCE

      do i=1,218
         DnMaxT(i) =STATEV(i)
         DnMaxC(i) =STATEV(i+218)
         DwMax(i)  =STATEV(i+436)
         fn(i) =STATEV(i+654)
         fs(i) =STATEV(i+872)
         ft(i) =STATEV(i+1090)
```

```
        FnMaxT(i) =STATEV(i+1308)
        FnMaxC(i) =STATEV(i+1526)
        FwMax(i)  =STATEV(i+1744)
        DnMaxTprev(i) =DnMaxT(i)
        DnMaxCprev(i) =DnMaxC(i)
        DwMaxprev(i) =DwMax(i)
        fnprev(i)=fn(i)
        fsprev(i)=fs(i)
        ftprev(i)=ft(i)
        fwprev(i)=sqrt(fsprev(i)*fsprev(i)+ftprev(i)*ftprev(i))
        FnMaxTprev(i) =FnMaxT(i)
        FnMaxCprev(i) =FnMaxC(i)
        FwMaxprev(i) =FwMax(i)

        end do

      CALL Read_Geom(KINC,Gn,Gs,Gt,Gxi)


      CALL Deltas(NTENS,Strain,deln,dels,delt,delw,deli,Gn,Gs,Gt)

      CALL Calc_D_prev(NTENS,STRAN,dnprev,dwprev,diprev,Gn,Gs,Gt,
     + dsprev,dtprev)


      CALL UpdateDeltaMax(DnMaxT,DnMaxC,deln,Dwmax,delw,
     + DnMaxTprev,DnMaxCprev,DwMaxprev)



C-----UPDATE STATE VARIABLES----------
C*********MAXIMUM DISPLACEMENT components
      do i=1, 218
        STATEV(i)=DnMaxT(i)
        STATEV(i+218)=DnMaxC(i)
        STATEV(i+436)=DwMax(i)
      end do

      CALL FKMu_prev(Gkijprev,Gn,Gs,Gt,dnprev,dwprev,fiprev,
     + DnMaxTprev,DnMaxCprev,DwMaxprev,STRESS,NTENS,fnprev,fwprev,
     + DTIME,FnMaxTprev,FnMaxCprev,FwMaxprev,deln,delw,
     + fsprev,ftprev,dsprev,dtprev,Gmuij,Qij,GMeanSt,GMstprev,
     + DnMaxT,DnMaxC,DwMax,DelV,Gkw)


      CALL Forces_Kij(STRESS,NTENS,deli,diprev,Gkijprev,Gmuij,Qij,
     + DTIME,deln,dels,delt,Gn,Gs,Gt,fi,fnprev,fsprev,ftprev,Gkij,
     + dnprev,dsprev,dtprev,fiprev,fwprev,fn,fw,fs,ft,DelV,Gkw)

      do i=1, 218
        STATEV(i+654)=fn(i)
```

```
        STATEV(i+872)=fs(i)
        STATEV(i+1090)=ft(i)
      end do

      CALL UpdateFMax(FnMaxT,FnMaxC,fn,Fwmax,fw,
     + FnMaxTprev,FnMaxCprev,FwMaxprev)

C-----UPDATE State Variables---------------
C*********PREVIOUS FORCE components
      do i=1, 218
        STATEV(i+1308)=FnMaxT(i)
        STATEV(i+1526)=FnMaxC(i)
        STATEV(i+1744)=FwMax(i)
      end do

      CALL Calc_Stress(NTENS,STRESS,fi,Gn,Gxi,Sij,
     + DSig,DEps)

      CALL Calc_Cijkl(Cijkl,Gkij,Gn,Gxi,DSig,DEps)

      CALL CijFromCijkl(NTENS,Cijkl,DDSDDE)

      RETURN
      END
C
C
C**********************************************************************
C   KMATERIAL_PROP: This subroutine calls the material model parameters
C**********************************************************************
C
      SUBROUTINE KMATERIAL_PROP(PROPS, NPROPS)

      INCLUDE 'ABA_PARAM.INC'
C
      real*8 PROPS(NPROPS)

      real*8 PI

      real*8 GA, GB, GC, GD, GR, GL, GNp, Galpha1, Galpha2,
     + Ga_M, Ga_D, GMst, GNst, GB_mu, Gmu_n0, Gmu_w0, GE1, GG1, GMst_mu,
     + GNst_mu
C
      COMMON/MatProp/ GA, GB, GC, GD, GR, GL, GNp, Galpha1, Galpha2,
     + Ga_M, Ga_D, GMst, GNst, GB_mu, Gmu_n0, Gmu_w0, GE1, GG1, GMst_mu,
     + GNst_mu

      GA = PROPS(1)
      GB = PROPS(2)
      GC = PROPS(3)
      GD = PROPS(4)
      GR = PROPS(5)
```

```
      GL = PROPS(6)
      GNp= PROPS(7)


      Galpha1=PROPS(8)
      Galpha2=PROPS(9)
      Ga_M=PROPS(10)
      Ga_D=PROPS(11)


      PI=4.D0*DATAN(1.D0)

c     Viscosity parameters (Mineralized tissue in Chapter 5)
      Gmu_n0=7.25E-04
      Gmu_w0=7.25E-04
      GMst=2*GA*GB*GR/PI/exp(1.)
      GNst=GA/GMst
      GB_mu=4
      GMst_mu=2*Gmu_n0*GB*GB_mu*GR/PI/exp(1.)
      GNst_mu=Gmu_n0/GMst_mu

c     Parameters E1 AND G1
      GE1=2.3*GA
      GG1=2.3*GC

      RETURN
      END



C
C*************************************************************************
C   Read_Geom: This subroutine reads the geometric data of the assembly
C   It reads n_i, s_i, t_i, and xi for the assembly from data file
C*************************************************************************
C

      SUBROUTINE Read_Geom(KINC,Gn,Gs,Gt,Gxi)

      INCLUDE 'ABA_PARAM.INC'
      real*8 Gxi(218),Gn(218,3),Gs(218,3),Gt(218,3)

      OPEN(125,
     + FILE='C:\RIZA\WithE1\nstxi.dat',
     + STATUS='OLD')
        do i=1, 218
          read(125,*) a1,a2,a3,b1,b2,b3,c1,c2,c3,x

          Gn(i,1)=a1
          Gn(i,2)=a2
```

```
          Gn(i,3)=a3

          Gs(i,1)=b1
          Gs(i,2)=b2
          Gs(i,3)=b3

          Gt(i,1)=c1
          Gt(i,2)=c2
          Gt(i,3)=c3

          Gxi(i)=x

        end do
        REWIND (UNIT=125)


      RETURN
      END


C
C
C*****************************************************************************
C   Deltas: This calculates deltas-from the Read_Geom results and
C   the applied strain
C*****************************************************************************
C
      SUBROUTINE Deltas(NTENS,Strain,deln,dels,delt,delw,deli,Gn,Gs,Gt)

      INCLUDE 'ABA_PARAM.INC'
      real*8 Strain(NTENS),deln(218),
     + dels(218),delt(218),delw(218),deli(218,3)

      real*8 Gn(218,3),Gs(218,3),Gt(218,3)

      real*8 GA, GB, GC, GD, GR, GL, GNp, Galpha1, Galpha2,
     + Ga_M, Ga_D, GMst, GNst, GB_mu, Gmu_n0, Gmu_w0, GE1, GG1, GMst_mu,
     + GNst_mu

      COMMON/MatProp/ GA, GB, GC, GD, GR, GL, GNp, Galpha1, Galpha2,
     + Ga_M, Ga_D, GMst, GNst, GB_mu, Gmu_n0, Gmu_w0, GE1, GG1, GMst_mu,
     + GNst_mu


      do i=1, 218
       deli(i,1)=GL*
     +        (Strain(1)*Gn(i,1)+Strain(4)*Gn(i,2)+Strain(5)*Gn(i,3))
       deli(i,2)=GL*
     +        (Strain(4)*Gn(i,1)+Strain(2)*Gn(i,2)+Strain(6)*Gn(i,3))
       deli(i,3)=GL*
     +        (Strain(5)*Gn(i,1)+Strain(6)*Gn(i,2)+Strain(3)*Gn(i,3))
```

```
      deln(i)=deli(i,1)*Gn(i,1)+deli(i,2)*Gn(i,2)+deli(i,3)*Gn(i,3)
      dels(i)=deli(i,1)*Gs(i,1)+deli(i,2)*Gs(i,2)+deli(i,3)*Gs(i,3)
      delt(i)=deli(i,1)*Gt(i,1)+deli(i,2)*Gt(i,2)+deli(i,3)*Gt(i,3)
      delw(i)=sqrt(dels(i)*dels(i)+delt(i)*delt(i))

    end do


    RETURN
    END


C
C**********************************************************************
C   Calc_D_prev: This calculates deltas at previous increment
C**********************************************************************
C


    SUBROUTINE Calc_D_prev(NTENS,STRAN,dnprev,dwprev,diprev,Gn,Gs,Gt,
   + dsprev,dtprev)
    INCLUDE 'ABA_PARAM.INC'

    real*8 GA, GB, GC, GD, GR, GL, GNp, Galpha1, Galpha2,
   + Ga_M, Ga_D, GMst, GNst, GB_mu, Gmu_n0, Gmu_w0, GE1, GG1, GMst_mu,
   + GNst_mu

    COMMON/MatProp/ GA, GB, GC, GD, GR, GL, GNp, Galpha1, Galpha2,
   + Ga_M, Ga_D, GMst, GNst, GB_mu, Gmu_n0, Gmu_w0, GE1, GG1, GMst_mu,
   + GNst_mu

    real*8 STRAN(NTENS),dnprev(218),dsprev(218),dtprev(218),
   + dwprev(218),diprev(218,3)

    real*8 Gn(218,3),Gs(218,3),Gt(218,3)

    do i=1, 218

     diprev(i,1)=GL*
   +        (STRAN(1)*Gn(i,1)+STRAN(4)*Gn(i,2)+STRAN(5)*Gn(i,3))
     diprev(i,2)=GL*
   +        (STRAN(4)*Gn(i,1)+STRAN(2)*Gn(i,2)+STRAN(6)*Gn(i,3))
     diprev(i,3)=GL*
   +        (STRAN(5)*Gn(i,1)+STRAN(6)*Gn(i,2)+STRAN(3)*Gn(i,3))

     dnprev(i)=diprev(i,1)*Gn(i,1)+diprev(i,2)*Gn(i,2)+
   +          diprev(i,3)*Gn(i,3)
     dsprev(i)=diprev(i,1)*Gs(i,1)+diprev(i,2)*Gs(i,2)+
   +          diprev(i,3)*Gs(i,3)
     dtprev(i)=diprev(i,1)*Gt(i,1)+diprev(i,2)*Gt(i,2)+
```

```
     +          diprev(i,3)*Gt(i,3)
      dwprev(i)=sqrt(dsprev(i)*dsprev(i)+dtprev(i)*dtprev(i))

      end do

      RETURN
      END

C
C*************************************************************************
C   UpdateDeltaMax: This calculates maximum deltas
C*************************************************************************
C


      SUBROUTINE UpdateDeltaMax(DnMaxT,DnMaxC,deln,Dwmax,delw,
     + DnMaxTprev,DnMaxCprev,DwMaxprev)
      INCLUDE 'ABA_PARAM.INC'
      real*8 DnMaxT(218),DnMaxC(218),deln(218),DwMax(218),delw(218),
     + DnMaxTprev(218),DnMaxCprev(218),DwMaxprev(218)

      do i=1,218
         if (deln(i).GE.0) then  ! Check Normal Tension
            if (deln(i).GT.DnMaxT(i)) then
               DnMaxT(i)=deln(i)
            end if
         else  ! Check Normal Compression
            if (deln(i).LT.DnMaxC(i)) then
               DnMaxC(i)=deln(i)
            end if
         end if

         if (delw(i).GT.DwMax(i)) then  ! Check Shear
            DwMax(i)=delw(i)
         end if
      end do


      RETURN
      END

C
C*************************************************************************
C   FKMu_prev: This calculates forces at previous increment
C*************************************************************************
C

      SUBROUTINE FKMu_prev(Gkijprev,Gn,Gs,Gt,dnprev,dwprev,fiprev,
     + DnMaxTprev,DnMaxCprev,DwMaxprev,STRESS,NTENS,fnprev,fwprev,
     + DTIME,FnMaxTprev,FnMaxCprev,FwMaxprev,deln,delw,
     + fsprev,ftprev,dsprev,dtprev,Gmuij,Qij,GMeanSt,GMstprev,
```

```
+ DnMaxT,DnMaxC,DwMax,DelV,Gkw)

 INCLUDE 'ABA_PARAM.INC'

 real*8 Gn(218,3),Gs(218,3),Gt(218,3)
 real*8 Gkijprev(654,3)
 real*8 Gmuij(654,3),Qij(654,3)
 real*8 DnMaxTprev(218),DnMaxCprev(218),DwMaxprev(218)
 real*8 DnMaxT(218),DnMaxC(218),DwMax(218)
 real*8 FnMaxTprev(218),FnMaxCprev(218),FwMaxprev(218)
 real*8 STRESS(NTENS),GMeanSt(1),GMstprev(1)
 real*8 fnprev(218),fwprev(218),fsprev(218),ftprev(218),
+ dnprev(218),dwprev(218),dsprev(218),dtprev(218),fiprev(218,3),
+ deln(218),delw(218),DelV(218),Gkw(218)

 real*8 GE2, GMUn, Dmod, betaPL, G2, GMUw, Gkn, Gks, Gkt,
+ Ggmun, Ggmuw, Gzetan, Gzetaw, Gdenomn, Gdenomw, GPn, GPw,
+ GCn, GCw, GQn, GQw

 real*8 GA, GB, GC, GD, GR, GL, GNp, Galpha1, Galpha2,
+ Ga_M, Ga_D, GMst, GNst, GB_mu, Gmu_n0, Gmu_w0, GE1, GG1, GMst_mu,
+ GNst_mu

 COMMON/MatProp/ GA, GB, GC, GD, GR, GL, GNp, Galpha1, Galpha2,
+ Ga_M, Ga_D, GMst, GNst, GB_mu, Gmu_n0, Gmu_w0, GE1, GG1, GMst_mu,
+ GNst_mu

 betaPL=0

 GMeanSt(1)=-((STRESS(1)+STRESS(2)+STRESS(3))/3)


 Galpha3=Ga_D*abs(GMeanSt(1))

 GMst=GMst*(1+Ga_M*(GMeanSt(1)))

 do i=1, 218

    if (deln(i).GE.0) THEN !!! Tension-normal

       Dmod=GD


       if (deln(i).EQ.DnMaxT(i)) THEN
          GE2=GA*exp(-(dnprev(i)-fnprev(i)/GE1)/GB)
             GMUn=Gmu_n0*exp(-(dnprev(i)-fnprev(i)/GE1)/GB_mu/
+              GB)
       else  !!! UNLOADING
          GE2=GA*exp(-(DnMaxTprev(i)-FnMaxTprev(i)/GE1)/GB)
          GMUn=Gmu_n0*exp(-(DnMaxTprev(i)-FnMaxTprev(i)/GE1)/
+           GB_mu/GB)
```

```
        end if
      endif

      if (deln(i).LT.0) THEN !!! Compression-normal



        if (deln(i).EQ.DnMaxC(i)) THEN
          if (dnprev(i).EQ.0) THEN
         GE2=GMst*GNst
         GMUn=GMst_mu*GNst_mu
         else
         GE2=GMst*atan(GNst*(dnprev(i)-fnprev(i)/GE1))/dnprev(i)
         GMUn=GMst_mu*atan(GNst_mu*(dnprev(i)-fnprev(i)/GE1/
     +     GB_mu))/dnprev(i)
         endif

         else  !!! UNLOADING
          if (DnMaxCprev(i).EQ.0) THEN
         GE2=GMst*GNst
         GMUn=GMst_mu*GNst_mu
         else
         GE2=GMst*atan(GNst*(DnMaxCprev(i)-FnMaxCprev(i)/GE1))/
     +       DnMaxCprev(i)
         GMUn=GMst_mu*atan(GNst_mu*(DnMaxCprev(i)-FnMaxCprev(i)/
     +       GE1/GB_mu))/DnMaxCprev(i)
         endif
        end if
!
      if (dnprev(i).GT.GD*(1-Galpha1)/Galpha2) THEN  !!! Normal-Shear coupling
        Dmod=GD-Galpha2*dnprev(i)
      else
        Dmod=Galpha1*GD
     +       +(GD*(1-Galpha1)/Galpha2-dnprev(i))*Galpha3
      endif
    endif
!

    if (delw(i).EQ.DwMax(i)) THEN  !!! Shear
      G2=GC*exp(-abs(dwprev(i)-fwprev(i)/GG1)/DMod)
      GMUw=Gmu_w0*exp(-abs(dwprev(i)-fwprev(i)/GG1)/GB_mu/DMod)

    else  !!! UNLOADING


      G2=GC*exp(-abs(DwMaxprev(i)-FwMaxprev(i)/GG1)/DMod)/
     +    (1-betaPL)

      GMUw=Gmu_w0*exp(-abs(DwMaxprev(i)-FwMaxprev(i)/GG1)/GB_mu/
     +    DMod)/(1-betaPL)
    end if
```

```
c Local stiffness
      Gkn=GE1*GE2/(GE1+GE2)
      Gkw(i)=GG1*G2/(GG1+G2)
      Gks=Gkw(i)
      Gkt=Gkw(i)
c Local viscosity
      Ggmun=GE1*GMUn/(GE1+GE2)
      Ggmuw=GG1*GMUw/(GG1+G2)

c Local relaxation
      Gzetan=GMUn/(GE1+GE2)
      Gzetaw=GMUw/(GG1+G2)

c Micro-scale force components
      Gdenomn=DTIME+Gzetan
      Gdenomw=DTIME+Gzetaw
      GPn=-Ggmun/Gdenomn
      GPw=-Ggmuw/Gdenomw
      GCn=(Gkn*DTIME)/Gdenomn-GPn
      GCw=(Gkw(i)*DTIME)/Gdenomw-GPw
      GQn=Gzetan/Gdenomn
      GQw=Gzetaw/Gdenomw


      Gkijprev(3*i-2,1)=GCn*Gn(i,1)*Gn(i,1)+GCw*(Gs(i,1)*Gs(i,1))
     +          +GCw*(Gt(i,1)*Gt(i,1))
      Gkijprev(3*i-1,2)=GCn*Gn(i,2)*Gn(i,2)+GCw*(Gs(i,2)*Gs(i,2))
     +          +GCw*(Gt(i,2)*Gt(i,2))
      Gkijprev(3*i-0,3)=GCn*Gn(i,3)*Gn(i,3)+GCw*(Gs(i,3)*Gs(i,3))
     +          +GCw*(Gt(i,3)*Gt(i,3))

      Gkijprev(3*i-2,2)=GCn*Gn(i,1)*Gn(i,2)+GCw*(Gs(i,1)*Gs(i,2))
     +          +GCw*(Gt(i,1)*Gt(i,2))
      Gkijprev(3*i-2,3)=GCn*Gn(i,1)*Gn(i,3)+GCw*(Gs(i,1)*Gs(i,3))
     +          +GCw*(Gt(i,1)*Gt(i,3))
      Gkijprev(3*i-1,3)=GCn*Gn(i,2)*Gn(i,3)+GCw*(Gs(i,2)*Gs(i,3))
     +          +GCw*(Gt(i,2)*Gt(i,3))

      Gkijprev(3*i-1,1)=Gkijprev(3*i-2,2)
      Gkijprev(3*i-0,1)=Gkijprev(3*i-2,3)
      Gkijprev(3*i-0,2)=Gkijprev(3*i-1,3)

      Gmuij(3*i-2,1)=GPn*Gn(i,1)*Gn(i,1)+GPw*(Gs(i,1)*Gs(i,1))
     +          +GPw*(Gt(i,1)*Gt(i,1))
      Gmuij(3*i-1,2)=GPn*Gn(i,2)*Gn(i,2)+GPw*(Gs(i,2)*Gs(i,2))
     +          +GPw*(Gt(i,2)*Gt(i,2))
      Gmuij(3*i-0,3)=GPn*Gn(i,3)*Gn(i,3)+GPw*(Gs(i,3)*Gs(i,3))
     +          +GPw*(Gt(i,3)*Gt(i,3))

      Gmuij(3*i-2,2)=GPn*Gn(i,1)*Gn(i,2)+GPw*(Gs(i,1)*Gs(i,2))
```

```
     +            +GPw*(Gt(i,1)*Gt(i,2))
      Gmuij(3*i-2,3)=GPn*Gn(i,1)*Gn(i,3)+GPw*(Gs(i,1)*Gs(i,3))
     +            +GPw*(Gt(i,1)*Gt(i,3))
      Gmuij(3*i-1,3)=GPn*Gn(i,2)*Gn(i,3)+GPw*(Gs(i,2)*Gs(i,3))
     +            +GPw*(Gt(i,2)*Gt(i,3))

      Gmuij(3*i-1,1)=Gmuij(3*i-2,2)
      Gmuij(3*i-0,1)=Gmuij(3*i-2,3)
      Gmuij(3*i-0,2)=Gmuij(3*i-1,3)

      Qij(3*i-2,1)=GQn*Gn(i,1)*Gn(i,1)+GQw*(Gs(i,1)*Gs(i,1))
     +            +GQw*(Gt(i,1)*Gt(i,1))
      Qij(3*i-1,2)=GQn*Gn(i,2)*Gn(i,2)+GQw*(Gs(i,2)*Gs(i,2))
     +            +GQw*(Gt(i,2)*Gt(i,2))
      Qij(3*i-0,3)=GQn*Gn(i,3)*Gn(i,3)+GQw*(Gs(i,3)*Gs(i,3))
     +            +GQw*(Gt(i,3)*Gt(i,3))

      Qij(3*i-2,2)=GQn*Gn(i,1)*Gn(i,2)+GQw*(Gs(i,1)*Gs(i,2))
     +            +GQw*(Gt(i,1)*Gt(i,2))
      Qij(3*i-2,3)=GQn*Gn(i,1)*Gn(i,3)+GQw*(Gs(i,1)*Gs(i,3))
     +            +GQw*(Gt(i,1)*Gt(i,3))
      Qij(3*i-1,3)=GQn*Gn(i,2)*Gn(i,3)+GQw*(Gs(i,2)*Gs(i,3))
     +            +GQw*(Gt(i,2)*Gt(i,3))

      Qij(3*i-1,1)=Qij(3*i-2,2)
      Qij(3*i-0,1)=Qij(3*i-2,3)
      Qij(3*i-0,2)=Qij(3*i-1,3)


      fiprev(i,1)=fnprev(i)*Gn(i,1)
     +           +fsprev(i)*Gs(i,1)+ftprev(i)*Gt(i,1)
      fiprev(i,2)=fnprev(i)*Gn(i,2)
     +           +fsprev(i)*Gs(i,2)+ftprev(i)*Gt(i,2)
      fiprev(i,3)=fnprev(i)*Gn(i,3)
     +           +fsprev(i)*Gs(i,3)+ftprev(i)*Gt(i,3)

    enddo


    RETURN
    END


C
C*********************************************************************
C   Forces_Kij: This calculates forces at current increment
C*********************************************************************
C
    SUBROUTINE Forces_Kij(STRESS,NTENS,deli,diprev,Gkijprev,Gmuij,
    + Qij,DTIME,deln,dels,delt,Gn,Gs,Gt,fi,fnprev,fsprev,ftprev,Gkij,
    + dnprev,dsprev,dtprev,fiprev,fwprev,fn,fw,fs,ft,DelV,Gkw)
```

```
      INCLUDE 'ABA_PARAM.INC'
      real*8 STRESS(NTENS)
      real*8 deli(218,3),diprev(218,3),Gkijprev(654,3),Gmuij(654,3),
     + Qij(654,3),deln(218),dels(218),delt(218),fnprev(218),fsprev(218),
     + ftprev(218),fiprev(218,3),fwprev(218),fw(218),fn(218),fs(218),
     + ft(218),DelV(218),Gkw(218)
      real*8 dnprev(218),dsprev(218),dtprev(218)
      real*8 Gn(218,3),Gs(218,3),Gt(218,3)
      real*8 fi(218,3),Gkij(654,3)

      real*8 vis1, vis12, vis2, vis22, vis3, vis32

      real*8 GA, GB, GC, GD, GR, GL, GNp, Galpha1, Galpha2,
     + Ga_M, Ga_D, GMst, GNst, GB_mu, Gmu_n0, Gmu_w0, GE1, GG1, GMst_mu,
     + GNst_mu

      COMMON/MatProp/ GA, GB, GC, GD, GR, GL, GNp, Galpha1, Galpha2,
     + Ga_M, Ga_D, GMst, GNst, GB_mu, Gmu_n0, Gmu_w0, GE1, GG1, GMst_mu,
     + GNst_mu

c total force calculation

      do i=1, 218

        fi(i,1)=Gkijprev(3*i-2,1)*deli(i,1)
     +         +Gkijprev(3*i-2,2)*deli(i,2)
     +         +Gkijprev(3*i-2,3)*deli(i,3)


        vis1=Gmuij(3*i-2,1)*diprev(i,1)
     +      +Gmuij(3*i-2,2)*diprev(i,2)
     +      +Gmuij(3*i-2,3)*diprev(i,3)

        vis12=Qij(3*i-2,1)*fiprev(i,1)
     +      +Qij(3*i-2,2)*fiprev(i,2)
     +      +Qij(3*i-2,3)*fiprev(i,3)

        fi(i,1)=fi(i,1)+vis1+vis12

        fi(i,2)=Gkijprev(3*i-1,1)*deli(i,1)
     +         +Gkijprev(3*i-1,2)*deli(i,2)
     +         +Gkijprev(3*i-1,3)*deli(i,3)

        vis2=Gmuij(3*i-1,1)*diprev(i,1)
     +      +Gmuij(3*i-1,2)*diprev(i,2)
     +      +Gmuij(3*i-1,3)*diprev(i,3)

        vis22=Qij(3*i-1,1)*fiprev(i,1)
     +      +Qij(3*i-1,2)*fiprev(i,2)
     +      +Qij(3*i-1,3)*fiprev(i,3)
```

```
      fi(i,2)=fi(i,2)+vis2+vis22

      fi(i,3)=Gkijprev(3*i-0,1)*deli(i,1)
     +        +Gkijprev(3*i-0,2)*deli(i,2)
     +        +Gkijprev(3*i-0,3)*deli(i,3)

      vis3=Gmuij(3*i-0,1)*diprev(i,1)
     +     +Gmuij(3*i-0,2)*diprev(i,2)
     +     +Gmuij(3*i-0,3)*diprev(i,3)

      vis32=Qij(3*i-0,1)*fiprev(i,1)
     +     +Qij(3*i-0,2)*fiprev(i,2)
     +     +Qij(3*i-0,3)*fiprev(i,3)

      fi(i,3)=fi(i,3)+vis3+vis32

c Micro-scale forces

      fn(i)=fi(i,1)*Gn(i,1)+fi(i,2)*Gn(i,2)+fi(i,3)*Gn(i,3)
      fs(i)=fi(i,1)*Gs(i,1)+fi(i,2)*Gs(i,2)+fi(i,3)*Gs(i,3)
      ft(i)=fi(i,1)*Gt(i,1)+fi(i,2)*Gt(i,2)+fi(i,3)*Gt(i,3)
      fw(i)=sqrt(fs(i)*fs(i)+ft(i)*ft(i))




CCC---------- calculate Secant Kij-for Secant Cijkl----------
      Gkij(3*i-2,1)=Gkijprev(3*i-2,1)
      Gkij(3*i-1,2)=Gkijprev(3*i-1,2)
      Gkij(3*i-0,3)=Gkijprev(3*i-0,3)

      Gkij(3*i-2,2)=Gkijprev(3*i-2,2)
      Gkij(3*i-2,3)=Gkijprev(3*i-2,3)
      Gkij(3*i-1,3)=Gkijprev(3*i-1,3)

      Gkij(3*i-1,1)=Gkij(3*i-2,2)
      Gkij(3*i-0,1)=Gkij(3*i-2,3)
      Gkij(3*i-0,2)=Gkij(3*i-1,3)

    end do


    RETURN
    END

C
C*********************************************************************
C   UpdateFMax: This calculates maximum forces
C*********************************************************************
```

```
C

      SUBROUTINE UpdateFMax(FnMaxT,FnMaxC,fn,Fwmax,fw,
     + FnMaxTprev,FnMaxCprev,FwMaxprev)
      INCLUDE 'ABA_PARAM.INC'
      real*8 FnMaxT(218),FnMaxC(218),fn(218),FwMax(218),fw(218),
     + FnMaxTprev(218),FnMaxCprev(218),FwMaxprev(218)



      do i=1,218

         if (fn(i).GE.0) then  ! Check Normal Tension
            if (fn(i).GT.FnMaxT(i)) then
               FnMaxT(i)=fn(i)
            end if
         else  ! Check Normal Compression
            if (fn(i).LT.FnMaxC(i)) then
               FnMaxC(i)=fn(i)
            end if
         end if

         if (fw(i).GT.FwMax(i)) then  ! Check Shear
            FwMax(i)=fw(i)
         end if


      end do


      RETURN
      END

C
C*****************************************************************************
C   Calc_Stress: This calculates stresses
C*****************************************************************************
C

      SUBROUTINE Calc_Stress(NTENS,STRESS,fi,Gn,Gxi,Sij,
     + DSig,DEps)
      INCLUDE 'ABA_PARAM.INC'
      real*8 STRESS(NTENS),fi(218,3),Sij(3,3),DSig(3,3),DEps(3,3),
     + DSTRAN(NTENS)
      real*8 Gn(218,3),Gxi(218)

      real*8 GA, GB, GC, GD, GR, GL, GNp, Galpha1, Galpha2,
     + Ga_M, Ga_D, GMst, GNst, GB_mu, Gmu_n0, Gmu_w0, GE1, GG1, GMst_mu,
     + GNst_mu
```

```
      COMMON/MatProp/ GA, GB, GC, GD, GR, GL, GNp, Galpha1, Galpha2,
     + Ga_M, Ga_D, GMst, GNst, GB_mu, Gmu_n0, Gmu_w0, GE1, GG1, GMst_mu,
     + GNst_mu

      do i=1, 6
         STRESS(i)=0.0
      end do

      do i=1, 3
         do j=1, 3
            Sij(i,j)=0.0
         end do
      end do

      do ic=1,218
         Sij(1,1)=Sij(1,1)+Gxi(ic)*GL*GNp*fi(ic,1)*Gn(ic,1)
         Sij(1,2)=Sij(1,2)+Gxi(ic)*GL*GNp*fi(ic,1)*Gn(ic,2)
         Sij(1,3)=Sij(1,3)+Gxi(ic)*GL*GNp*fi(ic,1)*Gn(ic,3)

         Sij(2,1)=Sij(2,1)+Gxi(ic)*GL*GNp*fi(ic,2)*Gn(ic,1)
         Sij(2,2)=Sij(2,2)+Gxi(ic)*GL*GNp*fi(ic,2)*Gn(ic,2)
         Sij(2,3)=Sij(2,3)+Gxi(ic)*GL*GNp*fi(ic,2)*Gn(ic,3)

         Sij(3,1)=Sij(3,1)+Gxi(ic)*GL*GNp*fi(ic,3)*Gn(ic,1)
         Sij(3,2)=Sij(3,2)+Gxi(ic)*GL*GNp*fi(ic,3)*Gn(ic,2)
         Sij(3,3)=Sij(3,3)+Gxi(ic)*GL*GNp*fi(ic,3)*Gn(ic,3)
      end do


C     Stress components order 1:11    2:22    3:33    4:12    5:13    6:23
      if (NTENS.EQ.6) then
         STRESS(1)=Sij(1,1)
         STRESS(2)=Sij(2,2)
         STRESS(3)=Sij(3,3)

         STRESS(4)=(Sij(1,2)+Sij(2,1))/2
         STRESS(5)=(Sij(1,3)+Sij(3,1))/2
         STRESS(6)=(Sij(2,3)+Sij(3,2))/2
      elseif (NTENS.EQ.4) then
         STRESS(1)=Sij(1,1)
         STRESS(2)=Sij(2,2)
         STRESS(3)=Sij(3,3)

         STRESS(4)=(Sij(1,2)+Sij(2,1))/2
      end if


      RETURN
      END

C
```

```
C***********************************************************************
C   Calc_Cijkl: This calculates stiffness matrix
C***********************************************************************
C

      SUBROUTINE Calc_Cijkl(Cijkl,Gkij,Gn,Gxi,DSig,DEps)
      INCLUDE 'ABA_PARAM.INC'
      real*8 Cijkl(3,3,3,3),Gkij(654,3),DSig(3,3),DEps(3,3)
      real*8 Gn(218,3),Gxi(218)

      real*8 GA, GB, GC, GD, GR, GL, GNp, Galpha1, Galpha2,
     + Ga_M, Ga_D, GMst, GNst, GB_mu, Gmu_n0, Gmu_w0, GE1, GG1, GMst_mu,
     + GNst_mu

      COMMON/MatProp/ GA, GB, GC, GD, GR, GL, GNp, Galpha1, Galpha2,
     + Ga_M, Ga_D, GMst, GNst, GB_mu, Gmu_n0, Gmu_w0, GE1, GG1, GMst_mu,
     + GNst_mu

      do i=1, 3
         do j=1, 3
            do k=1, 3
               do l=1, 3
                  Cijkl(i,j,k,l)=0
               end do
            end do
         end do
      end do


      do i=1, 3
      do j=1, 3
      do k=1, 3
      do l=1, 3
      do ic=1, 218
      Cijkl(i,j,k,l)=Cijkl(i,j,k,l)+GL**2*GNp*Gxi(ic)*Gkij(3*ic-(3-i),k)
     +               *Gn(ic,j)*Gn(ic,l)
      end do
      end do
      end do
      end do
      end do

      RETURN
      END


C
C***********************************************************************
C   CijFromCijkl: This sends the stiffness matrix information to solver
C***********************************************************************
C
```

```
SUBROUTINE CijFromCijkl(NTENS,Cijkl,DDSDDE)
INCLUDE 'ABA_PARAM.INC'
real*8 Cijkl(3,3,3,3),DDSDDE(NTENS,NTENS)

DDSDDE(1,1)=Cijkl(1,1,1,1)
DDSDDE(1,2)=Cijkl(1,1,2,2)
DDSDDE(1,3)=Cijkl(1,1,3,3)

DDSDDE(2,1)=Cijkl(2,2,1,1)
DDSDDE(2,2)=Cijkl(2,2,2,2)
DDSDDE(2,3)=Cijkl(2,2,3,3)

DDSDDE(3,1)=Cijkl(3,3,1,1)
DDSDDE(3,2)=Cijkl(3,3,2,2)
DDSDDE(3,3)=Cijkl(3,3,3,3)

if (NTENS.EQ.6) then  !!! 3D element

DDSDDE(1,4)=(Cijkl(1,1,1,2)+Cijkl(1,1,2,1))/2
DDSDDE(1,5)=(Cijkl(1,1,1,3)+Cijkl(1,1,3,1))/2
DDSDDE(1,6)=(Cijkl(1,1,2,3)+Cijkl(1,1,3,2))/2

DDSDDE(2,4)=(Cijkl(2,2,1,2)+Cijkl(2,2,2,1))/2
DDSDDE(2,5)=(Cijkl(2,2,1,3)+Cijkl(2,2,3,1))/2
DDSDDE(2,6)=(Cijkl(2,2,2,3)+Cijkl(2,2,3,2))/2

DDSDDE(3,4)=(Cijkl(3,3,1,2)+Cijkl(3,3,2,1))/2
DDSDDE(3,5)=(Cijkl(3,3,1,3)+Cijkl(3,3,3,1))/2
DDSDDE(3,6)=(Cijkl(3,3,2,3)+Cijkl(3,3,3,2))/2


DDSDDE(4,1)=(Cijkl(1,2,1,1)+Cijkl(2,1,1,1))/2
DDSDDE(5,1)=(Cijkl(1,3,1,1)+Cijkl(3,1,1,1))/2
DDSDDE(6,1)=(Cijkl(2,3,1,1)+Cijkl(3,2,1,1))/2

DDSDDE(4,2)=(Cijkl(1,2,2,2)+Cijkl(2,1,2,2))/2
DDSDDE(5,2)=(Cijkl(1,3,2,2)+Cijkl(3,1,2,2))/2
DDSDDE(6,2)=(Cijkl(2,3,2,2)+Cijkl(3,2,2,2))/2

DDSDDE(4,3)=(Cijkl(1,2,3,3)+Cijkl(2,1,3,3))/2
DDSDDE(5,3)=(Cijkl(1,3,3,3)+Cijkl(3,1,3,3))/2
DDSDDE(6,3)=(Cijkl(2,3,3,3)+Cijkl(3,2,3,3))/2

DDSDDE(4,4)=(Cijkl(1,2,1,2)+Cijkl(2,1,1,2)+Cijkl(1,2,2,1))/4
+      +Cijkl(2,1,2,1)/4
DDSDDE(5,4)=(Cijkl(1,3,1,2)+Cijkl(3,1,1,2)+Cijkl(1,3,2,1))/4
+      +Cijkl(3,1,2,1)/4
DDSDDE(6,4)=(Cijkl(2,3,1,2)+Cijkl(3,2,1,2)+Cijkl(2,3,2,1))/4
+      +Cijkl(3,2,2,1)/4
```

```
 DDSDDE(4,5)=(Cijkl(1,2,1,3)+Cijkl(2,1,1,3)+Cijkl(1,2,3,1))/4
+      +Cijkl(2,1,3,1)/4
 DDSDDE(5,5)=(Cijkl(1,3,1,3)+Cijkl(3,1,1,3)+Cijkl(1,3,3,1))/4
+      +Cijkl(3,1,3,1)/4
 DDSDDE(6,5)=(Cijkl(2,3,1,3)+Cijkl(3,2,1,3)+Cijkl(2,3,3,1))/4
+      +Cijkl(3,2,3,1)/4

 DDSDDE(4,6)=(Cijkl(1,2,2,3)+Cijkl(2,1,2,3)+Cijkl(1,2,3,2))/4
+      +Cijkl(2,1,3,2)/4
 DDSDDE(5,6)=(Cijkl(1,3,2,3)+Cijkl(3,1,2,3)+Cijkl(1,3,3,2))/4
+      +Cijkl(3,1,3,2)/4
 DDSDDE(6,6)=(Cijkl(2,3,2,3)+Cijkl(3,2,2,3)+Cijkl(2,3,3,2))/4
+      +Cijkl(3,2,3,2)/4

 else if (NTENS.EQ.4) then !!! Plane strain element

 DDSDDE(1,4)=(Cijkl(1,1,1,2)+Cijkl(1,1,2,1))/2
 DDSDDE(2,4)=(Cijkl(2,2,1,2)+Cijkl(2,2,2,1))/2
 DDSDDE(3,4)=(Cijkl(3,3,1,2)+Cijkl(3,3,2,1))/2

 DDSDDE(4,1)=(Cijkl(1,2,1,1)+Cijkl(2,1,1,1))/2
 DDSDDE(4,2)=(Cijkl(1,2,2,2)+Cijkl(2,1,2,2))/2
 DDSDDE(4,3)=(Cijkl(1,2,3,3)+Cijkl(2,1,3,3))/2
 DDSDDE(4,4)=(Cijkl(1,2,1,2)+Cijkl(2,1,1,2)+Cijkl(1,2,2,1))/4
+      +Cijkl(2,1,2,1)/4

 end if


 RETURN
 END
```

APPENDIX C: THE MATERIAL MODEL PARAMETERS ASSIGNED IN THE FE MODELS

The following tables present the sets of material parameters used in Chapter 2, Chapter 4, Chapter 5 and Chapter 6.

Table 10.1: Material model parameters assigned in the single patch test model in Chapter 2.

User-defined nonlinear material model parameters	The bovine cortical bone tissue
$E_{no}^{T\alpha}$	7 N/mm
R	12
G_w	2 N/mm
B_n	$7x10^{-7}$ mm
B_{n0}	$1.32x10^{-6}$ mm
α_1	10.5
α_2	7
α_3	0.0012
α_4	0.0265 MPa^{-1}

Table 10.2: Material model parameters assigned in FE models in Chapter 4.

User-defined nonlinear material model parameters	Mineralized tissue (Plain strain model)	Mineralized tissue (3D FE model)	Adhesive polymer
$E_{no}^{T\alpha}$	7 N/mm	0.1365 N/mm	0.1365 N/mm
R	12	12	12
G_w	2 N/mm	0.039 N/mm	0.039 N/mm
B_n	$7x10^{-7}$ mm	$1.87x10^{-4}$ mm	$1.87x10^{-4}$ mm
B_{n0}	$1.32x10^{-6}$ mm	$3.52x10^{-4}$ mm	$3.52x10^{-4}$ mm
α_1	10.5	10.5	10.5
α_2	7	7	7
α_3	0.0012	0.0012	0.0012
α_4	0.0265 MPa^{-1}	$2.65x10^{-5}$ MPa^{-1}	$2.65x10^{-5}$ MPa^{-1}

Table 10.3: Material model parameters used in FE models in Chapter 5.

User-defined nonlinear material model parameters	The mineralized tissue (The cortical bone)	E1 adhesive polymer	C1 adhesive polymer
$E_{no}^{T\alpha}$	0.180 N/mm	0.101 N/mm	0.052 N/mm
R	2	1.5	1.5
G_w	0.051 N/mm	0.029 N/mm	0.015 N/mm
B_n	2.67×10^{-4} mm	2.03×10^{-4} mm	3.86×10^{-4} mm
B_{n0}	5.03×10^{-4} mm	3.82×10^{-4} mm	7.28×10^{-4} mm
α_1	10.5	10.5	10.5
α_2	7	7	7
α_3	0.0012	0.0012	0.0012
α_4	2.65×10^{-5} MPa^{-1}	2.65×10^{-5} MPa^{-1}	2.65×10^{-5} MPa^{-1}

Table 10.4: Material model parameters used in FE models in Chapter 6.

UMAT parameters	C1 hybrid layer	E1 hybrid layer	E1 hybrid layer (remineralized)	E1 hybrid layer (degraded)
$E_{no}^{T\alpha}$	0.019 N/mm	0.055 N/mm	0.060 N/mm	0.049 N/mm
R	1.5	2	2	2
G_w	0.005 N/mm	0.016 N/mm	0.017 N/mm	0.014 N/mm
B_n	2.09×10^{-4} mm	1.22×10^{-4} mm	1.22×10^{-4} mm	1.22×10^{-4} mm
B_{n0}	4.60×10^{-4} mm	2.30×10^{-4} mm	2.30×10^{-4} mm	2.30×10^{-4} mm
α_1	10.5	10.5	10.5	10.5
α_2	7	7	7	7
α_3	0.0012	0.0012	0.0012	0.0012
α_4	2.65×10^{-5} MPa^{-1}	2.65×10^{-5} MPa^{-1}	2.65×10^{-5} MPa^{-1}	2.65×10^{-5} MPa^{-1}

APPENDIX D: THE TEST RESULTS FROM THE DIAMETRAL COMPRESSION TEST IN CHAPTER 3

The following table presents the mean, the minimum and the maximum failure force and failure displacement values obtained from the diametral compression tests in Chapter 3.

Table 11.1: The failure force and failure displacement results obtained in the experiments. The results are presented in the mean, minimum and maximum values for all specimens at all loading rates.

		Peak force [N]			**Peak displacement [mm]**		
Specimen	**Load rate [mm/min]**	**Mean**	**Min**	**Max**	**Mean**	**Min**	**Max**
Mineralized tissue	1	77.61	69.49	84.11	0.39	0.37	0.44
	0.2	51.50	48.90	56.44	0.28	0.27	0.31
C1 polymer	1	28.50	27.57	29.74	0.52	0.46	0.57
	0.2	21.56	21.30	22.06	0.55	0.46	0.71
E1 polymer	1	38.63	35.34	41.85	0.34	0.33	0.40
	0.2	27.48	26.95	28.05	0.32	0.29	0.33
Mineralized tissue - C1 interface	1	86.67	70.75	93.00	0.48	0.38	0.62
	0.2	81.69	69.70	88.07	0.41	0.37	0.45
Mineralized tissue - E1 interface	1	119.72	110.23	129.16	0.51	0.48	0.55
	0.2	103.49	93.25	112.63	0.48	0.43	0.50

LIST OF REFERENCES

[1] D.H. Pashley, F.R. Tay, L. Breschi, L. Tjaderhane, R.M. Carvalho, M. Carrilho, A. Tezvergil-Mutluay, State of the art etch-and-rinse adhesives, Dent. Mater. 27(1) (2011) 1-16.

[2] P. Kalesinskas, T. Kacergius, A. Ambrozaitis, V. Peciuliene, D. Ericson, Reducing dental plaque formation and caries development. A review of current methods and implications for novel pharmaceuticals, Stomatologija 16(2) (2014) 44-52.

[3] L. Tjaderhane, F.D. Nascimento, L. Breschi, A. Mazzoni, I.L.S. Tersariol, S. Geraldeli, A. Tezvergil-Mutluay, M. Carrilho, R.M. Carvalho, F.R. Tay, D.H. Pashley, Strategies to prevent hydrolytic degradation of the hybrid layer-A review, Dent. Mater. 29(10) (2013) 999-1011.

[4] L. Breschi, A. Mazzoni, A. Ruggeri, M. Cadenaro, R. Di Lenarda, E.D. Dorigo, Dental adhesion review: Aging and stability of the bonded interface, Dent. Mater. 24(1) (2008) 90-101.

[5] R.S. Schwartz, R. Fransman, Adhesive dentistry and endodontics: Materials, clinical strategies and procedures for restoration of access cavities: A review, J. Endod. 31(3) (2005) 151-165.

[6] J. De Munck, K. Van Landuyt, M. Peumans, A. Poitevin, P. Lambrechts, M. Braem, B. Van Meerbeek, A critical review of the durability of adhesion to tooth tissue: Methods and results, J Dent Res 84(2) (2005) 118-132.

[7] G.B.D.O.D. Collaborators, E. Bernabe, W. Marcenes, C.R. Hernandez, J. Bailey, L.G. Abreu, V. Alipour, S. Amini, J. Arabloo, Z. Arefi, A. Arora, M.A. Ayanore, T.W. Barnighausen, A. Bijani, D.Y. Cho, D.T. Chu, C.S. Crowe, G.T. Demoz, D.G. Demsie, Z.S. Dibaji Forooshani, M. Du, M. El Tantawi, F. Fischer, M.O. Folayan, N.D. Futran, Y.C.D. Geramo, A. Haj-Mirzaian, N. Hariyani, A. Hasanzadeh, S. Hassanipour, S.I. Hay, M.K. Hole, S. Hostiuc, M.D. Ilic, S.L. James, R. Kalhor, L. Kemmer, M. Keramati, Y.S. Khader, S. Kisa, A. Kisa, A. Koyanagi, R. Lalloo, Q. Le Nguyen,

S.D. London, N.D. Manohar, B.B. Massenburg, M.R. Mathur, H.G. Meles, T. Mestrovic, A. Mohammadian-Hafshejani, R. Mohammadpourhodki, A.H. Mokdad, S.D. Morrison, J. Nazari, T.H. Nguyen, C.T. Nguyen, M.R. Nixon, T.O. Olagunju, K. Pakshir, M. Pathak, N. Rabiee, A. Rafiei, K. Ramezanzadeh, M.J. Rios-Blancas, E.M. Roro, S. Sabour, A.M. Samy, M. Sawhney, F. Schwendicke, F. Shaahmadi, M.A. Shaikh, C. Stein, M.R. Tovani-Palone, B.X. Tran, B. Unnikrishnan, G.T. Vu, A. Vukovic, T.S.S. Warouw, Z. Zaidi, Z.J. Zhang, N.J. Kassebaum, Global, Regional, and National Levels and Trends in Burden of Oral Conditions from 1990 to 2017: A Systematic Analysis for the Global Burden of Disease 2017 Study, J Dent Res 99(4) (2020) 362-373.

[8] P. Spencer, Q. Ye, L.Y. Song, R. Parthasarathy, K. Boone, A. Misra, C. Tamerler, Threats to adhesive/dentin interfacial integrity and next generation bio-enabled multifunctional adhesives, J Biomed Mater Res B 107(8) (2019) 2673-2683.

[9] X. Zhou, X. Huang, M. Li, X. Peng, S. Wang, X. Zhou, L. Cheng, Development and status of resin composite as dental restorative materials, Journal of Applied Polymer Science 136(44) (2019) 48180.

[10] C.A. Stewart, Y. Finer, Biostable, antidegradative and antimicrobial restorative systems based on host-biomaterials and microbial interactions, Dent. Mater. 35(1) (2019) 36-52.

[11] J.P. Matinlinna, L.V. Lassila, I. Kangasniemi, A. Yli-Urpo, P.K. Vallittu, Shear bond strength of Bis-GMA resin and methacrylated dendrimer resins on silanized titanium substrate, Dent Mater 21(3) (2005) 287-96.

[12] P.E. Cardoso, R.R. Braga, M.R. Carrilho, Evaluation of micro-tensile, shear and tensile tests determining the bond strength of three adhesive systems, Dent Mater 14(6) (1998) 394-8.

[13] N. Kanemura, H. Sano, J. Tagami, Tensile bond strength to and SEM evaluation of ground and intact enamel surfaces, J Dent 27(7) (1999) 523-30.

[14] S.R. Armstrong, D.B. Boyer, J.C. Keller, Microtensile bond strength testing and failure analysis of two dentin adhesives, Dent Mater 14(1) (1998) 44-50.

[15] J.M. Patierno, F.A. Rueggeberg, R.W. Anderson, R.N. Weller, D.H. Pashley, Push-out strength and SEM evaluation of resin composite bonded to internal cervical dentin, Endod Dent Traumatol 12(5) (1996) 227-36.

[16] L. De Lorenzis, A. Rizzo, A. La Tegola, A modified pull-out test for bond of near-surface mounted FRP rods in concrete, Compos Part B-Eng 33(8) (2002) 589-603.

[17] Y. Shimada, S. Yamaguchi, J. Tagami, Micro-shear bond strength of dual-cured resin cement to glass ceramics, Dent. Mater. 18(5) (2002) 380-388.

[18] A. Hashimoto, H. Ohno, M. Kaga, H. Sano, F.R. Tay, H. Oguchi, Y. Araki, M. Kubota, Over-etching effects on micro-tensile bond strength and failure patterns for two dentin bonding systems, Journal of Dentistry 30(2-3) (2002) 99-105.

[19] S.S. Scherrer, P.F. Cesar, M.V. Swain, Direct comparison of the bond strength results of the different test methods: a critical literature review, Dent Mater 26(2) (2010) e78-93.

[20] J.L. Ferracane, J.M. Dossett, F. Pelogia, M.R. Macedo, T.J. Hilton, Navigating the dentin bond strength testing highway: lessons and recommendations, Journal of adhesion science and technology 23(7-8) (2009) 1007-1022.

[21] P. Spencer, A. Misra, Material-tissue Interfacial Phenomena: Contributions from Dental and Craniofacial Reconstructions, Woodhead Publishing2016.

[22] A. Misra, V. Singh, R. Parthasarathy, Material-tissue interfacial phenomena: challenges in mathematical modeling, Material-Tissue Interfacial Phenomena, Elsevier2017, pp. 253-264.

[23] V. Singh, A. Misra, O. Marangos, J. Park, Q. Ye, S.L. Kieweg, P. Spencer, Viscoelastic and fatigue properties of model methacrylate-based dentin adhesives, Journal of Biomedical Materials Research Part B: Applied Biomaterials 95(2) (2010) 283-290.

[24] V. Singh, A. Misra, R. Parthasarathy, Q. Ye, J. Park, P. Spencer, Mechanical properties of methacrylate-based model dentin adhesives: Effect of loading rate and moisture exposure, Journal of Biomedical Materials Research Part B: Applied Biomaterials 101(8) (2013) 1437-1443.

[25] N. Maruyama, Y. Shibata, M.V. Swain, Y. Kataoka, Y. Takiguchi, A. Yamada, K. Maki, T. Miyazaki, Strain-rate stiffening of cortical bone: observations and implications from nanoindentation experiments, Nanoscale 6(24) (2014) 14863-14871.

[26] A.D. Drozdov, A constitutive model for nonlinear viscoelastic media, International Journal of Solids and Structures 34(21) (1997) 2685-2707.

[27] A.E. Green, R.S. Rivlin, The mechanics of non-linear materials with memory, Archive for Rational Mechanics and Analysis 1(1) (1957) 1-21.

[28] J. Lai, A. Bakker, 3-D Schapery representation for non-linear viscoelasticity and finite element implementation, Computational mechanics 18(3) (1996) 182-191.

[29] A. Pipkin, T. Rogers, A non-linear integral representation for viscoelastic behaviour, Journal of the Mechanics and Physics of Solids 16(1) (1968) 59-72.

[30] R. Schapery, Nonlinear viscoelastic solids, International journal of solids and structures 37(1-2) (2000) 359-366.

[31] R.A. Schapery, On the characterization of nonlinear viscoelastic materials, Polymer Engineering & Science 9(4) (1969) 295-310.

[32] A. Wineman, Nonlinear viscoelastic solids—a review, Mathematics and Mechanics of Solids 14(3) (2009) 300-366.

[33] R.K.A. Al-Rub, M.K. Darabi, A thermodynamic framework for constitutive modeling of time-and rate-dependent materials. Part I: Theory, International Journal of Plasticity 34 (2012) 61-92.

[34] M. Brünig, O. Chyra, D. Albrecht, L. Driemeier, M. Alves, A ductile damage criterion at various stress triaxialities, International journal of plasticity 24(10) (2008) 1731-1755.

[35] C. Collard, V. Favier, S. Berbenni, M. Berveiller, Role of discrete intra-granular slip bands on the strain-hardening of polycrystals, International Journal of Plasticity 26(2) (2010) 310-328.

[36] L. Contrafatto, M. Cuomo, A new thermodynamically consistent continuum model for hardening plasticity coupled with damage, International journal of solids and structures 39(25) (2002) 6241-6271.

[37] M.K. Darabi, R.K.A. Al-Rub, E.A. Masad, C.-W. Huang, D.N. Little, A thermo-viscoelastic–viscoplastic–viscodamage constitutive model for asphaltic materials, International Journal of Solids and Structures 48(1) (2011) 191-207.

[38] K. Kamrin, Nonlinear elasto-plastic model for dense granular flow, International Journal of Plasticity 26(2) (2010) 167-188.

[39] K.K. Muraleetharan, C. Liu, C. Wei, T.C. Kibbey, L. Chen, An elastoplatic framework for coupling hydraulic and mechanical behavior of unsaturated soils, International Journal of Plasticity 25(3) (2009) 473-490.

[40] M. Naderi, S. Hoseini, M. Khonsari, Probabilistic simulation of fatigue damage and life scatter of metallic components, International Journal of Plasticity 43 (2013) 101-115.

[41] E. Ossa, V. Deshpande, D. Cebon, Triaxial deformation behavior of bituminous mixes, Journal of Materials in Civil Engineering 22(2) (2010) 124-135.

[42] R. Vignjevic, N. Djordjevic, V. Panov, Modelling of dynamic behaviour of orthotropic metals including damage and failure, International journal of plasticity 38 (2012) 47-85.

[43] G.Z. Voyiadjis, R.K.A. Al-Rub, A.N. Palazotto, Thermodynamic framework for coupling of non-local viscoplasticity and non-local anisotropic viscodamage for dynamic localization problems using gradient theory, International Journal of Plasticity 20(6) (2004) 981-1038.

[44] L. Chen, J.-F. Shao, H. Huang, Coupled elastoplastic damage modeling of anisotropic rocks, Computers and Geotechnics 37(1-2) (2010) 187-194.

[45] L. Contrafatto, M. Cuomo, A framework of elastic–plastic damaging model for concrete under multiaxial stress states, International Journal of Plasticity 22(12) (2006) 2272-2300.

[46] M.K. Darabi, R.K.A. Al-Rub, E.A. Masad, D.N. Little, A thermodynamic framework for constitutive modeling of time-and rate-dependent materials. Part II: Numerical aspects and application to asphalt concrete, International Journal of Plasticity 35 (2012) 67-99.

[47] V. Deshpande, D. Cebon, Micromechanical modeling of steady-state deformation in asphalt, Journal of materials in civil engineering 16(2) (2004) 100-106.

[48] A. Drescher, N. Kringos, T. Scarpas, On the behavior of a parallel elasto-visco-plastic model for asphaltic materials, Mechanics of Materials 42(2) (2010) 109-117.

[49] A.A.-C. Guéry, F. Cormery, J.-F. Shao, D. Kondo, A micromechanical model of elastoplastic and damage behavior of a cohesive geomaterial, International Journal of Solids and structures 45(5) (2008) 1406-1429.

[50] M.E. Kutay, M. Lanotte, Viscoelastic continuum damage (VECD) models for cracking problems in asphalt mixtures, International Journal of Pavement Engineering 19(3) (2018) 231-242.

[51] E. Levenberg, J. Uzan, Triaxial small-strain viscoelastic-viscoplastic modeling of asphalt aggregate mixes, Mechanics of Time-Dependent Materials 8(4) (2004) 365-384.

[52] E. Masad, L. Tashman, D. Little, H. Zbib, Viscoplastic modeling of asphalt mixes with the effects of anisotropy, damage and aggregate characteristics, Mechanics of Materials 37(12) (2005) 1242-1256.

[53] W. Shen, J.-F. Shao, D. Kondo, B. Gatmiri, A micro–macro model for clayey rocks with a plastic compressible porous matrix, International journal of plasticity 36 (2012) 64-85.

[54] Y. Yang, Y. Lai, Y. Dong, S. Li, The strength criterion and elastoplastic constitutive model of frozen soil under high confining pressures, Cold regions science and technology 60(2) (2010) 154-160.

[55] A. Misra, V. Singh, M.K. Darabi, Asphalt pavement rutting simulated using granular micromechanics-based rate-dependent damage-plasticity model, International Journal of Pavement Engineering (2017) 1-14.

[56] P. Poorsolhjouy, A. Misra, Effect of intermediate principal stress and loading-path on failure of cementitious materials using granular micromechanics, International Journal of Solids and Structures 108 (2017) 139-152.

[57] S. Armstrong, S. Geraldeli, R. Maia, L.H. Raposo, C.J. Soares, J. Yamagawa, Adhesion to tooth structure: a critical review of "micro" bond strength test methods, Dent Mater 26(2) (2010) e50-62.

[58] D. Zaytsev, P. Panfilov, Deformation behavior of human dentin in liquid nitrogen: A diametral compression test, Materials Science and Engineering: C 42 (2014) 48-51.

[59] C.S. Chang, A. Misra, Theoretical and experimental study of regular packings of granules, Journal of engineering mechanics 115(4) (1989) 704-720.

[60] C.S. Chang, A. Misra, Packing structure and mechanical properties of granulates, Journal of Engineering Mechanics 116(5) (1990) 1077-1093.

[61] H. Deresiewicz, Stress-strain relations for a simple model of a granular medium, COLUMBIA UNIV NEW YORK DEPT OF CIVIL ENGINEERING AND ENGINEERING MECHANICS, 1957.

[62] P. Digby, The effective elastic moduli of porous granular rocks, (1981).

[63] K. Walton, The effective elastic moduli of a random packing of spheres, Journal of the Mechanics and Physics of Solids 35(2) (1987) 213-226.

[64] C. Chang, P.-Y. Hicher, An elasto-plastic model for granular materials with microstructural consideration, International journal of solids and structures 42(14) (2005) 4258-4277.

[65] A. Misra, Y. Yang, Micromechanical model for cohesive materials based upon pseudo-granular structure, International Journal of Solids and Structures 47(21) (2010) 2970-2981.

[66] A. Misra, P. Poorsolhjouy, Granular micromechanics model for damage and plasticity of cementitious materials based upon thermomechanics, Mathematics and Mechanics of Solids (2015) 1081286515576821.

[67] A. Misra, V. Singh, Micromechanical model for viscoelastic materials undergoing damage, Continuum Mechanics and Thermodynamics 25(2-4) (2013) 343-358.

[68] A. Misra, V. Singh, Thermomechanics-based nonlinear rate-dependent coupled damage-plasticity granular micromechanics model, Continuum Mechanics and Thermodynamics 27(4-5) (2015) 787-817.

[69] A. Misra, V. Singh, Nonlinear granular micromechanics model for multi-axial rate-dependent behavior, International Journal of Solids and Structures 51(13) (2014) 2272-2282.

[70] A. Misra, R. Sarikaya, Computational analysis of tensile damage and failure of mineralized tissue assisted with experimental observations, Proceedings of the Institution of Mechanical Engineers, Part H: Journal of Engineering in Medicine (2019) 0954411919870650.

[71] A. Misra, P. Spencer, O. Marangos, Y. Wang, J.L. Katz, Parametric study of the effect of phase anisotropy on the micromechanical behaviour of dentin-adhesive interfaces, J R Soc Interface 2(3) (2005) 145-57.

[72] V. Singh, A. Misra, O. Marangos, J. Park, Q. Ye, S.L. Kieweg, P. Spencer, Fatigue life prediction of dentin-adhesive interface using micromechanical stress analysis, Dent Mater 27(9) (2011) e187-95.

[73] P. Spencer, Q. Ye, J. Park, E.M. Topp, A. Misra, O. Marangos, Y. Wang, B.S. Bohaty, V. Singh, F. Sene, J. Eslick, K. Camarda, J.L. Katz, Adhesive/Dentin interface: the weak link in the composite restoration, Ann Biomed Eng 38(6) (2010) 1989-2003.

[74] S. Phrukkanon, M.F. Burrow, M.J. Tyas, Effect of cross-sectional surface area on bond strengths between resin and dentin, Dent Mater 14(2) (1998) 120-8.

[75] B. Ramanathan, V. Raman, Split tensile strength of cohesive soils, Soils and Foundations 14(1) (1974) 71-76.

[76] Standard Test Method for Splitting Tensile Strength of Intact Rock Core Specimens, ASTM International, 2016.

[77] Standard Test Method for Splitting Tensile Strength of Cylindrical Concrete Specimens, ASTM International, 2004.

[78] P. Jonsen, H.A. Haggblad, K. Sommer, Tensile strength and fracture energy of pressed metal powder by diametral compression test, Powder Technol 176(2-3) (2007) 148-155.

[79] C. Shang, I.C. Sinka, J. Pan, Modelling of the break force of tablets under diametrical compression, Int J Pharmaceut 445(1-2) (2013) 99-107.

[80] D. Zaytsev, P. Panfilov, Deformation behavior of human enamel under diametral compression, Mater Lett 136 (2014) 130-132.

[81] C.A. Carrera, Y.-C. Chen, Y. Li, J. Rudney, C. Aparicio, A. Fok, Dentin-composite bond strength measurement using the Brazilian disk test, Journal of dentistry 52 (2016) 37-44.

[82] N. Nakabayashi, K. Kojima, E. Masuhara, The promotion of adhesion by the infiltration of monomers into tooth substrates, J. Biomed. Mater. Res. 16(3) (1982) 265-273.

[83] H. Sano, T. Shono, T. Takatsu, H. Hosoda, Microporous Dentin Zone beneath Resin-Impregnated Layer, Oper Dent 19(2) (1994) 59-64.

[84] L.E. Bertassoni, J.P.R. Orgel, O. Antipova, M.V. Swain, The dentin organic matrix - limitations of restorative dentistry hidden on the nanometer scale, Acta Biomater 8(7) (2012) 2419-2433.

[85] H. Sano, T. Yoshikawa, P. Pereira, N. Kanemura, M. Morigamui, J. Tagami, D.H. Pashley, Long-term durability of dentin bonds made with a self-etching primer, in vivo, J Dent Res 78(4) (1999) 906-911.

[86] M.J. Soappman, A. Nazari, J.A. Porter, D. Arola, A comparison of fatigue crack growth in resin composite, dentin and the interface, Dent. Mater. 23(5) (2007) 608-614.

[87] C.J. Kleverlaan, A.J. Feilzer, Polymerization shrinkage and contraction stress of dental resin composites, Dent. Mater. 21(12) (2005) 1150-1157.

[88] J.-F. Roulet, Benefits and disadvantages of tooth-coloured alternatives to amalgam, Journal of dentistry 25(6) (1997) 459-473.

[89] P. Spencer, Q.Y.J. PARK, A. Misra, B.S. Bohaty, V. Singh, R. Parthasarathy, F. Sene, S.E. de Paiva GONÇALVES, J. Laurence, Durable bonds at the adhesive/dentin interface: an impossible mission or simply a moving target?, Brazilian dental science 15(1) (2012) 4.

[90] J. Kruzic, R. Ritchie, Fatigue of mineralized tissues: cortical bone and dentin, Journal of the mechanical behavior of biomedical materials 1(1) (2008) 3-17.

[91] S.-X. Xie, K. Boone, S.K. VanOosten, E. Yuca, L. Song, X. Ge, Q. Ye, P. Spencer, C. Tamerler, Peptide Mediated Antimicrobial Dental Adhesive System, Applied Sciences 9(3) (2019) 557.

[92] L.Y. Song, Q. Ye, X.P. Ge, A. Misra, C. Tamerler, P. Spencer, Fabrication of hybrid crosslinked network with buffering capabilities and autonomous strengthening characteristics for dental adhesives, Acta Biomater 67 (2018) 111-121.

[93] L.Y. Song, Q. Ye, X.P. Ge, A. Misra, P. spencer, Mimicking Nature: Self-strengthening Properties in a Dental Adhesive Acta Biomater 35 (2016) 138-152.

[94] L. Song, Q. Ye, X. Ge, A. Misra, P. Spencer, Mimicking nature: Self-strengthening properties in a dental adhesive, Acta Biomater 35 (2016) 138-152.

[95] R. Sarikaya, L. Song, Q. Ye, A. Misra, C. Tamerler, P. Spencer, Evolution of Network Structure and Mechanical Properties in Autonomous-Strengthening Dental Adhesive, Polymers (Basel) 12(9) (2020).

[96] Y.M. Chen, T.F. Xi, Y.F. Zheng, L. Zhou, Y.Z. Wan, In vitro structural changes of nano-bacterial cellulose immersed in phosphate buffer solution, Journal of Biomimetics, Biomaterials and Tissue Engineering, Trans Tech Publ, 2011, pp. 55-66.

[97] X. Guo, Y. Wang, P. Spencer, Q. Ye, X. Yao, Effects of water content and initiator composition on photopolymerization of a model BisGMA/HEMA resin, Dent. Mater. 24(6) (2008) 824-831.

[98] L. Song, Q. Ye, X. Ge, A. Misra, J.S. Laurence, C.L. Berrie, P. Spencer, Synthesis and evaluation of novel dental monomer with branched carboxyl acid group, Journal of Biomedical Materials Research Part B: Applied Biomaterials 102(7) (2014) 1473-1484.

[99] Q. Ye, J. Park, E. Topp, P. Spencer, Effect of photoinitiators on the in vitro performance of a dentin adhesive exposed to simulated oral environment, Dent. Mater. 25(4) (2009) 452-458.

[100] R. Parthasarathy, A. Misra, J. Park, Q. Ye, P. Spencer, Diffusion coefficients of water and leachables in methacrylate-based crosslinked polymers using absorption experiments, Journal of Materials Science: Materials in Medicine 23(5) (2012) 1157-1172.

[101] U. Wolfram, J. Schwiedrzik, Post-yield and failure properties of cortical bone, BoneKEy reports 5 (2016).

[102] R.A. Abdullah, T. Tsutsumi, Evaluation of tensile strength of Brazilian test under solid and ring disks using finite element analysis, Sains Malaysiana 47(4) (2018) 683-689.

[103] D. Hobbs, The tensile strength of rocks, International Journal of Rock Mechanics and Mining Sciences & Geomechanics Abstracts, Elsevier, 1964, pp. 385-396.

[104] J. Hudson, Tensile strength and the ring test, International Journal of Rock Mechanics and Mining Sciences & Geomechanics Abstracts, Elsevier, 1969, pp. 91-97.

[105] D.-y. Li, W. Tao, T.-j. Cheng, X.-l. Sun, Static and dynamic tensile failure characteristics of rock based on splitting test of circular ring, Transactions of Nonferrous Metals Society of China 26(7) (2016) 1912-1918.

[106] N. Erarslan, D.J. Williams, Experimental, numerical and analytical studies on tensile strength of rocks, International Journal of Rock Mechanics and Mining Sciences 49 (2012) 21-30.

[107] D. Li, L.N.Y. Wong, The Brazilian disc test for rock mechanics applications: review and new insights, Rock mechanics and rock engineering 46(2) (2013) 269-287.

[108] J.H. Zhao, P.S. Yu, S.H. Dong, The Influence of Crosslink Density on the Failure Behavior in Amorphous Polymers by Molecular Dynamics Simulations, Materials 9(4) (2016).

[109] J. Yang, C.Y. Shao, L. Meng, Strain Rate-Dependent Viscoelasticity and Fracture Mechanics of Cellulose Nanofibril Composite Hydrogels, Langmuir 35(32) (2019) 10542-10550.

[110] I. Barszczewska-Rybarek, The role of molecular structure on impact resistance and bending strength of photocured urethane-dimethacrylate polymer networks, Polym Bull 74(10) (2017) 4023-4040.

[111] X.P. Ge, Q. Ye, L.Y. Song, P. Spencer, J.S. Laurence, Effect of crosslinking density of polymers and chemical structure of amine-containing monomers on the neutralization capacity of dentin adhesives, Dent. Mater. 31(10) (2015) 1245-1253.

[112] J.E. Elliott, L.G. Lovell, C.N. Bowman, Primary cyclization in the polymerization of bis-GMA and TEGDMA: a modeling approach to understanding the cure of dental resins, Dent. Mater. 17(3) (2001) 221-229.

[113] I.M. Barszczewska-Rybarek, Characterization of urethane-dimethacrylate derivatives as alternative monomers for the restorative composite matrix, Dent. Mater. 30(12) (2014) 1336-1344.

[114] J. Park, J. Eslick, Q. Ye, A. Misra, P. Spencer, The influence of chemical structure on the properties in methacrylate-based dentin adhesives, Dent. Mater. 27(11) (2011) 1086-1093.

[115] J. Bates, G. Stafford, A. Harrison, Masticatory function—a review of the literature: (II) Speed of movement of the mandible, rate of chewing and forces developed in chewing, Journal of Oral Rehabilitation 2(4) (1975) 349-361.

[116] R. DeLong, W.H. Douglas, An artificial oral environment for testing dental materials, IEEE Transactions on Biomedical Engineering 38(4) (1991) 339-345.

[117] T. Jemt, S. Karlsson, Mandibular movements of young adults recorded by intraorally placed light-emitting diodes, Journal of Prosthetic Dentistry 42(6) (1979) 669-673.

[118] C. Stappert, P. Guess, S. Chitmongkolsuk, T. Gerds, J. Strub, Partial coverage restoration systems on molars–comparison of failure load after exposure to a mastication simulator, Journal of Oral Rehabilitation 33(9) (2006) 698-705.

[119] R. Sarikaya, L. Song, E. Yuca, S.-X. Xie, K. Boone, A. Misra, P. Spencer, C. Tamerler, Bio-inspired multifunctional adhesive system for next generation bio-additively designed dental restorations, Journal of the Mechanical Behavior of Biomedical Materials (2020) 104135.